Functionalized Droplet Microfluidics: From Patterning to Sensing and Energy Harvesting

A thesis submitted

in partial fulfillment of the requirements

for the degree of

Doctor of Philosophy

by

Siddharth Thakur

Roll No. 156107004

Department of Chemical Engineering

Indian Institute of Technology Guwahati

November 2021

CERTIFICATE

It is certified that the work contained in the thesis entitled **"Functionalized Droplet Microfluidics: From Patterning to Sensing and Energy Harvesting"**, by Mr. Siddharth Thakur, has been carried out under our supervision and has not been submitted elsewhere for a degree.

Thesis supervisors

Dr. Ashok Kumar Dasmahapatra
Professor
Department of Chemical Engineering
Indian Institute of Technology
Guwahati

Dr. Dipankar Bandyopadhyay
Professor
Department of Chemical Engineering
Indian Institute of Technology
Guwahati

ACKNOWLEDGEMENT

The entire duration of this doctoral program has been full of memorable and enriching experiences for me. Not only have I been fortunate enough to understand my limitations and improve upon them on a professional front but I have also learned valuable lessons that have made me a better person. As I near the tenure of my PhD study, I would like to express my earnest and heartfelt gratitude to the people who have supported me throughout the journey. First and foremost, I would like to thank my thesis supervisor Dr. Dipankar Bandyopadhyay for his patience, wisdom and guidance which aided me to endure and resolve challenges that I encountered during my PhD tenure. I sincerely thank him for allowing me the latitude to explore scientific pursuits and provide a guiding light throughout this study. I would like to express my sincere gratitude to Dr. Ashok Kumar Dasmahapatra for always inspiring and supporting me during my PhD course. His wisdom and knowledge helped in building different analytical perspectives. I am grateful to the members of my doctoral committee, Dr. Siddhartha Sankar Ghosh, Dr. Tapas Kumar Mandal and Dr. Partho Sarathi Gooh Pattader, for accepting to evaluate my thesis and provide insightful comments.

I would also like to take this opportunity to express my sincere gratitude and regards to the Indian reviewer, Prof. Jitendra Sangwai, Dept. Of Chemical Engineering, IIT Madras, India and International reviewer, Prof. Nam-Trung Nguyen, Director of Queensland Micro- and Nanotechnology Centre, Griffith University, Australia for giving their valuable time to consider and evaluate my thesis.

During my PhD study, I had the wonderful experience of learning from my lab seniors Dr. Kartick Mondal, Dr. Seim Timung, Dr. Amit Kumar Singh, Dr. Bolledu Ravi, Dr. Sunny Kumar, Dr. Nayanmani Das (Institute Post-Doctoral Fellow) and Dr. Dhrubojyoti Das (Institute Post-Doctoral Fellow) who not only assisted me in developing technical knowledge but also provided constant encouragement. I would also like to particularly thank Dr. Saptak Rarotra and Dr. Mitradip Bhattacharjee for the stimulating discussions.

I am thankful to the members of our research group Ms. Satarupa Dutta, Ms. Snigdha Chakraborty, Mr. Joydip Chaudhuri, Mr. Ankur Pandey, Mr. Preetam Roy, Dr. Tamanna Bhuyan, Dr. Bhaskarjyoti Sharma, Dr. Abir Ghosh, Dr. Shirsendu Mitra, Mr. Surjendu Maity,

Acknowledgement

Mr. Nayanjyoti Kalita, Ms. Tanushree Ghoshal, Mr. Vinod Vanarse, Mr. Chintak Parashar, Mr. Jiwajyoti Mahanta, Mr. Sahil Jagnani, Mr. Prathu and Ms. Devirupa Gogoi.

I would grateful to all the faculty members and staff of the Department of Chemical Engineering, Centre for Nanotechnology and Central Instruments Facility, IIT Guwahati.

I would like to sincerely acknowledge the financial support provided by the DST Nano-Mission program, MeitY and DST SERB, Government of India.

This journey of mine would not have been possible without the help and support of my grandparents, parents, my wife Sutapa, family members and my friends. I extend my sincere thanks to them for their unwavering faith in me.

Siddharth Thakur

SYNOPSIS

Chapter I. Introduction

Mesoscopic liquid droplets are ubiquitous in nature. From sessile droplet-based diagnostic devices to rainwater energy harvesting - liquid droplets offer a versatile platform for the construction of functional systems. This unique geometry has been adapted across diverse scientific and engineering domains owing to its attractive characteristics. These characteristics have also aided in highlighting its potential to replace conventional processes at the macroscale. Some of the distinct advantages associated with liquid droplet systems at the micro/nanoscale includes: (i) limited usage of fluid volume with the smallest possible area available per unit mass, (ii) an incompressible system that is soft and deformable, (iii) thermodynamically an open system suitable for facile mass, momentum, and energy transfer through the surface, and (iv) facilitating the incorporation of different constituents that impart optically and electrochemically active properties.

Rapid progress in the field of science and technology has fostered the miniaturized devices that are more efficient than their macroscale counterparts. In this regard, the sessile droplet-based systems offer an attractive and alternate system configuration that can integrate and function on a large-scale to tackle numerous challenges. Since droplets- based systems have a high surface area to volume ratio, they are particularly prone to enhanced rates of mass and energy transfer with their surroundings. The confined system possessed by the droplet geometry allows uniform interaction with its surrounding environment via its curved interface, which lacks spatial inhomogeneities. Thus, in the presence of external fields, diffusion-limited processes such as chemical reactions, are facilitated owing to the formation of the convective flow patterns within a droplet, as characterized by a relatively high Reynolds number. For example, prior-art suggest the usages of thermal and solutal field gradients, for devising systems that can perform analyte sensing as well as energy harvesting.

Recent years have also witnessed the tremendous growth of hybrid systems in the healthcare sector. These alternate methodologies have employed facile and effective detection strategies for confronting the major issue of affordable diagnostic devices for low-resource settings. In this regard, microfluidic technologies have presented a promising route for facilitating storage, reaction, and separation of identifying biomarkers. For instance, liquid droplet systems have

carried out rapid analysis either by utilizing evaporative-based techniques or operating in the presence of other field-driven methodologies. Moreover, given the versatile nature of droplets-based systems, in particular water droplet-based platforms, it is not surprising that of late an increasing number of studies have focused on its usage for addressing another critical issue of harvesting ambient energy. For example, the triboelectric generators have exploited the polar nature of the water microdroplets for harvesting energy from the electrical-double layers formed near the surfaces where the droplets impinge. Other measures such as microscale fuel cells involve the addition of reactive components that can enhance the conversion of chemical to electrical energy. The advantage lies with their ability to incorporate elements such as photosensitive electrodes while connecting serially on a large-scale to generate high-density power. Such a range of adaptations has only aided in the deployment of droplet-based platforms for tackling futuristic issues.

On the other hand, different facets of liquid droplets offer opportunities for utilization towards different objectives. Physical characteristics such as the droplet curvature have been utilized for magnification purposes in optics-related tasks. In this aspect, modification of the droplet medium from isotropic to anisotropic have been reported to provide an additional handle over light-manipulation capabilities. For macroscale applications, it becomes vital to assimilate a multitude of such uniform optically-active structures that can be employed as fluidic lenses or photomasks. As compared to the expensive photo/electron lithographic-based techniques, dewetting processes involving fluids or soft-lithographic techniques offer an affordable route towards the realization of these structures. Furthermore, with regards to optics-related applications, functional materials such as the ionic liquids or liquid crystals (LC) have been increasingly investigated. The internal molecular ordering of LC can be tailored using various external stimuli such that the output light is transmitted accordingly. Exploring LC thin film dewetting processes on soft, slippery surfaces may present a facile way for creating numerous self-organized micro/nano-droplets for photonic applications.

Considering such characteristics of droplet platforms, it becomes abundantly clear that their role is expanding across different domains at the micro/nanoscale, leading to the generation of alternate technological solutions. In this dissertation, different field-driven systems including acoustic, photonic and chemical-potential, have been selectively utilized for exploring the underlying physics associated with droplet platforms towards patterning, sensing and energy harvesting applications. Micro-scale experimental setups employing solid and liquid substrates have been utilized to uncover the different phenomenon associated with such droplet systems. The point-wise objectives concerning the different chapters in this thesis are as follows:

- ❖ Investigation of acoustic wave catalyzed urea detection employing a pulsatile sonophillic microdroplet sensor.
- ❖ Exploring microdroplet photofuel cells for harvesting high-density energy capable of simultaneously working as a dye degradation platform.
- ❖ Generation of self-organized liquid crystal microdroplets for utilization as tunable soft-photomasks.
- ❖ Chemotactic dewetting of a nematic liquid crystal droplet on a liquid bath.

In the subsequent sections II–V of this report, primary details highlighting the different technical aspects belonging to the thesis chapters have been provided. A short summary of the various works along with the scope for future research in these areas has also been provided.

Chapter II. Acoustic Wave Catalyzed Urea Detection Utilizing a Pulsatile Microdroplet Sensor

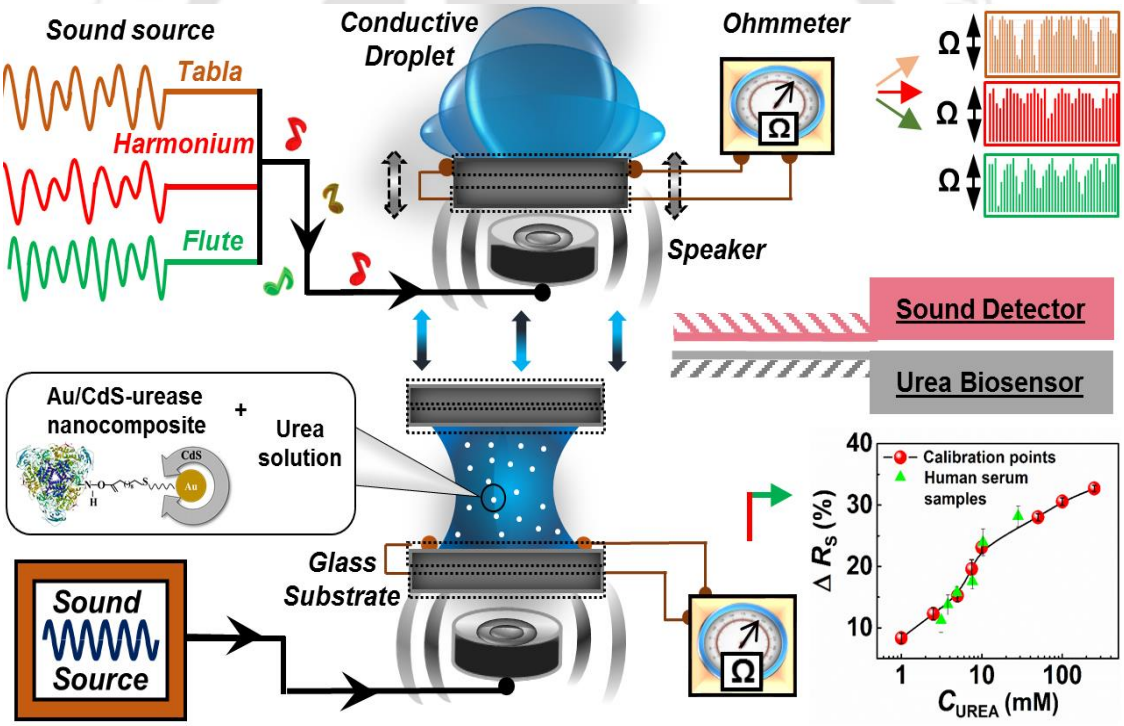

Figure 1. Overall schematic of droplet-based sensor. A freestanding configuration was used to sense the changes in acoustic signals emanating from different instruments. Further, a sandwich configuration was utilized to sense the urea concentrations within an unknown serum sample.

In this chapter, we observe and utilize the variations measured in the electrical resistance across a conducting water microdroplet when it is placed on a glass substrate and mechanically vibrated at the natural frequency of the setup with the help of an acoustic source. The reduction in the resistance across the droplet was magnified owing to the formation of vortices in the

matrix when the periodic oscillation of the substrate was increased. The variation in the resistance could be tuned with the frequency of the sound source, which was found to be maximum when a 10 µL droplet was vibrated at ~320 Hz. Interestingly, the variation in resistance across the oscillating droplet could follow and distinguish the musical notes in the octaves – "sur", or rhythmic cycles – "taal", originating from the Indian-origin musical instruments such as, flute, harmonium, whistle, and tabla.

Further, when a suspension of urease-stabilized gold-cadmium-sulfide nanocomposite was suspended inside the droplet, and mixed with an analyte containing urea solution, the change in the resistance during the operational time period was found to monotonically vary with the concentration of urea in the analyte. The enzymatic reaction between urea and urease was found to follow a faster first-order chemical kinetics than the commonly observed Michaelis–Menten pathway owing to the presence of the moving nanocomposites and mixing-vortices under the optimal acoustic excitations. The specific lock-and-key enzymatic reaction helped in extending these experimental results to estimate the unknown levels of urea in human blood serum samples.

Chapter III. Microdroplet PhotoFuel Cells to Harvest High Density Energy and Dye Degradation

This chapter presents the design and development of a membraneless photofuel cell, namely µ-DropFC, to harvest chemical and solar energies simultaneously. The droplet prototype also performed environmental remediation to demonstrate its multitasking potential as a sustainable hybrid device in a single embodiment. Hydrogen peroxide (H_2O_2) microdroplet at optimal pH and salt loading was utilized as the fuel, integrated with an Al anode and zinc phthalocyanine coated Cu cathode. The presence of n-type semiconductor zinc phthalocyanine in between the electrolyte and metal enabled the formation of a photo-active Schottky junction suitable for power generation under light. Concurrently, the oxidation and reduction of H_2O_2 on the electrodes helped in the conversion of chemical energy into the electrical one in the same membraneless setup. Suspension of Au nanoparticles (NPs) in the droplet helped in enhancing the overall power density under photonic illumination through the effects of localized surface Plasmon resonance (LSPR). Further, the presence of photo-active n-type CdS NPs enabled catalytic photo-degradation of dyes under light in the same embodiment.

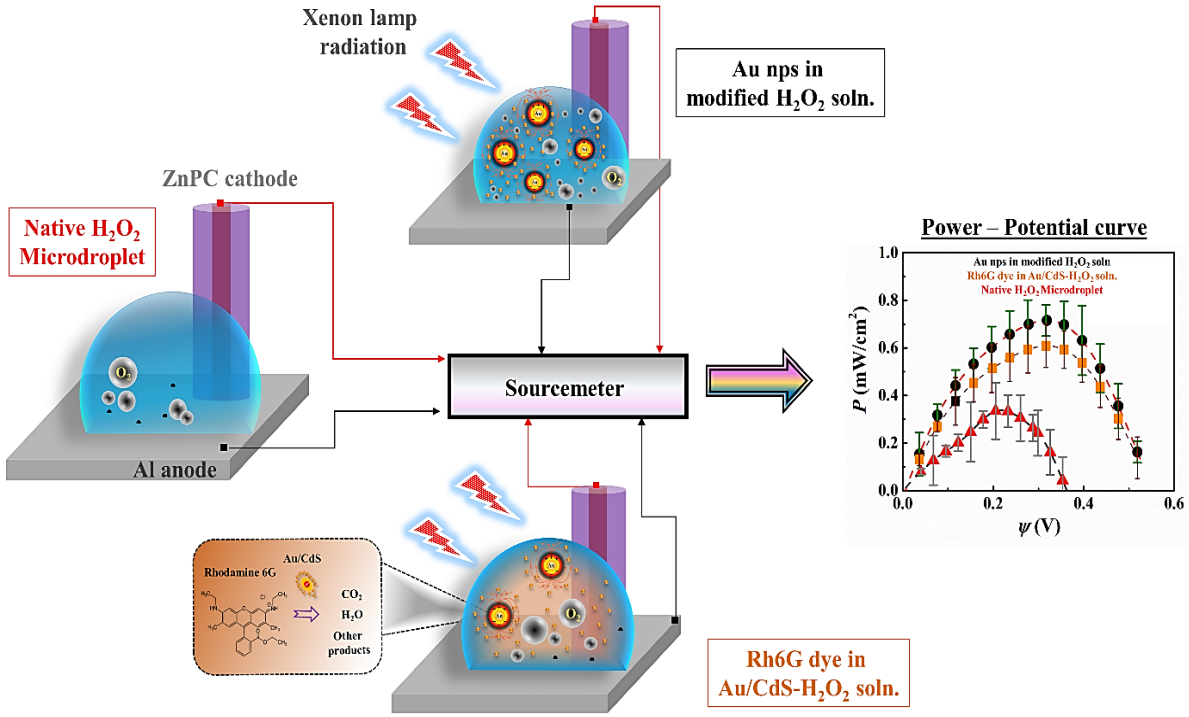

Figure 2. Overview of the hybrid membraneless droplet-based photofuel cell (μ-DropFC). Utilization of Au NPs in a H2O2 μ-DropFC enhanced the overall power density in presence of external radiations. Interestingly, the same droplet configuration could also harvest significant energy while being engaged in degradation of an environmental pollutant.

A 40 μL μ-DropFC could show a significantly high open circuit potential of ~0.58 V along with a power density of 0.72 mW/cm^2. Under the same condition, integration of ten such μ-DropFCs produced a power density of ~7 mW/cm^2 at an efficiency of 3.4%. Moreover, the μ-DropFC also degraded ~85% of an industrial pollutant Rhodamine 6G in 1 h while generating a power density of ~ 0.6 mW/cm^2. The performance parameters of μ-DropFC were found to be either comparable or superior to the existing prototypes. In a way, the membraneless and high-performance μ-DropFC harnessed energy from multiple sources while engaging in environmental remediation.

Chapter IV. Self-Organized Liquid Crystal Droplets as Tunable Soft-Photomasks

Utilization of liquid/liquid dewetting methodology for the generation of large-area, miniaturized, distinct, and stable droplets offer itself as a promising scalable technique for catering to a wide variety of micro/nano applications. In this chapter, a single-step pathway was presented to generate a multitude of quasi-monodispersed LC droplets obtained via the spreading of a 4-Cyano-4'-pentylbiphenyl (5CB)-laden hexane droplet over a CTAB-water bath. A facile soft-photolithography setup was prepared to incorporate these 5CB droplets as fluidic photomasks for the generation of distinct features over photoresist (PR) surfaces.

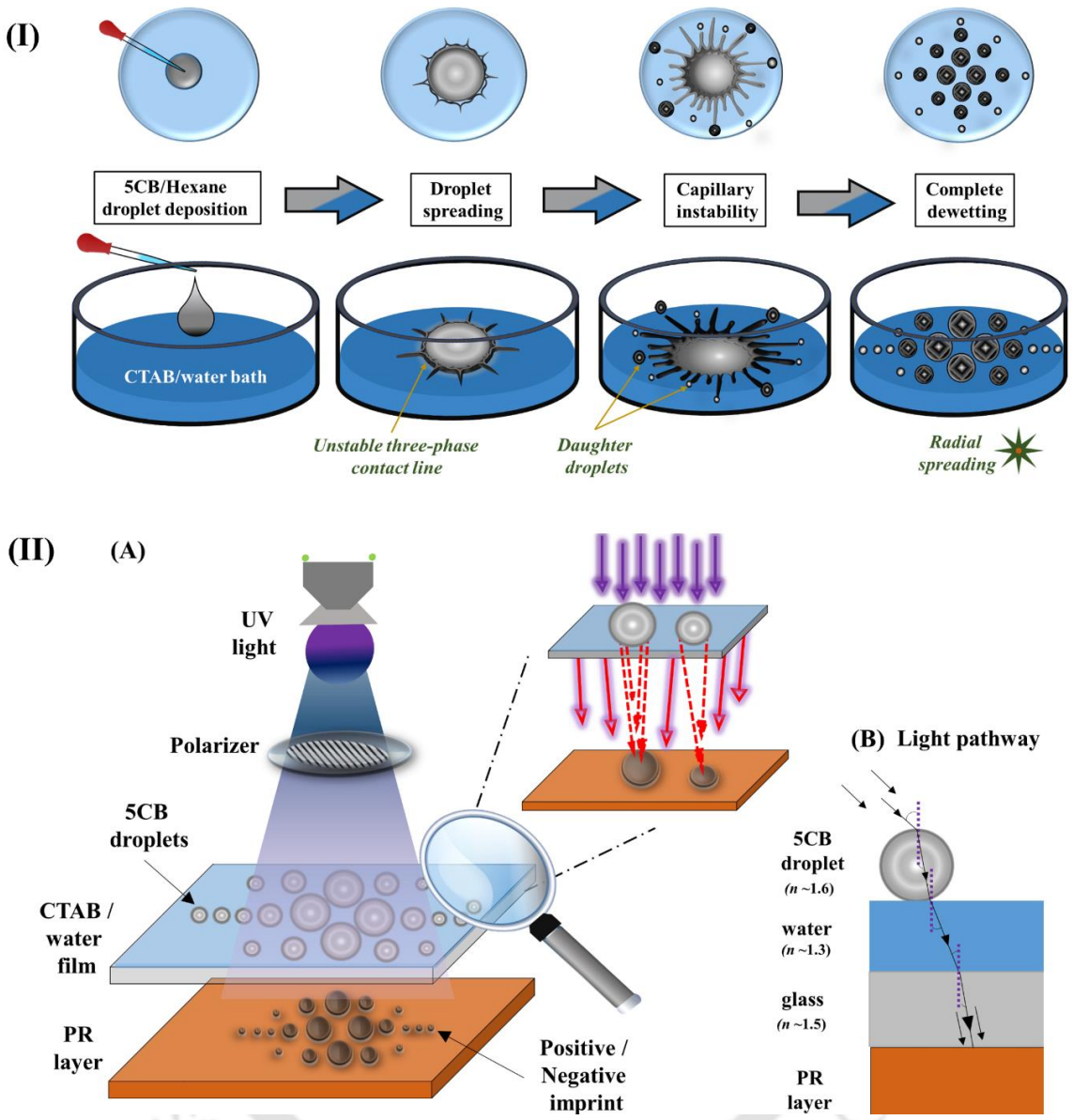

Figure 3. Schematic diagram highlighting the phenomenon and application of dewetting of the liquid bilayer. (I) A 5CB-hexane compound droplet was dispensed over a CTAB-laden water bath. Rapid spreading and subsequent retraction of the compound droplet led to generation of multitude of 5CB droplets from the contact line. (II) (A) 5CB droplets were used in a soft-photolithography setup for obtaining unique patterns on a photoresist (PR) substrate. (B) Light path from the surroundings to the PR surface. *n* represents the refractive index of material.

For two different PR tones, surface features with micron to nano-scale dimensions were obtained over a large area: flattened droplets were obtained on a positive photoresist substrate while donut-like features were obtained on a negative photoresist substrate. Solvent vapor annealing of the LC droplets led to their phase transition, which provided an additional handle over the diversity of patterns obtained. The dewetting dynamics concerning 5CB droplet dewetting was greatly influenced by the surface-active agent (CTAB) concentration. Low

concentrations favored laminar spreading of the droplet with gradual retraction, while at high concentrations (beyond critical concentration limit), droplet dynamics was difficult to follow due to rapid and uneven retraction profiles on account of a heterogeneous surface-energy substrate. The solvent selection also played a role in governing the overall dewetting period along with the dimensions of daughter droplets generated over the water-surfactant bath: hexane promoted a fast-dewetting phase with miniaturized droplets generation (1–90 μm) while heptanol resulted in slow dewetting dynamics with irregular, large daughter droplets (> 100 μm). Different dewetting modes for 5CB were observed across two other solvents viz. toluene and chloroform. Remarkably, the dewetting dynamics displayed by 5CB was not material-specific and was observed in polystyrene-toluene solution over the water-surfactant bath.

Chapter V. Chemotactic Dewetting of a Nematic Droplet on a Water Bath

Techniques involving the creation of miniaturized optically-active droplets without the need for cumbersome instrumentation highlight their potential for being adapted towards large-scale operations. In this chapter, experimental investigations uncover the dynamics associated with a nematic LC droplet when it is placed on an immiscible liquid bath, in the vicinity of a miscible solvent droplet. A 5CB droplet on a water bath displays various contact line dynamics when a hexane droplet is dispensed close to it. The highly volatile hexane interacts with the 5CB droplet during its adsorption on 5CB surface as well as during spreading on the water bath. In both case, this results in the lowering of local surface tension gradient within the 5CB droplet. This surface tension gradient across the droplet bulk led to the initiation of recirculation within the 5CB droplet matrix. An osmotic pressure gradient was also created on the water interface, which along with the convective forces within the water bath, aided in the 5CB droplet motility. Beyond a critical recirculation rate within the 5CB droplet, centripetal forces generated due to the recirculation overcome the surface tension forces resulting in the instantaneous distortion of the droplet boundary. It was observed that the recirculation ceases to exist at the point of distortion, and gradually picked-up over a period of time, with the process repeating itself. Furthermore, at the 5CB droplet boundary facing hexane, the spreading of the 5CB droplet on the water bath led to the creation of numerous 5CB droplets which resisted coalescence. The spreading of the droplet was followed by the occurrence of capillary instability at the droplet periphery.

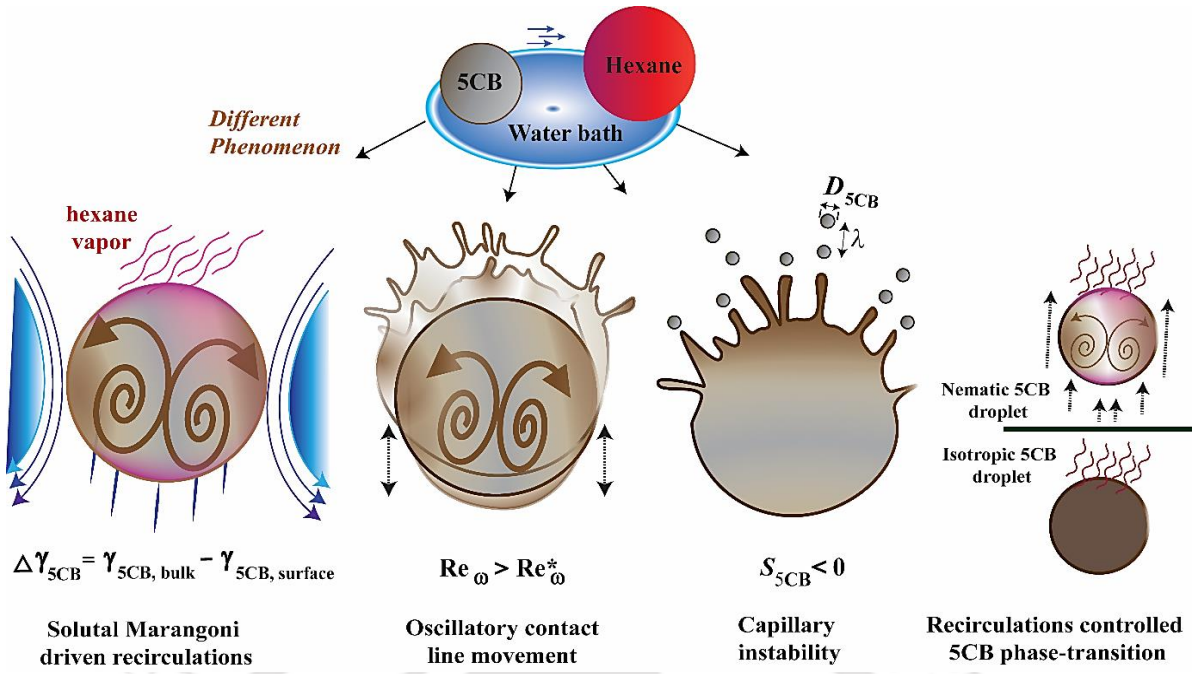

Figure 4. Overview of the entire process. Isolated 5CB and hexane droplets when placed at a close distance on a water bath display numerous spatiotemporal droplet dynamics. Initially, the solutal Marangoni effect initiates recirculation within the 5CB droplet owing to the surface tension gradient between the surface and bulk 5CB. This recirculation initiates convective flow within the water bath that aids in the droplet motility. Beyond a certain recirculation rate, centripetal forces generated within the droplet overcome surface tension at the periphery that results in periodic oscillations of the 5CB droplet. Moreover, the droplet region close to the hexane source undergoes spreading on the water bath. The thin film eventually undergoes capillary instability as the hexane evaporates and changes the local spreading coefficient. Remarkably, the recirculation set in within the droplet enhance the rate of adsorption of hexane which causes the phase transition of 5CB from nematic to isotropic. Once in the isotropic phase, the droplet no longer displays any lateral or longitudinal movement on the water bath.

Additionally, in presence of hexane, the recirculation was also observed to enhance the rate of phase transition in the 5CB droplet from nematic to isotropic as it led to faster uptake of hexane. Once in the isotropic state, the droplet resisted further oscillation or lateral/longitudinal movement because of the reduction in the surface tension gradient.

Chapter VI. Conclusions and Future Scope

This thesis presents various proof-of-concept droplet systems highlighting their versatility and applicability towards applications ranging from biosensing and energy harvesting to patterning. The second chapter highlights the utility of a facile setup that employs an acoustically vibrated conducting water microdroplet tailored for sensing purpose. It was observed that the vibrations imparted to the microdroplet resulted in the variation of electrical resistance across it, which was measured by the two electrodes placed at diametrically opposite ends of the droplet. The

change in the electrical resistance of the droplet could be correlated with the change in external acoustic signal. Variation in the external signal frequency and tempo could be distinguished thereby facilitating the droplet setup to be used as a sound sensor. Additionally, the similar detection principle was also employed for the development of a urea biosensor. Doping the droplet with Au/CdS nanocomposite linked urease enzyme and stimulating it with acoustic signals in presence of urea solution, led to the preparation of a calibration curve. Herein, the change in urea concentration within the droplet could be correlated to the change in electrical resistance across the droplet. It was also observed that the rate of urea-urease enzymatic reaction was significantly faster in presence of acoustic signals. Better interaction between constituents was due to presence of recirculation as a result of the vibrating substrate, and presence of Au/CdS nanocomposite which offered a higher interfacial area for the reaction. Comparison of the microdroplet-based urea biosensor with a standard laboratory technique revealed that the droplet sensor could determine unknown urea levels in serum samples within a 10% - 15% margin of error.

The third chapter explores the role of a microdroplet as a hybrid energy harvesting setup. The droplet utilized hydrogen peroxide as the fuel and oxidant, and ZnPC/Cu, and Al as cathode and anode, respectively. Electrochemical energy harvesting could be achieved as the droplet operated as a photofuel cell system. Presence of additives such as Au NPs aided in enhancing the power and current density values. In presence of external illumination, the LSPR effect of the Au NPs increased the localized electric field intensity which improved the charge transfer characteristics between electrodes and suppressed charge recombination at the ZnPC electrode. A 40 µL µ-DropFC could generate an open circuit potential of ~0.58 V and power density of 0.72 mW/cm^2. Utilizing the same droplet composition in a VLSI configuration of 10 cells generated a power density of ~7 mW/cm^2 at an efficiency of 3.4%. It was also observed that the same droplet setup could be employed as a dye degradation unit. Rhodamine 6G dye was added to the droplet and within an hour ~ 85% of the dye was degraded. Moreover, energy harvesting during this operation resulted in generation of ~ 0.6 mW/cm^2, thereby highlighting the hybrid characteristic of the setup of that being able to generate energy while being engaged in dye degradation.

The fourth chapter discusses a pathway to realize self-organized optically-active 5CB droplets on a large-scale that was employed as photomasks in a photolithography experiment. Experiments involving the deposition of a 5CB-in-hexane drop on a CTAB laden water bath were carried out. Rapid spreading of the 5CB-in-hexane droplet was assisted by the interfacial tension gradient. After reaching equilibrium, the leading edge of the drop was observed to

retract at a gradually slow rate. Varying the CTAB concentration led to the emergence of two modes of dewetting – spinodal (below CMC limit) and heterogeneous (above CMC limit). The retraction of the 5CB compound droplet led to the ejection of numerous daughter 5CB droplets from the three-phase contact line due to capillary instability. The dimensions of the daughter 5CB droplets could be primarily controlled by varying the 5CB concentration and CTAB concentration. Furthermore, these miniaturized 5CB droplets were utilized as soft photomasks in an unconventional photolithography setup to generate diverse 2D, 3D patterns. Solvent vapor annealing provided an additional handle over light modulation and subsequent generation of features. Experiments also revealed that changing the 5CB solvent led to new modes of dewetting over the CTAB bath. Additionally, these dewetting routes were not 5CB specific and were observed in case of polystyrene-solvent drop deposition as well.

The fifth chapter investigates the striking contact line dynamics displayed by the pristine 5CB droplet when it is deposited on a water bath in presence of a hexane droplet. A facile route for generation of multitudes of miniaturized 5CB droplets was uncovered. Hexane adsorption on the 5CB droplet surface as well as its contact with the 5CB droplet over the water bath, results in change of local surface tension within the nematic droplet. The solutal Marangoni stresses generates a plurality of instabilities such as recirculation within the 5CB droplet bulk, and oscillatory contact line motion along with 5CB droplet ejection at the three-phase contact line. It was observed that the recirculation within the 5CB droplet increased gradually until reaching a critical value. Thereafter, the centripetal forces overcame the surface tension forces leading to an instantaneous distortion of contact line, leading to droplet spreading. This was immediately followed by cessation of the recirculation which also led to restoration of the circular 5CB droplet imprint and this entire cycle repeated thereafter. Osmotic pressure gradient near 5CB periphery also enforces a net change in the *S* value across the 5CB droplet such that droplet motility on the water bath is observed. Experiments uncover that variation in the water bath level controls the rate of droplet motility. Furthermore, volume of hexane droplet deposited on water bath also influenced the rate of 5CB recirculation. Increasing the bath temperature led to faster recirculation on the account of thermal Marangoni effects, however it reduced the recirculation time period as 5CB phase transition occurred early. Increasing the salt concentration of the water bath also enhanced the rate of recirculation significantly, which as a result, increased hexane uptake, reducing overall recirculation period.

The different droplet-based applications and phenomena presented in this dissertation highlights the immense potential of these miniaturized systems. It further introduces a number of avenues for potential future research. Designing of acoustic sensors employing audible

sounds for droplet stimulation highlights a facile and affordable sensing methodology. Further improvement with respect to device efficiency can be brought out by analysing droplet-substrate interaction by incorporating patterned electrodes for contact line pinning and assessing ionization effects of electrode prior to analyte loading. Moreover, utilization of multiple enzyme-doped droplets for a multiplex assay can lead to a promising lab-on-a-chip point of care sensor. Microdroplet photofuel cells are an alternative energy harvesting system capable of fulfilling multi-functional objectives. As presented here, simultaneous dye degradation while generation of energy from the hydrogen peroxide based redox reaction, could be realized. Further research into areas such as fuel selection, anode stability and identification of low-onset potential cathode can significantly aid in enhancing the device parameters. Additionally, designing of better circuits for VLSI may lead to accomplishing stand-alone power sources for deployment in remote locations for low energy-intensive systems. Utilizing the different aspects of droplet-dynamics on various substrates can lead to emergence of alternate approaches for solving conventional issues.

Liquid-on-liquid dewetting phenomenon has been analysed incorporating LC, for obtaining multitudes of optically-active, miniaturized nematic droplets. These droplets have been utilized as soft photomasks in an unconventional photolithography setup for obtaining unique 2D, 3D patterns. This route of large-scale nematic droplet generation can be analysed for different LCs possessing smectic, cholesteric and other exotic LC phases, in order to get tailored photomasks generating diverse features on PR surfaces. Also, theoretical investigation of the spreading and retracting dynamics may lead to a better understanding of the governing forces and aid in controlling dimensions of daughter droplets. LC droplet interaction on an aqueous surface in presence of a solvent droplet has shown to display striking spreading dynamics. Different modes of instability have been visualized due to influence of solutal Marangoni effect. Moreover, this phenomenon also helps to obtain miniaturized LC droplets, with a 10^5 order of magnitude reduction. In-depth analysis into the various contact line instabilities near the LC droplet can lead to better understanding of the dewetting phenomenon. This may help explore the contact phase dynamics of miscible and immiscible systems on soft, deformable substrates. Furthermore, this technique can also be harnessed for generation of compound LC droplets utilized in biosensing, material synthesis and photonics applications.

Table of Contents

List of Figures

issued from SS. The intensity of change in R_N was represented by the length of the bar which had a corresponding value of 0.1. Image (c) shows the wave patterns of a particular 'Sa' syllable sound, belonging to two different instruments namely, flute and harmonium, which was issued through the SS. These acoustic waves have been analyzed using open source Audacity software. The scale bar represents the time period of 1 s. Image (d) shows the variation in R_N with t for the sounds of different "bol", mnemonic syllable of Tabla. The image also shows the response of the droplet for Tintaal, Dadra, and Jhaptal, respectively, at a tempo of 120 beats/min. The intensity of change in R_N was represented by the length of the bar which had a corresponding value of 0.05. Image (e) shows the corresponding wave patterns of different "taal" obtained from the Audacity software when their tempo was maintained at 120 beats/min. The scale bar represents the time period of 1 s. Image (f) shows the variation in R_N with t for Jhaptal, when it was played at S_V of ~ 97 dB for different values of tempo. The intensity of variation in R_N was represented by the length of the bar, which had a corresponding value of 0.1. Image (g) shows the corresponding wave patterns of taal dadra played at different tempo which were obtained using Audacity software. The respective scale bars represent the time period of 1 s for each tempo. The encircled portions highlight the coming together of the various "bols" with increasing tempo, which generated different wave pattern with changing tempo. **44**

Figure 2.9 Image shows the variation in the normalized resistance (R_N) of the droplet with different sound levels of the SS. The sound played belonged to taal dadra, when it was played at a tempo of 120 and at dissimilar sound levels – 82 dB, 86 dB and 97 dB, respectively. **46**

Figure 2.10 Images (a) and (b) show the two different arrangements of experiments with, (i) free droplet – 'FDrop' and (ii) sandwiched droplet – 'SDrop'. The motions of vortices inside the droplet is also sketched in the images. The image (a) also shows the electrode arrangement for FDrop configuration while the same for SDrop is shown in the image (b). For the SDrop configuration, another glass slide was placed on the droplet to make the sandwiched structure. Image (c) shows the complete arrangement of the proposed device with a SDrop configuration for the detection of urea. Image (d) shows the rotational speed (ω) of the particles and maximum

List of Tables

Chapter 01

Introduction

A portion of this chapter has been accepted for publication as Thakur, S.; Dasmahapatra, A. K.; Bandyopadhyay, D. Functional Liquid Droplets for Analyte Sensing and Energy Harvesting. *Adv. Colloid Interface Sci* **2021**, *294*, 102453-102483.

1.1 Overview

Liquid droplets are one of the many functional configurations observed frequently in nature. Of late, they have become an integral part of a plethora of modern applications because of their potential to replace a number of conventional processes. For example, at the micro/nanoscale the droplets offer, (i) a high interfacial area per unit mass, (ii) a limited usage of materials for the reduction in the wastage, (iii) an incompressible system, which is also deformable, and (iv) an open thermodynamic system for mass, momentum, and energy transfer.[1,2] Thus, it is not very surprising that droplet[3] or digital microfluidics[4], droplet actuators or sensors,[5] or compound-droplet drug transport modules[6] have emerged as cutting-edge engineering applications in the areas of electronics,[7] microfluidics,[8] or mass-momentum-energy transport.[9] While a pL volume droplet has been utilized for detecting single base pair mismatch in DNA[10], the nL and μL droplets have been employed for energy harvesting[11] and microlens[12] applications. Concisely, the miniaturized droplets have established their necessity from their earliest utilizations in microbiology[13] to the emerging energy and health care technologies.[3,14–16]

It is also important to note that the recent upsurge in the usage of micro-electro-mechanical/nano-electro-mechanical systems (MEMS/NEMS) in the healthcare and energy applications[14,17] have also opened up many avenues for industrial research. For example, the optimization of size, shape, architecture, functionality, and response time of a device are factors that directly impact the efficiency of a device. This has prompted investigations related to the integration of liquid droplets in the digital microfluidics or microtiter plate platforms.[2,18,19] Such explorations have also extended their base from a sessile droplet contact electrification to the very-large-scale integration (VLSI) of micro-photovoltaic units for a process-intensified energy harvesting.[20] The liquid droplet systems have also shown the potential to leverage the fluidic operations across a substantial range of volume scale spanning 10^{15} orders of magnitude from aL to mL, while offering structural simplicity and operational independence.[2] Thus, it is not surprising that a simple droplet configuration has found a wide technological acceptance from the health care and energy to photonic applications.

Considering the versatile nature of droplets, it is not surprising that their inherent geometrical configuration has been employed to stimulate a relatively unexplored domain of droplet-based optics. Utilizing the refractive index property of isotropic materials such as water, its droplets below a particular capillary length (for air-water interface, ~ 2.7 mm)[21], possess an inherent curvature due to surface tension which imparts light focussing abilities. In addition, since

liquids have minimal surface roughness[22], a reduced disruption to incoming light radiations leads to highly focussed images. It must be noted that morphological reconfiguration of micron-scale objects for enhanced visibility has been observed of late, in few optofluidic devices.[23] Different materials such as liquids and hydrogels have been utilized to form dynamic lenses, ideal for usage in optics-based biosensing or imaging devices.[24–26] Moreover, in presence of electric fields that provide an external control over modulation of droplet configuration, adaptive lenses have been developed in different applications involving micro-electromechanical systems.[27–29] In order to control the lensing behaviour and filter property of droplets, incorporation of dyes has also been performed.[30]

The adaptability of liquid droplets to modulate the incoming radiations stems from the flexibility to incorporate different components into it. Compound droplets have been studied which can impart varying focal lengths due to refractive index contrast and interfacial curvature contrast, in order to obtain a divergent to convergent nature of external radiations.[12] On the other hand, droplets formed from anisotropic materials such as LC, possess in-situ phase modulation properties.[31] These droplets can then be controlled using external field gradients such that their molecular arrangement can be tuned for realizing desired phase modulation of incoming radiations.[32] Various works in the literature have employed LC in different applications such as filters[33], lasers[34] and biosensors[35]. In most of the sensing applications, the LC are usually subjected to confinement in macroscopic cells wherein the difference in optical texture due to change in molecular arrangement corresponds to the degree of change in external field gradient such as temperature[36], chemical potential[37]. However, since the interaction is limited to a 2D interface, the sensitivity of such devices is limited. In this regard, not much research has been carried out with regards to deployment of LC in droplet configuration for sensing applications.

Droplets provides a tunable focal length and also the opportunity for creating a multi-focal lens developed by utilizing droplets of different diameters and different composition. In this regard, one of the most economically favourable routes for large-scale droplet generation involves the dewetting of a liquid layer on another liquid surface.[38] Spreading of liquids on surfaces is vitally important to a number of fields such as coating, medicine and petrochemical industries.[39] The interplay of inertia, gravity, surface tension as driving forces and viscosity as a resistant force dominates the dynamic spreading dynamics of liquids on another liquid substrate.[40] Interestingly, in presence of a surfactant solution or for liquid combinations such as partially miscible pairs, the interaction of liquids is influenced by Marangoni forces.[41–43]These forces usually lead to creation of spontaneous directional motion of fluidic structures

that undergo deformation or topological changes and are generally classified as active matter.[44] The Marangoni stresses are ubiquitous in liquid-liquid systems and manifest in various stages such as spreading, dewetting, interfacial fingering, or during formation of self-organized droplet structures.

1.1.1 Biosensing Application

Robust chemical/biochemical assays demand reproducible results concerning the target analyte species within a specified working volume. In this regard, the miniaturized droplet-based systems are best suited for applications requiring limited sample volume. Independent control over each droplet reactor affords unprecedented regulation of the downstream analytical operations. In this regard, reports in the literature also highlighted the effectiveness of monodispersed droplets, which not only ensure similar working environments within each droplet but also improve reproducibility of results.[45] Additionally, the output of the system has also been reported to improve allowing sensing of multiple analytes utilizing similar detection strategies within the monodispersed droplets.[46] The droplet-based systems possess the capability to easily integrate with industrial fluid-handling systems, since these droplet reactors can be dispensed at pre-defined locations on platforms that conform to existing microwell layout. Moreover, the literature also uncovers their unique characteristics and highlights these droplet systems as suitable replacements for micro-titre plates.[2] Although compared to the flourishing and well-established droplet-based microfluidics technology, droplet systems have been explored in a limited way. However, in recent years, promising research evidence has highlighted the potential of droplet systems with regards to mutated-DNA detection to multiplex protein assays.[17]

An aspect of bio-chemical sensing, which in recent years has witnessed a major drive towards advancing health-care sector and by virtue, given the common man an on-site access to devices, which monitor their wellbeing on a daily basis, concerns detection of vital biomarkers. In this direction, the sessile droplet-based sensing techniques are widely found across the literature employed for detection of proteins[47], glucose and urea[48–51], antioxidants[52] as well as reactive oxygen species.[53] Interestingly, most of the works involved in droplet-based systems for bio/chemical sensing applications reported in the literature have primarily explored the colorimetric induced evaporation-driven systems, owing to its facile detection strategy. These systems exploit the thermal gradients for improving mixing as well as particle sorting characteristics. However, concerns relating to the effects of ambient conditions, unwanted contaminants and contact line instabilities induced flow profiles have spurred the growth of

droplet-based devices that utilize external-field driven systems for performing controlled operations.

Utilization of electrochemical sensors employing redox-based FET's or non-Faradaic measurements, thermal-driven fluorescence methods, and optical phase-modulated LC droplets are the alternative detection methodologies that have demonstrated potential towards eventually being utilized at larger scales. In particular, redox based FET's are a promising, highly sensitive platform as they usually employ analyte-receptor interactions for modulating the electrostatic gating of the device. In other words, the population of reduced vs. oxidized moieties present on the reversible-redox material coated gate surface can be utilized as the sensing mechanism. In general, however, construction of devices for point-of-care-testing emphasizes development of economically-feasible techniques that are robust and accurate and preclude incorporation of bulky instrumentation. In this regard, unconventional techniques such as patterned paper based colorimetric assays[54], surfactant-induced phase change in complex droplets[55] and droplet self-splitting on substrates for multiplex detection [56] has been introduced to the literature. Thus, there is a need for construction of biosensors that employ a portable, reproducible and rapid sensing methodology.

Droplet-based systems offer a facile sensor construction. Incorporation of sensing transducers such as spectrophotometers, or electrochemical instrumentation is also facilitated due to a relatively easier setup. Multiplex detection in a relatively shorter time with a network of droplet reactors is possible. Different reports in the literature have presented droplet-based biosensors for a range of biological analytes from single-stranded DNA's to extracellular proteins[2,57] The different setups have exploited the characteristics of droplet-systems for developing different sensors capable of quantifying different indicators of bodily function. Since the biosensor working mostly depends on detecting enzyme's substrate concentration rather than actually quantifying the enzyme itself, incorporation of facile detection techniques is encouraged. Although prior-art suggests usage of droplet-systems in a compact and portable platform, yet incorporation of bulky instrumentation for detection purposes prevents deployment in resource-limited regions at an economically-feasible value. Hence, this presents an opportunity for designing a functional droplet-based biosensor that employs a robust working methodology capable of delivering precise measurements and can be disposed without affecting the environmental significantly.

1.1.2 Energy Harvesting Application

Miniaturized systems afford higher throughput and better device controllability in comparison to their bulk-counterparts. In this aspect, importance of droplet-based in terms of operational simplicity and effectiveness has been underscored in the literature.[17] Since liquid droplets promote unhindered bulk movement of ions and molecules under confined systems. This allows the seemingly two isolated fields of analyte detection and energy harvesting to be rather closely related to each other. Of late, few literatures have reported on this front, presenting multi-functional systems capable of sensing analyte concentration as a function of the output energy harvested.[58,59] As a result, considerable efforts have been devoted towards exploring avenues for utilization of droplets as energy harvesting platforms.

Utilization of natural resources for energy harvesting requires thorough relook for the creation of a greener and sustainable world. The traditional pathway of energy harvesting prefers a centralized production of the same before distribution through a technologically proficient network. However, the utilization of such energies for usage in modern portable systems faces economic viability issues. The present era of cellphones, laptops, ipads, or google glasses, demand the development of miniaturized power harvesters with capabilities of drawing high density power from their vicinity. Augmenting the inventions of Li-ion, or Li-polymer batteries, several novel micro power generators with the promise of harvesting high density energy have also been conceived and developed. In this regard, the cutting-edge research concerning micro to nanoscale technologies involving triboelectric nanogenerators, thermoelectric systems, piezoelectric devices and electromagnetic harvesters have witnessed significant upsurge over the past few decades.[60,61]

With regards to high-density energy systems that occupy minimal operational area, fuel cells have been widely regarded as one of the most promising technologies. Their capabilities for providing wide range of output power at different operating conditions has seen them being utilized on a large-scale in outer space, submarines, power plants and on a microscale.[62–65] Different types of fuel cells such as polymer electrolyte membranes, phosphoric acid, methanol or alkali-based have been developed over the years depending upon the requirement and operational conditions.[66–68] Considering their versatility, scope for further improvement lies in certain aspects as reduction of cell complexity, reduction in material usage, encouraging lighter, portable models with stable fuel sources for long-term generation and optimization of fuel electrodes having low-reduction potential.[69] In this direction, membraneless fuel cells offer

a promising alternative due to its low-cost nature, low-complexity design and portable, miniaturized device setup.[70]

Membraneless fuel cells having different configurations has been reported in the literature. Microchannel arrangement of setup promotes a co-laminar flow between the fuel and oxidant such that a physical membrane is not required, making the overall setup less bulky. Lack of convective mixing within the channel leads to development of an interface which ensures separation of reagents by avoiding cross-over.[71,72] However, since the reagents are required to be pumped within the microchannel, this causes a net reduction in output power density.[73] Thus, configurations such as paper-based membraneless fuel cells were designed such that the fuel flow was executed due to capillary action rather than external power requirement. Since the paper substrate is flexible, porous and also offers creation of different patterned channels, it presented a desirable alternative setup.[74] Another aspect which was modified in order to reduce the reagents contamination within the fuel cell module, included the development of fuel-selective electrodes. This allowed the utilization of single fuel source within a compartment that had reagent selective anodes and cathodes. Thus, this prompted the selection of reagent that could perform the roles of fuel and oxidant together.[74] One promising candidate is hydrogen peroxide as it is a portable, carbon-free fuel source, with high specific energy when utilized in combination with metal electrodes such has Al and Mg.[75,76]

Although paper-based fuel cells have shown significant potential towards an economically-favorable energy generation methodology, another alternative that offers a rapid energy production setup with the capability for large-scale network formation under spatial constraints, is the droplet-based setups.[77] Considering the requirement for portable, replicable, high-density energy systems with a facile device construction, droplet-based systems offer a promising alternative to the existing fuel cell architecture. This configuration delivers a higher output energy per unit mass that provides an ideal environment for low-energy intensive setups. Furthermore, droplet confinement also aids in increasing the interfacial interaction between the components and electrode.[77] In order to enhance the performance parameters of redox-based systems utilization of plasmonic NPs for increasing the charge transfer characteristics under illuminated conditions have been reported.[60,78] Utilizing the LSPR effect, these photoactive NPs improve the longevity of excitons and create higher potential gradient for electron transition between bands, thereby improving the open-circuit voltage and current density values.[79] Thus, development of droplet-based systems encouraging usage of additives for enhancing the overall output may be explored as an energy harvesting alternative.

1.1.3 Soft-photolithography based Patterning

Liquid droplet interaction with the solid substrate has been studies for a long time, owing to the relevance and presence of such interactions across different applications such as coating, evaporation and condensation processes in heat exchangers[80], semiconductor processing[81], sensing,[82] energy harvesting,[20] and optics.[83] For volatile liquids upon solid substrates, the thermodynamic equilibrium is attained with the vapour aiding in the formation of a molecularly thin layer on the substrate and thereby initiating a partial wetting state during the droplet deposition. For non-volatile liquids, however, equilibrium is established after a long period of time. In both cases, the thermodynamic parameter, which is used to determine the equilibrium behaviour is the spreading coefficient, $S = \gamma_{sv} - (\gamma_{sl} + \gamma_{lv})$, where γ_{sv}, γ_{sl}, and γ_{lv} represents solid-vapour, solid-liquid and liquid-vapour interfacial tensions, respectively. A positive value, $S > 0$, favours droplet spreading while a negative value, $S < 0$, indicates the droplet formation depending on the equilibrium contact angle (θ) from 0° to 180° and lipophilicity or lipophobicity of the surface.[84] The force balance at the TPCL decides the eventual shape of a liquid droplet resting on a planar, homogeneous and non-deformable solid substrate under thermodynamic equilibrium, which can be evaluated from Young's equation: $S = \gamma_{sv} - (\gamma_{sl} + \gamma_{lv})$.[85] The Young's equation clearly represents the wetting-state of a relatively large liquid droplet ($D >> 1$ μm). However, this equation does not take into consideration non-equilibrium effects such as droplet evaporation or the mechanical deformation of the underlying soft substrate as a result of droplet deposition. Interestingly, for smaller droplets ($D < 1$ μm), Young's equation is replaced by the form, $\gamma_{lv} \cos\theta + \tau / R = \gamma_{sv} - \gamma_{sl}$, where τ is line tension and R is radius of curvature of the contact line. The values of τ (generally less than 10^{-10} N) and $1/R$ is significantly small for the macroscopic droplets whereas for the microscopic ones these parameters come to prominence.[86,87]

As mentioned earlier, the wettability of the substrate determines the droplet configuration such that application of any external force results in the droplet spreading dynamics to generate either a wetted droplet state, or dewetted droplet phase.[88] The dewetting of the droplets on solid surfaces has been extensively explored via theoretical and experimental investigations.[89,90] At constant temperature, due to pre-patterned physico-chemical gradients, or random dust particles on the surfaces, can lead to a lateral wettability contrast which alters the S value of the spreading droplet and causes the contact line to destabilize. This engenders the formation of multitudes of droplets from the contact line as the mother droplet tends to move towards an equilibrium configuration.[91]

The droplet spreading dynamics on the liquid substrates have been reported to display similar dewetting patterns, however, the partial miscibility of liquids and relative absence of pinning at the droplet interfaces leads to emergence of striking droplet interactions at much faster rates.[92,93] Recent studies have explored different droplet-substrate systems involving presence of inert and volatile droplets on miscible and immiscible layers.[38,93,94] Subtle changes in the interplay of inertial, viscous and capillary forces primarily, determine the spreading and receding droplet dynamics. Although this technique has been investigated from the fundamental viewpoint of understanding the liquid/liquid dewetting process, it has not yet been explored from an application point of view utilizing generation of large-scale, miniaturized droplets.

Generation of patterned surfaces for optics-related applications is usually performed with the help of expensive lithographic instrumentation.[83,95] In this regard, deployment of soft-lithographic techniques provides an attractive alternative as it promotes economically viable methodology for creation of ordered, miniaturized patterns and offers opportunity for development of 3D patterns. Besides microcontact printing, replica molding and solvent-assisted micromolding, utilization of droplets as microlenses and photomasks have also been considered.[96] The inherent curvature possessed by the liquid droplets allows it to focus light precisely at defined locations. The focused light can then interact with the underlying photoactive substrate (photoresist) in order to generate tailored patterns. Furthermore, depending upon the droplet configuration (pristine or composite) and droplet radius, the focal length changes.[12] Utilization of anisotropic materials, as compared to isotropic materials, provides an additional edge in terms of controlling the light modulation. Materials such as LC, which display birefringence due to presence of two different refraction indices are able to focus and control incoming radiations in differently.[97] In comparison to isotropic materials, the molecular arrangement within the LC moiety (that is sensitive to ambient temperature, presence of surfactants or solvents) can be tuned in a desired manner.[98] Reports in the literature have presented the utilization of LC's as versatile, effective photolenses for generation of large-area patterned surfaces.[95] However, these surfaces are generally obtained under highly controlled environments or via incorporation of lithographically-etched pre-patterned substrates or external electric field modulators.[95,97,99]

In this regard, efforts can be dedicated for development of techniques that promote a rapid generation of large-scale, monodispersed or hierarchical droplets without the need of much auxiliary components. Interface-shearing technique is a prime example of such a methodology.[100,101] Using the inherent fluid properties for generation of self-organized droplets

has been reported for obtaining numerous droplet structures. Hence, considering the above, the work elaborated in this thesis builds on the development of different technologies introduced in the literature towards miniaturized photomask generation. An interfacial-shearing technique has been discussed, for generation of large-area, optically active droplets containing LC that have been utilized as soft photomasks.

1.1.4 Chemotactic Dewetting of a Nematic Droplet on a Water Bath

Presence of liquid droplets on soft, deformable substrates often leads to generation of unique spatiotemporal spreading dynamics.[102] The gradient in the spreading parameter near the droplet periphery disturbs the equilibrium at the three-phase contact line which can lead to erratic droplet motility.[103] Furthermore, anisotropic recoiling of the droplet leading edge due to presence of surface tension gradient in the underlying bath on the account of surfactant adsorption or miscibility difference, leads to breaking up of liquid threads into daughter droplets.[41,104] With the aim of generation of multitudes of droplet structures towards different applications such as drug-delivery[105], sensing[106] and optics-related applications[107] the mechanism of dewetting of liquid droplets on underlying liquid bath offers an attractive alternative.

Dewetting phenomenon at large, has been mainly investigated from the viewpoint of a droplet interaction with a solid substrate. Spreading of the thin film on the substrate leads to a critical film thickness below which perturbations resulting from either temperature variations, uniform physico-chemical gradient or random defects destabilize the film morphology. In ultra-thin films resting on a homogeneous surface, van der Waal's forces tend to stimulate spinodal dewetting of the film resulting in formation of holes. For thicker films, heterogeneous nucleation sets in that causes hole formation near physical or chemical defects.[20,108] In both mechanisms, the dewetting process proceeds via formation of tessellations that breaks down due to Rayleigh-Plateau instability to form numerous droplets.[90]

Recent studies show that besides these conventional routes, dewetting of a thin film on a liquid substrate can be another rapid, simple and inexpensive avenue for generation of multi-scale droplets.[93] The deposition of liquid on another liquid bath follows varying rates of spreading that depends upon factors such as top liquid's volatility rate, viscosity, density, interfacial tension and miscibility with liquid bath. Reports in the literature have highlighted striking spreading dynamics for partially miscible and relatively volatile fluids on another liquid bath.[38] The liquid drop spreading rate varies with relative change in the spreading co-efficient, which

also affects the configuration of the three-phase contact line.[109] Under certain conditions, droplet spreading may be succeeded by a retraction phase which leads to formation of liquid threads eventually culminating with generation of miniaturized droplets.[110] It may be noted that the change in the *S* may be caused due to either temperature changes[111], presence of surfactants[112] or adsorption of solutal vapors[113]. In terms of process complexity and droplet composition, surface tension gradient caused due to adsorption of volatile solutes offers the simplest route for large-scale generation that also does not lead to droplet contamination. Adsorption of volatile solute leads to creation of Marangoni stresses at the interface. This not only initiates change in the *S* at the three-phase contact line but also leads to recirculation in the bulk.[114] This technique presents a facile method of *in situ* mixing that is significantly faster than diffusion-based mixing. The main factors that determine the rate of recirculation within the bulk droplet is solute volatility, solute diffusion coefficient, distance from bulk droplet and bath depth. Different applications such as droplet sorting, droplet oscillator and droplet microreactors have been realized via this method.[103]

It is well known that LC are optically-active materials that have been extensively utilized in different applications such as in adaptive optics, vision corrections for virtual reality systems, microlens arrays and beam steering.[95,97] For applications that employ microscale droplet structures of these optically-active material for objectives such as optical field generation[95], diffraction gratings[115] and photolithography[83], genesis of these birefringence lenses generally employ complicated lithography techniques. Once the pre-patterned templates are obtained, spin casting of LC films on these surfaces leads to development of large-area droplet patterns. In this aspect, dewetting process involving deposition of a liquid on another liquid bath offers a relatively inexpensive, and facile route. The droplet spreading on the liquid bath is driven by the interfacial tension gradient and it generally results in a rapid generation of daughter droplets due to the different instabilities set at the three-phase contact line. To enhance the rate of dewetting, presence of an external vapor source can also be utilized. Hence, a chapter of this thesis presents a simple methodology to generate miniaturized optically-active LC droplets on a liquid bath in the vicinity of a volatile solvent source.

1.2 Objectives of the Thesis

Liquid droplets have been extensively studied owing to their functional nature. Their versatile configuration allows them to adapt to the eventual application such that an optimum functionality is delivered within a minimum mass per unit area of the system. Considering the versatile characteristics of liquid droplet platforms, it becomes abundantly clear that their role is expanding across different domains at the micro/nanoscale, leading to the generation of alternate technological solutions. Their responsiveness to the change in the external environment permits development of technologies that can be utilized to generate dynamic, real time devices. The present state-of-the-art technology concerning sensing and energy harvesting applications, focusses on design and development of miniaturized systems that are quick, portable and self-sufficient with regards to energy consumption. Droplet based devices may well supplement existing methodologies as it allows integration of auxiliary components towards generation of large-scale cohesive networks possessing multi-functional capabilities. Another facet of droplet geometry that has been tapped, albeit not thoroughly, for potential application towards optics-related applications concerns the droplet curvature. Desired control over light focusing abilities by varying the droplet dimensions and composition, imparts the droplet the ability to effectively utilize incoming radiations for patterning application. In this context, generation of numerous such optically-active droplets afford a facile, robust approach towards translation of soft-lithography developed patterned surfaces.

In view of the above, this dissertation presents few field-driven systems including chemical-potential, acoustic, and photonic have been utilized for selectively exploring the underlying physics associated with droplet platforms towards patterning, sensing and energy harvesting applications. Micro-scale experimental setups employing solid and liquid substrates have been utilized to uncover the different phenomenon associated with such droplet systems. The point-wise objectives concerning the different chapters in this thesis are as follows:

- Investigation of acoustic wave catalyzed urea detection employing a pulsatile microdroplet sensor.
- Exploring microdroplet photofuel cells for harvesting high-density energy capable of simultaneously working as a dye degradation platform.
- Developing a technique for creation of self-organized LC microdroplets to be utilized as tunable soft-photomasks.
- Analyzing the chemotactic dewetting of a nematic LC droplet on a liquid bath from an experimental and theoretical viewpoint for generation of numerous LC microdroplets.

1.3 Layout of the Thesis

This thesis is a collection of six chapters. In Chapter I, a brief literature review concerning the characteristics and significance of droplets-based systems with regards to applications such as bio-chemical sensing, energy harvesting and patterning has been presented. Following the overview sub-section, the objectives of the present thesis along with the overall layout of the thesis has been highlighted. Thereafter, the subsequent sections II–V of this report details the technical aspects belonging to the thesis chapters.

Chapter II discusses the development of pulsatile microdroplet sensor that is capable of sensing and distinguishing external sounds. Furthermore, the droplet setup is also capable of detecting unknown concentrations of serum urea thereby doubling-up as a portable biosensor. Experiments are performed to uncover the different parameters of the biosensor such as sensitivity, stability and response time. Acoustic waves induce recirculation within the droplet resting on a glass substrate. The convective flow within the droplet changes the ionic composition within the droplet such that it results in variation of droplet ionic resistance. The ionic resistance variation can be mapped with the change in analyte concentration.

Chapter III explores the development of a microdroplet photofuel cell that is capable of generating significant energy utilizing miniscule amount of peroxide fuel. In the presence of external illumination, additives such as Au NPs help increase the power density and current density values owing to their inherent LSPR property. The microdroplet setup is also capable of degrading an organic recalcitrant while simultaneously harvesting energy from the setup. Incorporation of Au/CdS nanocomposite aids in the dye degradation process while also assisting in enhancing output parameters of the hybrid setup. Networking of multiple cells parallelly connected in a VLSI configuration enhances the overall power density.

Chapter IV investigates the design and development of a liquid-on-liquid dewetting phenomenon for large-scale generation of optically-active LC microdroplets. A compound LC microdroplet in hexane undergoes rapid spreading and retraction on a surfactant bath, resulting in generation of multitudes of LC microdroplets from the leading edge. Increasing the surfactant concentration or decreasing the LC loading was found to enhance the capillary forces induced instability of the contact line, that resulted in higher frequency ejection of smaller LC microdroplets. The optically-active LC droplets were then employed as soft photomasks in an unconventional photolithography setup to generate large-area 2D and 3D patterns. Solvent vapor annealing also provided an additional handle over light transmission property of the microdroplet.

Chapter V presents an experimental and theoretical analysis of a LC droplet dewetting phenomenon on a water bath in the vicinity of another solvent droplet. Striking behavior of the LC droplet three-phase contact line is witnessed within a short time period of solvent droplet deposition. Different modes of instability such as oscillatory contact line instability, capillary instability at the LC droplet leading edge as well as *insitu* recirculation within the LC droplet bulk is witnessed. Experiments uncover that solutal Marangoni driven recirculation reach a peak value that precedes simultaneous disruption of droplet geometry, which follows gradual increment of recirculation rates leading to a cyclic process. The maximum rate of recirculation is increased as the volume of solvent droplet or volume of water in underlying bath is increased. Experiments also reveal that influence of surface tension forces destabilizes the contact line instability further leading to higher ejection of smaller LC droplets. A linear stability analysis of this phenomenon has also been employed to determine the size and spacing of the obtained daughter droplets and aid in validating the experimental observations.

In chapter VI, a short summary of the various works highlighting the key results from respective chapters has been presented. Additionally, scope for future research within the areas elaborated in this thesis has also been provided. The thesis concludes by presenting the research output generated from the different chapters.

References

(1) Dressler, O. J.; Casadevall i Solvas, X.; deMello, A. J. Chemical and Biological Dynamics Using Droplet-Based Microfluidics. *Annu. Rev. Anal. Chem.* **2017**, *10*, 1–24.

(2) Garcia-Cordero, J. L.; Fan, Z. H. Sessile Droplets for Chemical and Biological Assays. *Lab on a Chip*. **2017**, *13*, 2150–2166.

(3) Suea-Ngam, A.; Howes, P. D.; Srisa-Art, M.; Demello, A. J. Droplet Microfluidics: From Proof-of-Concept to Real-World Utility? *Chem. Commun.* **2019**, *55*, 9895–9903.

(4) Abdelgawad, M.; Wheeler, A. R. The Digital Revolution: A New Paradigm for Microfluidics. *Adv. Mater.* **2009**, *21*, 920–925.

(5) Dak, P.; Ebrahimi, A.; Swaminathan, V.; Duarte-Guevara, C.; Bashir, R.; Alam, A. M. Droplet-Based Biosensing for Lab-on-a-Chip, Open Microfluidics Platforms. *Biosensors*. **2016**, *6*, 14–29.

(6) Damiati, S.; Kompella, U. B.; Damiati, S. A.; Kodzius, R. Microfluidic Devices for Drug Delivery Systems and Drug Screening. *Genes*. **2018**, *9*, 103-127.

(7) Fallahi, H.; Zhang, J.; Phan, H. P.; Nguyen, N. T. Flexible Microfluidics: Fundamentals, Recent Developments, and Applications. *Micromachines*. **2019**, *10*, 830-848.

(8) Theberge, A. B.; Courtois, F.; Schaerli, Y.; Fischlechner, M.; Abell, C.; Hollfelder, F.; Huck, W. T. S. Microdroplets in Microfluidics: An Evolving Platform for Discoveries in Chemistry and Biology. *Angew. Chem. Int. Ed.* **2010**, *49*, 5846–5868.

(9) Forth, J.; Kim, P. Y.; Xie, G.; Liu, X.; Helms, B. A.; Russell, T. P. Building Reconfigurable Devices Using Complex Liquid–Fluid Interfaces. *Adv. Mater.* **2019**, *31*, 1806370-1806383.

(10) Salm, E.; Guevara, C. D.; Dak, P.; Dorvel, B. R.; Reddy, B.; Alam, M. A.; Bashir, R. Ultralocalized Thermal Reactions in Subnanoliter Droplets-in-Air. *Proc. Natl. Acad. Sci. U. S. A.* **2013**, *110*, 3310–3315.

(11) Kanik, M.; Marcali, M.; Yunusa, M.; Elbuken, C.; Bayindir, M. Continuous Triboelectric Power Harvesting and Biochemical Sensing Inside Poly(Vinylidene Fluoride) Hollow Fibers Using Microfluidic Droplet Generation. *Adv. Mater. Technol.* **2016**, *1*, 1600190-16600200 .

(12) Nagelberg, S.; Zarzar, L. D.; Nicolas, N.; Subramanian, K.; Kalow, J. A.; Sresht, V.; Blankschtein, D.; Barbastathis, G.; Kreysing, M.; Swager, T. M.; Kolle, M. Reconfigurable and Responsive Droplet-Based Compound Micro-Lenses. *Nat. Commun.* **2017**, *8*, 1–9.

(13) Lederberg, J. A Simple Method for Isolating Individual Microbes. *J. Bacteriol.* **1954**, *68*, 258–259.

(14) Ding, Y.; Howes, P. D.; Demello, A. J. Recent Advances in Droplet Microfluidics. *Analytical Chemistry*. **2019**, *92*, 132–149.

(15) Shang, L.; Cheng, Y.; Zhao, Y. Emerging Droplet Microfluidics. *Chemical Reviews*. **2017**, *117*, 7964–8040.

(16) Dutschk, V.; Karapantsios, T.; Liggieri, L.; McMillan, N.; Miller, R.; Starov, V. M. Smart and Green Interfaces: From Single Bubbles/Drops to Industrial Environmental and Biomedical Applications. *Adv. Colloid Interface Sci.* **2014**, *209*, 109–126.

(17) Lach, S.; Yoon, S. M.; Grzybowski, B. A. Tactic, Reactive, and Functional Droplets Outside of Equilibrium. *Chemical Society Reviews.* **2016**, *17*, 4766–4796.

(18) Pandey, C. M.; Augustine, S.; Kumar, S.; Kumar, S.; Nara, S.; Srivastava, S.; Malhotra, B. D. Microfluidics Based Point-of-Care Diagnostics. *Biotechnol. J.* **2018**, *13*, 1700047-1700059.

(19) Thakur, S.; Dasmahapatra, A. K.; Bandyopadhyay, D. Functional Liquid Droplets for Analyte Sensing and Energy Harvesting. *Adv. Colloid Interface Sci.* **2021**, 102453-102483.

(20) Thakur, S.; Rarotra, S.; Bhattacharjee, M.; Mitra, S.; Natu, G.; Mandal, T. K.; Dasmahapatra, A. K.; Bandyopadhyay, D. Self-Organized Large-Scale Integration of Mesoscale-Ordered Heterojunctions for Process-Intensified Photovoltaics. *Phys. Rev. Appl.* **2018**, *10*, 064012-064026.

(21) Brochard-Wyart, F. Droplets: Capillarity and Wetting. In *Soft Matter Physics*; Springer Berlin Heidelberg, **1999**, 1–46.

(22) Braslau, A.; Deutsch, M.; Pershan, P. S.; Weiss, A. H.; Als-Nielsen, J.; Bohr, J. Surface Roughness of Water Measured by X-Ray Reflectivity. *Phys. Rev. Lett.* **1985**, *54*, 114–117.

(23) Shi, J.; Stratton, Z.; Lin, S. C. S.; Huang, H.; Huang, T. J. Tunable Optofluidic Microlens through Active Pressure Control of an Air-Liquid Interface. *Microfluid. Nanofluidics* **2010**, *9*, 313–318.

(24) Werber, A.; Zappe, H. Tunable Microfluidic Microlenses. *Appl. Opt.* **2005**, *44*, 3238–3245.

(25) Dong, L.; Agarwal, A. K.; Beebe, D. J.; Jiang, H. Adaptive Liquid Microlenses Activated by Stimuli-Responsive Hydrogels. *Nature* **2006**, *442*, 551–554.

(26) Mishra, K.; Murade, C.; Carreel, B.; Roghair, I.; Oh, J. M.; Manukyan, G.; Van Den

Ende, D.; Mugele, F. Optofluidic Lens with Tunable Focal Length and Asphericity. *Sci. Rep.* **2014**, *4*, 1–4.

(27) Zeng, X.; Jiang, H. Liquid Tunable Microlenses Based on MEMS Techniques. *Journal of Physics D: Applied Physics*. **2013**, *46*, 323001-323019.

(28) Krogmann, F.; Mönch, W.; Zappe, H. A MEMS-Based Variable Micro-Lens System. *J. Opt. A Pure Appl. Opt.* **2006**, *8*, S330-339.

(29) Kuiper, S.; Hendriks, B. H. W. Variable-Focus Liquid Lens for Miniature Cameras. *Appl. Phys. Lett.* **2004**, *85*, 1128–1130.

(30) McDonald, C.; McGloin, D. Low-Cost Optical Manipulation Using Hanging Droplets of PDMS. *RSC Adv.* **2015**, *5*, 55561–55565.

(31) Cheng, C.-C.; Alex Chang, C.; Andrew Yeh, J. Variable Focus Dielectric Liquid Droplet Lens. *Opt. Express* **2006**, *14*, 4101-4106.

(32) Wang, B.; Ye, M.; Sato, S. Liquid Crystal Lens with Focal Length Variable from Negative to Positive Values. *IEEE Photonics Technol. Lett.* **2006**, *18*, 79–81.

(33) Stoltzfus, C.; Barbour, R.; Atherton, D.; Barber, Z. Micro-Sized Tunable Liquid Crystal Optical Filters. *Opt. Lett.* **2017**, *42*, 2090-2093.

(34) Humar, M. Liquid-Crystal-Droplet Optical Microcavities. *Liq. Cryst.* **2016**, *43*, 1937–1950.

(35) Lee, H. G.; Munir, S.; Park, S. Y. Cholesteric Liquid Crystal Droplets for Biosensors. *ACS Appl. Mater. Interfaces* **2016**, *8*, 26407–26417.

(36) Somerton, C. Measurement of Phase Transition Temperatures in Liquid Crystals Using the Temperature-Dependent Dielectric Constant. *Mol. Cryst. Liq. Cryst. Inc. Nonlinear Opt.* **1988**, *154*, 77–87.

(37) Ravi, B.; Mukherjee, R.; Bandyopadhyay, D. Solvent Vapour Mediated Spontaneous Healing of Self-Organized Defects of Liquid Crystal Films. *Soft Matter* **2015**, *11*, 139–146.

(38) Keiser, L.; Bense, H.; Colinet, P.; Bico, J.; Reyssat, E. Marangoni Bursting: Evaporation-Induced Emulsification of Binary Mixtures on a Liquid Layer. *Phys. Rev. Lett.* **2017**, *118*, 074504-074509.

(39) Gentili, D.; Foschi, G.; Valle, F.; Cavallini, M.; Biscarini, F. Applications of Dewetting in Micro and Nanotechnology. *Chem. Soc. Rev.* **2012**, *41*, 4430–4443.

(40) Berg, S. Marangoni-Driven Spreading along Liquid-Liquid Interfaces. *Phys. Fluids* **2009**, *21*, 032105-032118.

(41) Maass, C. C.; Krüger, C.; Herminghaus, S.; Bahr, C. Swimming Droplets. *Annu. Rev.*

Condens. Matter Phys **2016**, *7*, 171–193.

(42) Izri, Z.; Van Der Linden, M. N.; Michelin, S.; Dauchot, O. Self-Propulsion of Pure Water Droplets by Spontaneous Marangoni-Stress-Driven Motion. *Phys. Rev. Lett.* **2014**, *113*, 248302-248309.

(43) Liu, D.; Tran, T. Vapor-Induced Attraction of Floating Droplets. *J. Phys. Chem. Lett.* **2018**, *9*, 4771–4775.

(44) Pimienta, V.; Antoine, C. Self-Propulsion on Liquid Surfaces. *Curr. Opin. Colloid Interface Sci* **2014**, *19*, 290–299.

(45) Rondelez, Y.; Tresset, G.; Tabata, V. K.; Arata, H.; Fujita, H.; Takeuchi, S.; Noji, H. Microfabricated arrays of femtoliter chambers allow single molecule enzymlogy. *Nat. Biotechnol.*. **2005**, *23*, 361–366.

(46) Huang, Y.; Li, F.; Qin, M.; Jiang, L.; Song, Y. A Multi-Stopband Photonic-Crystal Microchip for High-Performance Metal-Ion Recognition Based on Fluorescent Detection. *Angew. Chemie - Int. Ed.* **2013**, *52*, 7296–7299.

(47) Chandramohan, A.; Chakraborty, M.; Weibel, J. A.; Garimella, S. V. Evaporation-Driven Micromixing in Sessile Droplets for Miniaturized Absorbance-Based Colorimetry. *ACS Omega* **2019**, *4*, 22385–22391.

(48) Hernandez-Perez, R.; Fan, Z. H.; Garcia-Cordero, J. L. Evaporation-Driven Bioassays in Suspended Droplets. *Anal. Chem.* **2016**, *88*, 7312–7317.

(49) Song, Y.; Xu, T.; Xiu, J.; Zhang, X. Mini-Pillar Microarray for Individually Electrochemical Sensing in Microdroplets. *Biosens. Bioelectron.* **2020**, *149*, 111845-111853.

(50) Thakur, S.; Bhattacharjee, M.; Dasmahapatra, A. K.; Bandyopadhyay, D. Acoustic Wave Catalyzed Urea Detection Utilizing a Pulsatile Microdroplet Sensor. *ACS Sustain. Chem. Eng.* **2019**, *7*, 12069–12082.

(51) Duan, R.; Li, Y.; Shi, B.; Li, H.; Yang, J. Real-Time, Quantitative and Sensitive Detection of Urea by Whispering Gallery Mode Lasing in Liquid Crystal Microdroplet. *Talanta* **2020**, *209*, 120513-120520.

(52) Yao, Y.; Zhang, C. A Novel One-Step Fabricated, Droplet-Based Electrochemical Sensor for Facile Biochemical Assays. *Sensors (Switzerland)* **2016**, *16*, 1231-1239.

(53) Yu, Z.; Park, Y.; Chen, L.; Zhao, B.; Jung, Y. M.; Cong, Q. Preparation of a Superhydrophobic and Peroxidase-like Activity Array Chip for H2O2 Sensing by Surface-Enhanced Raman Scattering. *ACS Appl. Mater. Interfaces* **2015**, *7*, 23472–23480.

(54) Martinez, A. W.; Phillips, S. T.; Butte, M. J.; Whitesides, G. M. Patterned Paper as a Platform for Inexpensive, Low-Volume, Portable Bioassays. *Angew. Chemie - Int. Ed.* **2007**, *46*, 1318–1320.

(55) Zarzar, L. D.; Kalow, J. A.; He, X.; Walish, J. J.; Swager, T. M. Optical Visualization and Quantification of Enzyme Activity Using Dynamic Droplet Lenses. *Proc. Natl. Acad. Sci. U. S. A.* **2017**, *114*, 3821–3825.

(56) Li, H.; Fang, W.; Zhao, Z.; Li, A.; Li, Z.; Li, M.; Li, Q.; Feng, X.; Song, Y. Droplet Precise Self-Splitting on Patterned Adhesive Surfaces for Simultaneous Multidetection. *Angew. Chemie Int. Ed.* **2020**, anie.202003839.

(57) Chiu, D. T.; Lorenz, R. M. Chemistry and Biology in Femtoliter and Picoliter Volume Droplets. *Acc. Chem. Res.* **2009**, *42*, 649–658.

(58) Wang, Z. L.; Chen, J.; Lin, L. Progress in Triboelectric Nanogenerators as a New Energy Technology and Self-Powered Sensors. *Energy Environ. Sci.* **2015**, *8*, 2250–2282.

(59) Bhattacharjee, M.; Pasumarthi, V.; Chaudhuri, J.; Singh, A. K.; Nemade, H.; Bandyopadhyay, D. Self-Spinning Nanoparticle Laden Microdroplets for Sensing and Energy Harvesting. *Nanoscale* **2016**, *8*, 6118–6128.

(60) Wang, Z. L.; Wu, W. Nanotechnology-Enabled Energy Harvesting for Self-Powered Micro-/Nanosystems. *Angew. Chemie Int. Ed.* **2012**, *51*, 11700–11721.

(61) Thakur, S.; Dasmahapatra, A. K.; Bandyopadhyay, D. Multifaceted Usage of Miniaturized Energy Technologies for Sustainable Energy Harvesting. In *Sustainable Fuel Technologies Handbook*; Elsevier. **2021**, 369–405.

(62) Staffell, I.; Scamman, D.; Velazquez Abad, A.; Balcombe, P.; Dodds, P. E.; Ekins, P.; Shah, N.; Ward, K. R. The Role of Hydrogen and Fuel Cells in the Global Energy System. *Energy Environ. Sci.* **2019**, *12*, 463–491.

(63) Luo, N.; Miley, G. H.; Gimlin, R. J.; Burton, R. L.; Rusek, J.; Holcomb, F. Hydrogen-Peroxide-Based Fuel Cells for Space Power Systems. *J. Propuls. Power* **2008**, *24*, 583–589.

(64) German, R. Aluminum-Hydrogen Peroxide Fuel Cell Power System for Ocean Bottom Electrical Power. *Proceedings OCEANS*. **1989**, *3*, 843–848.

(65) Modestino, M. A.; Fernandez Rivas, D.; Hashemi, S. M. H.; Gardeniers, J. G. E.; Psaltis, D. The Potential for Microfluidics in Electrochemical Energy Systems. *Energy Environ. Sci.* **2016**, *9*, 3381–3391.

(66) Hardman, S.; Chandan, A.; Steinberger-Wilckens, R. Fuel Cell Added Value for Early Market Applications. *J. Power Sources* **2015**, *287*, 297–306.

(67) Carrette, L.; Friedrich, K. A.; Stimming, U. Fuel Cells - Fundamentals and Applications. *Fuel Cells* **2001**, *1*, 5–39.

(68) O'Hayre, R. P.; Cha, S.-W.; Colella, W. G.; Prinz, F. B. *Fuel Cell Fundamentals*, **2005**.

(69) Dyer, C. K. Fuel Cells for Portable Applications. *J. Power Sources* **2002**, *106*, 31–34.

(70) Safdar, M.; Jänis, J.; Sánchez, S. Microfluidic Fuel Cells for Energy Generation. *Lab Chip* **2016**, *16*, 2754–2758.

(71) Zhang, H.; Xuan, J.; Xu, H.; Leung, M. K. H.; Wang, H.; Leung, D. Y. C.; Zhang, L.; Lu, X. A Numerical Study on Microfluidic Fuel Cell: Improving Fuel Utilization and Fuel Operation Concentration. *Energy Procedia*. **2014**, *61*, 250–253.

(72) Mousavi Shaegh, S. A.; Nguyen, N. T.; Chan, S. H. A Review on Membraneless Laminar Flow-Based Fuel Cells. *International Journal of Hydrogen Energy*. **2011**, *36*, 5675–5694.

(73) Mousavi Shaegh, S. A.; Mousavi Ehteshami, S. M.; Chan, S. H.; Nguyen, N.-T.; Tan, S. N. Membraneless Hydrogen Peroxide Micro Semi-Fuel Cell for Portable Applications. *RSC Adv.* **2014**, *4*, 37284–37287.

(74) Mousavi Ehteshami, S. M.; Asadnia, M.; Tan, S. N.; Chan, S. H. Paper-Based Membraneless Hydrogen Peroxide Fuel Cell Prepared by Micro-Fabrication. *J. Power Sources* **2016**, *301*, 392–395.

(75) Disselkamp, R. S. Energy Storage Using Aqueous Hydrogen Peroxide. *Energy & Fuels* **2008**, *22*, 2771–2774.

(76) Disselkamp, R. S. Can Aqueous Hydrogen Peroxide Be Used as a Stand-Alone Energy Source? *Int. J. Hydrogen Energy* **2010**, *35*, 1049–1053.

(77) Liu, T. W.; Ling, W.; Su, Y. C.; Liang, S. H.; Tai, C. H.; Tseng, F. G. On Demand Micro-Fuel-Droplets Supply System for Self-Sustained Direct Methanol Fuel Cells. *Transducers and Eurosensors XXVII: The 17th International Conference on Solid-State Sensors, Actuators and Microsystems, TRANSDUCERS and EUROSENSORS* **2013**, 470–473.

(78) Bhattacharjee, M.; Timung, S.; Mandal, T. K.; Bandyopadhyay, D. Microfluidic Schottky-Junction Photovoltaics with Superior Efficiency Stimulated by Plasmonic Nanoparticles and Streaming Potential. *Nanoscale Adv.* **2019**, *1*, 1155–1164.

(79) Su, Y.-H.; Ke, Y.-F.; Cai, S.-L.; Yao, Q.-Y. Surface Plasmon Resonance of Layer-by-Layer Gold Nanoparticles Induced Photoelectric Current in Environmentally-Friendly Plasmon-Sensitized Solar Cell. *Light Sci. Appl.* **2012**, *1*, e14.

(80) Wen, R.; Ma, X.; Lee, Y. C.; Yang, R. Liquid-Vapor Phase-Change Heat Transfer on

Functionalized Nanowired Surfaces and Beyond. *Joule*. **2018**, *2*, 2307–2347.

(81) Naffouti, M.; Backofen, R.; Salvalaglio, M.; Bottein, T.; Lodari, M.; Voigt, A.; David, T.; Benkouider, A.; Fraj, I.; Favre, L.; Ronda, A.; Berbezier, I.; Grosso, D.; Abbarchi, M.; Bollani, M. Complex Dewetting Scenarios of Ultrathin Silicon Films for Large-Scale Nanoarchitectures. *Sci. Adv.* **2017**, *3*, eaao1472.

(82) Bolleddu, R.; Chakraborty, S.; Bhattacharjee, M.; Bhandaru, N.; Thakur, S.; Gooh-Pattader, P. S.; Mukherjee, R.; Bandyopadhyay, D. Pattern-Directed Phase Transitions and VOC Sensing of Liquid Crystal Films. *Ind. Eng. Chem. Res.* **2020**, *59*, 1902–1913.

(83) Kim, Y. H.; Lee, J.-O.; Jeong, H. S.; Kim, J. H.; Yoon, E. K.; Yoon, D. K.; Yoon, J.-B.; Jung, H.-T. Optically Selective Microlens Photomasks Using Self-Assembled Smectic Liquid Crystal Defect Arrays. *Adv. Mater.* **2010**, *22*, 2416–2420.

(84) Chen, L.; Auernhammer, G. K.; Bonaccurso, E. Short Time Wetting Dynamics on Soft Surfaces. *Soft Matter* **2011**, *7*, 9084–9089.

(85) Young, T. III. An Essay on the Cohesion of Fluids. *Philos. Trans. R. Soc. London* **1805**, *95*, 65–87.

(86) Marmur, A. Line Tension and the Intrinsic Contact Angle in Solid-Liquid-Fluid Systems. *J. Colloid Interface Sci.* **1997**, *186*, 462–466.

(87) Dorrer, C.; Rühe, J. Some Thoughts on Superhydrophobic Wetting. *Soft Matter* **2009**, *5*, 51–61.

(88) Hoath, D. S. *Fundamentals of Inkjet Printing*; Hoath, S. D., Ed.; Wiley-VCH Verlag GmbH & Co. KGaA: Weinheim, Germany, **2016**.

(89) Sharma, A. Auto-Optimization of Dewetting Rates by Rim Instabilities in Slipping Polymer Films. *Phys. Rev. Lett.* **2001**, *87*, 166103-166109.

(90) Mukherjee, R.; Bandyopadhyay, D.; Sharma, A. Control of Morphology in Pattern Directed Dewetting of Thin Polymer Films. *Soft Matter* **2008**, *4*, 2086–2097.

(91) Bandyopadhyay, D.; Gulabani, R.; Sharma, A. Instability and Dynamics of Thin Liquid Bilayers. *Ind. Eng. Chem. Res.* **2005**, *44*, 1259–1272.

(92) Yamamoto, D.; Nakajima, C.; Shioi, A.; Krafft, M. P.; Yoshikawa, K. The Evolution of Spatial Ordering of Oil Drops Fast Spreading on a Water Surface. *Nat. Commun.* **2015**, *6*, 1–6.

(93) Pimienta, V.; Brost, M.; Kovalchuk, N.; Bresch, S.; Steinbock, O. Complex Shapes and Dynamics of Dissolving Drops of Dichloromethane. *Angew. Chemie Int. Ed.* **2011**, *50*, 10728–10731.

(94) Wodlei, F.; Sebilleau, J.; Magnaudet, J.; Pimienta, V. Marangoni-Driven Flower-like

Patterning of an Evaporating Drop Spreading on a Liquid Substrate. *Nat. Commun.* **2018**, *9*, 820.

(95) Ma, L.; Hu, W.; Zheng, Z.; Wu, S.; Chen, P.; Li, Q.; Lu, Y. Light-Activated Liquid Crystalline Hierarchical Architecture Toward Photonics. *Adv. Opt. Mater.* **2019**, *7*, 1900393-1900399.

(96) Biswas, S.; Chakrabarti, A.; Chateauminois, A.; Wandersman, E.; Prevost, A. M.; Chaudhury, M. K. Soft Lithography Using Nectar Droplets. *Langmuir* **2015**, *31*, 13155–13164.

(97) Lin, Y. H.; Wang, Y. J.; Reshetnyak, V. Liquid Crystal Lenses with Tunable Focal Length. *Liq. Cryst. Rev.*. **2017**, 111–143.

(98) Urbanski, M.; Reyes, C. G.; Noh, J.; Sharma, A.; Geng, Y.; Subba Rao Jampani, V.; Lagerwall, J. P. F. Liquid Crystals in Micron-Scale Droplets, Shells and Fibers. *J. Phys. Condens. Matter*. **2017**, 133003-133057.

(99) Ye, M.; Wang, B.; Sato, S. Liquid-Crystal Lens with a Focal Length That Is Variable in a Wide Range. *Appl. Opt.* **2004**, *43*, 6407–6412.

(100) Ziemecka, I.; Van Steijn, V.; Koper, G. J. M.; Kreutzer, M. T.; Van Esch, J. H. All-Aqueous Core-Shell Droplets Produced in a Microfluidic Device. *Soft Matter* **2011**, *7*, 9878–9880.

(101) Forigua, A.; Kirsch, R. L.; Willerth, S. M.; Elvira, K. S. Recent Advances in the Design of Microfluidic Technologies for the Manufacture of Drug Releasing Particles. *J. Control. Release*. **2021**, *333*, 258–268.

(102) Wyart, F. B.; Martin, P.; Redon, C. Liquid/Liquid Dewetting. *Langmuir* **1993**, *9*, 3682–3690.

(103) Cira, N. J.; Benusiglio, A.; Prakash, M. Vapour-Mediated Sensing and Motility in Two-Component Droplets. *Nature* **2015**, *519*, 446–450.

(104) Sharma, R.; Kalita, R.; Swanson, E. R.; Corcoran, T. E.; Garoff, S.; Przybycien, T. M.; Tilton, R. D. Autophobing on Liquid Subphases Driven by the Interfacial Transport of Amphiphilic Molecules. *Langmuir* **2012**, *28*, 15212–15221.

(105) Čejková, J.; Banno, T.; Hanczyc, M. M.; Štěpánek, F. Droplets As Liquid Robots. *Artificial Life*. **2017**, *23*, 528–549.

(106) Zhou, M.; Wu, Z.; Zhao, Y.; Yang, Q.; Ling, W.; Li, Y.; Xu, H.; Wang, C.; Huang, X. Droplets as Carriers for Flexible Electronic Devices. *Adv. Sci.* **2019**, *6*, 1901862-1901871.

(107) Chowdhury, F. A.; Chau, K. J. Variable Focus Microscopy Using a Suspended Water

Droplet. *J. Opt.* **2012**, *14*, 055501.

(108) Martin, G. D.; Hutchings, I. M. Fundamentals of Inkjet Technology. In *Inkjet Technology for Digital Fabrication*; wiley, **2012**, 21–44.

(109) Chen, Y. J.; Sadakane, K.; Sakuta, H.; Yao, C.; Yoshikawa, K. Spontaneous Oscillations and Synchronization of Active Droplets on a Water Surface via Marangoni Convection. *Langmuir* **2017**, *33*, 12362-12368.

(110) Mollaei, S.; Darooneh, A. H. Spreading, Fingering Instability and Shrinking of a Hydrosoluble Surfactant on Water. *Exp. Therm. Fluid Sci.* **2017**, *86*, 98–101.

(111) Grigoriev, R. O. Chaotic Mixing in Thermocapillary-Driven Microdroplets. *Phys. Fluids* **2005**, *17*, 033601-033607.

(112) Iasella, S. V.; Sun, N.; Zhang, X.; Corcoran, T. E.; Garoff, S.; Przybycien, T. M.; Tilton, R. D. Flow Regime Transitions and Effects on Solute Transport in Surfactant-Driven Marangoni Flows. *J. Colloid Interface Sci.* **2019**, *553*, 136–147.

(113) Kim, H.; Stone, H. A. Direct Measurement of Selective Evaporation of Binary Mixture Droplets by Dissolving Materials. *J. Fluid Mech.* **2018**, *850*, 769–783.

(114) Park, J.; Ryu, J.; Sung, H. J.; Kim, H. Control of Solutal Marangoni-Driven Vortical Flows and Enhancement of Mixing Efficiency. *J. Colloid Interface Sci.* **2020**, *561*, 408–415.

(115) Zola, R. S.; Bisoyi, H. K.; Wang, H.; Urbas, A. M.; Bunning, T. J.; Li, Q. Dynamic Control of Light Direction Enabled by Stimuli-Responsive Liquid Crystal Gratings. *Adv. Mater*. **2019**, *31*, 1806172-1807106.

Chapter 02

Acoustic Wave Catalyzed Urea Detection Utilizing a Pulsatile Microdroplet Sensor

This chapter has been published as Thakur, S.; Bhattacharjee, M.; Dasmahapatra, A. K.; Bandyopadhyay D. Acoustic Wave Catalyzed Urea Detection Utilizing a Pulsatile Microdroplet Sensor. *ACS Sustainable Chem. Eng.* **2019**, *7*, 12069-12082.

Abstract

We observe variations in the electrical resistance across a conducting water microdroplet when it was placed on a glass substrate before mechanically vibrated at natural frequency with the help of an acoustic source. The reduction in the resistance across the droplet was magnified owing to the formation of vortices in the matrix when the periodic oscillation of the surface was increased. The variation in the resistance could be tuned with the frequency of the sound source, which was found to be maximum when a 10 μL droplet was vibrated at ~ 320 Hz. Interestingly, the variation in resistance across the oscillating droplet could follow and distinguish the musical notes in the octaves – "sur", or rhythmic cycles – "taal", originating from the musical instruments such as, flute, harmonium, whistle, and tabla. Further, when a suspension of urease-stabilized gold-cadmium-sulfide nanocomposite was suspended inside the droplet, and mixed with an analyte containing urea solution, the change in the resistance during the operational time period was found to monotonically vary with the concentration of urea in the analyte. The enzymatic reaction between urea and urease was found to follow a faster first order chemical kinetics than the commonly observed Michaelis–Menten pathway owing to the presence of the moving nanocomposites and mixing-vortices under the optimal acoustic excitations. The specific lock-and-key enzymatic reaction helped in extending these experimental results to estimate the unknown levels of urea in human blood serum samples.

2.1 Introduction

In the recent years, the design and development of sustainable health care diagnostic devices suitable for low-resource settings have made an exceptional progress.[1–3] These diagnostic devices aided with the support of alternative form of energy supply, nanoscience and technology, data analytics and artificial intelligence, are envisioned to replenish the more widely employed energy heavy, expensive, expert-driven, and complicated diagnostics processes in the centralized path-labs to detect essential biomarkers.[4–6] In light of this paradigm-shift, a potential antidote has emerged in the form of energy efficient microfluidic biosensors[7], which have been employed for the detection of bio-molecules[8,9], diagnostics[10], and therapeutics[11]. In particular, the microfluidic assays have become more popular owing to their long-term sustainability, low energy demand, ease of fabrication, portability, lower cost, and higher efficiency[7,12–15]. Applicability of microfluidic kits also span diverse areas of engineering which include mixing[16], robotics[17], sustainable energy harvesting[7] , drug delivery[18] and digital electronics[12], among others. Importantly, the commercially available point-of-care-testing (POCT) microfluidic devices such as pregnancy kit[4,19] and glucometer[20,21] have now enabled the detection of health parameters at the patients site[22]. Thus, extensive research activities have been observed in the development of such tools targeting various other potential biomarkers, which are powered by sustainable cum alternative energy resources.

In this direction, of late, the performance of these microdevices have improved significantly when integrated with the alternative forms of energy alongside the incorporation of effective nanomaterials. For example, metal or metal-oxide nanoparticles (NPs)[23,24], polymeric nanofibers[25], nanotubes[26], and carbon allotropes[27] are now integrated with the transistors[28], actuators[28–30], piezoelectric [31] , flexible electronic devices[32,33] and micro-electro-mechanical systems (MEMS) devices[34–36] to improve their selectivity and specificity. For improving their sensitivity on the other hand, different measures such as combining immunosensors-linked plasmonic NPs[1,23], incorporating modified substrates possessing high aspect ratio electrodes[4], and inclusion of current amplifiers may also assist in enhancing signal/noise ratio[22]. Further, the scientific principles associated with the propagation of acoustic waves through diverse solid or fluidic materials and the subsequent change in the materials properties have also been employed for sensing and detection[37–40]. At the micro or nanoscale, the surface acoustic wave (SAW) devices have been successfully employed for the detection of bio-molecules[41], gases[42], and vapors[43]. The ultrasound techniques also have been employed for the biomedical diagnostics and bio-sensing[44–46]. Surprisingly, although the ultrasonic waves have been

employed extensively in the development of biomedical devices, there are not many studies that employ audible sounds for bio-sensing.

On the other hand, among the other biosensing arrangements, serum urea has long been known as a critical renal or metabolic biomarker which is crucial for detecting the uremic toxins present in the body[47,48]. Irregular levels of urea in blood serum can lead to increased toxins level, whereas its lower levels can cause lower protein intake and indigestion or onset of chronic liver diseases[49,50]. A higher serum urea concentrations can result in renal failure, shock, or gastrointestinal bleeding, among other diseases[48,50,51]. For the normal functioning of the human body, the acceptable range of urea in blood serum is around 15-40 mg/dL (or 2.5-7.5 mmol/L)[52,53]. In order to detect the urea concentrations in the body fluids, a variety of sensors have been developed over the years based on different sensing principles such as electro-chemiluminescence[54], electrochemical techniques[55–58], aptasensors[59], piezoelectric sensors[60], conductometric detectors[61,62], organic field effect transistors (OFET) devices[63], and potentiometric[64] or amperometric techniques[65]. However, all the above-mentioned methodologies are reported to have certain issues associated with either the response time, portability, specificity, selectivity, or eco-friendliness.

In the present study, we demonstrate a proof-of-concept acoustically-driven-microdroplet sensor, which is capable of detecting unknown levels of urea present in the blood serum. For this purpose, initially, we synthesized an aqueous suspension of a composite of gold-cadmium sulfide (Au/CdS) NPs coated with urease enzyme. Subsequently, the analyte solution containing urea moieties was mixed with the above suspension and a droplet of the same was dispensed on the glass substrate. The entire system was then exposed to sinusoidal acoustic waves at a particular frequency which corresponded to the natural frequency of the system. The sound waves induced a controlled vibration to the glass slide which in turn formed steady mixing vortices inside the droplet matrix. The acoustics induced mechanical vibration facilitated the lock-and-key enzymatic reaction between urea and urease through augmented mixing. The periodic oscillation also led to the variation in the electrical resistance across the droplet owing to its periodic change in the shape as well as the vortex induced movement of the ions/NPs inside the drop-matrix. The change in the electrical resistance was found to monotonically vary with the urea loading, which was exploited to develop a sensor to measure the unknown urea levels in the human blood serum.

Remarkably, the proposed microdroplet sensor was also capable of immediate sensing and differentiation of diverse audible sounds such as musical notes in the octave or “sur” – sargam, rhythms or “Taal” – tintal, dadra and jhaptal, and sounds issuing out of flute, harmonium,

whistle, and tabla. The perturbations in the acoustic wave transmitted a vibration to the glass slide which in turn induced a controlled agitation in the microdroplet. The time-periodic mechanical oscillations generated different types of flow vortices inside a 10 μL droplet at an optimized frequency of 320 Hz to distinguish these diverse sound sources. A detailed parametric study has been presented to show the variations in the normalized electrical resistance of the oscillating droplet with the changes in the sounds emanated from different sound sources. The results reported can significantly influence the design and development of energy efficient, low cost, and sustainable microdroplet acoustic wave detectors, which can also be translated as a simple, low-cost, portable, sensitive, and reliable alternative as a POCT diagnostic tool for serum urea detection.

2.2 Materials and Methods

2.2.1 Materials

Sodium hydroxide (NaOH) pellets, sodium citrate ($NaC_6H_7O_7$), cadmium chloride ($CdCl_2$), sodium sulphide (Na_2S) was procured from Merck, India. Gold (III) chloride ($HAuCl_4.3H_2O$), Tween 20 solution, PBS buffer, 11- Mercaptoundecanoic acid (11-MUDA), N-(3-dimethylaminopropyl)-N'-ethylcarbodiimide hydrochloride (EDC) and N-Hydroxysuccinimide, were all obtained from Sigma-Aldrich, India. Copper wire, double sided tape, and glass slide were procured from local vendors. Solvents and chemicals utilized were of analytical grade and employed in the experiments without further purification. Milli-Q grade water was used for cleaning purpose and also for preparation of the solutions.

2.2.2 Methods

Surface morphologies and lattice structures (SAED patterns) of the nanocomposites were detected using transmission electron microscope (TEM, Jeol India Pvt. Ltd). Characterization of the nanocomposites was performed using UV-Visible spectroscopy (SHMIADZU UV-2600 model) and Fourier-Transform Infrared spectroscopy (FTIR) (SHIMADZU IR Affinity-1 model). Droplet deformation dynamics under the influence of oscillating substrate was captured using PHOTRON FASTCAM VIEW high-speed camera. Particle movement inside the deforming droplet under different system configurations was captured using SONY FDR AX-40 video camera. MASTECH multimeter (M92A(H) model) was employed to find out the changes in normalized resistances for the different systems. Philips BT50B Bluetooth speaker was utilized to stimulate the system and generate the oscillations in the glass substrate.

2.2.2.1 Synthesis of Au/CdS nanocomposites

In order to synthesize the Au/CdS nanocomposite, initially, a solution of Au NPs was prepared employing the following method. An aqueous solution of 11.8 M $HAuCl_4$ was formed and 16 µl of the prepared solution was mixed with 30 ml of DI water under vigorous stirring for 45 min, while the temperature of the system was gradually raised. After the solution had reached boiling stage, 3 mL of 38.8 mM sodium citrate solution was added into the mixture and the system was heated until the dull yellow color of the solution turned to dark wine red. Thereafter the heating was stopped and the solution was continuously stirred for another 30 min. The color change indicated the formation of Au NPs. In order to synthesize the Au/CdS NPs, initially, 0.01 M $CdCl_2$ and 0.01 M Na_2S were taken. Following this, another solution was prepared by adding 2.5 mL of methanol to 20 mL of 0.1M NaOH solution. The as-prepared methanol-NaOH solution was sonicated for 1 h. The concentration of NaOH in the sonicated solution was further reduced to 5 mM by adding additional water. About 5 ml of the above prepared solution was then mixed to freshly prepared 0.01M Na_2S solution to form solution A. 5 ml of solution A was mixed with freshly prepared 0.01M $CdCl_2$ solution. 10 ml of previously prepared Au NPs solution was then added to the above mixture, and the entire system was vigorously stirred overnight at 70°C. This eventually resulted in the formation of Au/CdS nanocomposite.

2.2.2.2 Urease attachment to Au/CdS nanocomposites

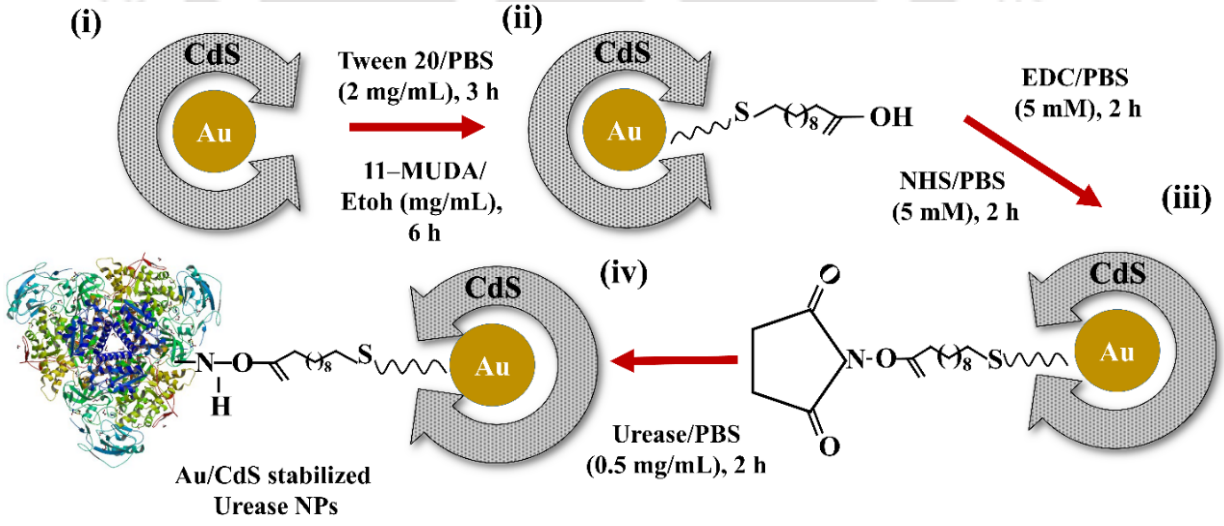

Figure 2.1 Schematic diagram showing the steps undertaken to prepare the Au/CdS-urease nanocomposite. (i) Functionalization of the Au/CdS surface with Tween 20 surfactant followed by the thiol (11-MUDA) moiety, (ii) attaching the functionalized Au/CdS NPs with EDC-NHS functional groups for amine coupling, (iii) addition of urease enzyme to the reaction mixture, (iv) formation of Au/CdS stabilized urease NPs.

In order to attach urease to the prepared nanocomposites, 5 mL of Tween 20 solution in PBS buffer (2 mg/mL) was added to as-prepared 5 mL of Au/CdS nanocomposite solution and stirred for 45 min at room temperature. Then, 5 mL of 11-MUDA solution (1 mM) in ethanol was prepared and added to the above reaction mixture, which was then allowed to incubate for 5-6 h at room temperature. Afterwards, the above solution was centrifuged at 10000 rpm for 10 min to remove excess 11-MUDA before redistributing it again in the buffer. In order to accomplish the amide linkage between urease and Au/CdS nanocomposites, the synthesized nanocomposites were activated with EDC-NHS mixture. For this purpose, about 5 mM EDC and NHS solution were prepared in buffer simultaneously. Thereafter, 5 mL of this mixture was mixed with 11-MUDA activated nanocomposites before the mixture was allowed to rest for ~ 1.5 h. Different concentrations of urease in buffer solutions were prepared and 1 mL of this solution was added to the activated nanocomposites mixture before the solution was kept at room temperature for 2 h. Thereafter the solution was kept at 5°C for 10-12 h.

A brief overview of the methodology undertaken to prepare the Au/CdS-urease nanocomposite has been shown schematically in the steps (i) – (iv) in **Figure 2.1**. The following section provides the detailed optical characterizations (UV-Visible spectroscopy and FTIR spectroscopy) of the different nanomaterials and nanocomposite prepared.

2.2.2.3 Optical Characterization of Nanocomposites

The Au/CdS nanocomposites was prepared using different concentrations of precursor salts. However, at a particular concentration of 0.01 M of the respective precursor salt, the composite UV spectra in **Figure 2.2 (a)** showed both, Au and CdS peaks, implying presence of the components in relatively similar proportions. Above and below this particular concentration of precursor salts, the UV spectra had unequal peak areas and was dominated by either of the two components spectra based on their concentration. For the particular case of 0.01 M of respective precursor salts, the Au and CdS peaks were observed at ~ 532 nm and ~ 450 nm, respectively.

These peaks were observed because of the coupling between the Au NPs core and CdS NPs shell. An efficient charge transfer of the photo induced electrons took place from CdS shell to Au core because of the overlap between the exciton absorption band and surface plasmon band between the two groups[66]. The bio-conjugation of urease with Au/CdS nanocomposites was also captured by the UV-Vis spectroscopy. **Figure 2.2 (a)** shows the presence of urease peak around 280 nm [67]. The aromatic acids responsible for the π- π^* transition signify the presence of urease. The composite on the other hand, showed peaks from both the metal and metal-

sulfide components (Au and CdS) along with the red-shifting of the urease peak indicating the conjugation of the biomolecule with the Au/CdS nanocomposite.

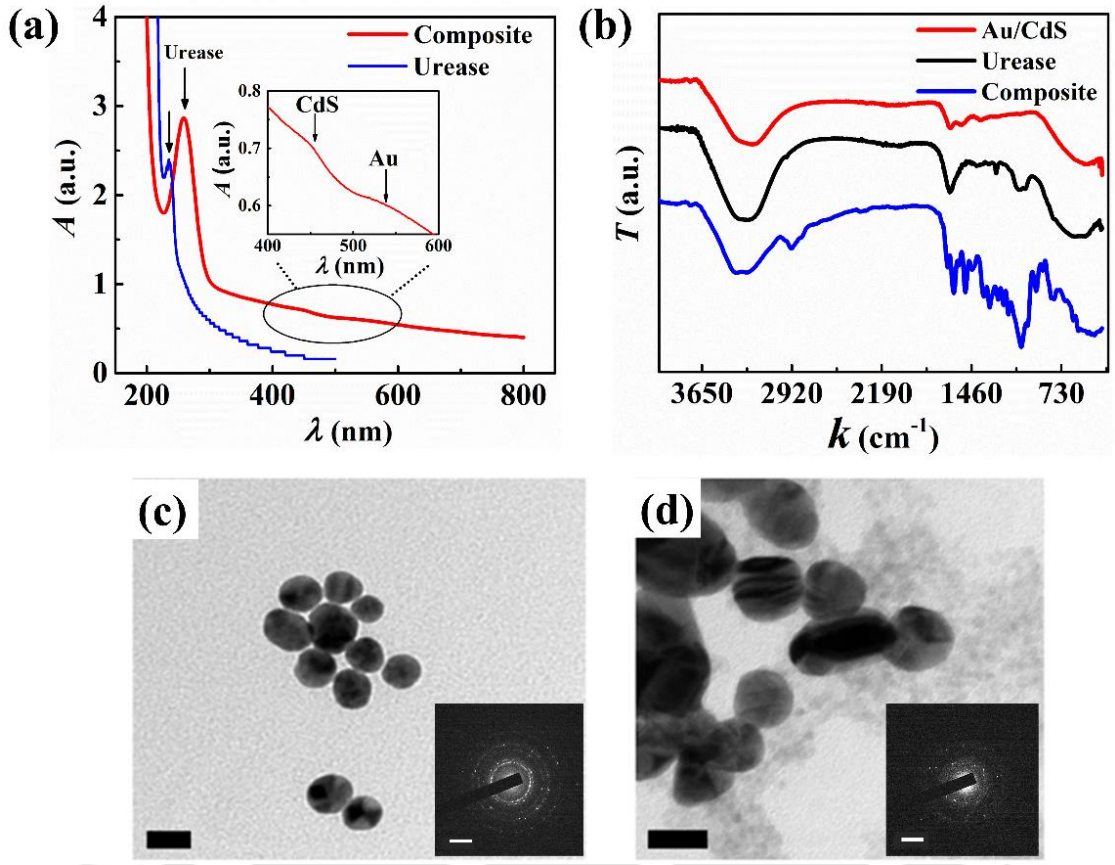

Figure 2.2 Characterization of the synthesized Au/CdS nanocomposite. Images (a) and (b) show the UV-Vis spectra and FTIR plot of the individual components as well as the synthesized nanocomposite, respectively. Image (c) and (d) shows the TEM image of synthesized Au nanoparticle and Au/CdS nanocomposite, respectively. Inset images in (c) and (d) show the SAED patterns of the Au NP and CdS NP respectively. Scale bar for the inset images is 5 nm^{-1}. Scale bar for images (c) and (d) are 10 nm and 20 nm, respectively.

The FTIR spectra of the different materials are shown in **Figure 2.2 (b)**. For the functionalization of the Au/CdS nanocomposites, MUDA was used to form the initial platform for EDC/NHS coupling of urease. As shown in the spectra, peaks at 1715 cm^{-1} and 3400 cm^{-1} are assigned to C=O and –OH functional groups on the Au/CdS nanocomposites. Further, peak shifting with significant narrowing indicated the existence of thiol functionalization on the nanocomposite surface[68]. The additional peaks seen at 1109 cm^{-1}, 1470 cm^{-1}, 1654 cm^{-1}, and 3400 cm^{-1} confirmed the immobilization of urease on Au/CdS and formation of amide bond between enzyme and Au/CdS. The peak at 1150 cm^{-1} represents the –C–N stretching and 1654 cm^{-1} represents the C=O stretching (also known as the amide I band), respectively. The peak

at 3400 cm^{-1} is assigned to –N–H deformation (amide II band)[67,69,70]. The TEM images in the **Figure 2.2 (c)** and **Figure 2.2 (d)** show the presence of Au nanoparticles and Au/CdS nanocomposites, respectively.

2.2.3 Experimental procedure

A stepwise representation of the experiments undertaken have been represented in **Figure 2.3**. Initially, a salt water solution consisting of 0.85 M $FeSO_4$ in 5 mL of water was prepared. The glass substrates were washed with ethanol and acetone solvents and dried with N_2 gas. Thereafter, a 10 µL droplet of the salt solution was placed on the glass substrate of dimensions 75 mm × 25 mm × 1 mm, as shown in **Figure 2.3 (a)**. The substrate was covered with a thin layer of a hydrophobic adhesive tape, which ensured that the droplet maintained a convex meniscus with a contact angle of 110°±3°. Since, a clean glass substrate has a relatively low surface energy, a water droplet may spread on it upon deposition. This would reduce the mixing region and hence lower overall sensitivity. To prevent this, a thin layer of tape is attached. Thereafter, the sound source (SS) was introduced from the bottom of the glass substrate with the help of a Bluetooth speaker, as shown in **Figure 2.3 (b)**. The SS was connected wirelessly to a smartphone, which generated different types of sound waves.

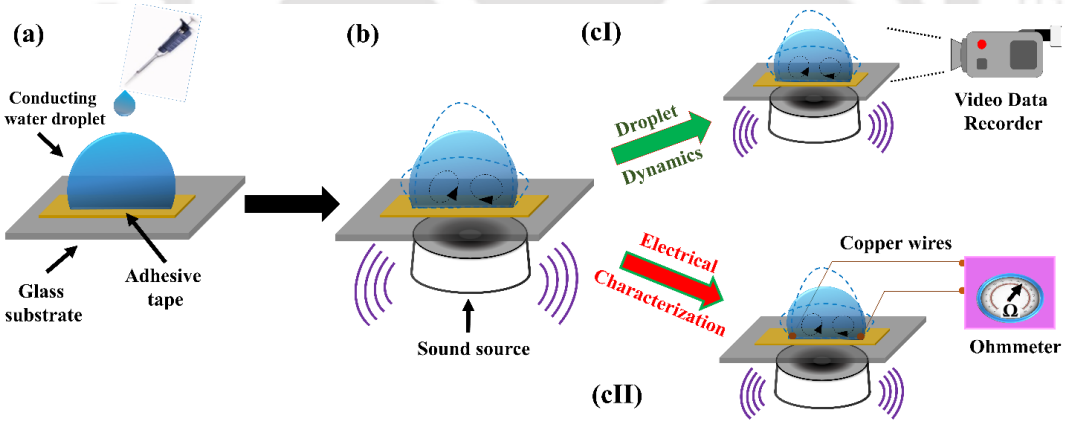

Figure 2.3 Schematic diagram of the experimental steps followed for characterizing the acoustically stimulated droplet system. (a) A micro droplet (10 µL) of salt water solution was placed on a glass substrate on which an adhesive tape was already stuck. (b) After the exposure of sinusoidal acoustic waves, the glass substrate started vibrating which in turn caused vortex formation in the oscillating droplet. Thereafter, this system was analyzed in two different pathways: (cI) depicts the optical and morphological characterizations of the droplet dynamics with the help of a video camera and (cII) shows the method setup for the electrical characterizations.

The acoustic waves issued out of the underlying SS and caused the glass substrate to vibrate which in turn led to the oscillations of the water droplet. These oscillations created vortices inside the microdroplet. This setup was subsequently analyzed in two different ways, as shown in the **Figure 2.3**. In order to uncover the droplet dynamics a video data recorder was employed, which helped to capture the effects of different SS frequencies on the droplet deformation, as shown in the **Figure 2.3 (cI)**. The data was also utilized to analyze the vibration characteristics of the glass substrate. Different frequencies of sounds were issued out from the SS and the deformation of the droplet interface at different time-intervals was measured. **Figure 2.3 (cII)** shows the pathway for the electrical characterization in which a pair of copper terminals, connected to ohmmeter, were placed at the base of the microdroplet. Upon the exposure of sinusoidal acoustic waves, a variation in the electrical resistance was observed owing to the vortices generated as well as due to the deformation of the droplet.

2.3 Results and discussions

2.3.1 The Phenomenon

Initially, experiments were performed to uncover the sensitivity and responsiveness of the proposed concept. The acoustic waves from the SS created time-periodic vibrations in the glass slide which in turn stimulated the droplet to deform time-periodically, as shown schematically in **Figure 2.4 (a)**. The actual snapshots of the oscillating droplet were captured using a high-speed camera, as shown in **Figure 2.4 (b)**. The image shows the side view as well as the top view of the droplet oscillations at a much higher frames per second (8000 fps) and at a much higher time resolution. Image analysis helped in extracting a single cycle of deformation to restoration of the droplet shape, which corresponded to a time period of ~ 140 ms when the SS frequency was set at ~ 320 Hz. This also meant that the droplet and the glass substrate oscillated at a frequency of ~7 Hz with a time period of 140 ms when the SS frequency was fixed to ~ 320 Hz.

The experiments suggest that the acoustic waves from the SS helped in the mechanical vibration of the glass substrate when reflected from the same. Subsequently, the droplet on the glass surface underwent time-periodic variations, which could be observed from the time-periodic deformation of the shape of its free surface, as shown in **Figure 2.4 (b)**. In order to uncover the influence of the acoustic waves on the glass substrate, the variation in the time averaged amplitude of vibration ($A_{avg.}$) of the glass substrate was recorded and analyzed, when it was exposed to sinusoidal sound waves of different frequencies generated from the underlying SS. The results obtained are shown in **Figure 2.4 (d).**

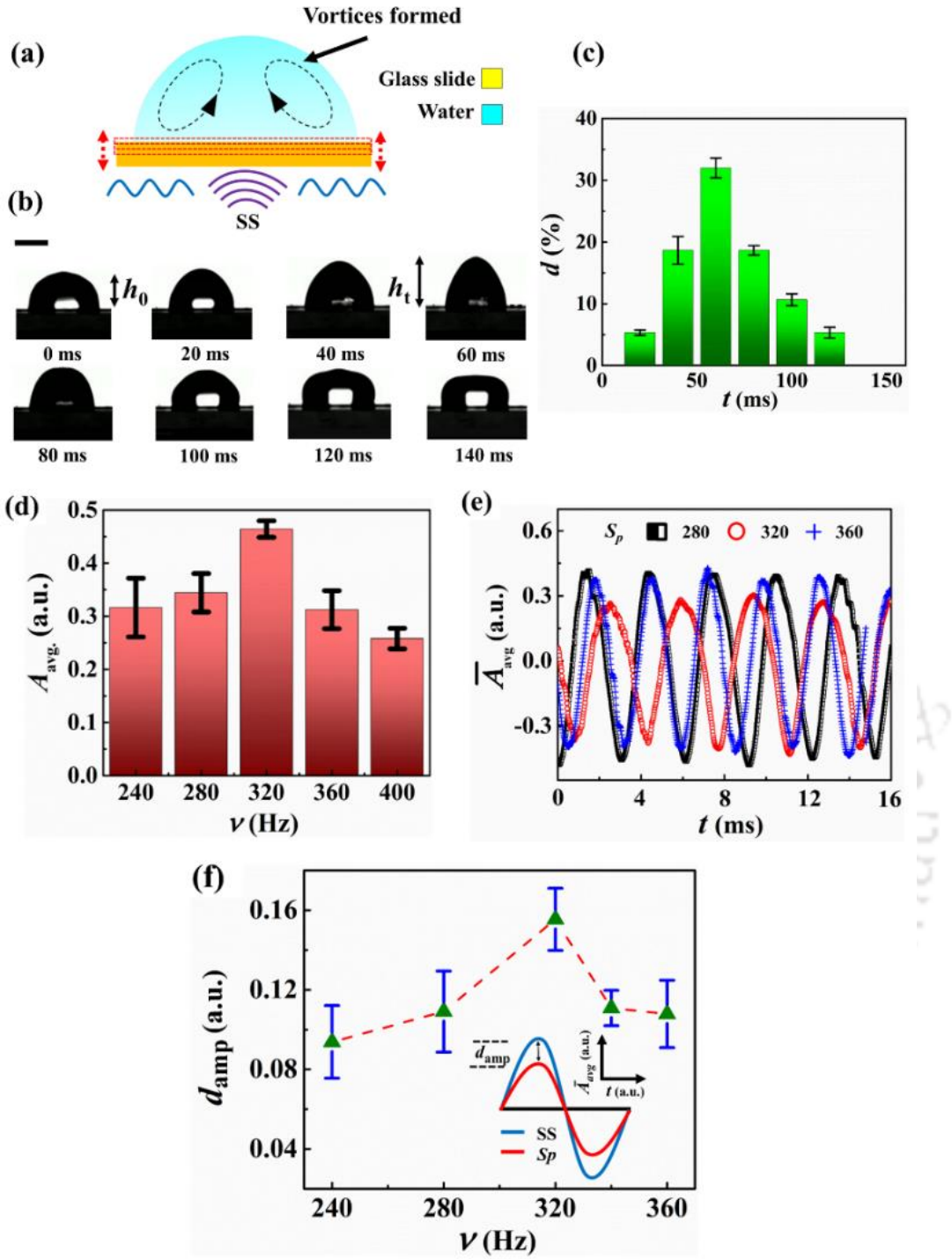

Figure 2.4 Image (a) schematically shows the effect of the vibrating substrate on the above placed droplet. Images in (b) show the snapshots of the deformed droplet at different time intervals for a 140 ms cycle (7 Hz) when the frequency acoustic wave was 320 Hz at the sound source (SS). The rows show the time required for the deformation from the base state (h_0) to the perturbed state (h_t) and vice versa in a full cycle of 140 ms, observed at 1x magnification, with a scale bar of 1 mm. Image (c) shows the percentage deformation (d) of the droplet with time during one cycle. Image (d) corresponds to the time averaged amplitude of vibration ($A_{avg.}$) of the droplet on the substrate at different frequencies (ν) of the acoustic waves. The time span for obtaining the average value was 1 s. Image (e) shows the time average amplitude of the periodic sound waves, $\bar{A}_{avg}$, when the SS was placed under the glass substrate (S_p), at three

different frequencies (ν) of the acoustic waves – 280, 320 and 360 Hz, respectively. Image (f) corresponds to the difference between the average values of time-periodic amplitudes of acoustic waves, d_{amp}, between free SS and the condition when the SS was placed under the glass substrate (S_p). Inset shows the method to obtain d_{amp}, i.e. subtracting the amplitude of average time-periodic variation of emanated sound waves ($\bar{A}_{avg}$) of S_p from the free SS, at different acoustic frequencies. The time span for obtaining the average value was 1 s for both cases, (e) and (f) respectively. In such a cycle, the temporal percentage deformation (d) of the 10 µL droplet from the state of rest was found to pass through a maximum with time (t), as shown in the **Figure 2.4 (c)**. The percentage deformation was estimated with the help of the image analysis of the photographs as, $d = \left[(h_t - h_0)/r_0\right] \times 100$ where h_0 and r_0 are the height and radius of the droplet at $t = 0$ and h_t denotes the height of the droplet under the acoustic influence at a particular time, t.

The amplitude of deformations of the substrate and droplet were found to increase with the frequency of the acoustic wave until they reached a maximum at ~ 320 Hz for a 10 µL droplet resting on a glass substrate, as shown in the **Figure 2.4 (d)**. It may be noted here that the time averaged amplitude of vibration ($A_{avg.}$) of the substrate was calculated by measuring the relative displacement of the droplet at different time intervals, as shown in **Figure 2.4 (b)**. It was assumed that the water microdroplet did not affect the oscillating characteristics significantly because of its insignificant mass as compared to the glass substrate. Rather, the deflection of the droplet surface at various time intervals was measured, which originated due to the deflection of glass substrate. Importantly, vibrations of the substrate gradually waned off below and beyond 320 Hz for the experiments shown in the **Figure 2.4**. The experiments suggested that at ~320 Hz the acoustic wave could commensurate with the natural frequency of the glass substrate leading to a resonance, which resulted in a maximum amplitude of vibration of the glass substrate.

Subsequently, the vibrations at the glass substrate stimulated the deformation in the droplet, which was also found to be maximum at ~320 Hz. In this study, since quantitatively, only the frequency of oscillation of the droplet was measured, it was assumed that the frequency of oscillation of the glass substrate would be the same as of the droplet. A number of previous studies have shown the effects of the resonance when a fluidic medium was oscillated at its natural frequency[71,72]. Herein it was anticipated that the acoustic waves issuing out of the SS would match the natural frequency of the glass substrate at about 320 Hz,[73] which in turn facilitated the abrupt large deformation in the droplet. Below and above this frequency, the amplitude of vibration of the glass substrate as well as the droplet was found to be much less, as can be seen in **Figure 2.4 (d)**.

Figure 2.4 (e) represents the wave patterns of the sound from the combined system of substrate (S_p) and SS, in absence of the droplet. Audacity software was used to find out the profiles of generated wave patterns from the combined system for three different acoustic frequencies – 280, 320 and 360 Hz, respectively. The figure suggested that the minimum value of $\bar{A}_{avg}$ was obtained for frequencies close to 320 Hz, which was previously found to be close to the natural frequency of the system. The relatively lower value of $\bar{A}_{avg}$ around 320 Hz occurred because a considerable part of the emanated sound energy was absorbed by the substrate. Subsequently, the overall amplitude of the sound waves received by the sound recorder decreased. Below and above this natural frequency, $\bar{A}_{avg}$ was relatively higher as most of the sound energy either reflected from or transmitted through the substrate. In the present study, SS had a larger opening diameter as compared to the glass substrate. Thus, the acoustic waves were rather uniformly distributed and emulated a multiple-point sound generating system. The recording device was placed very close to the substrate-SS setup without physically disturbing the system. Since the speaker was placed in a vertical position with respect to ground and the opening of the speaker itself was circular, the sound issued out was assumed to be equal in intensity in all the directions. Subsequently, the recordings were measured in an environment devoid of any external noise, which enabled the recording of the transmitted waves with high accuracy and at a large intensity.

Further, under such circumstances, the substrate displayed maximum displacement from its mean position owing to the maximum transfer of energy from the source to substrate. **Figure 2.4 (f)** corresponds to the difference between the time-periodic amplitudes of emanated acoustic waves, d_{amp}, between free SS and the condition when the SS was placed under the glass substrate (S_p). The $\bar{A}_{avg}$ value of the sound emanated from a free SS was also recorded and observed to be maximum. Thereafter, as the glass substrate was placed on the SS the sound emanated from the system had a lower $\bar{A}_{avg}$ value because the acoustic energy was either absorbed in or reflected from the glass substrate. The plot suggested a maximum value of d_{amp} at 320 Hz, which was indicative of the maximum energy absorbed by substrate at its natural frequency. Consequently, a minimum energy was transferred to the recorder from the surroundings. Before and after this frequency value of 320 Hz, the emanated sounds were either reflected or transmitted from the glass substrate to the surroundings. As a result, the value of $\bar{A}_{avg}$ was higher and d_{amp} was relatively lower. The natural frequency of the experimental system was found to be very similar to an ad-hoc theoretical estimation of ~306 Hz[74] , which has been clearly elucidated in the following paragraphs.

In the experiments, the glass substrate was allowed to vibrate freely without any constraints. In order to find the natural frequency of such a system we may need a detailed understanding of the interaction between the acoustic waves and the substrate. However, such an analysis is perhaps beyond the scope of present work. In such a situation, a theoretical natural frequency of the substrate can still be evaluated by assuming that, during the period of oscillation a section of the substrate is in contact with the SS while the other section is vibrating freely. For such an experimental system emulating a cantilever-like setup the following expression has been employed to evaluate the resonant frequency[74],

$$\omega_0 = \sqrt{\frac{EWT^3}{4L^3 m_{eq}}}\,. \tag{2.1}$$

Here, ω_0 is the resonant frequency, E is the Young's modulus of the substrate, W, T and L are the width, thickness and length of the substrate, respectively. The parameter m_{eq} is equivalent surface area/unit mass of the object. The respective values of the different variables for the proposed system are, E is 50×10^9 Pa, W, T and L are 0.025 m, 0.001 m and 0.07 m, respectively, and m_{eq} ($= L \times T / wt$) is 0.0117 m^2/kg. Replacing these values in the Eq (2.1) we obtain, $\omega_0 \sim 306$ Hz. The theoretical value thus obtained was very close to the experimental resonance frequency. In addition to the experiments performed above, it was also found that the size and mass of the glass substrate influenced the oscillating characteristics of the droplet. For example, few experiments were performed along similar lines as shown in the **Figure 2.4**, with the only difference being the altered dimensions of the substrate which were employed. The details have been presented in **Figure 2.5** and **Table 2.1** respectively**.**

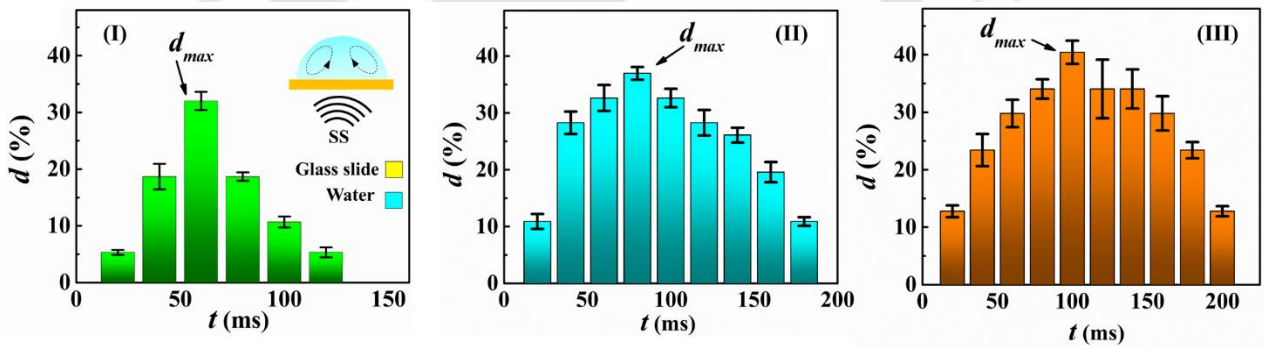

Figure 2.5 Plots (I) - (III) show the variations in the droplet deformation % (d %) with time (t) for different substrate dimensions, as shown in the **Table 2.1**, under the influence of the SS which generated acoustic sinusoidal waves at 320 Hz.

The change in the underlying substrate dimensions brought about a variation in the droplet distortion frequency. The plots suggest that for a 10 µL droplet, the time for a single cycle of distortion and restoration of shape, increased with reduction in the substrate mass when the SS

issued an acoustic wave of ~320 Hz. The same droplet on the glass surfaces with three-fourth and half of the mass, oscillated at ~6 Hz and ~5 Hz, respectively, which led to the increase in the response time of the droplet as compared to the one reported in **Figure 2.4**. This is because, as the mass of the glass substrate reduced, the energy required to oscillate the system also reduced, even though the source frequency was fixed at 320 Hz. In a way, the droplet vibrated with a higher amplitude when the substrate mass was decreased even though the frequency of the acoustic wave source remained unchanged. Thus, the time required for the droplet to attain back its original shape after deformation increased with the reduction in size and mass of the underlying substrate as shown in the images (I) – (III) of **Figure 2.5**. Furthermore, experiments were also performed to optimize the placement of the SS, whose analysis has been represented with the help of **Figure 2.6.**

Table 2.1 Characteristics of the different glass substrates along with the time periods of oscillation of the droplets.

Sr. No.	Substrate dimensions (mm)	Weight (gm)	Droplet oscillation time period (ms)	Droplet oscillation frequency (Hz)
(I)	75 × 25 × 01	6	140	~ 7
(II)	56 × 25 × 01	4.5	180	~ 6
(III)	37 × 25 × 01	3	200	~ 5

Different sets of trials were performed wherein the SS position was changed with respect to the substrate in order to find its optimum location. **Figure 2.6** schematically shows the three configurations, which were tested. The setup shown in the image (a) yielded the maximum change in the normalized electrical resistance (R_N) at the desired frequency of 320 Hz. In such a situation, the sound waves from SS were found to have maximum interaction with the glass substrate. Subsequently, the arrangement was able to generate maximum recirculation in the droplet placed on the substrate. The enhanced fluidic motion in the droplet resulted in the maximum variation in R_N , as has been shown in the image (d). The arrangement showed in the image (b) did not have that much responsiveness as the variation in R_N was not that significant. This might be due to the reduced area of influence of the SS on the substrates when the sound waves were issued from the sides of the substrate. In comparison, in case (c) wherein the electrodes were kept on both the confining substrates, the variation in R_N was not as significant, as was in the case (a). Thus, we opted for the configuration (a) while performing

all further experiments in this study. It may also be noted here that the periodic deformation and restoration of the droplet shape due to the mechanical vibration of the underlying substrate also led to the formation of recirculation currents inside the droplet, as schematically shown in **Figure 2.4 (a)**.

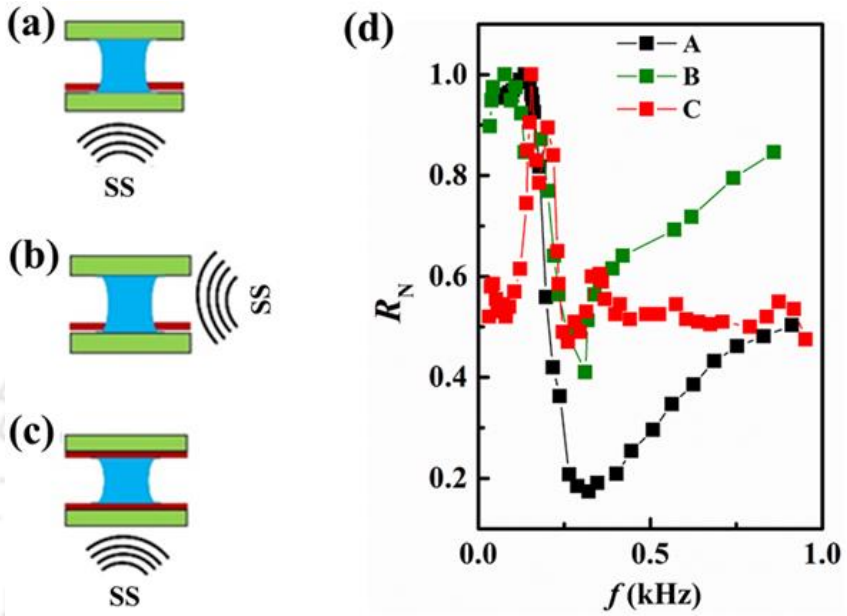

Figure 2.6 Images (a) – (c) show the schematic diagram of the different experimental set-ups, which were employed to test the electrical response of the droplet. Image (d) shows the variation in the normalized electrical resistance (R_N) of the droplet with the change in source frequency varied over a wide range, from f = 30 Hz to f =1 kHz.

In order to understand the phenomenon more clearly, a parametric study on the responsiveness of the droplet with the variations in physical properties of the proposed configuration was performed. For this purpose, the viscosity (η) and density (ρ) of the test droplet was varied by the addition of a proportional amount of glycerol in the salt-water solution before exposing the droplet to the acoustic waves. The frequencies of the acoustic waves were varied from 20 Hz to 1 kHz with 100% volume of the SS at a sound intensity of ~97 dB. The experiments suggested the requirement of a minimum value of frequency of acoustic waves at the SS (f_{min}) to vibrate the underlying substrate and subsequently deform the droplet. **Figure 2.7 (a)** shows an increase in f_{min} with increase in viscosity (η) and density (ρ) of the droplet. It may be noted here that f_{min} was the minimum frequency required to deform the droplet surface under 1x magnification.

The magnitude of f_{min} was evaluated by placing a microparticle inside the droplet and then finding out the minimum frequency required to initiate particle motion in the droplet. The

droplets with higher viscosity and density allowed a higher resistance against the droplet deformation. Thus, a higher source frequency was required to facilitate the droplet deformation and subsequent microparticle motion inside the droplet. The experiments also unveiled that the maximum percentage of droplet deformation (d_{max}) increased with reduction in the η and ρ of the droplet, as shown in the **Figure 2.7 (b)**. Importantly, the increment in the intensity of the sound wave (S_v) also helped in enhancing the d_{max}, as shown in **Figure 2.7 (c)**. Interestingly, a periodic deformation and restoration of the shape of the droplet under acoustic wave stimulation led to the formation of steady vortices inside the droplet, as schematically shown in **Figure 2.3 (b)**. **Figure 2.7 (d)** shows that a minimum frequency at the SS (f_{min}) was required to initiate the formation of the steady vortices.

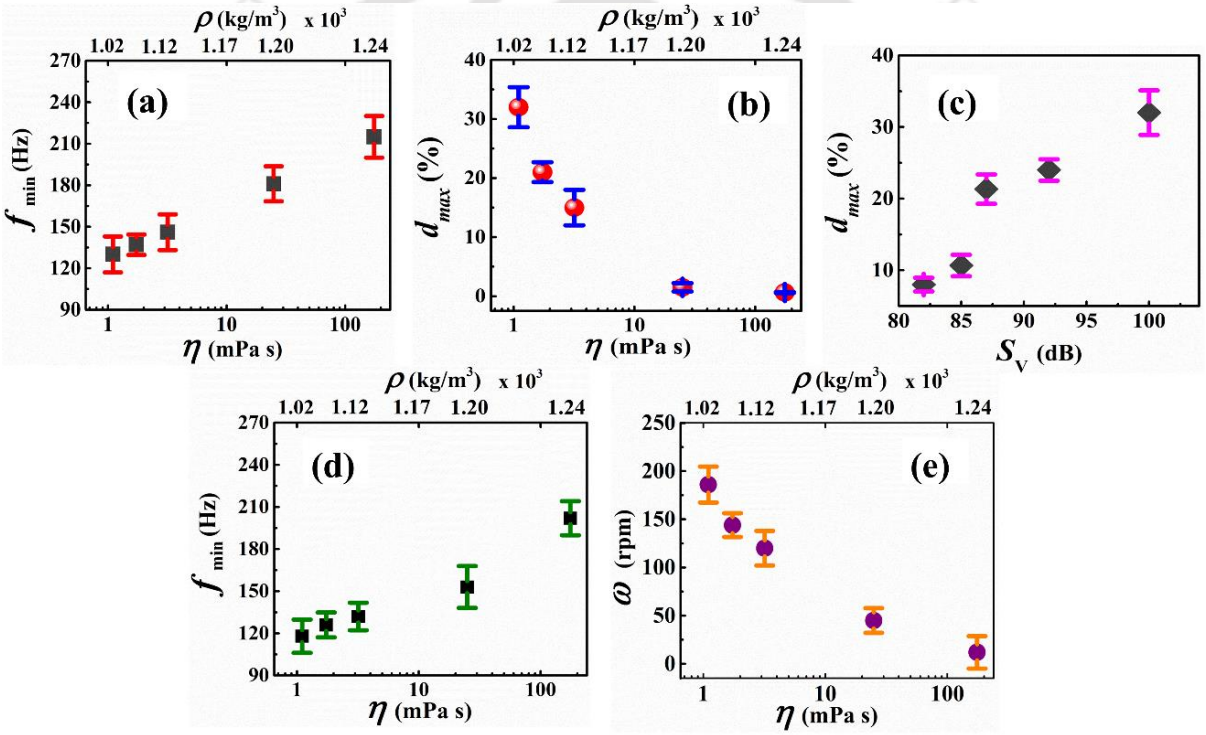

Figure 2.7 Images (a) and (b) show the variations of minimum frequency of sound wave from SS, required to deform the droplet (f_{min}) and maximum percentage of droplet deformation (d_{max}) with viscosity (η) and density (ρ) of the droplet fluid. Image (c) shows the variation in d_{max} with the varying intensity of sound from the SS (S_v). Furthermore, in this experiment, many particles of size ~ 180 µm were floated and followed in the droplet in presence of the exposure of the acoustic wave to measure the strength of the rotational current. Image (d) shows the variation in the minimum frequency of the SS required (f_{min}) for initiating the rotational motion of the particle inside with η and ρ of the droplet fluid. Image (e) shows the variation in the rotational velocity (ω) of the particle with η and ρ of the droplet fluid at a particular SS frequency of 320 Hz.

In order to unfold the formation of these vortices, a microparticle of size ~ 180 µm was floated in the droplet and followed in presence of the exposure of the acoustic wave from SS. A number

of microparticles were suspended in the droplet to follow the pathway developed due to the recirculation. Since, strength of the recirculation was directly proportional to the intensity of sound at a particular frequency, lower sound intensities helped in visualizing the recirculation while the higher sound intensities helped in visualizing the droplet deformations. In order to better visualize the vortex formation generated inside the microdroplet due to the external acoustic waves, we utilized chlorophyll particles to depict the same. The rate of recirculation of these vortices was found out to be as high as ~200 rpm for a 10 µL droplet when SS generated an acoustic wave of ~320 Hz and at a sound intensity level of 97 dB. Understandably, while the f_{min} showed an increasing trend with the increase in η and ρ of the droplet fluid, the strength of the rotational speed (ω) of the microparticle suspended inside the droplet was found to decrease, with increase in η and ρ of the droplet fluid at a particular SS frequency, as shown in **Figure 2.7 (e)**.

2.3.2 Electrical Characterization

Further experiments were undertaken to characterize the electrical response of the system when it was exposed to sound waves belonging to various musical instruments. The experimental setup followed has been represented in **Figure 2.3 (cII)**. For the purpose of clarity, **Figure 2.8 (a)** also represents a similar setup, which was employed to carry out electrical characterization of the droplet system. In the beginning, musical notes of the octave of Indian classical music and different "bol", mnemonic syllables, corresponding to the different rhythmic patterns were played from the SS. The temporal variations in the electrical resistance across the conducting water droplet was measured using a multimeter integrated to the Cu electrodes. The experiments uncovered that the variation in the normalized resistance followed the changing syllables and the tones which issued out from the SS, as shown in the **Figures 2.8 (b) to 2.8 (g)**. Here, R_{max} is maximum resistance obtained in the beginning of measurements and $R_{(t)}$ is resistance of the solution at time t. Furthermore, in order to check the responsiveness of the proposed system, we have also performed experiments with the sounds of different Indian classical instruments[75] such as flute, harmonium, and tabla. **Figure 2.8 (b)** shows that the droplet was able to detect and differentiate the musical notes of the octave for different sounds.

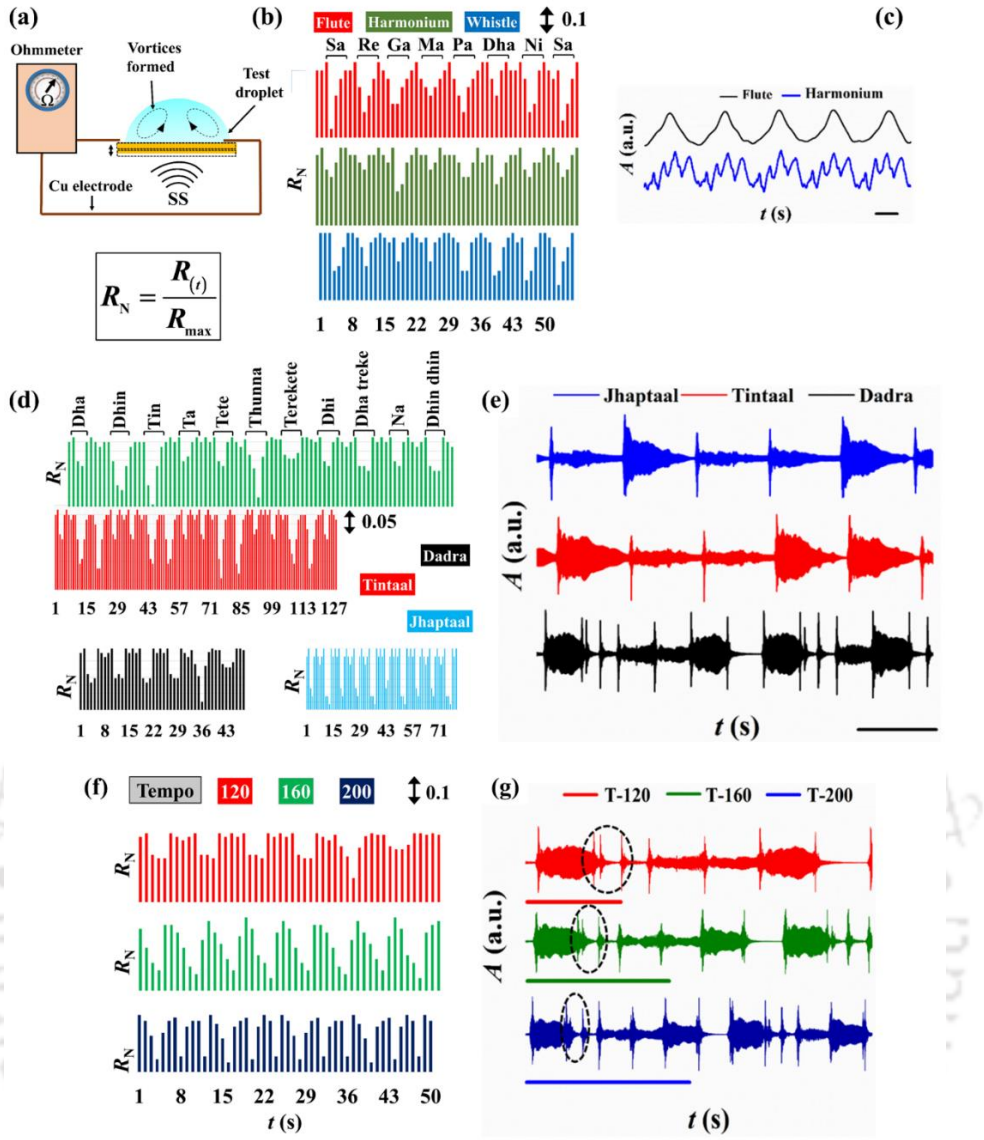

Figure 2.8 Image (a) shows the schematic of the experimental setup used to determine the normalized resistance, $R_N = R_{(t)} / R_{max}$. Image (b) shows the variation in R_N with *t* when sounds of flute, harmonium and whistle for the 8 notes of the octave were issued from SS. The intensity of change in R_N was represented by the length of the bar which had a corresponding value of 0.1. Image (c) shows the wave patterns of a particular 'Sa' syllable sound, belonging to two different instruments namely, flute and harmonium. Image (d) shows the variation in R_N with *t* for the sounds of different "bol", mnemonic syllable of Tabla. The image also shows the response of the droplet for Tintaal, Dadra, and Jhaptal, respectively, at a tempo of 120 beats/min. The intensity of change in R_N was represented by the length of the bar which had a corresponding value of 0.05. Image (e) shows the corresponding wave patterns of different "taal" when their tempo was maintained at 120 beats/min. Image (f) shows the variation in R_N with *t* for Jhaptal, when it was played at *S*v of ~97 dB for different values of tempo. The intensity of variation in R_N was represented by the length of the bar, whose value was 0.1. Image (g) shows the corresponding wave patterns of taal dadra played at different tempo. The different wave patterns were obtained using Audacity software. The different scale bars

represent the time period of 1 s. The encircled portions highlight the coming together of the various "bols" with increasing tempo.

The change in the resistance values of the droplet, which followed the different notes emanating from the SS, could be attributed to the additional convective vortices generated inside the electrically conducting droplet on the account of the acoustic wave stimulated mechanical vibration of the glass substrate. **Figure 2.8 (c)** shows an analysis of the particular "Sa" syllable of the sound waves, belonging to two different instruments namely, flute and harmonium. These particular sound waves which issued out from the SS, were analyzed with the help of open-source platform Audacity. A comparison between the wave patterns generated from the resistance change in the droplet (**Figure 2.8 (b)**) and software confirmed that the variation in R_N could follow the sound waves which emanated from flute and harmonium. **Figure 2.8 (d)** shows the change in R_N due to the sound of different "bol", mnemonic syllable of the instrument tabla [75]. It also shows the response of the droplet due to three different popular rhythms, namely, tintaal (4-4-4-4), dadra (3-3) and jhaptal (2-3-2-3), respectively [76]. The tempo of the music was maintained at 120 beats/min while the volume of the speaker was maintained at an intensity of ~97 dB corresponding to a power of ~3 dBW. The change in the resistance during these experiments was recorded to be ~5-10%. Again, the reason behind the decrease in the electrical resistance was attributed to the time-periodic change of shape of the droplet and the subsequent generation of vortices of different strength due to the acoustic wave induced mechanical vibration on the glass substrate. The convective vortices helped in additional transportation of ions between the electrodes, which led to the reduction in electrical resistance across the droplet[7].

The characterizations of the musical instruments were further extended to different rhythmic pattern or taal of tabla[75] using the SS. The response of the droplet system for different rhythmic cycles was found to be different, as shown in **Figure 2.8 (d)**. **Figure 2.8 (e)** shows the respective patterns of sound waves which issued out of the SS and which were analyzed with the help of the software Audacity. Since taal is composed of syllables in a particular pattern, the spikes in **Figure 2.8 (e)** represented the sudden change in rhythm for a respective taal, and due to this sudden change in sound, the corresponding changes in resistance (troughs) was seen as observed in **Figure 2.8 (d).** The response of the droplet was also found to vary with the tempo of the same rhythmic cycle, as shown in **Figure 2.8 (f)**. The tempo of a rhythmic pattern could be defined as the frequency of the pattern in which a higher tempo could be deciphered by quick repetitions of the cycles, as shown in the **Figure 2.8 (f)**.

Figure 2.8 (g) shows the respective beat patterns of the acoustic waves of taal dadra, which were emanated from the SS and were captured and analyzed using Audacity software. The encircled portions in the plots in **Figure 2.8 (g)** showed the increase in the beat patterns of the sounds generated by the SS. A comparison between the plots of **Figures 2.8 (f)** and **2.8 (g)** suggest that the droplet system was also able to track the increase in the frequency of the beats. In case of the lower tempo, the droplet had longer time to recover while in the case of a higher tempo, the droplet had lower time to recover from the changes in beats, but could still follow the beat patterns, which led to the increased number of crests and troughs in R_N with t plot. Separate experiments were also performed to decipher the effect of varying sound intensity levels on the system.

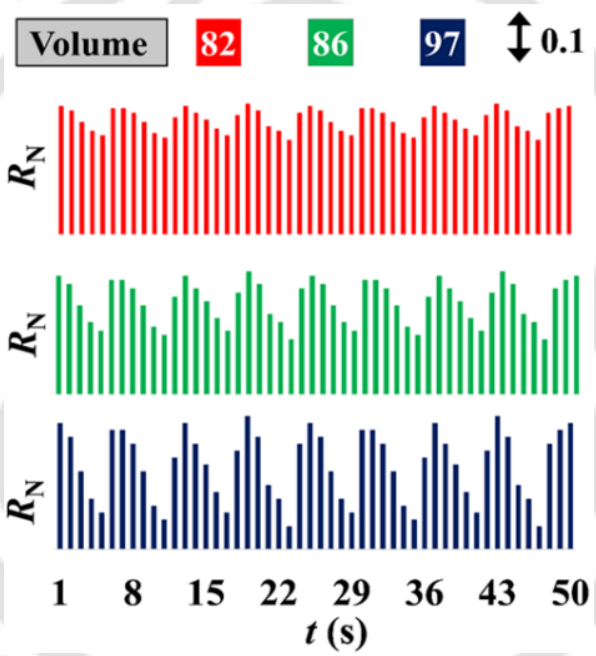

Figure 2.9 Image shows the variation in the normalized resistance (R_N) of the droplet with different sound levels of the SS. The sound played belonged to taal dadra, when it was played at a tempo of 120 and at dissimilar sound levels – 82 dB, 86 dB and 97 dB, respectively.

The response of the droplet was also measured in the presence of varying sound levels of SS. For this experiment, taal *dadra* was played at a tempo of 120. **Figure 2.9** shows the variation in R_N with time at three different volume levels of the SS. The plot suggests that the R_N parameter of the droplet was able to follow the variations in the different sound profiles emanated from the SS. Thus, it could be concluded that even at higher values of S_v, the smaller notes could be distinctly distinguished by employing the droplet setup.

2.3.3 Optimization of Prototype for Sensing

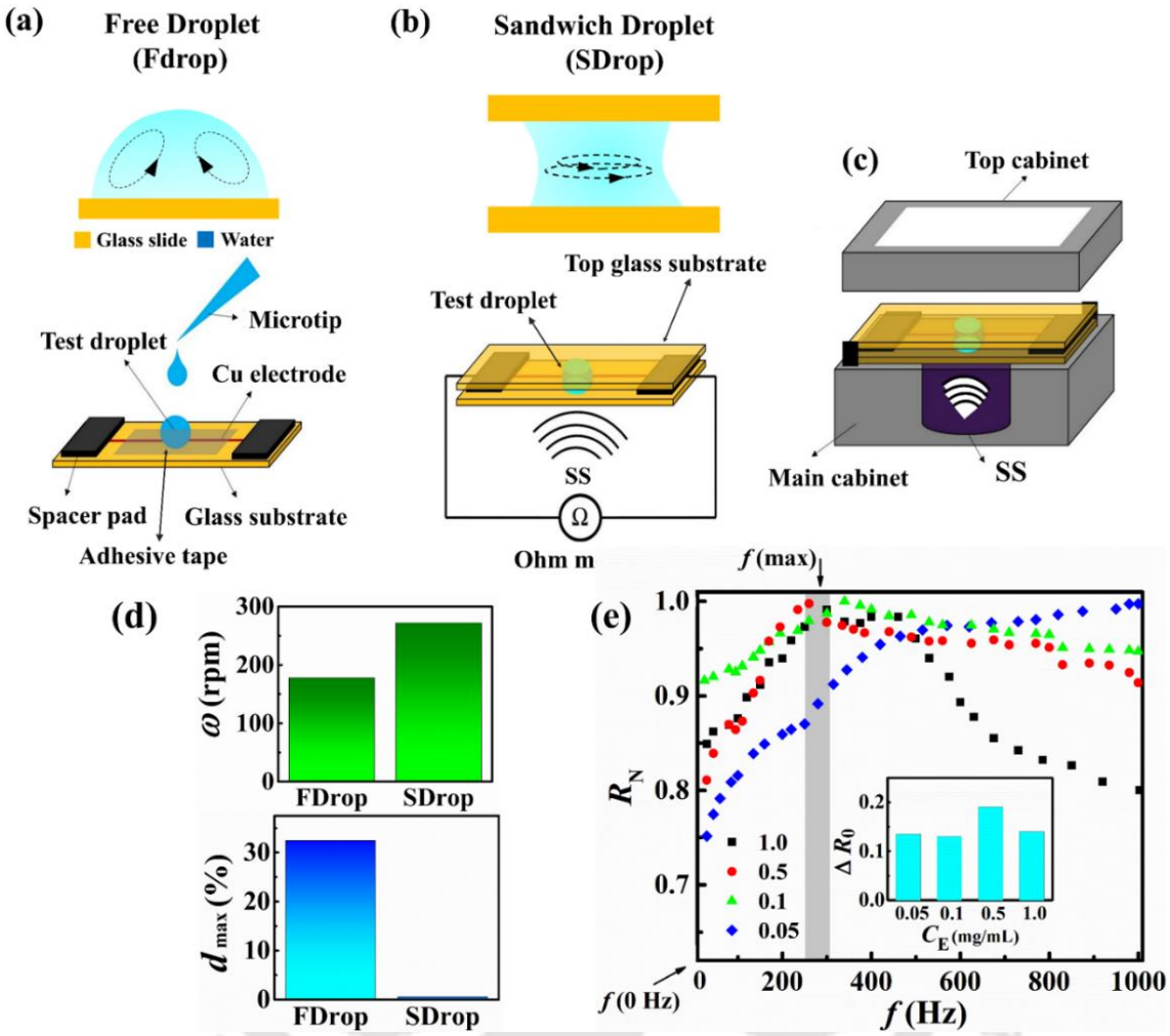

Figure 2.10 Images (a) and (b) show the two different arrangements of experiments with, (i) free droplet – 'FDrop' and (ii) sandwiched droplet – 'SDrop'. The motions of vortices inside the droplet is also sketched in the images. The image (a) also shows the electrode arrangement for FDrop configuration while the same for SDrop is shown in the image (b). For the SDrop configuration, another glass slide was placed on the droplet to make the sandwiched structure. Image (c) shows the complete arrangement of the proposed device with a SDrop configuration for the detection of urea. Image (d) shows the rotational speed (ω) of the particles and maximum percentage deformation (d_{max}) of the droplet surface for the FDrop and SDrop configurations. The image (e) shows the change in R_N with f of the SS ranging from 30-1000 Hz for different concentrations of urease, as shown by the different symbols. The grey region shows the operating zone of the SDrop configuration. Inset figure shows the relative change in the normalized resistance, ΔR_0, with urease loading, C_E. The parameter, $\Delta R_0 = R_N^{f_{max}} - R_N^{f_0}$, represents the difference between the maximum change in the normalized resistance obtained at 320 Hz where d_{max} was achieved. Here $R_N^{f_{max}}$ correspond to the normalized resistance at 320 Hz and $R_N^{f_0}$ is the same at 0 Hz.

The proposed methodology could also be employed for the ultrafast detection of urea in the blood serum samples. For this purpose, the experiments were performed in a setup where the droplet was sandwiched in between a pair of glass slides rather than a free droplet as shown in the **Figures 2.10 (a)** and **2.10 (b)**. **Figure 2.10 (a)** shows a free droplet (FDrop) arrangement utilized so far while **Figure 2.10 (b)** shows a sandwiched droplet (SDrop) configuration in which the droplet is confined between the substrates. Experiments uncovered that the latter configuration was more useful in the development of an electrochemical device for urea detection, as illustrated in the **Figure 2.10 (c)**. The SDrop arrangement ensured the vibration of both the confining glass substrates at their natural frequencies at 320 Hz when a 10 μL droplet was sandwiched between them, which facilitated the formation of stronger vortices inside the droplet, as schematically shown in the **Figures 2.10 (a)** and **2.10 (b)**. In a way, the vibration of both the confining surfaces allowed a larger fluid motion inside the droplet, which facilitated the development of the biosensor as discussed later. **Figure 2.10 (d)** shows that under similar condition the droplet under SDrop configuration could show a larger rotational speed of the vortices as compared to the FDrop configuration. Hence, this arrangement was further extended for urea sensing.

For the biosensing application study, in order to determine the optimal urease concentration, different amounts of urease were attached to the Au/CdS nanocomposites in buffer solutions in a way similar to that has already been discussed in the experimental section. The strength of the urease in buffer was varied from 0.05 mg/ml to 1 mg/ml and subsequently the prepared solutions were kept at room temperature for 2 h. Thereafter, the solutions were kept at 5°C for ~12 h in order to attach and stabilize urease on the surface of Au/CdS nanocomposite. As discussed previously, the details of the characterizations of the nanocomposite and the attachment of the same with urease have already been discussed in methods section. Following this, a droplet with urease coated Au/CdS nanocomposites was exposed to the SS in the SDrop configuration in which the frequency of the SS was varied from 30 Hz to 1000 Hz. Again, for this arrangement, the R_N was found to be maximum at ~320 Hz, as shown in **Figure 2.10 (e)**. In absence of the sound wave excitation from the SS, the increase in base resistance of the droplet could be attributed to the addition of less conducting Au/CdS-urease nanocomposite in the droplet.

Subsequently, introduction of the sound wave excitation led to the fragmentation and dispersion of these composites into the droplet matrix which in turn influenced the ionic movements inside the droplet to cause a progressive increase in R_N until ~320 Hz. Moreover, since this frequency

was close to the natural frequency of the setup, the recirculation rates inside the droplet due to the vortices were highest and it caused the maximum reduction in the electrical resistance of the solution. The fragmentation and dispersion of the Au/CdS-urease nanocomposite in presence of the acoustic waves were confirmed through a TEM analysis, as shown later in the **Figure 2.12**. **Figure 2.10 (e)** suggests that at 0.5 mg/ml urease concentration, largest magnitude in the normalized resistance, $\Delta R_0 = R_N^{f_{max}} - R_N^{f_0}$, was achieved. The parameter, ΔR_0, represents the difference between the maximum change in the normalized resistance obtained at 320 Hz, where d_{max} was achieved. Here $R_N^{f_{max}}$ correspond to the normalized resistance at 320 Hz and $R_N^{f_0}$ is the same at 0 Hz. Hence, for performing further experiments, this optimal urease concentration was selected.

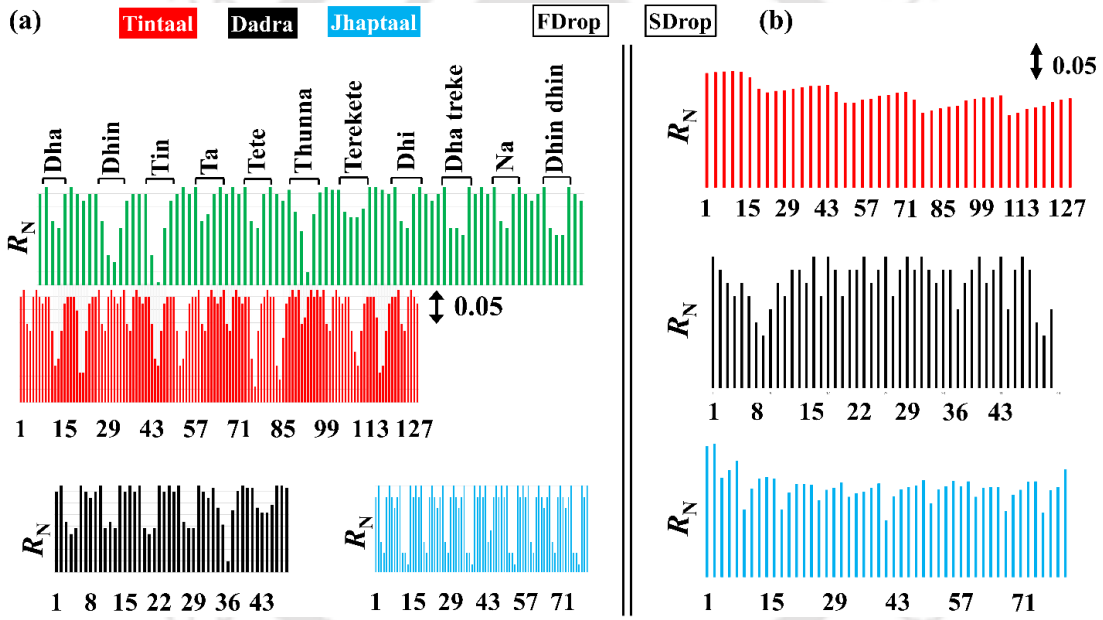

Figure 2.11 Image (a) shows the variation in R_N with t for the sounds of different "bol", mnemonic syllable of Tabla. The image also shows the response of the droplet for Tintaal, Dadra, and Jhaptal, respectively, at a tempo of 120 beats/min. The intensity of change in R_N was represented by the length of the bar which had a corresponding value of 0.05. Image (b) shows the corresponding wave patterns of different "taal" obtained using the SDrop configuration when the conditions of the incident acoustic waves were kept similar to that in the former case.

At this juncture, it is also important to note that the FDrop arrangement was more suitable for the detection of external sounds than the SDrop setup. This observation was made after experiments were performed in order to compare and contrast the effects of the droplet configurations on the sound sensing capabilities. Therein, a set of experiments was performed

with SDrop configuration for different '*Taals*' namely, tintaal (16 beats), dadra (6 beats) and jhaptal (10 beats), respectively. A similar system was taken as earlier for the FDrop configuration, which consisted of a 10 µL microdroplet containing 0.85 M $FeSO_4$ ions in water. Subsequently, the microdroplet was stimulated with the different sounds at a sound intensity level of 97 dB. The results obtained have been plotted in **Figure 2.11**, which also represents the data acquired previously by using FDrop configuration. The figure suggests that the different 'bols' were more easily distinguishable in the FDrop as compared to the SDrop configuration. The variations in the result could be attributed to the additional confinement in the SDrop configuration, which led to lesser vibration of the free surface and more recirculation inside the droplet. Thus, while the FDrop configuration was more suitable for sound detection, the SDrop arrangement was found to be more suitable for the biosensing arrangement.

2.3.4 Point-of-care Urea Detection

The SDrop embodiment shown in the **Figure 2.10c** was further employed to detect urea in human blood serum. To this end, in order to develop a calibration plot, a salt-water solution was initially loaded with Au/CdS-urease nanocomposite before mixing a known concentration of urea in buffer solution (C_U) to the same. Thereafter, a 10 µL droplet of this mixture was dispensed in the SDrop arrangement and a 320 Hz sound wave was generated through SS at sound intensity level of 97 dB. The calibration was performed at an optimized Au/CdS-urease loading, as mentioned in the previous section, for a range of concentrations of urea in the buffer solution, C_U. **Figure 2.12** outlines the details of the dispersion of Au/CdS-urease nanocomposites, into the droplet under the SDrop arrangement, and subsequently the development of the calibration plot. The schematics in the **Figures 2.1** and **2.12** suggest that during synthesis a cluster of many units of Au/CdS-urease nanocomposites were formed. Following this, a salt-water droplet loaded with such nanocomposites was exposed to the acoustic waves employing the SDrop arrangement, as shown in the **Figures 2.12 (a)** and **2.12 (b)**.

A TEM analysis of the aggregates before and after the experiments confirmed that the nanocomposites were fragmented into smaller parts during the experiments, as can be seen in the TEM images in **Figures 2.12 (c)** and **2.12 (d)**. The experiment provided a passive proof for the increase in the electrical resistance of the droplet owing to, (i) the loading of the nanocomposite before the exposure of the acoustic wave, and (ii) the fragmentation and dispersion of these nanocomposites in the entire droplet matrix after the exposure to the sound

waves. In order to understand the relationship between the electrical resistance of the solution as a function of time during the analysis, a study was undertaken to plot the same and observe the results and the subsequent trend which emerged.

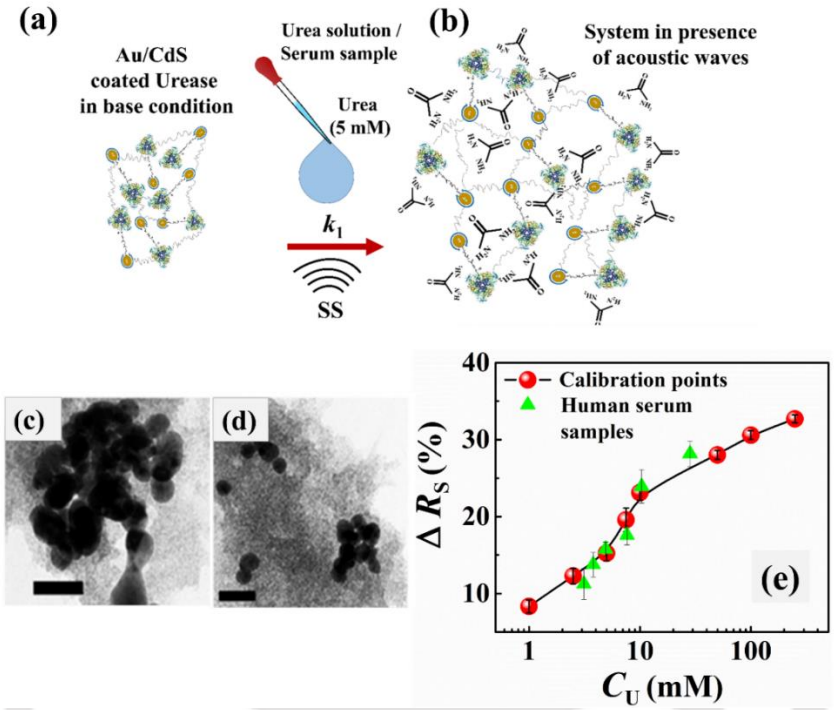

Figure 2.12 The schematic diagram shows the urease moiety attachment to the cluster of units of Au/CdS nanocomposite. Images (a) and (b) show the breaking of the Au/CdS-urease nanocomposite into smaller fragments under the SS when a nanocomposite loaded salt-water droplet was mixed with urea-buffer solution (e.g. 5 mM) and then exposed to the sound wave from the SS. The images show that the bigger fragments of the nanocomposite were broken into multiple smaller ones owing to the acoustic stimulation. Images (c) and (d) show the TEM micrographs of the Au/CdS-urease nanocomposites before and after sound exposure, respectively, in which the scale bars are of 20 nm. Plot (e) shows the variation in the percentage normalized resistance, $\Delta R_s = (R_{max} - R_{sat}) \times 100 / R_{max}$, across the droplet when different concentrations of urea-buffer solutions (C_U) were added. The line following the circular symbols shows the calibration plot for urea detection. Scattered points with triangular symbol show the results obtained from human serum samples. The urease concentration utilized for detection in the latter case was 0.5 mg/ml.

Therefore, to analyze the electrochemical behavior of the proposed sensor, two parameters based on electric resistance of the droplet had been defined, namely, R_{max} and R_{sat}. **Figure 2.13** showed the initial droplet resistance as R_{max}, which progressively reduced to a saturated value of R_{sat} over a period of time. The decrease in the droplet resistance during the course of the urea-urease reaction in the presence of acoustic excitation, occurred as a result of higher rates

of formation of product ions. Presence of vortices also contributed towards the further reduction in the electrical resistance

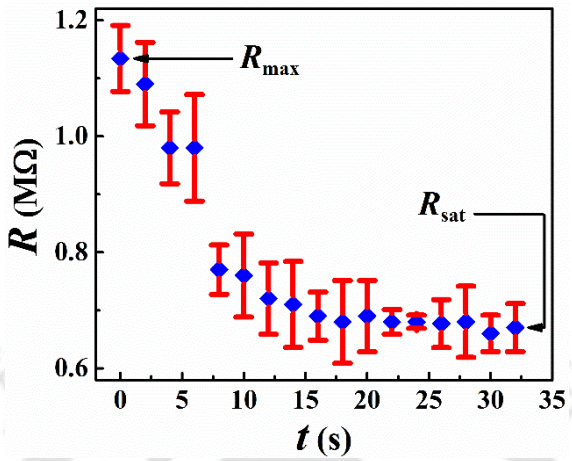

Figure 2.13 Image shows the variation in the resistance of droplet (R) with time for 10 mM urea solution in presence of 0.5 mg/mL urease and 2.5 mM buffer. Two parameters have been presented in the plot - R_{max}, which denotes the maximum resistance at the beginning of the experiment and R_{sat}, which denotes the saturation resistance after a long time, respectively.

Thus, ΔR_s represents the percentage of difference between R_{max} and R_{sat}, which is the measure of the urea loading in the analyte. **Figure 2.12 (e)** shows the variation in the percentage normalized resistance of the droplet, $\Delta R_s = (R_{max} - R_{sat}) \times 100 / R_{max}$, with the urea concentration (C_U). **Figure 2.12 (e)** shows that ΔR_s increased with C_U in the analyte. For lower values of C_U, we found that R_{sat} had relatively lesser values. This is because, for lower levels of urea concentration, lesser concentration of products in the form of ammonium and carbonate ions were produced from the enzymatic reaction. A relatively lower difference between R_{max} and R_{sat} manifested lower values of ΔR_s. However, increment in C_U values subsequently led to more interactions between the enzyme and the analyte molecules, which results in greater differences between R_{max} and R_{sat}, leading to a larger ΔR_s. Thus, **Figure 2.12 (e)** shows a nearly linear and monotonic increase in ΔR_s (%) with C_U, which was found to be suitable for a point-of-care device. It may be noted here that the urea-urease enzymatic reaction was very specific in these experiments. Thus, when human serum samples were employed, we could also measure the urea level of serum from the calibration shown in the **Figure 2.12 (e)**. The triangular symbol in the **Figure 2.12 (e)** shows the measurement of the urea level of human serum from the proposed method and a standard method was nearly comparable.

It may be noted here that, experiments were also performed in order to compare and contrast the detection capabilities between FDrop and SDrop arrangements, the results of which have been summarized in **Figure 2.14**. Since in the FDrop configuration, the droplet surface was free to deform upon the exposure to the incident acoustic waves, the strength of recirculation inside the system was relatively lower as compared to the SDrop arrangement which resulted in high recirculation rates. This caused the difference in results obtained based upon the ΔR_S values for the two systems. While the FDrop configuration initially provided high ΔR_S values at lower reactant concentrations, at higher reactant concentrations, more amounts of unreacted analyte species probably contributed towards the reduction in ΔR_S values. This observation was in stark contrast to the results obtained for SDrop configuration wherein higher recirculation aided in achieving better mixing characteristics and more product formation, which eventually led to a monotonic increase in ΔR_S with C. Thus, SDrop configuration was found to be more sensitive to the different analyte concentrations.

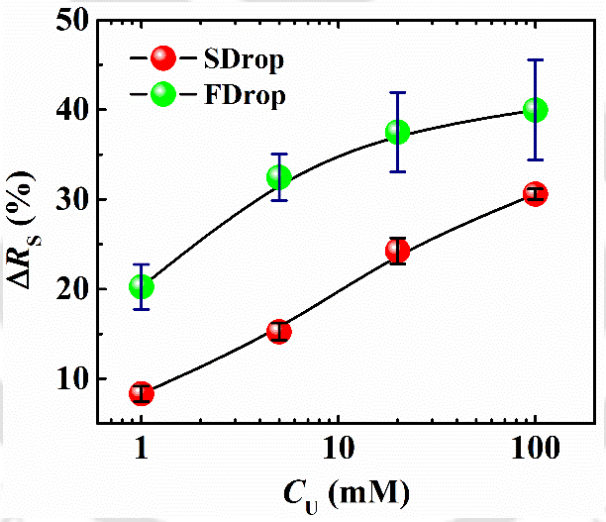

Figure 2.14 Image shows the difference in the ΔR_S values obtained for the two configurations, SDrop and FDrop, in the presence of urea-Au/CdS attached urease reaction.

2.3.5 Sensor Statistics

In order to validate the effectiveness of the microdroplet based urea biosensor, real-time analysis incorporating unknown serum samples from a nearby diagnostic center was performed. It may be noted here that the tests associated with the detection of unknown urea levels in human serum samples were carried out by trained medical professionals in a nearby diagnostic center under the supervision of medical experts, after duly following ethical guidelines. **Table 2.2** presents the variation in the urea concentration in the human serum

detected by a standard technique and the proposed sensor. It may be noted here that the standard values of the urea levels in the different human serum samples were measured by employing, Dimension RxL Max Integrated Chemistry System, SIEMENS. **Table 2.2** presents the urea concentration values of 6 unknown samples obtained from the standard technique and also from the proposed sensing method. The results show that the values obtained using the microdroplet sensor was comparable with the same obtained from the standard method.

Table 2.2 Comparison between standard technique and proposed method for human serum samples.

Urea concentration (mM)			
Sr. No.	**Standard Technique**	**Microdroplet Method**	**± *error***
1	3.21	2.89	0.32
2	4.44	4.12	0.28
3	5.17	5.11	0.08
4	8.26	7.79	0.47
5	10.40	12.36	1.87
6	28.37	30.82	3.08

Furthermore, in this regard, the stability, repeatability and response-time of the proposed sensor was also analyzed. The proposed sensor worked on the principle of variation in electrical resistance of a conducting droplet. Thus, when testing with serum samples, the efficacy of the sensor was expected to be affected by the strength of the buffer solution, presence of a non-specific binding protein, and/or salt concentration (range ~150-200 mM) in human blood serum.[61,70] However, as the salt loading in the proposed droplet sensor was significantly higher (850 mM), the sensitivity test with variations in salt loading was not performed.

Presence of buffer in blood is an important factor because it helps to maintain the pH range. Any excess amount of acids or bases can cause either acidemia (pH < 7.35) or alkalemia (pH >7.45).[61,77] Thus, we studied the performance of the proposed sensor, in terms of the variation in the percentage normalized resistance, $\Delta R_s = (R_{max} - R_{sat}) \times 100 / R_{max}$. This parameter was studied for different buffer loadings for a range of urea concentrations (C_U). **Figure 2.15 (a)** shows that ΔR_s increases with enhancement in C_U. The experiments suggested that, as the urea was converted to ammonium and carbonate ions in the presence of Au/CdS-urease nanocomposite, the R_{sat} values decreased with increased values of C_U. This eventually led to an increase in the overall resistance ΔR_s. Although the buffer salts present in the medium

attempted to neutralize the change, the setup was sensitive enough to track the changes in different analyte concentrations, even at high buffer values.

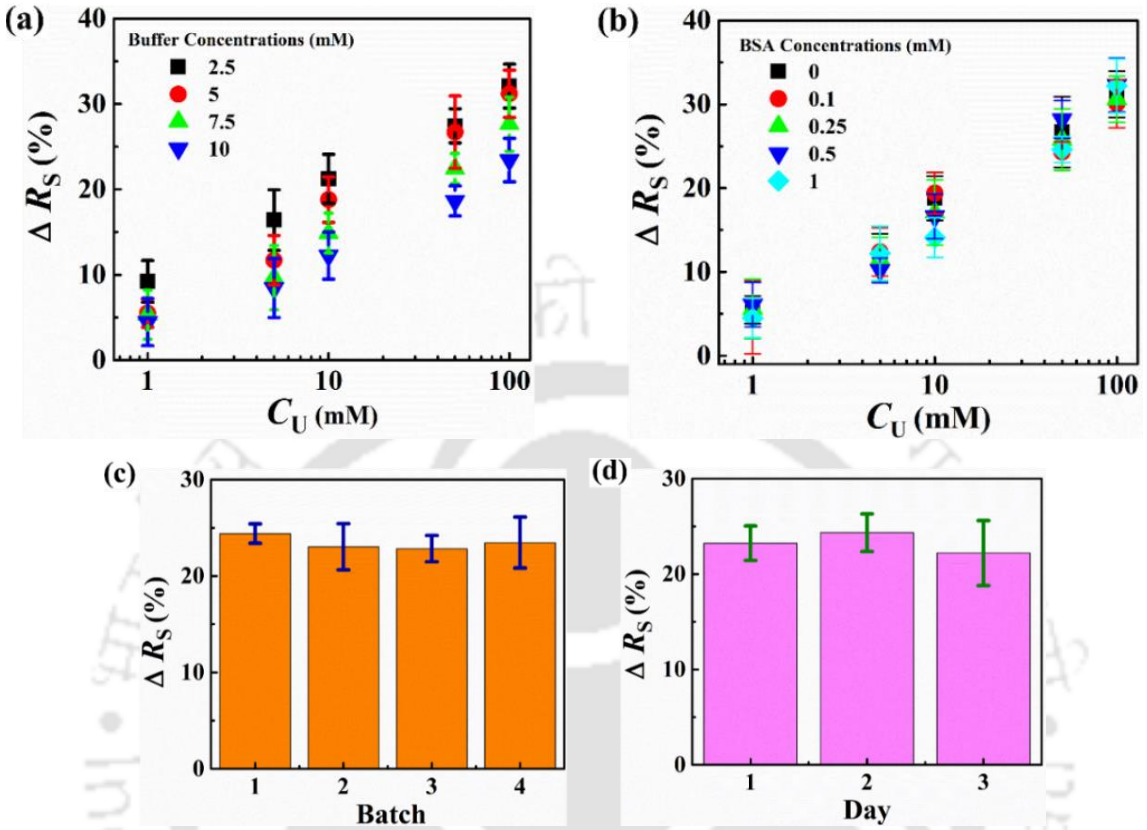

Figure 2.15 Sensitivity studies were performed to check the ΔR_s (%), value for different urea concentrations (C_U) - 1, 5, 10, 50 and 100 mM respectively, for a fixed Au/CdS-urease concentration (0.5 mg/mL) in presence of (a) varying buffer conc. and (b) varying BSA conc. Image (c) represents the repeatability feature of the setup, by checking the ΔR_s (%) value for a fixed urea concentration (10 mM) and fixed urease concentration (0.5 mg/mL) over a number of batches. Image (d) represents the stability feature of the setup, by checking the ΔR_s (%) value for a fixed urea concentration (10 mM) and fixed urease concentration (0.5 mg/mL), performed over a period of 3 days.

In order to check the specificity of the prototype, we utilized bovine serum albumin (BSA) as the non-specific/interfering constituent in the Urea-Au/CdS-urease reaction. The sensor was tested with various BSA loadings in presence of different urea concentrations (C_U), and a fixed urease Au/CdS-concentration, as depicted in **Figure 2.15 (b)**. Increasing concentration of the non-specific protein sample was found to have minimal effect on the overall resistance trend. The experiments confirmed that the sensitivity of the system under consideration was not affected by the presence of non-specific binding proteins.

Table 2.3 Analytical characteristics of diverse urea biosensors.

Type of measurement	Sensing materials	Response time	Sensing range	Sensitivity	References
Electro-chemiluminescence	ABEI/AuNP/ GONR SPE	n.a.	2 - 5.8mM 5.8 - 30 mM	170.58 mM^{-1} 16.23 mM^{-1}	49
Electrochemical	Nano-Tin Oxide thin film	n.a.	1-5 mM 5-20 mM	18.9 µA/mM 2.3 µA/mM	50
Amperometric	CDI immobilised on PANi-Nafion-Cu-modified SPE	15 s	1-100 µM	85 ± 3.4 $mA/M/cm^2$	52
Piezoelectric	Molecularly imprinted TiO_2	< 2 s	0.04-120 µM	n.s.v*	55
Conductometric	Sol-gel immobilized urease on SPE IDA	8.3 s (for 90% response)	0.03-2.5 mM	204 µS/mM	57
Potentiometric	Urease in polypyrrole matrix	n.a.	10-5000 µM	35.07 mV/decade	59
Microdroplet based Resistive measurement	**Au/CdS-urease nanocomposite**	**30 s**	**1-150 mM**	**~5.80 kΩ/mM#**	**Present work**

no specific value (n.s.v.) provided. # Considering average base resistance value to be 1 MΩ.

Furthermore, to check the repeatability of the results under similar conditions, we measured the sensor response for a reaction involving a particular concentration of urea (10 mM): Au/CdS-urease (5 mg/mL), for 4 different batches. **Figure 2.15 (c)** shows that the variation in ΔR_s was insignificant for different batches. The results confirmed that the proposed sensing principle was able to give a relatively stable measure of urea-urease reaction over different batches.

The stability and performance of the sensors for a longer period of time was also tested. For this purpose, reactions involving the same reactant-catalyst ratio as mentioned above, urea (10 mM): Au/CdS-urease (5 mg/mL), were performed and analyzed over a period of three days. The results shown in the **Figure 2.15 (d)** suggests that ΔR_s remained ~ 24 % for three days. Since all the experimental results obtained were in a time period of ~ 30 s, we defined the same as the response time of the sensor. The results elaborated above suggested that the presence of buffer loading and BSA did not interfere with the urea detection. Moreover, the sensor response was fast and stable for a longer duration, which could be suitable for a POCT application. A comparison on the performance parameters of the proposed sensor with the other available

ones in the literature has also been provided in the **Table 2.3** so as to highlight the characteristic features of this biosensor. The comparison suggests that the proposed sensor possesses comparable or better device features, as compared to the other available sensors.

The proposed droplet based-biosensor offers a potential low-cost device which can be suitably modified to provide a point-of-care alternative to the existing commercial biosensors. **Table 2.4** highlights the different components of the biosensor device. An overall estimate of the single biosensor device is ~ Rs. 1230/unit. In comparison to the existing equipment for detection of urea serum in central pathological laboratories as well as different portable sensing kits which may cost in the range Rs. 700 – Rs. 2200 per unit, the proposed droplet based biosensor offers a cost-effective alternative. Steps such as scaled-up manufacturing with more number of field tests will allow the cost of the device to reduce further.

Table 2.4 Component estimate of the microdroplet biosensor setup.

Sl. No.	Items	Max. Unit Price (INR)	Amount Required	Price (INR)
A. Materials				
1	Glass slide	2/piece	1	2.00
2	Copper Wire (180 μm diameter)	0.3/gm	10 gm	3.00
3	Nanoparticle Synthesis Cost	10.00/gm	20 mg	0.20
4	Silver Paste	125.00/gm	5 mg	0.63
5	Electronic components	-	-	15.00
6	Sound source	1200/piece	1 piece	1200.00
			Total cost (INR)	**1220.83**
B. Fabrication				
1	Double sided tape (0.5 inch)	12/m	0.1 m	1.20
2	Substrate Cutter	10/piece	1 piece	10.00
			Total cost (INR)	**11.20**

2.3.6 Sensing Mechanism

Figure 2.16 (a) schematically shows the steps of urea decomposition in presence of Au/CdS-urease nanocomposite to ammonium and carbonate ions. The formation of ions in the solution [61] contributed to the further reduction in the electrical resistance across the droplet upon sound exposure.

Thus, during the sensing process, the reduction in the electrical resistance across the droplet happened due to the combined influence of the salt-loading as well as the generation of additional NH_4^+ ions from the urea-urease reaction, apart from the reasons discussed previously.

Previously, **Figure 2.12 (e)** showed a nearly linear and monotonic increase in ΔR_s with C_U,

which could be explained from the generation of a greater number of NH_4^+ ions during the urea-urease reaction in presence of a larger urea loading in the analyte. This led to a gradual change in the solution conductivity and contributed to the nearly linear and monotonic increase of ΔR_s with C_U.

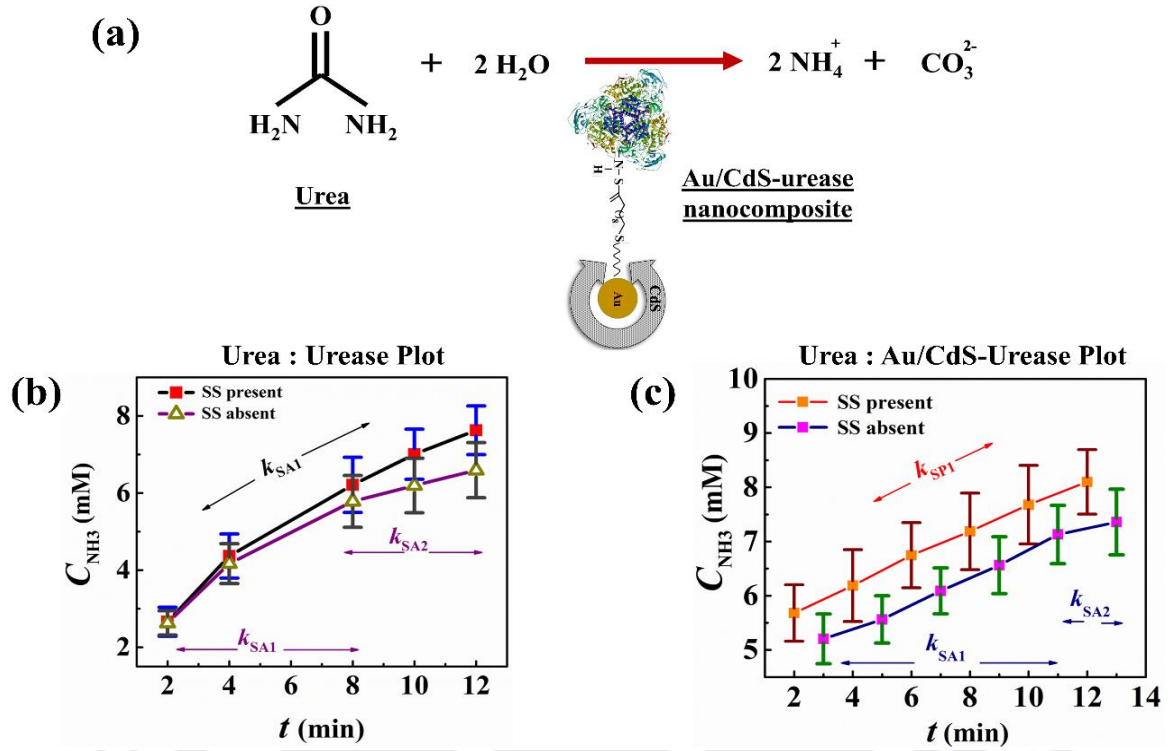

Figure 2.16 Image (a) schematically shows the steps of urea decomposition in presence of Au/CdS-urease nanocomposite to ammonium and carbonate ions. The images (b) and (c) show the reaction kinetics for the urea-urease decomposition without and with Au/CdS NPs, respectively. In case (b), in absence of Au/CdS NPs, the SS facilitated a faster pseudo-first order reaction kinetics between urea-urease whereas in its absence a standard but slower Michealis-Menten kinetics was observed. In case (c), in presence of Au/CdS-urease nanocomposites, the SS facilitated a faster first order reaction kinetics between Au/CdS-urease nanocomposites and urea, however, in its absence the first order reaction kinetics was relatively slower. The kinetics data for the reaction have been presented in **Table 2.5**.

Figures 2.16 (b) and **2.16 (c)** show a systematic analysis of urea decomposition under various conditions. It may be noted here that, for the studies related to the chemical kinetics of the proposed system, the concentration of urease (0.5 mg/mL) and urea (5 mM) were kept fixed. Initially, Au/CdS NPs were attached to the urease molecules through the process already explained in the methods section. Following this, the reaction kinetics of urea-urease was analyzed using a UV-Visible spectrophotometer. For this purpose, we allowed the urea-urease reaction to take place in a test-tube while the product ammonia was reacted with Nessler's reagent to form a yellow colored complex. The absorbance spectra at 405 nm, corresponding

to this complex, was measured with respect to time. The amount of ammonia formed was determined using the calibration chart previously prepared with the help of an ammonium standard. The amount of the yellow colored complex formed was assumed to be directly proportional to the amount of ammonia produced in the urea-urease reaction. For the system with urea-urease homogeneous reaction, 5 mM urea solution (1.5 mL) was reacted with 0.5 mg/mL urease solution (0.5 mL) in PBS buffer at pH 7.2. Thereafter, 60 µL of NR was added to the resulting reaction mixture. The experiments were repeated in the presence and absence of the external sound source (SS). For the system with heterogeneous reaction of urea with Au/CdS-urease, 5 mM urea solution (1.5 mL) was taken along with 0.5 mL of the Au/CdS-urease nanocomposite solution in PBS buffer at pH 7.2. This was diluted with 1 mL of water and then 60 µL of NR was added to the reaction. The experiments were repeated in the presence and absence of the external sound source (SS) following the above-mentioned protocol. Therefore, eventually the variation in C_{NH3} with time was assumed to be similar to the decomposition of urea in the proposed system.

Table 2.5 Rate constants for urea decomposition reaction in presence and absence of acoustic waves when 5 mM urea solution reacted with only 0.5 mg/mL urease solution and 0.5 mg/mL Au/CdS-urease nanocomposites, respectively.

Reaction	SS absent		SS present
	k_{SA1} (s^{-1})	k_{SA2} (mM s^{-1})	k_{SP1} (s^{-1})
Urea : Urease	0.103	0.075	0.131
Urea : Au/CdS-Urease	0.124	0.111	0.172

In order to determine the reaction kinetics, we made use of the rate equation, $v = -\frac{dc}{dt} = \frac{dp}{dt} = kc^n$, where v is the rate of reaction, c is the concentration of reactant, p is the concentration of product, t is the time period elapsed between two successive reactant concentration values, k is the reaction rate constant and n is the order of the reaction. The variation of the ammonia concentration (product) with time was plotted before the slope of the same was analyzed to evaluate the rate constant. Initially, we studied the urea-urease kinetics in the absence of the acoustic wave and nanocomposites, which led to the well-known Michealis-Menten enzymatic reaction kinetics of urea decomposition.[78,79] The results are represented by the triangular symbols in the **Figure 2.16 (b)**, which suggests that the kinetics was first order initially and then zero-order at the later part.

In contrast, in the presence of the acoustic waves, overall interaction between the reactants

enhanced due to the periodic oscillation of the substrate and subsequent vortices generated inside the droplet. Thus, as represented by the red square symbols in **Figure 2.16 (b),** the product formation shows an almost monotonic increment with the passage of time, maintaining a first order reaction kinetics for a longer period, as compared to the former case. The values provided in **Table 2.5** also show a higher rate constant for the case wherein SS was present as compared to ones wherein it was absent. The effect of the SS on the reaction kinetics was found to be more pronounced when the Au/CdS-urease nanocomposite was utilized to catalyze the urea hydrolysis reaction. The presence of Au/CdS NPs had two-fold advantages, (i) they were able to better attach to the enzyme, thereby providing a structural support and (ii) they helped to increase the inherent conductivity of the solution, which made the droplet more responsive towards changes in urea concentration in the analyte.

Figure 2.16 (c) depicts the relationship between product formation and reaction time for both cases - in presence and absence of the external SS. As shown by the rate constant values in **Table 2.5**, the nanocomposite catalyzed reaction showed higher k values compared to the case wherein it was absent. The trend followed a first order reaction kinetics for a longer duration of time, as compared to the former case. The freely moving NPs coated enzymes could more effectively couple with urea in the analyte owing to the availability of a higher surface-to-volume ratio for the reaction.[80] Remarkably, in the presence of an external SS, the reaction rate was found to be even more faster, as shown by the orange square boxes in the **Figure 2.16 (c).** Again, the reaction followed a first order kinetics for the entire duration of the measurement under such a scenario. This was possibly due to the much-improved interaction between the Au/CdS-urease nanocomposites and urea in the analyte, which was facilitated by the vortices in the droplet-fluid and fragmentation of the CdS NPs-Au NPs-urease nanocomposite in presence of the acoustic waves. Concisely, the presence of the acoustic waves together with the heterogeneous enzyme catalysis at the surface of the Au/CdS-urease nanocomposite facilitated the faster depletion of urea, whose concentration could be tracked inside the droplet by measuring the parameter, ΔR_s, as shown in the **Figure 2.12**. Thus, this study proposes a stable sensor which has a fast response time, and which also possesses the capability to detect specifically the urea concentrations in different situations. These features indicate towards the potential usage of this technique as a promising POCT diagnostic tool in the near future.

2.4 Conclusions

In summary, we made use of alternative sources of energy such as audible sounds to stimulate time-periodic pulsations of a glass surface and found out the condition at which the same

oscillates at its natural frequency. Placement of a salt-water microdroplet on such a pulsatile glass substrate led to the periodic deformation and restoration of the droplet shape. A time-periodic variation of the electrical resistance was observed across such droplet when it was integrated with a pair of electrodes. The variations in the electrical resistance could follow the musical notes emanated from various instruments, which were played through a sound source. Remarkably, the droplet oscillation and subsequently the variation in the electrical resistance could commensurate with the intensity, periodicity, and frequency of the musical sounds. The time-periodic deformations of droplet due to the acoustic wave mediated mechanical vibrations at glass substrate could form flow vortices of varying strength with the variations in the intensity, periodicity, and frequency of the musical sounds. Confining the droplet from both the sides with similar glass surfaces led to the increase in the strength of the recirculation and mixing inside the droplet. Such configuration was employed to perform enzymatic urea-urease reaction targeting point-of-care detection of urea in human blood serum. Usage of acoustic waves and Au/CdS-urease nanocomposite helped in faster rate of depletion of urea under such an embodiment. The reaction kinetics for such a system was found to shift to a much faster first order kinetics from more commonly observed Michealis-Menten pathways. A comparison with the standard methods of the detection of urea in human blood serum showed that the proposed proof-of-concept prototype could emerge as a low-cost and sustainable alternative for point-of-care detection of such biomarkers.

References

(1) Aćimović, S. S.; Ortega, M. A.; Sanz, V.; Berthelot, J.; Garcia-Cordero, J. L.; Renger, J.; Maerkl, S. J.; Kreuzer, M. P.; Quidant, R. LSPR Chip for Parallel, Rapid, and Sensitive Detection of Cancer Markers in Serum. *Nano Lett.* **2014**, *14*, 2636–2641.

(2) Pandey, C. M.; Augustine, S.; Kumar, S.; Kumar, S.; Nara, S.; Srivastava, S.; Malhotra, B. D. Microfluidics Based Point-of-Care Diagnostics. *Biotechnol. J.* **2018**, *13*, 1700047.

(3) Xia, Y.; Si, J.; Li, Z. Fabrication Techniques for Microfluidic Paper-Based Analytical Devices and Their Applications for Biological Testing: A Review. *Biosens. Bioelectron.* **2016**, *77*, 774–789.

(4) Dincer, C.; Bruch, R.; Kling, A.; Dittrich, P. S.; Urban, G. A. Multiplexed Point-of-Care Testing - XPOCT. *Trends Biotechnol.* **2017**, *35*, 728–742.

(5) Vashist, S. K. Point-of-Care Diagnostics: Recent Advances and Trends. *Biosensors* **2017**, *7*.

(6) Gomez, F. A. The Future of Microfluidic Point-of-Care Diagnostic Devices. *Bioanalysis*

2013, *5*, 1–3.

(7) Bhattacharjee, M.; Pasumarthi, V.; Chaudhuri, J.; Singh, A. K.; Nemade, H.; Bandyopadhyay, D. Self-Spinning Nanoparticle Laden Microdroplets for Sensing and Energy Harvesting. *Nanoscale* **2016**, *8*, 6118–6128.

(8) Novo, P.; Chu, V.; Conde, J. P. Integrated Fluorescence Detection of Labeled Biomolecules Using a Prism-like PDMS Microfluidic Chip and Lateral Light Excitation. *Lab Chip* **2014**, *14*, 1991–1995.

(9) Wang, A.-B.; Fang, P.-H.; Chu Su, Y.; Hsieh, Y.-W.; Lin, C.-W.; Chen, Y.-T.; Hsu, Y.-C. A Novel Lab-on-a-Chip Design by Sequential Capillary–Gravitational Valves for Urinary Creatinine Detection. *Sensors Actuators B Chem.* **2016**, *222*, 721–727.

(10) Rivet, C.; Lee, H.; Hirsch, A.; Hamilton, S.; Lu, H. Microfluidics for Medical Diagnostics and Biosensors. *Chem. Eng. Sci.* **2011**, *66*, 1490–1507.

(11) Kang, L.; Chung, B. G.; Langer, R.; Khademhosseini, A. Microfluidics for Drug Discovery and Development: From Target Selection to Product Lifecycle Management. *Drug Discov. Today* **2008**, *13*, 1–13.

(12) Boles, D. J.; Benton, J. L.; Siew, G. J.; Levy, M. H.; Thwar, P. K.; Sandahl, M. A.; Rouse, J. L.; Perkins, L. C.; Sudarsan, A. P.; Jalili, R.; et al. Droplet-Based Pyrosequencing Using Digital Microfluidics. *Anal. Chem.* **2011**, *83*, 8439–8447.

(13) Dak, P.; Ebrahimi, A.; Swaminathan, V.; Duarte-Guevara, C.; Bashir, R.; Alam, A. M. Droplet-Based Biosensing for Lab-on-a-Chip, Open Microfluidics Platforms. *Biosensors*. **2016**, 14–29.

(14) Guo, F.; Lapsley, M. I.; Nawaz, A. A.; Zhao, Y.; Lin, S.-C. S.; Chen, Y.; Yang, S.; Zhao, X.-Z.; Huang, T. J. A Droplet-Based, Optofluidic Device for High-Throughput, Quantitative Bioanalysis. *Anal. Chem.* **2012**, *84*, 10745–10749.

(15) Leung, K.; Zahn, H.; Leaver, T.; Konwar, K. M.; Hanson, N. W.; Pagé, A. P.; Lo, C.-C.; Chain, P. S.; Hallam, S. J.; Hansen, C. L. A Programmable Droplet-Based Microfluidic Device Applied to Multiparameter Analysis of Single Microbes and Microbial Communities. *Proc. Natl. Acad. Sci. U. S. A.* **2012**, *109*, 7665–7670.

(16) Wang, J.; Wang, J.; Feng, L.; Lin, T. Fluid Mixing in Droplet-Based Microfluidics with a Serpentine Microchannel. *RSC Adv.* **2015**, *5*, 104138–104144.

(17) Kumar, S.; Ali Faridi, M. R.; Dasmahapatra, A. K.; Bandyopadhyay, D. Magnetic Field Induced Push-Pull Motility of Liquibots. *RSC Adv.* **2016**, *6*, 107049–107056.

(18) Bhutani, U.; Laha, A.; Mitra, K.; Majumdar, S. Sodium Alginate and Gelatin Hydrogels: Viscosity Effect on Hydrophobic Drug Release. *Mater. Lett.* **2016**, *164*, 76–79.

(19) Li, J.; Macdonald, J. Multiplexed Lateral Flow Biosensors: Technological Advances for Radically Improving Point-of-Care Diagnoses. *Biosens. Bioelectron.* **2016**, *83*, 177–192.

(20) St John, A.; Davis, W. A.; Price, C. P.; Davis, T. M. E. The Value of Self-Monitoring of Blood Glucose: A Review of Recent Evidence. *J. Diabetes Complications* **2010**, *24*, 129–141.

(21) King, K. R.; Grazette, L. P.; Paltoo, D. N.; McDevitt, J. T.; Sia, S. K.; Barrett, P. M.; Apple, F. S.; Gurbel, P. A.; Weissleder, R.; Leeds, H.; et al. Point-of-Care Technologies for Precision Cardiovascular Care and Clinical Research: National Heart, Lung, and Blood Institute Working Group. *JACC Basic to Transl. Sci.* **2016**, *1*, 73–86.

(22) Sharma, S.; Zapatero-Rodríguez, J.; Estrela, P.; O'Kennedy, R.; Sharma, S.; Zapatero-Rodríguez, J.; Estrela, P.; O'Kennedy, R. Point-of-Care Diagnostics in Low Resource Settings: Present Status and Future Role of Microfluidics. *Biosensors* **2015**, *5*, 577–601.

(23) Pingarrón, J. M.; Yáñez-Sedeño, P.; González-Cortés, A. Gold Nanoparticle-Based Electrochemical Biosensors. *Electrochim. Acta* **2008**, *53*, 5848–5866.

(24) Solanki, P. R.; Kaushik, A.; Agrawal, V. V; Malhotra, B. D. Nanostructured Metal Oxide-Based Biosensors. *NPG Asia Mater* **2011**, *3*, 17–24.

(25) Venugopal, J.; Ramakrishna, S. Applications of Polymer Nanofibers in Biomedicine and Biotechnology. *Appl. Biochem. Biotechnol.* **2005**, *125*, 147–158.

(26) Yang, N.; Chen, X.; Ren, T.; Zhang, P.; Yang, D. Carbon Nanotube Based Biosensors. *Sensors Actuators B Chem.* **2015**, *207*, *Part*, 690–715.

(27) Kuila, T.; Bose, S.; Khanra, P.; Mishra, A. K.; Kim, N. H.; Lee, J. H. Recent Advances in Graphene-Based Biosensors. *Biosens. Bioelectron.* **2011**, *26*, 4637–4648.

(28) Bergveld, P. The Development and Application of FET-Based Biosensors. *Biosensors* **1986**, *2*, 15–33.

(29) Kimura, M.; Toshima, K. Vibration Sensor Using Optical-Fiber Cantilever with Bulb-Lens. *Sensors Actuators A Phys.* **1998**, *66*, 178–183.

(30) Lange, K.; Blaess, G.; Volgt, A.; Rapp, M.; Hansjosten, E.; Schygulla, U. Packaging of Surface Acoustic Wave (SAW) Based Biosensors: An Important Issue for Future Biomedical Applications. *Proceedings of the 2004 IEEE International Frequency Control Symposium and Exposition, 2004.* 2004, pp 321–325.

(31) Länge, K.; Rapp, B. E.; Rapp, M. Surface Acoustic Wave Biosensors: A Review. *Anal. Bioanal. Chem.* **2008**, *391*, 1509–1519.

(32) Manjakkal, L.; Dang, W.; Yogeswaran, N.; Dahiya, R.; Manjakkal, L.; Dang, W.;

Yogeswaran, N.; Dahiya, R. Textile-Based Potentiometric Electrochemical PH Sensor for Wearable Applications. *Biosensors* **2019**, *9*, 14–25.

(33) Manjakkal, L.; Vilouras, A.; Dahiya, R. Screen Printed Thick Film Reference Electrodes for Electrochemical Sensing. *IEEE Sens. J.* **2018**, *18*, 7779–7785.

(34) Rivnay, J.; Owens, R. M.; Malliaras, G. G. The Rise of Organic Bioelectronics. *Chem. Mater.* **2014**, *26*, 679–685.

(35) Matta, D. P.; Tripathy, S.; Krishna Vanjari, S. R.; Sharma, C. S.; Singh, S. G. An Ultrasensitive Label Free Nanobiosensor Platform for the Detection of Cardiac Biomarkers. *Biomed. Microdevices* **2016**, *18*, 111–120.

(36) Vashishth, P.; Sen, P. A Novel Method for Fabricating Graphene Sensors in Channel for Biomedical Applications. In *2018 IEEE 13th Annual International Conference on Nano/Micro Engineered and Molecular Systems (NEMS)*; IEEE, 2018; pp 405–408.

(37) Curthoys, I. S. A Critical Review of the Neurophysiological Evidence Underlying Clinical Vestibular Testing Using Sound, Vibration and Galvanic Stimuli. *Clin. Neurophysiol.* **2010**, *121*, 132–144.

(38) Beeby, R. T. and P. G.-J. and M. T. and T. O. and S. R. and S. Self-Powered Autonomous Wireless Sensor Node Using Vibration Energy Harvesting. *Meas. Sci. Technol.* **2008**, *19*, 125202.

(39) Sun, Q.; Liu, D.; Wang, J.; Liu, H. Distributed Fiber-Optic Vibration Sensor Using a Ring Mach-Zehnder Interferometer. *Opt. Commun.* **2008**, *281*, 1538–1544.

(40) Amirtharajah, R.; Chandrakasan, A. P. Self-Powered Signal Processing Using Vibration-Based Power Generation. *IEEE Journal of Solid-State Circuits*. 1998, pp 687–695.

(41) Länge, K.; Blaess, G.; Voigt, A.; Götzen, R.; Rapp, M. Integration of a Surface Acoustic Wave Biosensor in a Microfluidic Polymer Chip. *Biosens. Bioelectron.* **2006**, *22*, 227–232.

(42) Jakubik, W. P. Surface Acoustic Wave-Based Gas Sensors. *Thin Solid Films* **2011**, *520*, 986–993.

(43) Grate, J. W.; Klusty, M. Surface Acoustic Wave Vapor Sensors Based on Resonator Devices. *Anal. Chem.* **1991**, *63*, 1719–1727.

(44) Ifantis, A.; Kalis, A. On the Use of Ultrasonic Communications in Biosensor Networks. *2008 8th IEEE International Conference on BioInformatics and BioEngineering*. 2008, pp 1–6.

(45) Moreno-Bondi, M.-C.; Mobley, J.; Alarie, J.-P.; Vo-Dinh, T. Antibody-Based Biosensor

for Breast Cancer with Ultrasonic Regeneration. *J. Biomed. Opt.* **2000**, *5*, 350–354.

(46) Hawkes, J. J.; Long, M. J.; Coakley, W. T.; McDonnell, M. B. Ultrasonic Deposition of Cells on a Surface. *Biosens. Bioelectron.* **2004**, *19*, 1021–1028.

(47) Israel Gotsman, D. Z. D. P. D. A. C. L. A. K. The Significance of Serum Urea and Renal Function in Patients With Heart Failure. *Medicine (Baltimore).* **2010**, *89*, 197–203.

(48) Soldatkin, O. O.; Kucherenko, I. S.; Marchenko, S. V; Ozansoy Kasap, B.; Akata, B.; Soldatkin, A. P.; Dzyadevych, S. V. Application of Enzyme/Zeolite Sensor for Urea Analysis in Serum. *Mater. Sci. Eng. C* **2014**, *42*, 155–160.

(49) Gutiérrez, M.; Alegret, S.; del Valle, M. Potentiometric Bioelectronic Tongue for the Analysis of Urea and Alkaline Ions in Clinical Samples. *Biosens. Bioelectron.* **2007**, *22*, 2171–2178.

(50) Ahmad, R.; Tripathy, N.; Hahn, Y.-B. Highly Stable Urea Sensor Based on ZnO Nanorods Directly Grown on Ag/Glass Electrodes. *Sensors Actuators B Chem.* **2014**, *194*, 290–295.

(51) Bayramoğlu, G.; Altınok, H.; Bulut, A.; Denizli, A.; Arıca, M. Y. Preparation and Application of Spacer-Arm-Attached Poly(Hydroxyethyl Methacrylate-Co-Glycidyl Methacrylate) Films for Urease Immobilisation. *React. Funct. Polym.* **2003**, *56*, 111–121.

(52) Pundir, C. S.; Jakhar, S.; Narwal, V. Determination of Urea with Special Emphasis on Biosensors: A Review. *Biosens. Bioelectron.* **2019**, *123*, 36–50.

(53) Dhawan, G.; Sumana, G.; Malhotra, B. D. Recent Developments in Urea Biosensors. *Biochem. Eng. J.* **2009**, *44*, 42–52.

(54) Ismail, N. S.; Hoa, L. Q.; Huong, V. T.; Inoue, Y.; Yoshikawa, H.; Saito, M.; Tamiya, E. Electrochemiluminescence Based Enzymatic Urea Sensor Using Nanohybrid of Isoluminol-Gold Nanoparticle-Graphene Oxide Nanoribbons. *Electroanalysis* **2017**, *29*, 938–943.

(55) Ansari, S. G.; Fouad, H.; Shin, H.-S.; Ansari, Z. A. Electrochemical Enzyme-Less Urea Sensor Based on Nano-Tin Oxide Synthesized by Hydrothermal Technique. *Chem. Biol. Interact.* **2015**, *242*, 45–49.

(56) Shalini, J.; Sankaran, K. J.; Lee, C.-Y.; Tai, N.-H.; Lin, I.-N. An Amperometric Urea Bisosensor Based on Covalent Immobilization of Urease on N2 Incorporated Diamond Nanowire Electrode. *Biosens. Bioelectron.* **2014**, *56*, 64–70.

(57) Zhybak, M.; Beni, V.; Vagin, M. Y.; Dempsey, E.; Turner, A. P. F.; Korpan, Y. Creatinine and Urea Biosensors Based on a Novel Ammonium Ion-Selective Copper-

Polyaniline Nano-Composite. *Biosens. Bioelectron.* **2016**, *77*, 505–511.

(58) Arain, M.; Nafady, A.; Sirajuddin; Ibupoto, Z. H.; Hussain Sherazi, S. T.; Shaikh, T.; Khan, H.; Alsalme, A.; Niaz, A.; Willander, M. Simpler and Highly Sensitive Enzyme-Free Sensing of Urea via NiO Nanostructures Modified Electrode. *RSC Adv.* **2016**, *6*, 39001–39006.

(59) Kumar, P.; Ramulu Lambadi, P.; Kumar Navani, N. Non-Enzymatic Detection of Urea Using Unmodified Gold Nanoparticles Based Aptasensor. *Biosens. Bioelectron.* **2015**, *72*, 340–347.

(60) Yang, Z.; Liu, X.; Zhang, C.; Liu, B. A High-Performance Nonenzymatic Piezoelectric Sensor Based on Molecularly Imprinted Transparent TiO2 Film for Detection of Urea. *Biosens. Bioelectron.* **2015**, *74*, 85–90.

(61) Velychko, T. P.; Soldatkin; Melnyk, V. G.; Marchenko, S. V.; Kirdeciler, S. K.; Akata, B.; Soldatkin, A. P.; El'skaya, A. V.; Dzyadevych, S. V. A Novel Conductometric Urea Biosensor with Improved Analytical Characteristic Based on Recombinant Urease Adsorbed on Nanoparticle of Silicalite. *Nanoscale Res. Lett.* **2016**, *11*, 1–6.

(62) Lee, W.-Y.; Kim, S.-R.; Kim, T.-H.; Lee, K. S.; Shin, M.-C.; Park, J.-K. Sol–Gel-Derived Thick-Film Conductometric Biosensor for Urea Determination in Serum. *Anal. Chim. Acta* **2000**, *404*, 195–203.

(63) Werkmeister, F. X.; Koide, T.; Nickel, B. A. Ammonia Sensing for Enzymatic Urea Detection Using Organic Field Effect Transistors and a Semipermeable Membrane. *J. Mater. Chem. B* **2016**, *4*, 162–168.

(64) Varadharaj, E. K.; Jampana, N. Non-Invasive Potentiometric Sensor for Measurement of Blood Urea in Human Subjects Using Reverse Iontophoresis. *J. Electrochem. Soc.* **2016**, *163*, B340–B347.

(65) Puliyalil, H.; Slobodian, P.; Sedlacik, M.; Benlikaya, R.; Riha, P.; Ostrikov, K.; Cvelbar, U. Plasma-Enabled Sensing of Urea and Related Amides on Polyaniline. *Front. Chem. Sci. Eng.* **2016**, *10*, 265–272.

(66) Zhang, W.; Zheng, J.; Tan, C.; Lin, X.; Hu, S.; Chen, J.; You, X.; Li, S. Designed Self-Assembled Hybrid Au@CdS Core-Shell Nanoparticles with Negative Charge and Their Application as Highly Selective Biosensors. *J. Mater. Chem. B* **2015**, *3*, 217–224.

(67) Kumar, V.; Chopra, A.; Arora, S.; Yadav, S.; Kumar, S.; Kaur, I. Amperometric Sensing of Urea Using Edge Activated Graphene Nanoplatelets. *RSC Adv.* **2015**, *5*, 13278–13284.

(68) Aslan, K.; Pérez-Luna, V. H. Surface Modification of Colloidal Gold by Chemisorption

of Alkanethiols in the Presence of a Nonionic Surfactant. *Langmuir* **2002**, *18*, 6059–6065.

(69) Parashar, U. K.; Nirala, N. R.; Upadhyay, C.; Saxena, P. S.; Srivastava, A. Urease Immobilized Fluorescent Gold Nanoparticles for Urea Sensing. *Appl. Biochem. Biotechnol.* **2015**, *176*, 480–492.

(70) Sahoo, B.; Sahu, S. K.; Pramanik, P. A Novel Method for the Immobilization of Urease on Phosphonate Grafted Iron Oxide Nanoparticle. *J. Mol. Catal. B Enzym.* **2011**, *69*, 95–102.

(71) Deepu, P.; Chowdhuri, S.; Basu, S. Oscillation Dynamics of Sessile Droplets Subjected to Substrate Vibration. *Chem. Eng. Sci.* **2014**, *118*, 9–19.

(72) Morozov, M.; Manor, O. Vibration-Driven Mass Transfer and Dynamic Wetting. *Curr. Opin. Colloid Interface Sci.* **2018**, *36*, 37–45.

(73) Al-Tememee, N. A. A.; Al-Ani, S. K. J.; Al-Mashhadani, D. Y. S. *The Response of a Window Glass to the Frequencies of Sound*; 2013; Vol. 6.

(74) Li, R.; Ye, H.; Zhang, W.; Ma, G.; Su, Y. An Analytic Model for Accurate Spring Constant Calibration of Rectangular Atomic Force Microscope Cantilevers. *Sci. Rep.* **2015**, *5*, 15828.

(75) Bovermann, T.; Campo, A. de; Egermann, H.; Hardjowirogo, S.-I.; Weinzierl, S. *Musical Instruments in the 21st Century*; Bovermann, T., de Campo, A., Egermann, H., Hardjowirogo, S.-I., Weinzierl, S., Eds.; Springer Singapore: Singapore, 2017.

(76) Mathur, A.; Vijayakumar, S. H.; Chakrabarti, B.; Singh, N. C. Emotional Responses to Hindustani Raga Music: The Role of Musical Structure. *Front. Psychol.* **2015**, *6*, 513.

(77) Salenius, P. A Study of the Ph and Buffer Capacity of Blood, Plasma and Red Blood Cells. *Scand. J. Clin. Lab. Invest.* **1957**, *9*, 160–167.

(78) Laidler, K. J.; Hoare, J. P. The Molecular Kinetics of the Urea-Urease System. I. The Kinetic Laws. *J. Am. Chem. Soc.* **1949**, *71*, 2699–2702.

(79) Kistiakowsky, G. B.; Rosenberg, A. J. The Kinetics of Urea Hydrolysis by Urease1. *J. Am. Chem. Soc.* **1952**, *74*, 5020–5025.

(80) Meryam Sardar, R. A.; Sardar, M. Enzyme Immobilization: An Overview on Nanoparticles as Immobilization Matrix. *Biochem. Anal. Biochem.* **2015**, *04*, 1–8.

Chapter 03

Microdroplet photofuel cells to harvest high-density energy and dye degradation

This chapter has been published as Thakur, S.; Das, N. M.; Kumar, S.; Dasmahapatra, A. K.; Bandyopadhyay D. Microdroplet photofuel cells to harvest high-density energy and dye degradation. *Nanoscale Adv.* **2020**, *2*, 1613-1620.

Abstract

A membraneless photofuel cell, namely μ-DropFC, has been designed and developed to harvest chemical and solar energies simultaneously. The prototypes can also perform environmental remediation to demonstrate their multitasking potential as a sustainable hybrid device in a single embodiment. Hydrogen peroxide (H_2O_2) microdroplet at optimal pH and salt loading has been utilized as the fuel integrated with Al as anode and zinc phthalocyanine (ZnPC) coated Cu as cathode. The presence of n-type semiconductor ZnPC in between the electrolyte and metal enabled the formation of a photo-active Schottky junction suitable for power generation under light. Concurrently, the oxidation and reduction of H_2O_2 on the electrodes helped in conversion of chemical energy into the electrical one in the same membraneless setup. Suspension of Au nanoparticles (Au NPs) in the droplet helped in enhancing the overall power density under photonic illumination through the effects of localized surface Plasmon resonance (LSPR). Further, the presence of photo-active n-type CdS NPs enabled catalytic photo-degradation of dyes under light in the same embodiment. A 40 μL μ-DropFC could show a significantly high open circuit potential of ~ 0.58 V along with a power density of 0.72 mW/cm^2. Under the same condition, integration of ten such μ-DropFCs could produce a power density of ~7 mW/cm^2 at an efficiency of 3.4%, showing the potential of the prototype for a very large scale integration (VLSI). The μ-DropFC could also degrade ~ 85% of an industrial pollutant Rhodamine 6G in 1 h while generating a power density of ~ 0.6 mW/cm^2. The performance parameters of μ-DropFC were found to be either comparable or superior to the existing prototypes. In a way, the affordable, portable, membraneless, and high-performance μ-DropFC could harness energy from multiple resources while engaging in environmental remediation.

3.1 Introduction

Infusing the efficacies of nanoscale science[1,2] in the microfluidic devices for the development of affordable and portable energy harvesters with a significantly high power density have attracted a major research attention in the recent years. The inventions of state-of-art thermoelectric, triboelectric, piezo-acoustic, electrokinetic, or Marangoni energy harvesters are directed towards this end.[3–9] Interestingly, the traditional renewable[10] or non-renewable[11] energy harvesting technologies have also been undergoing a paradigm-shift from the regime of macroscopic to the very large scale integration (e.g. VLSI) of micro or nanoscopic prototypes for enhanced efficiency, higher throughput, and escalated power density.[12] In this regard, optimized arrangement of energy harvesters will not only reduce overall resistance but will also improve the output voltage. This can be further utilized for storing energy in off-grid systems such as capacitors for powering remote, low-power intensive systems for long-term. Thus, it is not very surprising that a flurry of research activities has also been observed in the miniaturization along with process intensification[13] of more widely employed commercial energy harvesters such as batteries,[14,15] photovoltaic cells,[16] or fuel cells[17,18] for a better efficiency.

In particular, since the path-breaking invention by Sir William Grove in the 18th century[19] to convert chemical energy into the electrical one, fuel cells (FCs) have shown remarkable progress[20] despite numerous setbacks[21]. For example, the utility of the FCs as isolated or distributed power resources has now been translated into a few megawatt plants for power supply.[17] A large varieties of FCs composed of polymer electrolyte membranes, phosphoric acid, methanol or alkali have made appearance at different length and performance scales not only to power energy intensive rockets but also to run the miniaturized micro-transmitters or biomedical devices.[22–25] Presently, the fuels utilized in the FCs are either hydrogen (H_2), methanol (CH_3OH), methane (CH_4) or their different combinations.[26] Especially, H_2 has been the preferred fuel over others owing to its higher energy density and green chemistry to produce water during the energy harvesting.[26,27]

On the other hand, as an alternative, hydrogen peroxide (H_2O_2) has lately been employed as an alternative fuel for FCs because of its high energy density and non-toxicity until a concentration of 20 M.[28] Much like H_2, peroxide is also a carbon-free and green energy source producing water and oxygen during energy harvesting.[29] In short time, the peroxide FCs has evolved from simple oxidizers to a standalone energy sources[28,30] because, (i) the existence of peroxide in the liquid state under ambient conditions makes it better candidate for fuel storage than H_2; (ii)

although peroxide possesses a lower gravimetric energy density, however, has a significantly higher volumetric energy density; (iii) they have higher fuel efficiency suitable for the space or underwater applications.[23,24] However, the peroxide FCs also face limitations associated with the production,[31] preservation,[32,33] supply, and storage[28] of rather unstable H_2O_2 at industrial scale.

On the other hand, the utilization of membranes in FCs has been found to be slowly waning, which is paving the way to the much simpler membraneless single compartment FCs. The concept was first realized by Yamazaki et al.[34] who employed H_2O_2 as both an electron acceptor and fuel with a Ag cathode alongside using Au, Pt, Pd or Ni anodes. Subsequently, various cathodic (e.g. metals, inert materials, conducting dyes or their combinations)[34,35] and anodic (e.g. Al, Ni, C, and noble metals)[30,36,37] materials have been experimented for the membraneless FCs over the years. In particular, ferrocyanides along with phthalocyanines and porphyrins[38] (PCs) have been found to be excellent candidates for H_2O_2 reduction owing to their low onset potentials and cost-effectiveness.[30,36,39–41] Interestingly, an Al (anode)-H_2O_2 (fuel) combination is found to possess a significantly higher specific energy (~ 17000 Wh/kg),[18,42] which is even higher than some of the state-of-art Li-ion batteries(~ 12000 Wh/kg).[43] However, the membraneless peroxide FCs also suffer from the limitations associated with the crossover of reactants and thus are suitable for only the low-power intensive systems.

In view of this background, we report the design and development of a peroxide microdroplet based membraneless FC, namely μ-DropFC, which is capable of binding the combined influences of the chemical and light energies into the electrical one under the same embodiment. In a sense, the droplet based device is found to be an exception to the most of the previous attempts where film based approaches were preferred.[5,44] While the usage of the microdroplet architecture helps in gaining advantages from the confinement effects due to miniaturization, the photo-activity of the droplet helps in improving the open circuit voltage (ψ_{oc}) and current density (J) of the μ-DropFC.16 The photo-activity[45,46] inside μ-DropFC has been facilitated by the localized surface plasmon resonance (LSPR)[46] of the suspended gold nanoparticles (Au NPs) under light sources. The presence of Au NPs further, also enhances the rate of charge transfer between the electrodes by improving the electrical conductivity of the microdroplet.[47] In order to ensure a lower economic footprint, the μ-DropFC is integrated with an Al-foil anode and a Cu-ZnPC cathode, which promote an augmented catalytic breakdown of H_2O_2 under photonic excitation.[48,49] A low work-function Cu also facilitates a stronger adhesion with ZnPC to provide a strong electronic conductivity.[50–53] Importantly, in such a

simple embodiment, a single μ-DropFC can show a significantly high ψ_{oc} of ~ 0.58 V and power density of ~ 0.72 mW/cm^2 per unit mass of fuel. Ten such μ-DropFCs show a power density of ~ 7 mW/cm^2 at an efficiency of 3.4 %, which highlights the potential of such device for μ-VLSI and scale up.

Furthermore, in order to enhance the overall utility of the prototype, the μ-DropFC setup has been utilized in environmental remediation processes such as the dye degradation, while simultaneously being involved in energy harvesting from the peroxide fuel and photonic excitations. For this purpose, we synthesized a nanocomposite of Au NPs embedded in a matrix of cadmium sulfide nanoparticles (CdS NPs) before suspending them in the peroxide fuel to breakdown the "stubborn" organic dyes under photonic excitation.[54] As a model system, we show that the Au and CdS NPs with a powerful photocatalytic activity[55] can break the rhodamine 6G dye under light while demonstrating a significantly higher power density of ~0.62 mW/cm^2. In some way, the simple and affordable μ-DropFC emulate the state-of-art microbial FCs, which have been operated in tandem with dye degradation to simultaneously perform dual objectives.[56,57] Concisely, the study showcases the versatility of a droplet[44] or digital58 microfluidic device loaded with the efficacies of nanoscience for efficient energy harvesting from electrochemical and solar resources together with performing environmental remediation.[56,57,59]

3.2 Materials and Methods

3.2.1 Materials

The chemicals, 50% (w/v) hydrogen peroxide solution (H_2O_2), cadmium nitrate ($CdNO_3$), sodium sulfide (Na_2S), hydrochloric acid (37% (w/w), HCl) and sodium hydroxide (NaOH) were purchased from Merck, India. The chemicals, zinc phthalocyanine (ZnPC) and rhodamine 6G (Rh6G) were purchased from Sigma Aldrich, India. The copper wires and aluminum foil were purchased from a local vendor. The de-ionized water was employed for cleaning, washing and the preparation of the solutions. The gold (III) chloride hydrate, sodium borohydride, trisodium citrate dihydrate, and sodium chloride were purchased from Sigma Aldrich, India. All the chemicals were of analytical grade and were utilized without further purification.

3.2.1.1 Characterization Techniques

The open circuit voltage (ψ_{oc}) was measured with the help of a digital nanovoltmeter (SES Instruments). The Keithley 2640A sourcemeter in connection with Kickstarter software were used for potentio-amperometry (*I*-ψ) and chrono-amperometry (*J*-*t*) characterizations. The

surface morphologies and lattice structures (SAED patterns) of the nanocomposites were detected using field emission transmission electron microscope (FETEM, Jeol India). A field emission scanning electron microscopy with energy dispersive X-ray (FESEM-EDX, Zeiss) was used to confirm the elemental composition of the different materials. The materials characterizations of the nanocomposites and electrodes were carried out using UV-Visible (SHMIADZU UV-2600 model) and Raman (Horriba) spectroscopies. Kelvin Probe Force Microscopy (KPFM) was also employed to determine the work function of the electrode after the cell operation.

3.2.2 Methods

3.2.2.1 Synthesis of Au and CdS NPs:

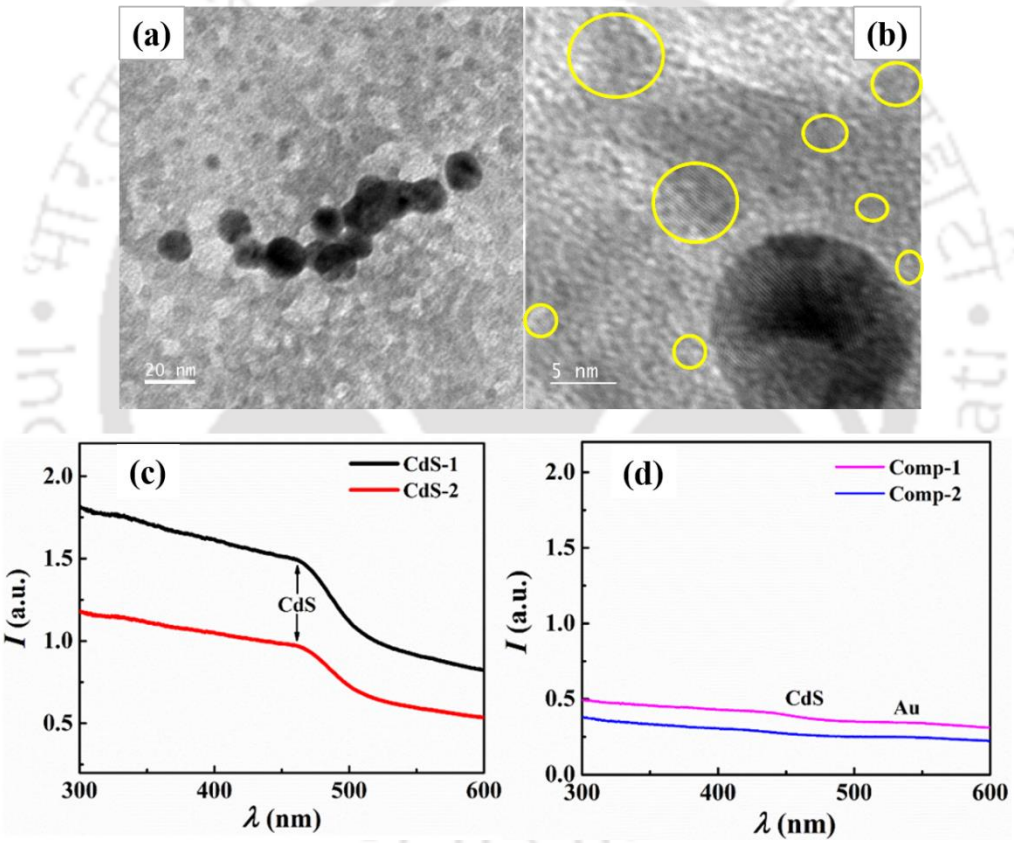

Figure 3.1 FETEM images of Au and CdS NPs. Image (a) shows the average size of AuNPs to be ~ 15 nm to 20 nm. Image (b) shows the HRTEM image of the Au (darker patch) and CdS NPs (encircled). The UV-Visible spectroscopy of bare CdS NPs and Au/CdS NPs in the presence of H_2O_2 has been shown. In image (c), CdS-1 and CdS-2 refers to UV-Visible spectra of CdS NP before and after treatment with H_2O_2. In the image (d) Au/CdS-1 and Au/CdS-2 refers to UV-Visible spectra of Au/CdS NPs before and after treatment with H_2O_2.

Initially, Au NPs were prepared by the reduction of the gold chloride salt in the presence of trisodium citrate. For this purpose, a 30 mL of HAuCl4 solution (0.5 mM) in water was prepared and stirred for 30 min. Gradually its temperature was increased and when the solution

started to boil, then 3 mL of 38.8 mM trisodium citrate was added drop by drop. Thereafter, the solution was stirred at the boiling temperature for 15-20 min while it changed colour from yellow to purple to eventually red. Thereafter the solution was allowed to cool down gradually while being stirred, which led to the formation of Au NPs in the size range of 15-20 nm, as confirmed by the FETEM and UV-Visible spectra, in **Figure 3.1**. In order to prepare the composite of Au and CdS NPs, initially, a 20 mL of prepared Au NPs solution (20 nM) was added to a beaker, where 10 mL each of aqueous solution of 0.01M $CdNO_3$ and 0.01 M Na_2S solution in 0.1 M NaOH were added simultaneously. The reaction temperature was maintained at 60°C for 12 h while the solution was stirred continuously. The FETEM and UV-Visible spectra confirmed the formation of the composite of Au and CdS NPs. The sizes of the Au NPs in the composite were around 20 nm, while CdS NPs were around 2-5 nm. This was confirmed by the FETEM images, which have been shown in **Figures 3.1 (a)** and **(b)**. The smaller CdS NPs (lighter gray shade) compose the base surface on which the islands of the Au NPs (darker gray shade) form a composite arrangement. UV-Visible spectroscopy was used to characterize the stability of the Au-CdS nanocomposite after peroxide treatment.

The plots (c) and (d) in the **Figure 3.1** show the characteristic peaks of Au (520 nm) and CdS (450 nm) before and after the treatment with peroxide fuel. The plot (c) shows that the CdS peak intensity (as depicted in the ordinate values of the plot) drastically decreased and there was a peak shift due to the oxidation of CdS to $CdSO_4$ during peroxide treatment. However, for the other case in the plot (d) we observe that there is a slight decrease in the peak intensity with a negligible shift in peak wavelength thereby verifying the stability of the Au-CdS nanocomposites against H_2O_2.

3.2.2.2 Nomenclature of Fuels*:*

In order to identify the overall characteristics of the μ-DropFCs, different compositions of fuel have been prepared. For this purpose, additives such as the suspensions of Au and/or CdS NPs and Rh6G of different volume and strength have been added to the primary system of 0.3 M H_2O_2, 0.1 M HCl and 1 M NaCl solution, as tabulated in the **Table 3.1**.

The fuels 1 – 6 shown in the table have been employed to perform the various parametric studies reported in what follows throughout this work. It may be noted here that the fuels 2 and 3 had also five variants each based on the volume of the suspension of nanoparticles added, namely, fuels 2I – 2V and fuels 3I – 3V.

Table 3.1 Different fuel compositions and their respective abbreviations.

Sl. No.	Compositions
Fuel 1	Mixture of 10 µL 0.3M aqueous H_2O_2 with 10 µL of 0.1M aqueous HCl and 10 µL of 1M of aqueous NaCl
Fuels 2I – 2V	I. 10 µL of Fuel 1 with 10 µL of 20nM aqueous Au NPs II. 10 µL of Fuel 1 with 20 µL of 20nM aqueous Au NPs III. 10 µL of Fuel 1 with 30 µL of 20nM aqueous Au NPs IV. 10 µL of Fuel 1 with 40 µL of 20nM aqueous Au NPs V. 10 µL of Fuel 1 with 50 µL of 20nM aqueous Au NPs
Fuels 3I – 3V*	I. 10 µL of Fuel 1 with 10 µL of aqueous Au/CdS NPs mixture II. 10 µL of Fuel 1 with 20 µL of aqueous Au/CdS NPs mixture III. 10 µL of Fuel 1 with 30 µL of aqueous Au/CdS NPs mixture IV. 10 µL of Fuel 1 with 40 µL of aqueous Au/CdS NPs mixture V. 10 µL of Fuel 1 with 50 µL of aqueous Au/CdS NPs mixture
Fuel 4	10 µL of Fuel 1 with 10 µL of 0.5 mg/ml aqueous Rhodamine 6G
Fuel 5	10 µL of Fuel 1 with 10 µL of 0.5 mg/ml aqueous Rhodamine 6G + and 10 µL of 20nM aqueous Au NPs
Fuel 6*	10 µL of Fuel 1 with 10 µL of 0.5 mg/ml aqueous Rhodamine 6G + and 10 µL of aqueous Au/CdS NPs mixture

****Concentration of Au/CdS NPs mixture was unknown since they were synthesized in situ, as discussed below.***

3.2.2.3 µ-DropFC Setup

An overview of the experimental setup for the µ-DropFC and its different components has been shown in **Figure 3.2**. The membraneless energy harvester was composed of a ~30 µL droplet of 0.3 M aqueous hydrogen peroxide (H_2O_2) mixed with 1 M aqueous NaCl electrolyte and 0.1M HCl. In order to infuse the photo-activity to the µ-DropFC aqueous suspension of 20 nM Au NPs was mixed. The volume of the Au NPs suspension was varied from 10 µL – 50 µL in order to uncover the effects of the LSPR on the performance of the µ-DropFC. A 150 W Xenon (Xe) lamp was used as a light source to excite the Plasmonic Au NPs and enhance the output characteristics of the system in terms of ψ_{oc} and P values. The light source was always placed ~ 15 cm from the top of the droplet. The µ-DropFC was integrated with an anode composed of a rectangular aluminum foil (Al) of dimension 2.5 cm × 2.5 cm attached to a glass substrate

and cylindrical Cu cathode (dia. 1 mm) coated with a layer of ZnPC of thickness 200 nm – 300 nm. Glass substrates were cleaned following a protocol mentioned in the **Appendix**.

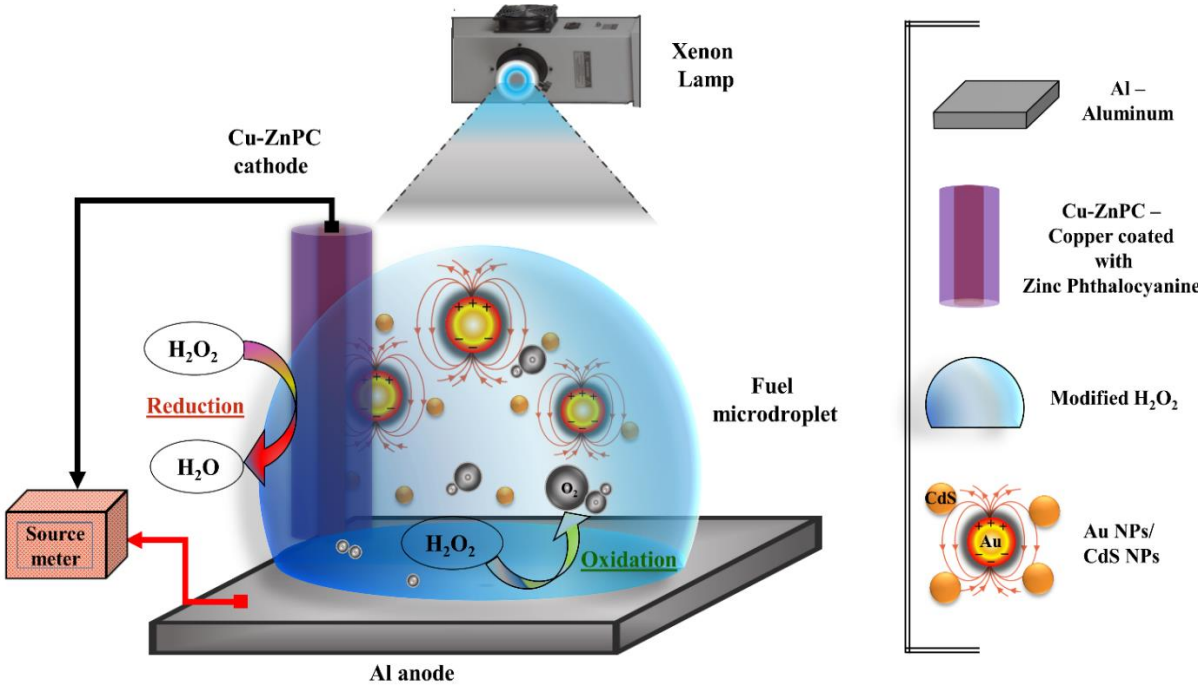

Figure 3.2 Schematic diagram of the μ-DropFC setup comprising of Cu-ZnPC cathode, Al foil anode, microdroplet with the fuel (0.3 M H2O2, 0.1 M HCl, 1 M NaCl), additives (Au/CdS NPs) and light source. The image also schematically shows the redox half-reactions at the cathode and anode, $\mathbf{H_2O_2 \rightarrow O_2 + 2H^+ + 2e^-}$ and $\mathbf{H_2O_2 + 2H^+ + 2e^- \rightarrow 2H_2O}$ respectively. The legends aid in the identification of the different components and their placements.

3.3 Results and Discussion

3.3.1 Mechanistic Details

Figure 3.3 justifies the choices of different materials chosen for the proposed μ-DropFC. Subsequently, the energy band diagrams shown also uncover the working principle of the μ-DropFC, under different conditions.[60] **Figure 3.3 (a)** schematically depicts the basic state of μ-DropFC before any reaction started or light illumination took place.[60] The schematic diagram shows the Fermi levels (E_F) of Cu, ZnPC, peroxide solution, and Al alongside showing the band-gap for the p-type semiconductor ZnPC with the conduction and valance bands at, E_C = – 3.8 eV and E_V = – 5.8 eV.[60,61] The presence of ZnPC ensured the formation of a Schottky junction between metallic Cu, p-type SC ZnPC, and electrolyte. Further, the peroxide electrolyte was reactive at room temperature and the typical energy levels D_{ox} (e.g. – 5.3 eV)[30,62] and D_R (e.g. – 6.4 eV)[30,62] denote their oxidation and reduction potentials.

It may be noted here that once the droplet was integrated with the electrodes, the setup started harvesting energy even under dark condition and the energy band diagram after such equilibration has been shown in the **Figure 3.3 (b)**.

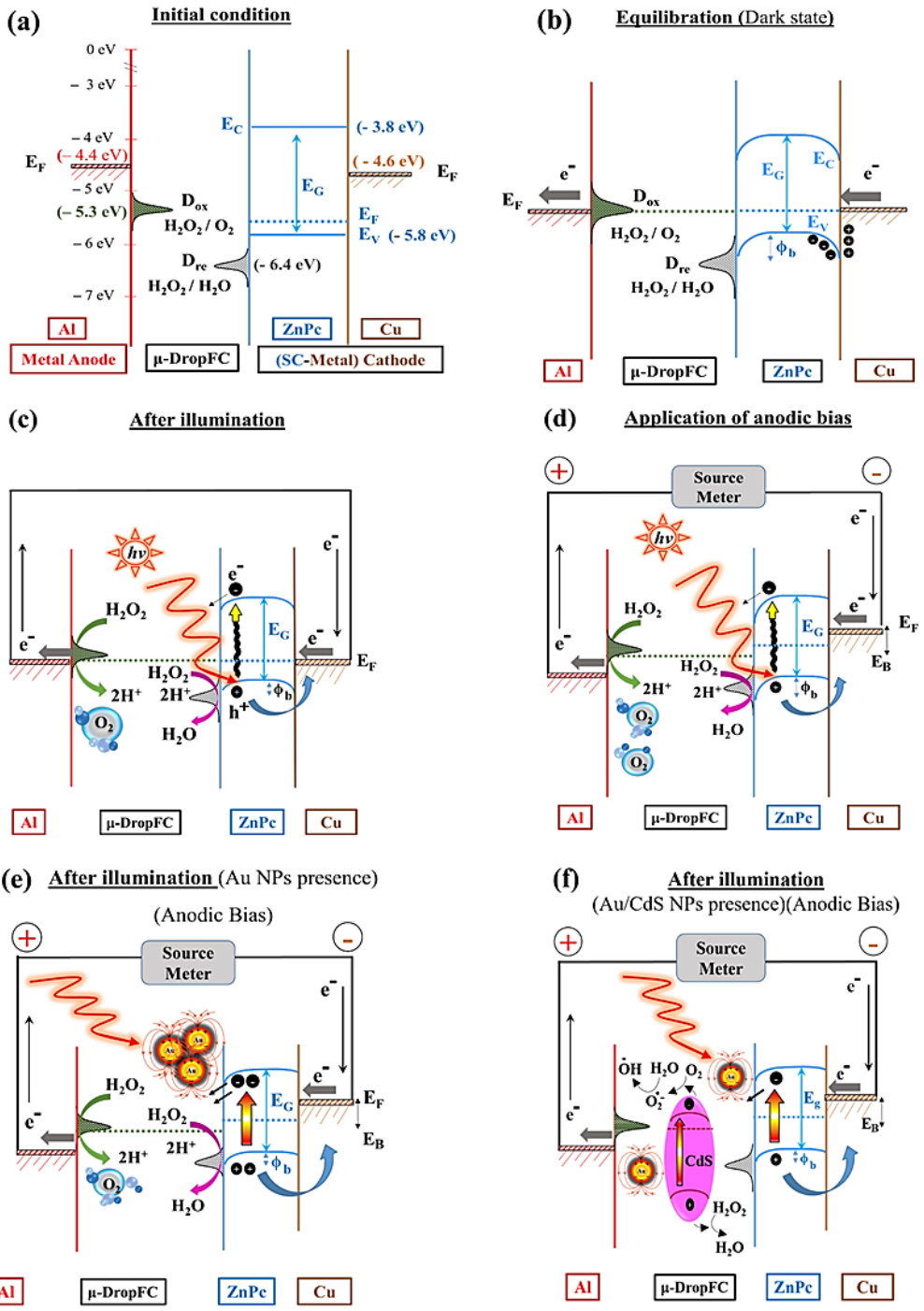

Figure 3.3 Schematics of the energy band diagrams displaying the various stages of the operation of μ-DropFC. Image (a) shows the initial condition, even before equilibration, when contact has just been established between the components. Image (b) shows the equilibrium under the dark condition when the Fermi levels of different materials equilibrated before photonic illumination. Image (c) shows the effects after illumination of the Xe lamp. Image (d) shows the situation when an anodic bias has been applied to the setup shown in the image (c). Image (e) shows the influence of the LSPR of the Au NPs under illumination. Image (f) shows

the influence of the Au/CdS NPs. The images also depict overviews of redox reactions occurring at the anode and cathode.

The electrolytic loaded with H_2O_2 underwent oxidation at the Al-foil-anode to release O_2 gas in the atmosphere and produce H^+ ions in the solution following the half-reaction, $H_2O_2 \rightarrow O_2 + 2H^+ + 2e^-$.[36] The peroxide decomposition in the bulk under acidic and basic conditions have been elucidated in detail in the following section. The oxidation of anode led to a progressive deposition of oxide at the Al-foil-anode when Al combined with hydroxyl ions of the droplet. This was confirmed by the Raman and KPFM characterization of the electrodes before and after the analysis, as shown in the **Figures 3.4 (b)**, **3.4 (c)**, and **3.5**.[63] The reduction of H_2O_2 occurred at the ZnPC-Cu cathode, which eventually formed water, following the half-reaction, $H_2O_2 + 2H^+ + 2e^- \rightarrow 2H_2O$.[36] The electrode degradation was characterized by Raman spectra, as summarized in the **Figure 3.4**. The plot (a) shows the variation of ψ_{oc} with *t* of the Fuel 2I when integrated with the same set of electrodes for 3 cycles each spanning 50 min. The plot suggests that after each cycle the degradation was not that significant and even after 150 min of operation, the change in the ψ_{oc} was not that significant. In these experiments, as soon as peroxide touched the Al surface, the peroxide decomposition led to the etching of Al surface to form $Al(OH)_3$. This anodic oxidation was one of the major reasons behind the reduction of ψ_{oc} in each cycle, which prevented charge transfer to some extent.

The plot (b) shows the Raman spectra of the anode before and after the reaction. After a reaction time of 50 min, new peaks were observed on the Al surface owing to the formation of the hydroxide layer.[64] The plot also shows that the variation in the spectra was not that significant and the electrode could be used further for performing experiments. Importantly, the cathode surface did not change much due to the chemical stability of the ZnPC on Cu, as shown in the plot (c). We also determined the change in surface potential using the Kelvin Probe Force Microscopy (KPFM) of the electrodes before and after the exposure of H_2O_2. In the topography AFM image, plot (a) of **Figure 3.5,** a clear surface belonging to the unused Al foil electrode could be observed along with its surface potential, as shown in plot (b).

However, after the exposure to peroxide solution in the presence of an anodic bias, the change in the topography as well as the surface potential could be visible in the images (c) and (d). The images suggest the surface topography and potential changed significantly due to the chemical reaction between peroxide and electrode. In order to further understand this observation, we have employed the KPFM model to investigate the change in work function

of the electrodes in the presence of corrosive material. A modulation voltage of 0.5 V was maintained in between the cantilever and the sample surface to attain a resonance frequency of cantilever in order to map the surface potential over the Al foil electrode. A Pt/Ir coated Si tip whose work function had been optimized to be 4.58 eV by using the known work function of a HOPG surface had been used for the analysis. We could quantitatively measure the surface potential by applying the following equation:

$$CPD = \left(\phi_{tip} - \phi_{sample}\right)/e. \qquad (3.1)$$

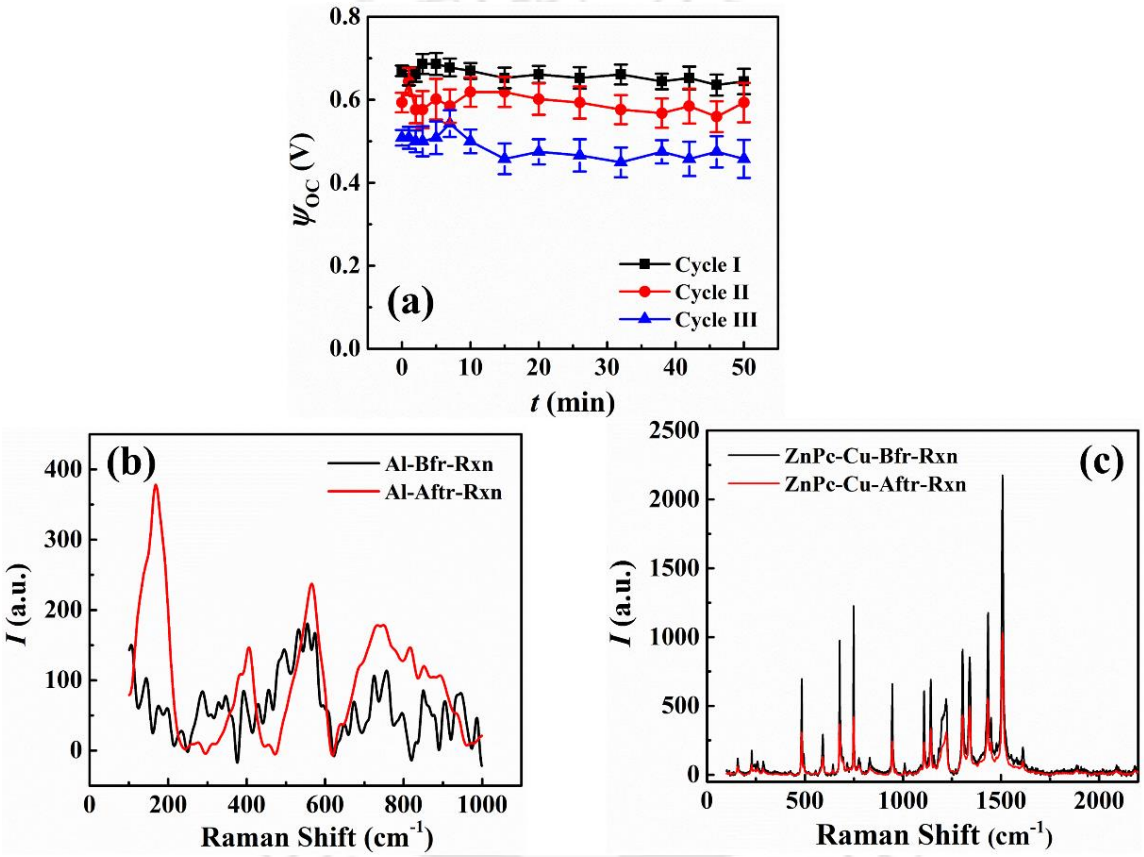

Figure 3.4 Image (a) shows variation of ψ_{oc} with t of the Fuel 2I when the electrodes were utilized for three times. Image (b) shows the Raman spectra of the Al anode before (Al-Bfr-Rxn) and after the reaction (Al-Aftr-Rxn). Image (c) shows the same for ZnPC-Cu cathode before (ZnPC-Cu-Bfr-Rxn) and after (ZnPC-Cu-Aftr-Rxn) reaction.

The KPFM aids in the determination of the contact potential difference (CPD) between the work function of the tip (ϕ_{tip}) and the work function of the material (ϕ_{sample}) when, e, is the elementary electronic charge. From the calculations using the software nanoscope analysis, the CPD of the unused Al foil electrode was calculated to be ~0.0033 eV, as represented by plot (b). Therefore, using the above equation, the work function of the electrode before applying the peroxide solution was found to be 4.577 eV. After the Al foil electrode was exposed to the

peroxide solution in presence of an anodic bias, the CPD of the substrate changed by ~ 0.545 eV, as represented by plot (d). Thus, after applying the equation mentioned above, the work function of the electrode after the exposure of peroxide was found to be 5.125 eV.

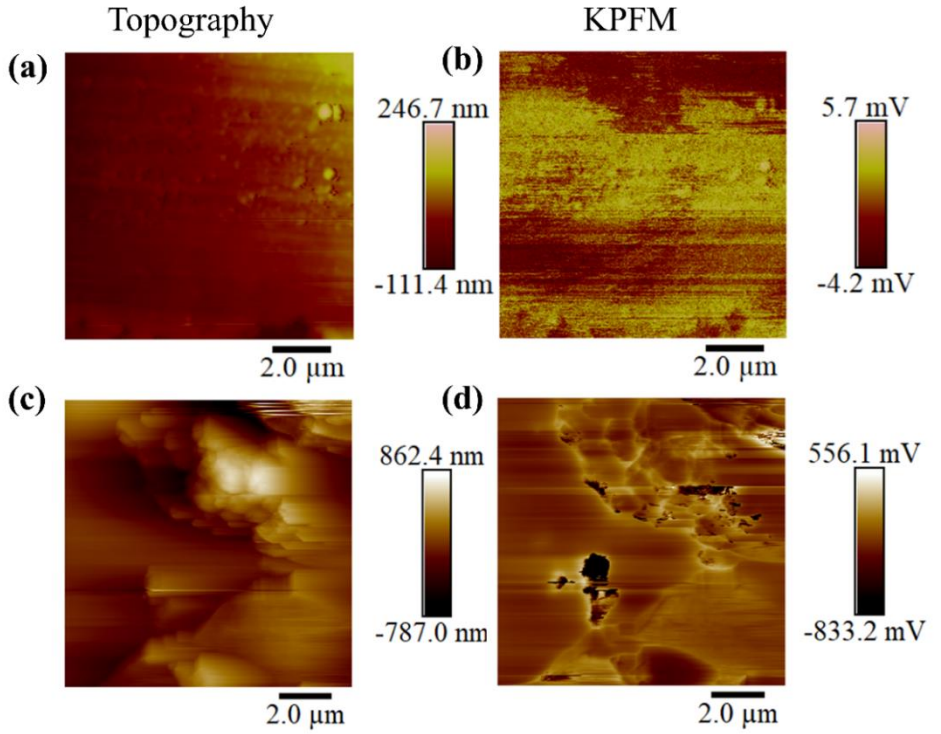

Figure 3.5 Image (a) shows the topographic profile of the unused Al foil electrode. Image (b) shows the corresponding surface potential plot of the Al foil electrode. Image (c) shows the surface profile of the Al foil electrode after exposure to peroxide solution in the presence of an anodic bias. Image (d) shows the corresponding surface potential profile of the reacted Al foil electrode.

Interestingly, the KPFM helped in identifying the work function of Al anode before the reaction to be ~ 4.577 eV, as depicted in the **Figure 3.3 (a)**. The schematic diagram in **Figure 3.3 (b)** shows that these redox reactions initiate a charge transport across the electrodes, which was the initiation of the conversion of chemical to electrical energy. Since the circuit was complete, the different components of the µ-DropFC strived to equilibrate their Fermi level. However, upon contact with the low work function Cu, an electron flow occurred from the metal to ZnPC via the formation of mixed states,[52,53] which led to the balancing of the potentials at these two surfaces, as shown in **Figure 3.3 (b)**. Further, during equilibration of the Fermi level, the conduction and valance bands of the p-type semiconductor ZnPC underwent a band bending near the SC-electrolyte and metal-SC interfaces, as shown in **Figure 3.3 (b)**.[60,61]

The band diagram under dark condition also helped the charge transfer at the mixed-molecule ZnPC-Cu interface. Previous studies have shown that interfacial dipoles could be created at the metal-SC junctions, which influenced the Schottky barrier height.[52,53] Especially when the SC

layer has been physisorbed on a metal surface, charge redistribution might take place across the junction to affect the interface dipoles. In such a scenario, in order to maintain the Pauli exclusion principle valid, the charges present around the interface have been pushed back into the metal, leading to a slight reduction in its work-function. Importantly, the interactions between the ZnPC and Cu in the proposed μ-DropFC could be explained along the similar lines. The physisorbed ZnPC on Cu created interfacial states at the junction and the ZnPC molecules were "pulled" towards the Cu core owing to the lower work function of the metal.[53] This made the interaction between SC and metal surfaces result in a stronger bond and subsequently, the charge transfer from Cu to the HOMO of ZnPC facilitated the reduction of peroxide into water near the SC-electrolyte interface.[53]

Figure 3.3 (c) shows the effect of the illumination of Xe lamp on the μ-DropFC wherein the photonic excitation pumps in more electrons into the system due to the electron transfer from valance to conduction bands of ZnPC molecules.[61] Subsequently, the influence of anodic bias to the pattern of band bending of the p-type ZnPC has been shown in the **Figure 3.3 (d)** under the illumination of Xe lamp. The image also suggests a redistribution of the Fermi levels with the application of the anodic bias. It can be seen that at the anode, the Fermi level went down due to introduction of positive charges, which facilitated the reaction further as more electron transfer could take place from the oxidation reaction of H_2O_2. Subsequently, on the cathode side, the Fermi level increased due to injection of negative charges, which further increased the rate of reduction reaction. In a way, at the electrode interfaces, charges were either introduced (cathode) or removed (anode), which influenced the rate of reaction. This led to higher electron transfer from the metal to the p-type SC. Furthermore, since the inherent charge density over the p-type SC increased under light, this facilitated higher rate of charge transfer to the adjacent electrolyte due to the Fermi energy difference. The effect of the addition of the Au NPs to the μ-DropFC and the subsequent effect of LSPR have been schematically shown in the **Figure 3.3 (e)**. The photonic excitation on the Au NPs promoted LSPR on the same which in turn improved the photoactivity of the μ-DropFC. The presence of Au NPs also increased the electrical conductivity of the microdroplet, which improved the rate of electron transfer through the circuit.

Concisely, the **Figure 3.3** helps in understanding that the usage of the each and every component contributed to the increased performance of the μ-DropFC. Importantly, the μ-DropFC setup was found to be rather robust because the output characteristics did not alter much when the experiments were repeated on the same system. This was shown by reporting the small reduction in the ψ_{oc} measured for the duration of a single operation cycle when the

same set of electrodes were operated 3 times, as shown in **Figure 3.4 (a)**. However, the change in the ψ_{oc} values changed significantly after three cycles, owing to the electrode degradation. KPFM analysis revealed a significant change in the surface potentials upon exposure of the Al-foil-anode to peroxide in the presence of an anodic bias, as shown in **Figure 3.5**.

Figure 3.3 (f) depicts the variations in the band configurations upon the addition of n-type CdS NPs in the solution in the form of Au/CdS NPs. This facilitated the formation of a p-n junction when some of the n-type CdS NPs got adsorbed at the p-type ZnPC. Although the configuration ensured a flow of electron from CdS to ZnPC under forward bias and inside dark condition, under light, the electronic transitions of both the ZnPC and CdS molecules changed the scenario. The transition in the n-type CdS facilitated its oxidation into in CdSO4 in presence of peroxide fuel[65] while the electron in the conduction band of ZnPC after transition due to photonic excitation was transferred to CdS for further oxidation of the same. In this manner, the configuration ensured that the addition of CdS did not disturb the mainstream flow of electrons in the μ-DropFC. It may be noted here that the major purpose of addition of CdS NPs were to degrade the dyes under light. However, in order to ensure such activity, we did not compromise much with the power density of the μ-DropFC owing to the photoactivity of the CdS NPs, as shown in the **Figure 3.3 (f)**. It may also be noted here that the Au/CdS NPs were mostly suspended in the bulk rather than adsorbed on the electrodes, which influenced the kinetics of the electron flow rather than the thermodynamics. Further, these nanoparticles increased the rate of decomposition of the peroxide fuel due to catalytic activity. The charge transfer in the electrolyte was also facilitated by the presence of the Na^+ and Cl^- ions in the electrolyte.[44]

3.3.2 μ-DropFC Characterization

Experiments performed revealed a clear distinction between the performances of the μ-DropFCs under dark and illuminated conditions. Clearly, the setup generated a higher output under light following the mechanism mentioned previously. The electrical characterization of the μ-DropFCs have been performed with the help of a set of nanovolmeter and sourcemeter. For this purpose, a linear sweep voltammetry (LSV) was employed with a voltage scan from 0 V to the open circuit voltage (ψ_{oc}) of the system. The testing parameters were kept the same for all experiments reported unless mentioned otherwise. In what follows, we discuss the results associated with the μ-DropFCs under the light. It may be noted here that all the P-ψ plots show a progressive increase in P with ψ until they reach a maximum value of P_{max} before they

decrease with further increase in ψ to a zero value at ψ_{oc}. It may also be noted here that, initially, we optimized the loading of salt and acid in the native μ-DropFCs before we performed the experiments with the NPs.

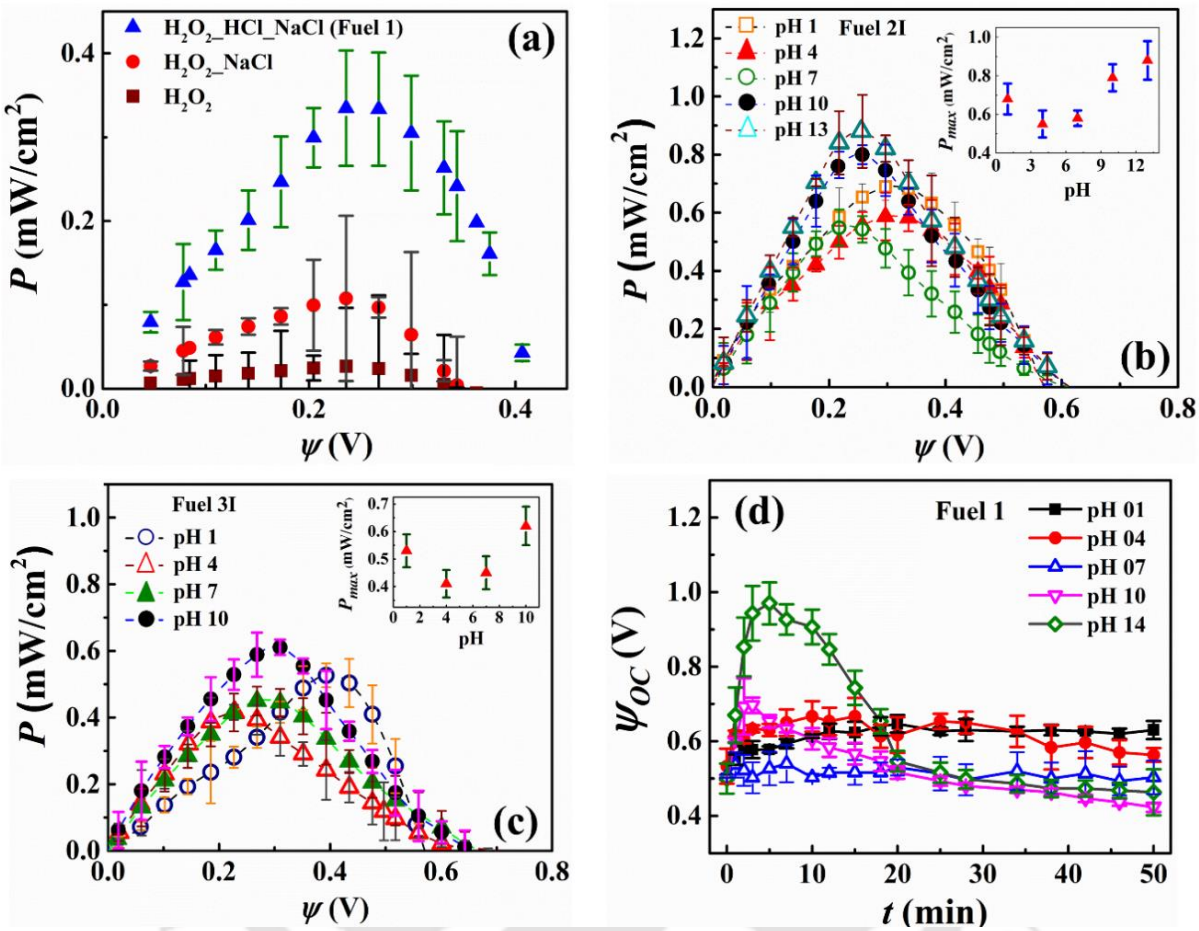

Figure 3.6 Image (a) shows the P-ψ characteristics of a few native μ-DropFC setups, which comprise of three different solutions, (i) 10 μL of 0.3M aqueous H_2O_2 and 10 μL of 0.1M HCl, (ii) a 20 μL droplet obtained by mixing 10 μL aqueous 0.3M H_2O_2 with 10 μL of aqueous 0.1M HCl, and (iii) 30 μL of fuel 1 – mixing 10 μL aqueous H_2O_2 (0.3 M) with 10 μL aqueous HCl (0.1 M) and 10 μL aqueous NaCl (1M). Images (b) and (c) show the effect of pH on the P-ψ plots of the 10 μL droplet of Fuels 2I and 3I. Image (d) shows the variation of ψ_{oc} of Fuel 1 at different pH.

A few major parameters associated with the μ-DropFC setups were the pH of the droplet, electrical conductivity of the droplet, maximum power generated (P_{max}) and open circuit voltage (ψ_{oc}). **Figure 3.6** shows the results obtained during the tuning of all these parameters to extract an optimal performance from the native μ-DropFC, before the addition of the nanoparticles. It may be noted here that all these experiments were carried out under illuminated conditions. The plot (a) shows the *P*-ψ characteristics of three different solutions, (i) 10 μL of 0.3M aqueous H_2O_2, (ii) a 20 μL droplet obtained by mixing 10 μL aqueous 0.3M

H_2O_2 with 10 µL of aqueous 0.1M HCl, and (iii) 30 µL of Fuel 1 – mixing 10 µL aqueous H_2O_2 (0.3 M) with 10 µL aqueous HCl (0.1 M) and 10 µL aqueous NaCl (1M). All the *P*-ψ plots in the images (a) – (c) show a progressive increase in *P* with ψ until they reach a maximum value of P_{max} before they decreased with the increase in ψ to arrive at ψ_{oc}.

The plots suggest that since the pristine 0.3M aqueous H_2O_2 was itself a highly reactive medium, it decomposed rapidly due to the interaction with the electrode materials and photonic excitations. However, as suggested by the blue *P*-ψ plot in the plot (a), this system was unable to generate significant power. It may be noted here that the H_2O_2 procured always contained some amount of HCl during its supply to maintain its stability during transport under dark condition. Importantly, when we increased the stability of the H_2O_2 procured by mixing the same with 0.1M aqueous HCl solution, the presence of the H^+ ions in the solution negatively catalyzed the system to provide further stability. In such a scenario, the µ-DropFC decomposed with a significant rate for a longer duration when integrated with the electrodes and exposed to light, which helped in improving P_{max} and ψ_{oc}, as shown in the plot (a). The cell characteristics could be improved further when the aqueous NaCl solution was added to the system. Subsequently, a 30 µL droplet of µ-DropFC at pH 1 and in presence NaCl produced a P_{max} ~ 0.35 mW/cm^2 and 0.38 V. This we have chosen as the native system for all other experiments and named as Fuel 1.

Importantly, the µ-DropFC performance varied significantly with the pH of the droplet. The plots (b) and (c) in the **Figure 3.6** depict the *P*-ψ measurements of Fuels 2I and 3I, respectively, when pH was varied from 1 to 13. The inset in the plots show the variations in P_{max} with pH. It may be noted here that the alkalinity (acidity) of the solutions was varied by adding aqueous NaOH (HCl) solution before measuring the pH with pH meter. The plots show that P_{max} could be improved significantly with the increase in the alkalinity of the solutions for the Fuels 2 and 3. It is well known that the OH^- positively catalyzes peroxide decomposition, which could be further aided by Au and CdS NPs. The highly alkaline solutions not only degraded the fuel quickly but also neutralized the Au/CdS NP. However, the major issues associated with the alkaline system were smaller shelf-life and marginal ψ_{oc}, which has been summarized in the plot (d) of **Figure 3.6** for the Fuel 1. The reactive decomposition of H_2O_2 under alkaline condition can be shown in the following way:[29]

$$H_2O_2 + OH^- \rightarrow HO_2^- + H_2O, \quad (3.2)$$

$$HO_2^- + H_2O + 2e^- \rightarrow 3OH^-, \quad (3.3)$$

$$HO_2^- + OH^- \rightarrow O_2 + H_2O + 2e^-, \quad (3.4)$$

$$O_2 + 2H_2O + 4e^- \rightarrow 4OH^-. \quad (3.5)$$

The plot (d) shows that ψ_{oc} varied with time (t) considerably for solutions with different pH. At higher pH values, peroxide existed as hydroperoxyl ions in the solution, as shown below in Eq. (3.2). These ions then combined with water to give hydroxyl ions, as shown in Eq. (3.3). In these highly alkaline conditions, sudden increase in the ψ_{oc} was observed because the change in the concentration of OH^- ions facilitated faster breakdown of H_2O_2, as shown in the Eq. (3.4). Moreover, since oxygen was present, its reduction could also take place at such potential values following the Eq. (3.5). Thus, such alkaline conditions were found not so sustainable for long-term power generation because the rapid degradation of peroxide due to combination with the reactive oxygen species (ROS).

On the other hand, at low pH values, the hydrogen peroxide was more stable as the reactive species were generally kept under control, which led to a much more consistent ψ_{oc}. The decomposition of peroxide fuel in acidic media can be shown by the following equations:[1]

$$H_2O_2 + 2H^+ + 2e^- \rightarrow 2H_2O, \quad (3.6)$$

$$H_2O_2 \rightarrow O_2 + 2H^+ + 2e^-, \quad (3.7)$$

$$O_2 + 4H^+ + 4e^- \rightarrow 2H_2O. \quad (3.8)$$

Over longer periods of time, these conditions were found to be favourable for a controlled decomposition of peroxide fuel, which led to a higher ψ_{oc} value compared to the alkaline conditions, as shown by the black line in the plot (d) of **Figure 3.6**. This mechanisms for this phenomenon is also a well-established one in the existing literature.[30,34] Under such conditions, the H_2O_2 molecules reduced at the electrodes into water in the presence of charges, as shown in Eq. (3.6). Subsequently, at these potential values, H_2O_2 oxidation could also take place at the anode, as shown in the Eq. (3.7). Since, oxygen was also present in the system, it also reduced at the electrodes, as shown in Eq. (3.8), which was the main cause of the increased overpotential and decrease in the overall ψ_{oc} values. Concisely, the plots (a) – (d) in the **Figure 3.6** suggests that pH 1 was optimal for significant power generation at an adequate open circuit voltage for the proposed μ-DropFC, which justified the usage of Fuel 1 as the native system for all the experiments performed. Subsequently, all the other Fuels 2 – 6 were synthesized by mixing Au or CdS NPs or dyes with the Fuel 1, as summarized in the **Table 3.1**.

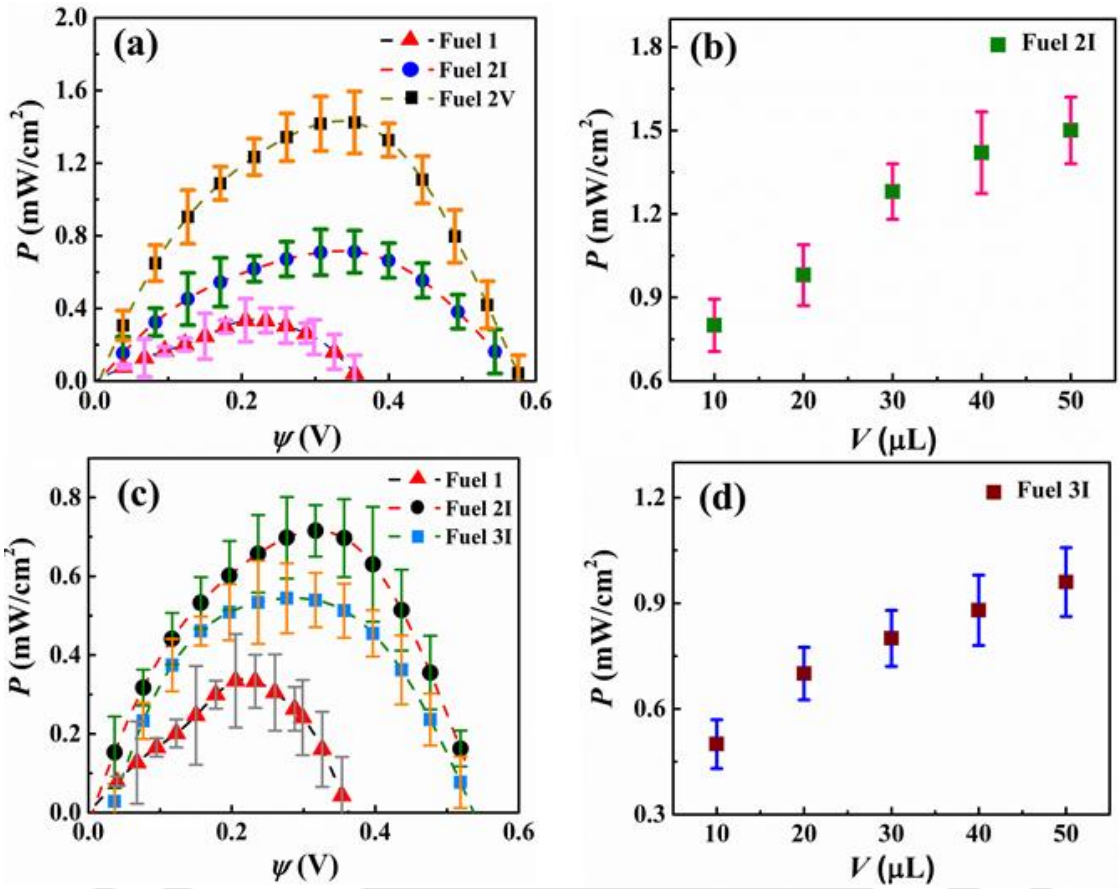

Figure 3.7 Power-potential (*P-ψ)* curves for the different µ-DropFCs containing varying volumes of additives - Au NPs and Au/CdS NPs, respectively. Image (a) shows the performance curves indicating the variation in power density (*P*) with ψ of three different fuels 1, 2I and 2V. Image (b) shows the effect of changing the volume (*V*) of the Au NPs suspension on the overall power generation (*P*). Image (c) shows the power-potential (*P-ψ*) curves for the fuels 1, 2I and 3I. Image (d) shows the effect of changing the volume (V) of the Au/CdS NPs suspension on the overall power generation, *P*. All the results were obtained under the application of a voltage sweep from 0 V to ψ_{oc}, and then by measuring the resulting output currents. Details of fuels 1 – 6 are provided in **Table 3.1**.

Figure 3.6 shows the characteristics of a few native µ-DropFCs when the salt and acid/alkali loading were varied. The **Figure 3.6** also shows that although the alkalinity of the solution improved the power density of the energy harvester, it reduced the life time and ψ_{oc}. In contrast, at an acidic pH 1, a steady and continuous degradation of peroxide for a longer duration led to a better performing and long-lasting µ-DropFC. These experiments uncovered that the Fuel 1 in the **Table 3.1**, a mixture of 10 µL 0.3M aqueous H_2O_2 with 10 µL of 0.1M aqueous HCl and 10 µL of 1M of aqueous NaCl, was the near optimal native system, which led to P_{max} ~0.35 mW/cm^2 at ψ_{oc} = 0.38 V, as shown in the **Figure 3.7 (a)**.

Interestingly, **Figure 3.7 (a)** also shows nearly a four-fold increase in P_{max} when the native system was loaded with a suspension of Au NPs, named as Fuel 2V. The combined influence

of the LSPR of the Au NPs under light and enhanced electrical conductivity of the system led to the improvement of the power harvesting parameters, P_{max} ~ 1.5 mW/cm^2. The plot (b) shows the effect of variation of the volume of Au NPs, Fuel 2I – 2V, on the *P*-ψ values of the μ-DropFCs. The plot suggests that although increasing the volume of the Au NPs led to higher *P* values, however, the increment saturated due to diffusional resistance at higher values. The Au NPs improved the output parameters because, (i) the LSPR under light improved charge transfer between the electrodes, (ii) under acidic conditions Au NPs catalyzed the degrading of peroxide fuel, (iii) they also acted as electron relays for a better charge transfer, and (iv) they reduced the electrical resistance of the composite fuel droplet marginally.[47,57] The incorporation of the Au NPs or Au/CdS NPs primarily affected the kinetics of the process as they were suspended in the bulk rather than adsorbed at the electrodes. With increasing solution volume, more quantity of NPs participated in the charge transfer processes and thereby facilitated faster redox reaction at the electrodes which resulted in higher output. Furthermore, with increasing the volume of NPs solution, the area occupied by the composite fuel droplet also increased marginally since the anode surface was partially hydrophilic. This led to the increase in number of reaction sites available for the redox reaction to occur. Although it may be noted here that by gradually increasing the droplet volume in the system, output cell characteristics were enhanced under external radiation due to the various reasons mentioned above. Since the droplet volume increased, the resistance to diffusion near the electrodes also decreased however, a saturation limit was observed beyond a certain volume of NPs.

The performance of the Fuel 3I – 3V have been summarized in the plots (c) and (d). The plot (c) suggests that, in comparison to the Fuel 1, they performed better showing a P_{max} ~ 0.59 mW/cm^2, however, the performance was not as good as with Fuel 2. Again, the plot (d) shows the increase in the performance characteristics before saturation with the loading of Au/CdS NPs. It may be noted here that the addition of Au/CdS NPs was intended towards their capability of photocatalytic degradation of dyes, which is to be discussed later. However, from the purely energy harvesting point of view, Fuel 2 with optimal loading of AuNPs was found to be superlative, as summarized by the **Figure 3.7**. **Figure 3.8 (a)** shows the *J* (current density) - *t* (time) plot, for the Fuels 2I and 3I. The plots suggest that the solution containing only Au NPs displayed an initial higher current density of ~ 5 mA/cm^2 when compared with the solution containing Au/CdS NPs (~ 3.5 mA/cm^2), on the application of a bias of 0.1 V. Thereafter, the decay during initial ~ 200 s could be because of the mismatch between the high rate of redox reactions occurring at the interface and limited charge transfer at the cathode. In such a scenario, the μ-DropFCs with Au NPs showed enhancement was because of the higher

ionic conductivity, better charge-transfer rates due to the presence of charge mediators, and occurrence of faster chemical kinetics at the electrode interface due to the enhanced Plasmonics.[44,46,57] However, the plot also shows that the μ-DropFCs with Fuel 3I registered a sustained charge density of about 1.7 mA/cm^2, which was higher than that of Fuel 2I even after long period of time. The ratios of *J* values after 0 s and 1500 s were ~ 0.3 (Fuel 2I) and ~ 0.5 (Fuel 3I), which indicated slower degradation of the Au/CdS NPs system.

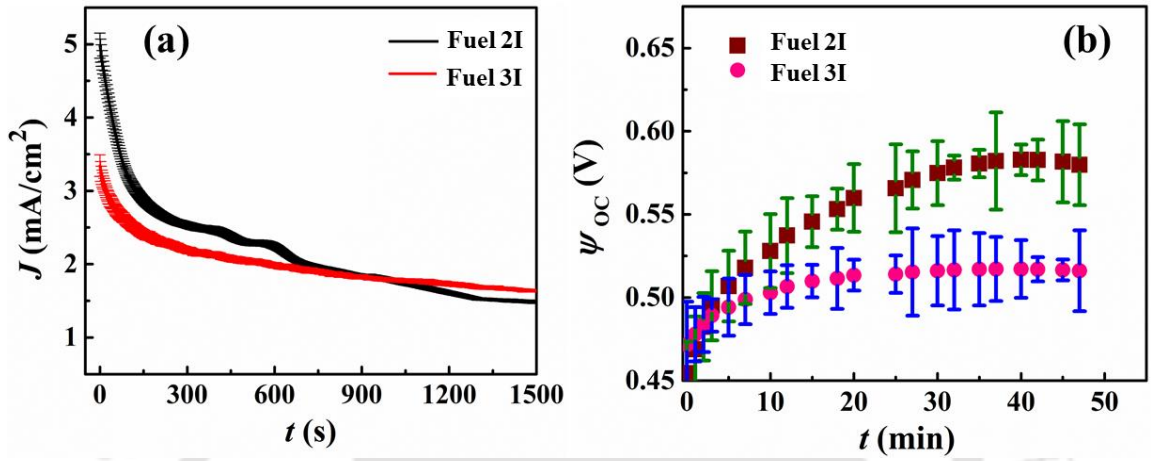

Figure 3.8 Image (a) shows the chronoamperometric current density (*J*) versus time (*t*) studies for different μ-DropFCs with the Fuels 2I and 3I at an applied voltage of 0.1 V. Image (b) shows the corresponding open-circuit potential (ψ_{oc}) with *t* for 50 min. In order to demonstrate long-term performance of μ-DropFCs, chronoamperometry test was performed for the different systems.

The plot (b) in the **Figure 3.4** highlights the difference in ψ_{oc} for the Fuels 2I (0.58 V) and 3I (0.52 V). The plots suggest the generation of a high ψ_{oc} upon the addition of the photo-sensitive NPs under a longer duration of light illumination for ~ 50 min. Here the ψ_{oc} values signify the overall driving force of the system, which is a measure of the thermodynamic potential difference between the electrodes. It may be noted here that for the system containing additional additives in electrolyte, ψ_{oc} is the difference between the chemical potential ($\boldsymbol{\mu}$) of the electrolyte and the potential of the conduction band of the photo-sensitive electrode (e,g ZnPC in the present setup), $\boldsymbol{\psi_{OC} = E_C - \mu}$.[44,66] The external irradiation might cause intense localized electric field to develop on Au NPs, which effectively could reduce μ to, $\boldsymbol{\mu' = \mu - qV}$, where *q* represents the charge of the particle and V, the potential developed due to the field around the excited particle.[44,66]

Subsequently, an enhancement in ψ_{oc} could be expected in a μ-DropFC loaded with Au NPs under a prolonged light exposure, as shown in the plot (b). In comparison, for the case of

Au/CdS NPs, a lower ψ_{oc} value was observed, which could be attributed to the generation of lower value of potential difference between the electrodes. In the presence of light, the photo-excitation generated the electron-hole pair in CdS NPs in which the conduction band was at a lower potential value. This caused electron transfer from CdS NPs to oxidize the peroxide fuel. In the process, a fraction of the photonic energies was taken up by CdS NPs for peroxide degradation in the bulk rather than at the electrode, which contributed to a reduced ψ_{oc}.

3.3.3 Energy Harvesting with Dye Degradation

As discussed previously, the μ-DropFC setup could also be utilized as a dye degradation system without much alteration of the components. For this purpose, Au/CdS NPs were involved to exploit their act as superior photo-catalysts under light. The energy harvesting performance involving *P*-ψ characteristics and *J*-*t* curves of such μ-DropFCs have been summarized in the **Figure 3.9**. Initially, we added a fixed amount of an aqueous solution of Rhodamine 6G (Rh6G) (0.5 mg/mL) in the μ-DropFC to prepare the Fuels 4 – 6, as described in the **Table 3.1** of the chapter. The plot (a) in the **Figure 3.9** show that in presence of additives such as Au NPs (Fuel 5) and Au/CdS NPs (Fuel 6), the μ-DropFC was able to generate decent P_{max} ~ 0.61 mW/cm^2 and 0.51 mW/cm^2, respectively. Even without these additives also the Fuel 4 produced a slightly lower P_{max} while simultaneously performing the dye degradation. The plot (b) shows the chronoamperometric current density (*J*) – time (*t*) studies for μ-DropFC at an applied potential of 0.1 V in presence of Rh6G solution (0.5 mg/mL). Again, as expected, the system containing only dye molecules displayed the least amount of current density.

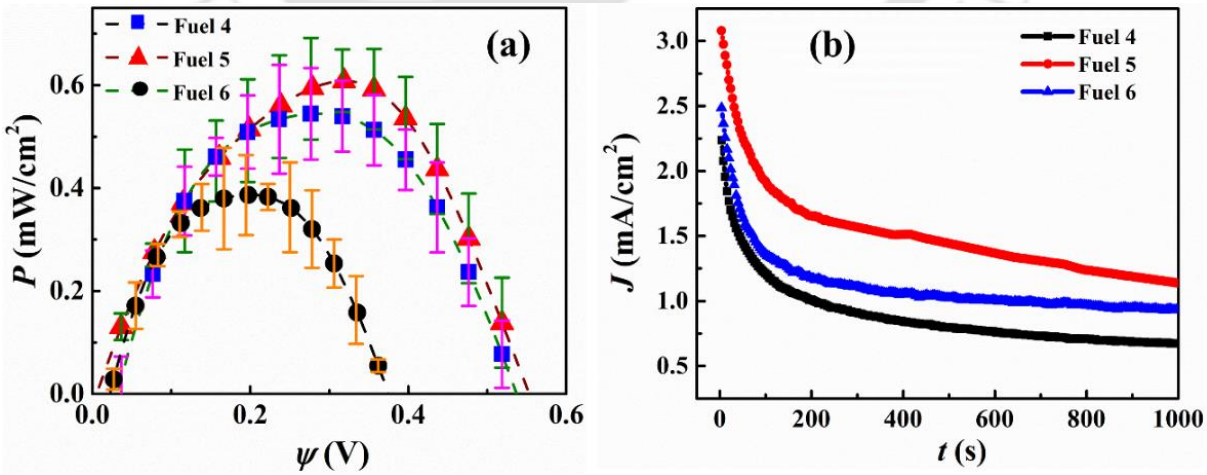

Figure 3.9 The plot (a) shows *P*-ψ characteristics of μ-DropFC with Fuels 4 – 6 containing the organic pollutant, Rhodamine (Rh6G). The plot (b) shows the chronoamperometric current density (*J*) versus time (*t*) studies for the same μ-DropFCs at an applied potential of 0.1 V. The plots correspond to the Fuels 4 – 6 in the Table 1 of the chapter.

However, on addition of Au and/or CdS NPs there was significant improvement in which use of Au NPs showed maximum energy harvesting. In a way, the Au/CdS NP system showed effective photocatalytic properties for the dye degradation.[55,67] Under the illuminated conditions, these photocatalysts degraded the organic dye molecules by breaking down their backbone. Subsequently, rather than facilitating the breakdown of the peroxide fuel at the electrodes, the additives engaged in dye degradation. Thus, when only Au NPs were present, the setup showed a higher *J* value wherein the rate of energy harvesting was larger and rate of dye degradation was rather less. However, for Au/CdS NPs, the dye degradation rate was faster while the rate of energy harvesting was found to be little less. Importantly, these effects stabilized the cell in relation to the *J* values because a stable current density could be achieved for a long period of time, as shown in plot (b).

Figure 3.10 (a) schematically shows the energy band diagrams displaying the various stages of the operation of μ-DropFC when loaded with the Fuels 4 – 6. In the presence of light, the Au NPs catalyzed the formation of OH radicals via the degradation of peroxide molecule,[68] which formed one of the many reactive oxygen species (ROS) engaged in the degradation of the dye, as shown by the Eqs. (3.9) and (3.10). The OH radicals were also produced due to the oxidation of the water in presence of holes generated by the n-type CdS NPs under photonic excitations, as shown by the Eq. (3.10).

Subsequently, the dissolved oxygen accepted the electrons from the LSPR prone Au NPs to form the superoxide radicals, which subsequently broke down the dye molecules, as shown by the Eqs. (3.11) and (3.12). The mechanism for the degradation of dye can be summarized as follows:[57]

$$\text{Au-CdS} + \hbar\nu \rightarrow \text{Au}(e^-)\text{-CdS}(h^+), \tag{3.9}$$

$$\text{Au}(e^-)\text{-CdS}(h^+) + H_2O \rightarrow \text{Au}(e^-)\text{-CdS} + \dot{O}H + H^+, \tag{3.10}$$

$$\text{Au}(e^-)\text{-CdS} + O_2 \rightarrow \text{Au-CdS} + O_2^{-}, \tag{3.11}$$

$$O_2^{-} + \dot{O}H + \text{Rh6G} \rightarrow CO_2 + H_2O + \text{Organic Products}. \tag{3.12}$$

The Au/CdS nanocomposites are known to have significantly better photocatalytic properties than bare CdS NPs. The increment in the degradation efficiency was because of the improved charge generation and transfer rates for CdS NPs in presence of Au NPs.[69] Importantly, the setup showed reduced ~ 85% of Rh6G in 50 min along with harvesting of redox energy.

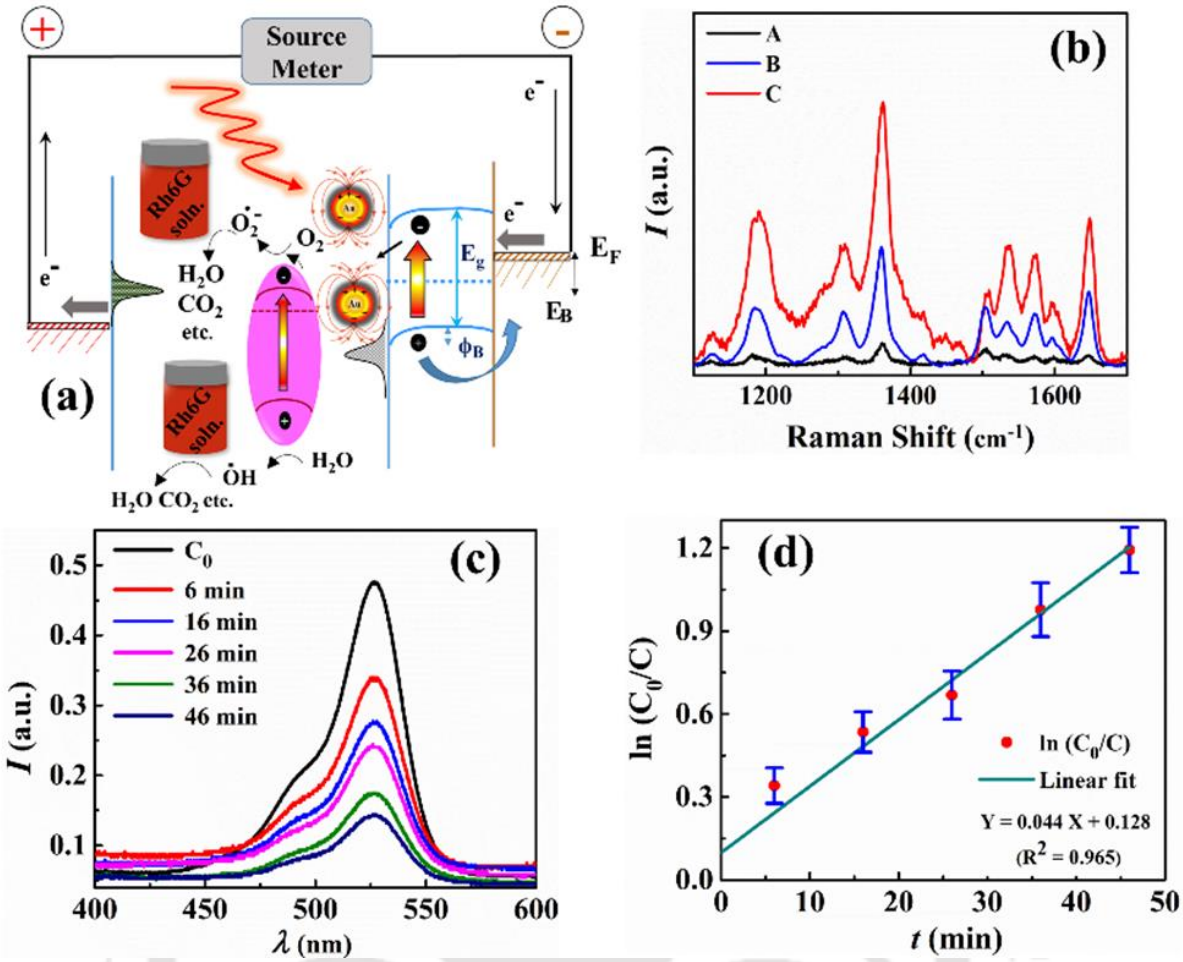

Figure 3.10 Image (a) schematically shows the energy band diagrams displaying the various stages of the operation of μ-DropFC when loaded with the Fuels 4 – 6. Image (b) shows the Plasmonic effect of Au NPs in the form of enhanced Raman spectra of Rh6G molecule. The spectrum A corresponds to a pure Rh6G solution in water (0.5 mg/mL), the spectrum B shows the same when 0.5 mg/mL of aqueous Rh6G solution was mixed with 0.3M aqueous H_2O_2 loaded with Au/CdS NPs and spectrum C shows the same when only Au/CdS NPs were added to the Rh6G solution in absence of peroxide. Image (c) shows the UV-Visible plots at different time intervals for Fuel 6, measured from 6 min (t_1) to 46 min (t_5). Image (d) shows the variation in the normalized concentration of Rh6G (ln C_0/C_t) with time where initial concentration is C_0 and concentration at time, t is C_t. The kinetics was found to be similar to a pseudo-first order reaction with a rate constant of, $k \sim 0.044$ min^{-1}.

In order to confirm the LSPR effect of Au NPs, we performed the Surface Enhanced Raman Spectroscopy (SERS) study, as summarized in the **Figure 3.10 (b)**. The plot shows that, upon irradiation with a 633 nm laser in the Rh6G solution loaded with either Au NPs or Au/CdS NPs, enhanced Raman peaks were observed. We also analyzed the rate of dye degradation of the μ-DropFCs employing UV-Visible spectroscopy. **Figure 3.10 (c)** shows the variation in the peak intensity of Rh6G with time for Fuel 6. The plot also shows that the intensity of peak decreased with time to mark degradation of the complex dye molecule inside the μ-DropFC.

The image (d) shows the variation in the normalized concentration of Rh6G (ln C_0/C_t) with time where initial concentration is C_0 and concentration at time, t is C_t. The kinetics for this system was found to be a pseudo-first order with a rate constant of $k \sim 0.044$ min^{-1}.[54]

3.3.4 Performance, VLSI, and Efficiency

The μ-DropFC system showed enhanced output characteristics in presence of the additives like Au NPs and Au/CdS NPs. The additives played an important role in not only enhancing the power densities but also aided the transformation of the μ-DropFC setup to be realized as a dye degradation setup. In what follows, we have analyzed the role of diverse additives in promoting the output characteristics: (i) addition of salt NaCl led to an increase in the electrical conductivity, which was further increased when salts like $CdSO_4$ was formed during the operation due to oxidation of CdS NPs; (ii) in presence of high H^+ loading at a lower pH value the controlled breakup of peroxide fuel in presence of the Au NPs[57,68] aided high density power generation for a longer period; (iii) since the cell operated under a light source, the incident radiation caused LSPR to create Plasmonic hot-spots around the Au NPs; (iv) the Au NPs displayed electron relay effect under a large potential difference between the two electrodes to transfer charges at a higher rate. **Table 3.2** provides an overall outlook on the performance of the different fuels utilized for the μ-DropFC. The results presented so far uncovered that the addition of Au NPs in the Fuel 1 to generate Fuels 2I – 2V helped in enhancing the P_{max}, ψ_{oc}, and ψ_{max} (the voltage corresponding to P_{max}).

Table 3.2 Output parameters for μ-DropFC loaded with Fuels 1-6.

Fuels	ψ_{oc} (V)	ψ_{max} (V)	P_{max} (mW/cm^2)
Fuel 1	0.38	0.24	0.35
Fuel 2I	0.59	0.38	0.72
Fuel 3I	0.55	0.36	0.57
Fuel 4	0.36	0.22	0.39
Fuel 5	0.56	0.44	0.61
Fuel 6	0.54	0.41	0.51

Further, addition of Au/CdS NPs (Fuels 3I – 3V) did improve the overall characteristics of the system over the native fuel 1, however, the values were lower compared to the Fuels 2I – 2V.

Importantly, addition of Rh6G solution did reduce the output values significantly because it hardly contributed to the energy production attributes. In order to optimize the NPs additives in the fuel, we performed further experiments, which have been summarized in the following section. **Figure 3.11 (a)** shows the case studies wherein different volumes of Au/CdS NP solutions 10 µL to 80 µL was added to Fuel 1 and the variation in the P_{max} was noted down. The plot suggests that increasing the volume of the NP increased P_{max} but the increase was not always linear. As the volume increased, the reactants delivered to the electrodes increased, which increased the rate of reaction and hence P_{max}. However, this also increased the diffusional resistance faced by the different species and once this effect was prominent the P_{max} values saturated. Plot (b) shows that the increase in P_{max} was rather more significant when only the Au NPs volume proportion was increased in the peroxide fuel. However, in this plot too, we observed that the peak power density tends to saturate at higher solution volume. From these results, the adequate volume of NPs required for a single cell to obtain a high power density was optimized. Hence, we utilized ~ 70 µL of solution for every cell in the VLSI system to get the maximum power density in an optimal manner.

Figure 3.11 shows that addition of ~70 µL of Au NPs solution in the Fuel 1may be optimal for harvesting high density energy for a longer duration. Thus, we chose this fuel to show a pilot scale µ-VLSI potential of the proposed µ-DropFC setup in the following **Figure 3.12**. **Figure 3.12 (a)** shows the pilot scale µ-VLSI setup comprised of 10 µ-DropFCs connected in parallel with each other. The plots (b) and (c) show the corresponding P-ψ analysis for Fuels 2 and 3 with the exception that 70 µL Au NPs and Au/CdS NPs were added to prepare each µ-DropFC.

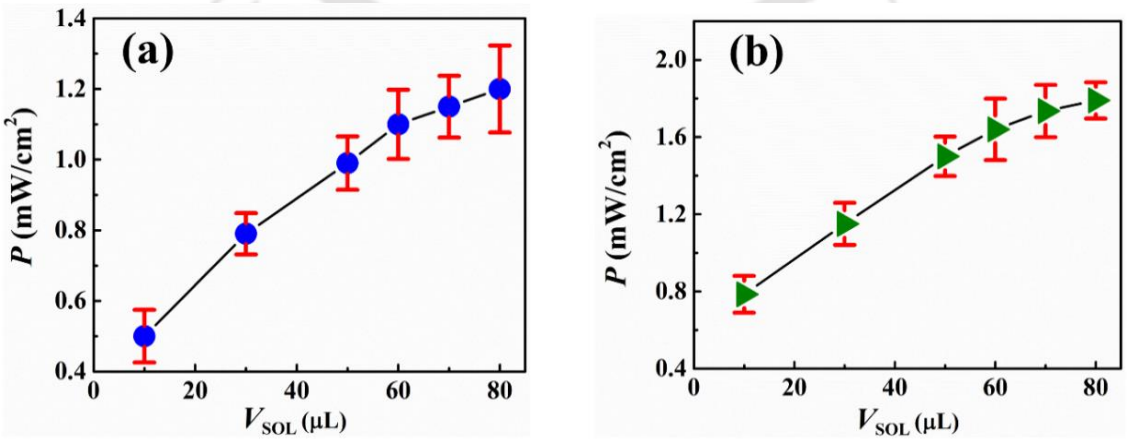

Figure 3.11 Plots show the variation of P_{max} with varying volume of fuels (V_F). Image (a) depicts the effects of the volume of Au/CdS NP solutions while image (b) reveals the effects of the volume of Au NP solutions.

Figure 3.12 (b) shows a 14-fold increase in P_{max} to ~ 7 mW/cm^2 when the number of µ-DropFC with Fuel 2 was increased from one to ten. It may also be noted that we achieved such power density for the maximum fuel mixture volume of 1 mL (100 µL per cell for 10 cells). **Figure 3.12 (c**) shows a 10-fold increase in P_{max} to ~ 5 mW/cm^2 when the number of µ-DropFC with Fuel 3 was increased from one to ten. Again, the usage of Au NPs led to a better performance than the Au/CdS NPs for the reasons discussed previously.

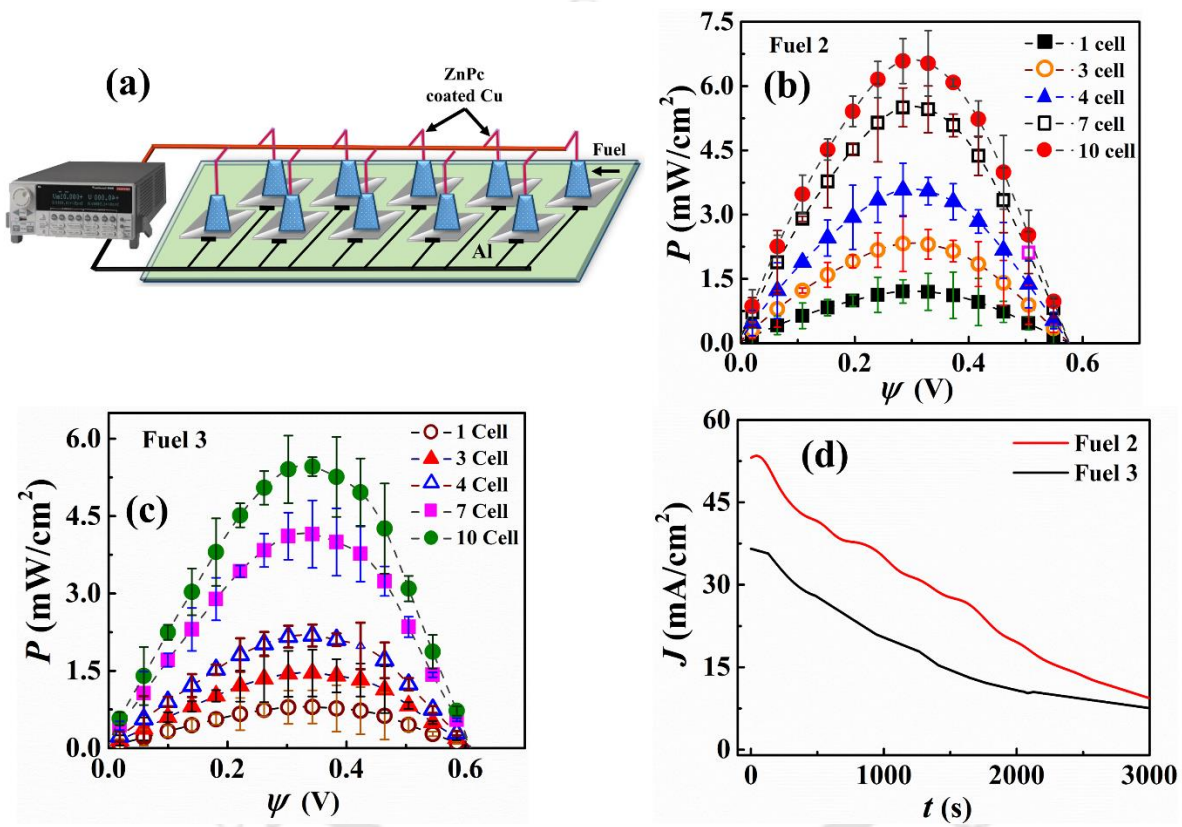

Figure 3.12 Image (a) shows the schematic diagram of the µ-VLSI setup comprised of 10 µ-DropFCs connected in parallel with each other. The plot (b) and (c) represent the *P*-ψ curves for the VLSI with increasing number of µ-DropFCs. In the plot (b) for each µ-DropFCs 70 µL of Au NPs was added to the 10 µL of native system while in the plot (c) 70 µL of Au/CdS NPs was added to the 10 µL of native system. Plot (d) represents the *I*-*t* data for the VLSI setup of 10 µ-DropFC consisting of the fuels mentioned for Plots (b) and (c).

It may be noted here that, initially for a single cell, it was observed that the power density value reached ~ 0.72 mW/cm^2 when it contained 10 µl of Au NPs along with other constituents making up the total cell volume to be nearly 40 µl. The power density thereafter, increased to ~1.8 mW/cm^2 when the Au NPs volume increased to 80 µl. For the VLSI circuit, an optimal value of 70 µl of Au NPs was chosen which increased the cell volume to 100 µl. Subsequently, different number of cells (3,4,7,10) were connected and the system was analyzed using fuel-

cell characterization techniques. Due to the parallel connection within the system, the current values added up and resulted in the overall enhancement of the output power values. This circuit design allowed us to harvest high power densities from the setup.

There was also a change in the ψ_{oc} values observed, however, the change was not significant when compared with that of the single cell. As the number of cells increased, there was a gradual increase in the maximum power density of the configuration and upon employing linear sweep voltammetry technique, it was observed that the P_{max} value was obtained near 0.36 V. Thereafter, the 10 cells that were connected in parallel to harvest a high power density value from the system eventually resulted in generating ~7 mW/cm^2. There was an overall loss in the output efficiency which could be assigned to various factors including, the ohmic resistances arising from different cell connections, non-uniform cathode coating (ZnPC) across different cells and peroxide decomposition.

Figure 3.12 (d) shows the chroamperometry plot for the VLSI system with 10 cells, which confirmed that the overall current density for the Fuel 2 was higher than Fuel 3. The tests were performed for 50 min to obtain a variation of *J* from 55 mA/cm2 to 10 mA/cm^2 (35 mA/cm^2 to 10 mA/cm^2) for Fuel 2 (Fuel 3) with a potential of 0.1 V. The enhanced current density values could be attributed to the inherent electronic and optical properties of the proposed prototype, which substantially improved under the presence of light.

Table 3.3 Comparison of membraneless H_2O_2 fuel cells with μ-DropFC.

An	Ct	ψ_{oc} (V)	H_2O_2 [M]	P_{max} (mW/cm^2)	V_F (mL)	Ref
Mg	PB	2.3	0.5	4.9	2	18
Ni	PB	0.6	0.5	1.5	50	36
Ni	$[Fe^{II}(H_2O)_2]_3[Co^{III}(CN)6]_2$	0.8	0.3	9.9	-*	37
Ni	Pedot:PSS	0.5	0.1	0.3	-*	41
Ni	FePC	0.5	0.3	0.01	-*	47
Al	PB	0.6	0.5	0.8	0.5	61
Al	**ZnPC-Cu**	**0.6**	**0.3**	**1.4-*1cell* 7.1-*10cells***	**0.07-*1cell* 0.1-*10cells***	**This work**

**** not explicitly mentioned. An - Anode, Ct - Cathode, V_F - volume of fuel utilized per cell, FePC - Iron Phthalocyanine, PB - Prussian Blue.***

The **Table 3.3** shows a comparison of the different performance parameters of the proposed μ-DropFC with the others available in literature. The values summarized in the table suggest that P_{max} of μ-DropFC are quite comparable if not better than the others referred with respect to the working volume of the fuel. In a way the proposed setup has its uniqueness in the development of a portable and affordable μ-DropFC for harvesting high density power from both chemical and light energies utilizing significantly low fuel volumes, which can also be simultaneously utilized for dye degradation. The calculations of efficiencies for the different μ-DropFCs have been discussed hereafter.

Effect of the external radiations was analyzed by performing the power-potential analysis for the μ-DropFC system employing Fuel 1, under dark condition. As can be observed by the **Figure 3.13**, very less *P* values from the system could be obtained as compared to the condition when the system was operating under external radiations. Thus, the incoming external radiations not only had influence on the overall current generation but also on the overall potential value. Furthermore, in order to evaluate the performance criteria for the μ-DropFC system, the overall efficiency of the the μ-DropFC was determine employing the following formula:

$$\varepsilon_O = \varepsilon_T \times \varepsilon_E \times \varepsilon_{PV} \,. \qquad (13)$$

where, ε_O is the overall efficiency of the system, ε_T is the thermodynamic efficiency of the system, ε_E is the electrochemical efficiency and ε_{PV} is the photovoltaic efficiency of the system.

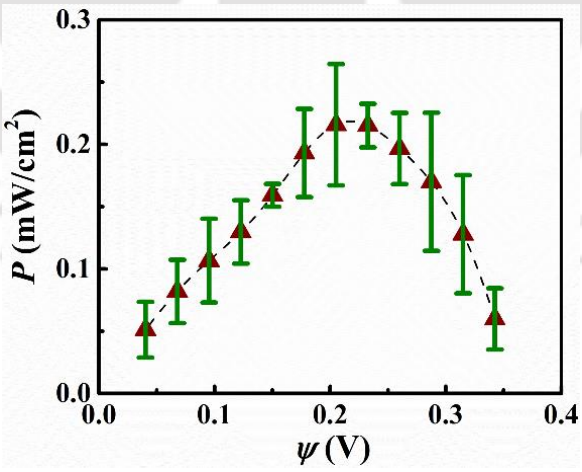

Figure 3.13 Plot showing the variation of *P* with ψ for the μ-DropFC under dark condition for when Fuel 1 was employed.

The thermodynamic efficiency of the system represents the overall allowed driving force for the redox reactions owing due to the inherent chemical energy of the fuel utilized. The electrochemical efficiency of the system represents the maximum driving force involved during

the fuel cell operation as it takes into consideration the different over potentials involved and the corresponding losses occurring due to them. The photovoltaic efficiency highlights the increment in the overall charge transfer processes due to the presence of external radiation. Briefly, these efficiencies can be represented by:

$$\varepsilon_T = \frac{\Delta G}{\Delta H}\ , \tag{3.14}$$

$$\varepsilon_E = \frac{\psi_{oc}}{\psi_{th}}\ , \tag{3.15}$$

$$\varepsilon_{PV} = \frac{\psi_{max} \times J_{max}}{P_{in}}\ . \tag{3.16}$$

Here, ΔG and ΔH represent the free energy and enthalpy values of the overall hydrogen peroxide disproportion reaction.[28,42] It has been assumed that the enthalpy of the reaction and free energy values for the system does not vary significantly upon addition of the different additives. The parameters ψ_{oc} and ψ_{th} represents the open-circuit potential and the actual redox potential of the system under standard conditions. The parameters J_{max} and ψ_{max} represents the maximum current density achieved by the system at the corresponding applied potential and P_{in} represents the input energy of the system due to external radiations.

Table 3.4 Comparison of efficiency of Fuels in the μ-DropFC.

System	ψ_{oc}	P_{max}	ε_{PV}	ε_T	ε_E	ε_O (%)
Fuel 1	0.38	0.35	0.005	0.63	0.35	0.11
Fuel 2I	0.59	0.72	0.01	0.63	0.55	0.36
Fuel 2V	0.62	1.5	0.021	0.63	0.57	0.75
Fuel 3I	0.55	0.57	0.008	0.63	0.51	0.26
Fuel 3V	0.57	0.95	0.014	0.63	0.53	0.47
Fuel 5	0.56	0.61	0.008	0.63	0.52	0.26
Fuel 2*	0.63	7.2	0.102	0.63	0.53	3.54
Fuel 3*	0.61	5.7	0.08	0.63	0.54	2.83

70 μL of fuel 2 or 3 was taken for the VLSI system.

For the proposed systems, the values for the different parameters corresponding to the different fuels have been laid out in the **Table 3.4**. For a particular fuel composition, in this case Fuel 2I, the parametric values which determine the overall μ-DropFC efficiency have been given as follows: ΔG = 120 kJ/mol, ΔH = 190 kJ/mol, ψ_{oc} = 0.58 V, ψ_{th} = 1.08 V, $\psi_{max} \times J_{max}$ = 0.8 W/cm^2 and P_{in} = ~70 mW/cm^2. The efficiencies of the system were determined utilizing equations (13) – (16). In all the calculations, area was the circular footprint of the droplet of diameter 5 ± 1 mm. **Table 3.4** shows the efficiency of different μ-DropFCs reported.

The data suggests that the efficiency of the Au NPs loaded μ-DropFCs performed the best among the proposed systems. The output power density increased by ~ 10-fold when 10 such units were integrated under the same amount of photonic illumination, which highlighted the scope for improving the overall efficiency of the setup through VLSI. The data reported in the **Table 3.4** show the capacity of the proposed μ-DropFC for harvesting high density power in a very efficient manner, which can be improved further with the help of process intensification and VLSI in future.

3.4 Conclusions

A peroxide microdroplet has been designed and developed into a high-performance fuel cell, namely μ-DropFC, which is also capable of harvesting solar energy. For this purpose, a peroxide microdroplet at optimal pH and salt loading has been utilized as the native system integrated to Al-anode and ZnPC-Cu cathode. The n-type ZnPC enable the formation of a photo-active Schottky junction at the electrolyte and metal interfaces, which is found to be suitable for power generation under light. Oxidation and reduction of H_2O_2 on the electrodes helped in conversion of chemical energy into the electrical one in a membraneless setup. Usage of suspended Au NPs enhance power density under photonic illumination through LSPR. Addition of n-type CdS NPs infuse the capacity of catalytic photo-degradation of dyes under light. The simple, low-cost, portable, and membraneless setup possess significant power densities of ~ 0.8 mW/cm^2 per cell and 7 mW/cm^2 at an efficiency of 3.5% when used a group of 10 cells have been integrated. The single-cell setup requires significantly less working fluid volume and can give a high-power density at a voltage of ~ 0.38 V. The single-cell setup also delivers a current density of ~ 1.5 mA/cm^2 under an applied voltage of 0.1 V for 30 min. Further, the single-cell setup is capable of degrading ~ 85% of rhodamine 6G dye in 1 h while simultaneously generating energy at a power density of ~ 0.6 mW/cm^2. A comparison with previous works shows the superiority of the proposed μ-DropFC for harvesting high density

power, which can be improved further with the help of process intensification and VLSI in future.

References

(1) Dhathathreyan, K. S.; Rajalakshmi, N.; Balaji, R. Nanomaterials for Fuel Cell Technology. *Nanotechnology for Energy Sustainability*; Wiley-VCH Verlag GmbH & Co. KGaA **2017**, 569–596.

(2) Zhu, F.; Kim, J.; Tsao, K.-C.; Zhang, J.; Yang, H. Recent Development in the Preparation of Nanoparticles as Fuel Cell Catalysts. *Curr. Opin. Chem. Eng.* **2015**, *8*, 89–97.

(3) Wang, Z. L.; Wu, W. Nanotechnology-Enabled Energy Harvesting for Self-Powered Micro-/Nanosystems. *Angew. Chemie Int. Ed.* **2012**, *51*, 11700–11721.

(4) Wang, N.; Han, L.; He, H.; Park, N.-H.; Koumoto, K. A Novel High-Performance Photovoltaic–Thermoelectric Hybrid Device. *Energy Environ. Sci.* **2011**, *4*, 3676-3681.

(5) Bhattacharjee, M.; Pasumarthi, V.; Chaudhuri, J.; Singh, A. K.; Nemade, H.; Bandyopadhyay, D. Self-Spinning Nanoparticle Laden Microdroplets for Sensing and Energy Harvesting. *Nanoscale* **2016**, *8*, 6118–6128.

(6) Das, S. S.; Pedireddi, V. M.; Bandopadhyay, A.; Saha, P.; Chakraborty, S. Electrokinetic Power Harvesting from Wet Textile. **2019**, arXiv:1907.09999.

(7) Xuan, X. Recent Advances in Direct Current Electrokinetic Manipulation of Particles for Microfluidic Applications. *Electrophoresis* **2019**, *40*, 2484–2513.

(8) Bhattacharjee, M.; Timung, S.; Mandal, T. K.; Bandyopadhyay, D. Microfluidic Schottky-Junction Photovoltaics with Superior Efficiency Stimulated by Plasmonic Nanoparticles and Streaming Potential. *Nanoscale Adv.* **2019**, *1*, 1155–1164.

(9) Manjakkal, L.; Vilouras, A.; Dahiya, R. Screen Printed Thick Film Reference Electrodes for Electrochemical Sensing. *IEEE Sens. J.* **2018**, *18*, 7779–7785.

(10) Chen, J.; Cui, J.-H.; Wang, L. RF Power Management via Energy-Adaptive Modulation for Self-Powered Systems. *IEEE Trans. Very Large Scale Integr. Syst.* **2015**, *23*, 1931–1935.

(11) Vooradi, R.; Anne, S. B.; Tula, A. K.; Eden, M. R.; Gani, R. Ene, Vooradi, R.; Anne, S. B.; Tula, A. K.; Eden, M. R.; Gani, R. Energy and CO2 Management for Chemical and Related Industries: Issues, Opportunities and Challenges. *BMC Chem. Eng.* **2019**, *1*, 7-24.

(12) Selvan, K. V.; Mohamed Ali, M. S. Micro-Scale Energy Harvesting Devices: Review

of Methodological Performances in the Last Decade. *Renew. Sustain. Energy Rev.* **2016**, *54*, 1035–1047.

(13) Kundu, A.; Jang, J. H.; Gil, J. H.; Jung, C. R.; Lee, H. R.; Kim, S.-H.; Ku, B.; Oh, Y. S. Micro-Fuel Cells—Current Development and Applications. *J. Power Sources* **2007**, *170*, 67–78.

(14) Gür, T. M. Review of Electrical Energy Storage Technologies, Materials and Systems: Challenges and Prospects for Large-Scale Grid Storage. *Energy Environ. Sci.* **2018**, *11*, 2696–2767.

(15) Mamidi, S.; Kakunuri, M.; Sharma, C. S. Fabrication of SU-8 Derived Three-Dimensional Carbon Microelectrodes as High Capacity Anodes for Lithium-Ion Batteries. *ECS Trans.* **2018**, *85*, 21–27.

(16) Thakur, S.; Rarotra, S.; Bhattacharjee, M.; Mitra, S.; Natu, G.; Mandal, T. K.; Dasmahapatra, A. K.; Bandyopadhyay, D. Self-Organized Large-Scale Integration of Mesoscale-Ordered Heterojunctions for Process-Intensified Photovoltaics. *Phys. Rev. Appl.* **2018**, *10*, 064012-064026.

(17) Hardman, S.; Chandan, A.; Steinberger-Wilckens, R. Fuel Cell Added Value for Early Market Applications. *J. Power Sources* **2015**, *287*, 297–306.

(18) Mousavi Shaegh, S. A.; Mousavi Ehteshami, S. M.; Chan, S. H.; Nguyen, N.-T.; Tan, S. N. Membraneless Hydrogen Peroxide Micro Semi-Fuel Cell for Portable Applications. *RSC Adv.* **2014**, *4*, 37284–37287.

(19) Grove, W. R. XXIV. *On Voltaic Series and the Combination of Gases by Platinum*. *London, Edinburgh, Dublin Philos. Mag. J. Sci.* **1839**, *14*, 127–130.

(20) Perry, M. L.; Fuller, T. F. A Historical Perspective of Fuel Cell Technology in the 20th Century. *J. Electrochem. Soc.* **2002**, *149*, S59-S67.

(21) Steele, B. C. H.; Heinzel, A. Materials for Fuel-Cell Technologies. *Nature* **2001**, *414*, 345–352.

(22) Staffell, I.; Scamman, D.; Velazquez Abad, A.; Balcombe, P.; Dodds, P. E.; Ekins, P.; Shah, N.; Ward, K. R. The Role of Hydrogen and Fuel Cells in the Global Energy System. *Energy Environ. Sci.* **2019**, *12*, 463–491.

(23) Luo, N.; Miley, G. H.; Gimlin, R. J.; Burton, R. L.; Rusek, J.; Holcomb, F. Hydrogen-Peroxide-Based Fuel Cells for Space Power Systems. *J. Propuls. Power* **2008**, *24*, 583–589.

(24) German, R. Aluminum-Hydrogen Peroxide Fuel Cell Power System for Ocean Bottom Electrical Power. In *Proceedings OCEANS*; IEEE **1989**, *3*,843–848.

(25) Modestino, M. A.; Fernandez Rivas, D.; Hashemi, S. M. H.; Gardeniers, J. G. E.; Psaltis, D. The Potential for Microfluidics in Electrochemical Energy Systems. *Energy Environ. Sci.* **2016**, *9*, 3381–3391.

(26) Carrette, L.; Friedrich, K. A.; Stimming, U. Fuel Cells - Fundamentals and Applications. *Fuel Cells* **2001**, *1*, 5–39.

(27) O'Hayre, R. P.; Cha, S.-W.; Colella, W. G.; Prinz, F. B. *Fuel Cell Fundamentals;* John Wiley and Sons, **2016** .

(28) Disselkamp, R. S. Can Aqueous Hydrogen Peroxide Be Used as a Stand-Alone Energy Source? *Int. J. Hydrogen Energy* **2010**, *35*, 1049–1053.

(29) An, L.; Zhao, T.; Yan, X.; Zhou, X.; Tan, P. The Dual Role of Hydrogen Peroxide in Fuel Cells. *Sci. Bull.* **2015**, *60*, 55–64.

(30) Fukuzumi, S.; Yamada, Y. Hydrogen Peroxide Used as a Solar Fuel in One-Compartment Fuel Cells. *ChemElectroChem* **2016**, *3*, 1978–1989.

(31) Edwards, J. K.; Freakley, S. J.; Lewis, R. J.; Pritchard, J. C.; Hutchings, G. J. Advances in the Direct Synthesis of Hydrogen Peroxide from Hydrogen and Oxygen. *Catal. Today* **2015**, *248*, 3-8.

(32) Fukuzumi, S.; Yamada, Y.; Karlin, K. D. Hydrogen Peroxide as a Sustainable Energy Carrier: Electrocatalytic Production of Hydrogen Peroxide and the Fuel Cell. *Electrochim. Acta* **2012**, *82*, 493–511.

(33) Yamada, Y.; Fukunishi, Y.; Yamazaki, S.; Fukuzumi, S. Hydrogen Peroxide as Sustainable Fuel: Electrocatalysts for Production with a Solar Cell and Decomposition with a Fuel Cell. *Chem. Commun.* **2010**, *46*, 7334-7339.

(34) Yamazaki, S.; Siroma, Z.; Senoh, H.; Ioroi, T.; Fujiwara, N.; Yasuda, K. A Fuel Cell with Selective Electrocatalysts Using Hydrogen Peroxide as Both an Electron Acceptor and a Fuel. *J. Power Sources* **2008**, *178*, 20–25.

(35) Asadnia, M.; Mousavi Ehteshami, S. M.; Chan, S. H.; Warkiani, M. E. Development of a Fiber-Based Membraneless Hydrogen Peroxide Fuel Cell. *RSC Adv.* **2017**, *7*, 40755–40760.

(36) Mousavi Shaegh, S. A.; Nguyen, N.-T.; Mousavi Ehteshami, S. M.; Chan, S. H. A Membraneless Hydrogen Peroxide Fuel Cell Using Prussian Blue as Cathode Material. *Energy Environ. Sci.* **2012**, *5*, 8225-8229.

(37) Yamada, Y.; Yoneda, M.; Fukuzumi, S. High and Robust Performance of H_2O_2 Fuel Cells in the Presence of Scandium Ion. *Energy Environ. Sci.* **2015**, *8*, 1698–1701.

(38) Lisak, G.; Tamaki, T.; Ogawa, T. Dualism of Sensitivity and Selectivity of Porphyrin

Dimers in Electroanalysis. *Anal. Chem.* **2017**, *89*, 3943–3951.

(39) Kozawa, A.; Zilionis, V. E.; Brodd, R. J. Oxygen and Hydrogen Peroxide Reduction at a Ferric Phthalocyanine-Catalyzed Graphite Electrode. *J. Electrochem. Soc.* **1970**, *117*, 1470.

(40) Karyakin, A. A. Prussian Blue and Its Analogues: Electrochemistry and Analytical Applications. *Electroanalysis* **2001**, *13*, 813–819.

(41) Miglbauer, E.; Wójcik, P. J.; Głowacki, E. D. Single-Compartment Hydrogen Peroxide Fuel Cells with Poly(3,4-Ethylenedioxythiophene) Cathodes. *Chem. Commun.* **2018**, *54*, 11873–11876.

(42) Sanli, A. E.; Aytaç, A. Response to Disselkamp: Direct Peroxide/Peroxide Fuel Cell as a Novel Type Fuel Cell. *Int. J. Hydrogen Energy* **2011**, *36*, 869–875.

(43) Scrosati, B.; Garche, J. Lithium Batteries: Status, Prospects and Future. *J. Power Sources* **2010**, *195*, 2419–2430.

(44) Bhattacharjee, M.; Timung, S.; Mandal, T. K.; Bandyopadhyay, D. Microfluidic Schottky-Junction Photovoltaics with Superior Efficiency Stimulated by Plasmonic Nanoparticles and Streaming Potential. *Nanoscale Adv.* **2019**, *1*, 1155–1164.

(45) Haruta, M. Gold as a Novel Catalyst in the 21st Century: Preparation, Working Mechanism and Applications. *Gold Bull.* **2004**, *37*, 27–36.

(46) Daniel, M.-C. and; Astruc*, D. Gold Nanoparticles: Assembly, Supramolecular Chemistry, Quantum-Size-Related Properties, and Applications toward Biology, Catalysis, and Nanotechnology. *Chem. Rev.* **2003**, *104*, 293–346.

(47) Mallick, K.; Witcomb, M. J.; Scurrell, M. S. Redox Catalytic Property of Gold Nanoclusters: Evidence of an Electron-Relay Effect. *Appl. Phys. A* **2005**, *80*, 797–801.

(48) Yamada, Y.; Yoshida, S.; Honda, T.; Fukuzumi, S. Protonated Iron–Phthalocyanine Complex Used for Cathode Material of a Hydrogen Peroxide Fuel Cell Operated under Acidic Conditions. *Energy Environ. Sci.* **2011**, *4*, 2822-2825.

(49) Forest I. Bohrer; Corneliu N. Colesniuc; Jeongwon Park; Ivan K. Schuller; Andrew C. Kummel, Trogler, W. C. Selective Detection of Vapor Phase Hydrogen Peroxide with Phthalocyanine Chemiresistors. J. Am. Chem. Soc. **2008**, *130*, 3712-3714.

(50) Yeo, I.-H.; Johnson, D. C. Electrochemical Response of Small Organic Molecules at Nickel–Copper Alloy Electrodes. *J. Electroanal. Chem.* **2001**, *495*, 110–119.

(51) Maizelis, A. Multilayer Nickel-Copper Anode for Direct Glucose Fuel Cell. *J. Electrochem. En. Conv. Stor.* **2019**, *16*, 041003-041009.

(52) Ferretti, A.; Baldacchini, C.; Calzolari, A.; Felice, R. Di; Ruini, A.; Molinari, E.; Betti,

M. G. Mixing of Electronic States in Pentacene Adsorption on Copper. *Phys.Rev.Lett.* **2007**, *99*, 046802-046807.

(53) Amin, B.; Nazir, S.; Schwingenschlögl, U. Molecular Distortion and Charge Transfer Effects in ZnPc/Cu(111). *Sci. Rep.* **2013**, *3*, 1705-1711.

(54) Chen, C.; Ma, W.; Zhao, J. Semiconductor-Mediated Photodegradation of Pollutants under Visible-Light Irradiation. *Chem. Soc. Rev.* **2010**, *39*, 4206-4219.

(55) Jiao, Y.; Ma, X.-M.; Wang, F.-F.; Wang, K.; Zhang, P.-P.; Wang, Z.-Z.; Yang, L. Facile and Low-Cost Synthesis of Gold Nanoparticles Supported on Cadmium Sulphide Flower-like Three-Dimensional Assemblies. *Micro Nano Lett.* **2012**, *7*, 631-635.

(56) Kalathil, S.; Lee, J.; Cho, M. H. Efficient Decolorization of Real Dye Wastewater and Bioelectricity Generation Using a Novel Single Chamber Biocathode-Microbial Fuel Cell. *Bioresour. Technol.* **2012**, *119*, 22–27.

(57) Han, T. H.; Khan, M. M.; Kalathil, S.; Lee, J.; Cho, M. H. Simultaneous Enhancement of Methylene Blue Degradation and Power Generation in a Microbial Fuel Cell by Gold Nanoparticles. *Ind. Eng. Chem. Res.* **2013**, *52*, 8174–8181.

(58) Chen, G.; Liu, X.; Li, S.; Dong, M.; Jiang, D. A Droplet Energy Harvesting and Actuation System for Self-Powered Digital Microfluidics. *Lab Chip* **2018**, *18*, 1026–1034.

(59) Liu, Y.; Liu, L.; Yang, F. Energy-Efficient Degradation of Rhodamine B in a LED Illuminated Photocatalytic Fuel Cell with Anodic Ag/AgCl/GO and Cathodic $ZnIn_2S_4$ Catalysts. *RSC Adv.* **2016**, *6*, 12068–12075.

(60) Nozik*, A. J.; Memming*, R. Physical Chemistry of Semiconductor−Liquid Interfaces. *J. Phys. Chem.* **1996**, *100*, 13061-13078.

(61) Grynko, D. O.; Fedoryak, O. M.; Smertenko, P. S.; Ogurtsov, N. A.; Pud, A. A.; Noskov, Y. V; Dimitriev, O. P. Application of a CdS Nanostructured Layer in Inverted Solar Cells. *J. Phys. D. Appl. Phys.* **2013**, *46*, 495114.

(62) Mousavi Ehteshami, S. M.; Asadnia, M.; Tan, S. N.; Chan, S. H. Paper-Based Membraneless Hydrogen Peroxide Fuel Cell Prepared by Micro-Fabrication. *J. Power Sources* **2016**, *301*, 392–395.

(63) Tuschel, D. Photoluminescence Spectroscopy Using a Raman Spectrometer *SpectroscopyOnline* **2016**, *31*, 14-21.

(64) Suwathy, R.; Reddy, K. M.; Pramoth Kumar, M.; Venkatesan, M. Droplet Impinging Behavior on Surfaces Part I - Hydrogen Peroxide on Aluminium Surface. *IOP Conf. Ser. Mater. Sci. Eng.* **2016**, *149*, 012219-0122223.

(65) Lee, W.; Kim, H.; Jung, D.-R.; Kim, J.; Nahm, C.; Lee, J.; Kang, S.; Lee, B.; Park, B. An Effective Oxidation Approach for Luminescence Enhancement in CdS Quantum Dots by H2O2. *Nanoscale Res. Lett.* **2012**, *7*, 672-676.

(66) Su, Y.-H.; Ke, Y.-F.; Cai, S.-L.; Yao, Q.-Y. Surface Plasmon Resonance of Layer-by-Layer Gold Nanoparticles Induced Photoelectric Current in Environmentally-Friendly Plasmon-Sensitized Solar Cell. *Light Sci. Appl.* **2012**, *1*, e14–e14.

(67) Torimoto, T.; Horibe, H.; Kameyama, T.; Okazaki, K.; Ikeda, S.; Matsumura, M.; Ishikawa, A.; Ishihara, H. Plasmon-Enhanced Photocatalytic Activity of Cadmium Sulfide Nanoparticle Immobilized on Silica-Coated Gold Particles. *J. Phys. Chem. Lett.* **2011**, *2*, 2057–2062.

(68) He, W.; Zhou, Y.-T.; Wamer, W. G.; Hu, X.; Wu, X.; Zheng, Z.; Boudreau, M. D.; Yin, J.-J. Intrinsic Catalytic Activity of Au Nanoparticles with Respect to Hydrogen Peroxide Decomposition and Superoxide Scavenging. *Biomaterials* **2013**, *34*, 765–773.

(69) Wang, L.; Li, R.; Liu, J.; Han, J.; Huang, M. Synthesis of Au@CdS Core–Shell Nanoparticles and Their Photocatalytic Capacity Researched by SERS. *J. Mater. Sci.* **2017**, *52*, 1847–1855.

Chapter 04

Self-Organized Liquid Crystal Droplets as Tunable Soft-Photomasks

This chapter has been published as Thakur, S.; Dasmahapatra, A. K.; Bandyopadhyay D. *ACS Appl. Mater. Interfaces* **2021** (Accepted). Self-Organized Liquid Crystal Droplets as Phototunable Softmasks.

Abstract

A single-step pathway has been invented for the generation of a large-area and high-density liquid crystal (LC) droplets via rapid spreading of an LC-laden hexane film on an aqueous surfactant bath. The LC droplets floating on the air-water interface have been employed as fluidic photomasks with tunable optical properties suitable for soft-photolithography (SPL). Such masks help in the decoration of a host of mesoscale three-dimensional features on the films of photoresists (PR) when photons are guided through the LC droplets. For example, an array of flattened droplets is obtained on a positive-resist while donut features are observed on the negative tone. Phase transition of LC droplets under solvent vapor annealing has been employed to control the movement of photons through LC droplets and subsequently control the light exposure on PR surfaces. Remarkably, during the solvent vapor exposure, even though the orientational order of nematogens in the bulk of the droplet has been transformed into the isotropic one, the LC molecules retained their anchoring at the LC-water-air three-phase contact line (TPCL). Thus, while the photons could undergo a facile migration through the bulk or the droplet, the phase boundaries reflect them back to develop interesting patterns on the positive or negative tones of the PR surface. Importantly, the surfactant loading on the water bath helps in tuning the size, periodicity, and ordering of LC droplets of the photomask floating on the water bath. For example, at lower (higher, beyond CMC) surfactant concentration shows a slower (faster) spreading with a gradual (random) retraction of TPCL. On the other hand, use of hexane as a solvent promoted a rapid spreading, dewetting, and evaporation to produce photomasks with LC droplets as small as 1 μm while the use of long-chain alcohol such as heptanol as a solvent lead to LC droplets larger than 100 μm. The droplet size and periodicity could also be tuned by changing the LC loading in the solvent. In the process, a host of unprecedented drop formation modes such as, spreading, retraction, dewetting, evaporation and 'fire-cracking' have also been uncovered.

4.1 Introduction

Decoration of self-organized patterns have found their utility in the micro/nano fabrication arena owing to the possibility of their low-cost footprints in the diverse cutting-edge applications such as miniaturized display units,[1] photodetectors,[2] sensors,[3] opto-fluidic devices,[4] micro/nanoelectronics[5] and photovoltaic cells.[6] In particular, among the other available techniques, soft-lithography[7] has emerged as a simpler and scalable alternative for the assemblage of large-area and ordered patterns. Interestingly, such micropatterns have already been tested in a number of proof-of-concept futuristic applications which include plenoptic cameras[8], micro-mirrors,[9] or optical switches.[10] More importantly, the use of smart materials such as the liquid crystals (LCs) on such patterned surfaces have also opened up the opportunity for further phase-modulation and light manipulation capabilities of the devices.[11,12,13] A few recent seminal contributions highlight that the tunable optical properties of LC droplets and their intrinsic curvature can be some of the many attractive features to exploit for a number of futuristic applications.[14] In fact, flat panels,[15] smart windows,[16] solar cells,[17] optical wave guides,[14] 3-D displays,[18] and optical traps[19] already employ such tailor-made properties of LC materials.[19,20] Thus, there is a need to further innovate and explore the exceptional features of the miniaturized LC droplets leading to reliable and inexpensive optofluidic technologies.

In this direction, the prior-art has already demonstrated that the self-organized nanoassembly of colloidal particles at the air-water interface can lead to the formation of low-cost photomasks suitable for a number of top-down lithography applications.[21] The presence (or absence) of the colloidal particles under a light exposure enable the reflection (or passage) of photons to decorate positive or negative replica of the patterns decked by the colloidal assembly at the air-water interface. However, the colloidal particles are rather dormant in terms of their light modulation capabilities and the use of LC droplets with the tunable optical properties can become a game changer in this regard. In a way, replacing the colloidal assemblage with the LC droplets can help in the regulation the photonic exposure on the diverse photoactive resists.[22] For example, while an LC droplet may reflect the plane polarized light, in the isotropic phase the same droplet may allow the full exposure of the photons to the resist.[23] Further, in such a scenario, the curvature of the droplet meniscus and the surrounding contact line can also play a crucial roles in the reflection, scattering and transmission of the photons through an LC or isotropic phase under varied conditions.

However, some of the major challenges in this direction has been, (i) the formation of miniaturized LC droplets from the films through the destruction of inherent elasticity originating from their orientational order[24] and (ii) decoration of large-scale assemblage of miniaturized LC droplets.[25] Traditionally, the destruction of orientational order of an LC film has been achieved through thermal annealing beyond its phase transition temperature, T_p.[26] A few recent studies uncover that the same can also be achieved under a solvent exposure at room temperature.[27] Subsequently, self-organization[28] under long-rage interactions or spin-dewetting[29] of an LC film on a patterned surface can lead to an ordered array of LC droplets. Once such droplet arrays are formed, the reflection, scattering and transmission of the photons through such LC droplets can indeed be controlled through a solvent exposure.[29]

It is important to note here that the self-organization of liquid films on the air-water interface can be an optimal single step soft-lithography method to generate multitude of droplet patterns.[30–32] From the scientific standpoint, the self-organized dewetting of films are generally governed by the interplay of viscous, interfacial tension, intermolecular, and adhesive forces.[33–35] In particular, the spacing and size of the droplets are decided by the reduction (increase) in the stabilizing (destabilizing) influence of the interfacial tension (intermolecular force).[34,36] Particularly, the reduction in the interfacial tension is achieved either by the addition of surfactants[37] at the air-water interface or by the use of liquid/liquid interface wherein the interfacial tension is at least one order of magnitude less than the same at the liquid-air interface.[38] The evaporation of the volatile solvents from the films,[39] slippage of the films on the fluid interface,[40] or the thermal/solutal Marangoni effects[41] are found to be some other important factors in deciding the size and spacing of the droplets. While the prior-art related to soft-lithography has mainly focused on the generation of such liquid droplets on the liquid surfaces,[42,43] there is hardly any study that considers, (i) decoration of miniaturized array of LC droplets at the air-water interface and (ii) use them as low-cost photomasks with the capability to modulate the polarized rays.

In view of this background, we demonstrate a single-step technique to generate high-density and quasi-monodispersed nematic LC droplets, which are later employed as photomasks to decorate miniaturized pattern on the photoresists. For this purpose, initially, a droplet of 5CB laden hexane has been dispensed on a water bath loaded with a surfactant (e.g. cetyltrimethylammonium bromide – CTAB). The rapid spreading of the immiscible hexane-5CB droplet with a lower surface tension on the slippery water surface with a higher surface tension immediately fragments into an array of 5CB laden hexane islands. Subsequently, a swift evaporation of hexane leaves an array of miniaturized LC droplets floating on the air-

water interface. Experiments uncover that the LC loading in the solvent, surfactant concentration in water bath and volatility and viscosity of the solvent are some of the important handles to control the size and periodicity of the droplets. For example, at low CTAB loading in water, we observe a spinodal dewetting of the LC laden hexane droplet followed by the contact-line instabilities (CI) to generate uniform 5CB droplets. On the other hand, beyond the critical micellar concentration (CMC) in water, islands of CTAB micelles at the air-water interface promote a heterogeneous nucleation induced dewetting leading to formation of poly-dispersed 5CB droplets.

Finally, a proof-of-concept application has been demonstrated by employing the anisotropic 5CB droplets as fluidic photomasks in an alternative soft-photolithography (SPL) setup. For this purpose, plane polarize light has been passed through the array of LC droplets before exposing the rays on the thin films of positive (PPR) or negative (NPR) photoresists. During this experiment, the LC droplets are also brought under the solvent vapor exposure to stimulate a phase transition from nematic to isotropic states. Remarkably, such a low-cost setup could easily develop miniaturized patterns with the shapes of castle-moats, cavities, drops or donuts on the surface of the PR films. Importantly, while the solvent exposure could easily destroy the director orientation in the bulk of the droplet, the LC molecules at the contact line retained their orientational order even after a long-time solvent exposure. Thus, even though the polarized rays could pass through the bulk of the isotropic LC droplet after the phase transition, the surrounding three-phase contact line (TPCL) reflected them back to facilitate the castle-moat or donut patterns on the PR surfaces. In a way, the shape of the droplets floating on the air-water interface and the modulation of the optical properties of the LC droplets at the different stages solvent vapor induced phase transition help in decorating such complex patterns on the surface of the photoresists, which are rather difficult to fabricate using other conventional lithography techniques[44,45] or the colloidal masks.[46]

4.2 Materials and Methods

4.2.1 Materials

4-Cyano-4'-pentylbiphenyl (5CB), PS (avg. Mw 192,000), Cetrimonium bromide (CTAB), sodium dodecyl sulfate (SDS) was purchased from Sigma Aldrich, India. Ammonia, hydrogen peroxide (30% v/v), hexane, toluene, heptanol, chloroform, isopropyl alcohol (IPA), ethanol and acetone were purchased from Merck, India. The chemicals utilized for PL experiments – NPR (SU8-2002), SU-8 Developer, PPR (S1813), MBK were purchased from MICROCHEM, USA and hexamethyldisilazane (HMDS) was purchased from HIMEDIA, India. The AR grade

chemicals were directly used for experiments without any further purification. Silicon wafers was procured from MACWIN, India. Cover glass (24 x 24 mm, avg. thickness ~ 0.11 mm) was supplied from Borosil. Ultra-violet (UV) light source (intensity ~ 20 mW/cm^2) was acquired from a local vendor. Milli-Q grade water was employed to prepare all the solutions and for cleaning the glassware.

4.2.1.1 Characterization

Imaging ellipsometer (EP3, Nanofilm, Accurion Scientific Instruments Pvt. Ltd) was employed to measure the film thickness of PR layers. Surface morphologies were characterized by the field emission scanning electron microscope (FESEM, Jeol India Pvt. Ltd), an atomic force microscopy (AFM, Bruker, Innova series), and an optical microscope (Leica, DM 2500 upright microscope, with POM mode). ST and IFT measurements of different liquid systems were carried out using an automatic surface tensiometer (KYOWA, DY-300).

4.2.2 Methods

4.2.2.1 Dewetting of a 5CB droplet on CTAB-water bath

Initially a glass petridish of 45 mm diameter was filled with 5 mL CTAB solution. Upon deposition of a 2 μL hexane droplet containing varying concentrations of 5CB (5-500 mM), a film formed on the surface of the surfactant-water bath, which initiated a cascade of events culminating with an ensemble of numerous self-organized micro/nano droplets. **Figure 4.1** schematically shows the different stages of droplet generation involved: (i) dispensation of the LC laden hexane droplet on the CTAB-water bath, as shown in the image (I); (ii) rapid expansion of the 5CB-hexane film due to a positive spreading coefficient ($S > 0$) of the LC loaded hexane droplet on the water surface, as shown by the image (II); (ii) generation of multitude of droplets from the retracting TPCL after hexane evaporation, as shown by the image (III). In this stage only, the formation of holes take place on the 5CB-LC film alongside the formation of the fingers through the retraction of TPLC at the edges of the evaporating droplet; and (iv) finally, simultaneous evaporation of hexane leading to the generation of high-density 5CB droplets, as shown by the image (IV). The various stages of such dynamics were recorded under an upright microscope (Leica DM 2500) attached with a high-speed resolution digital camera (Fastcam Mini UX100, Photron Ltd.

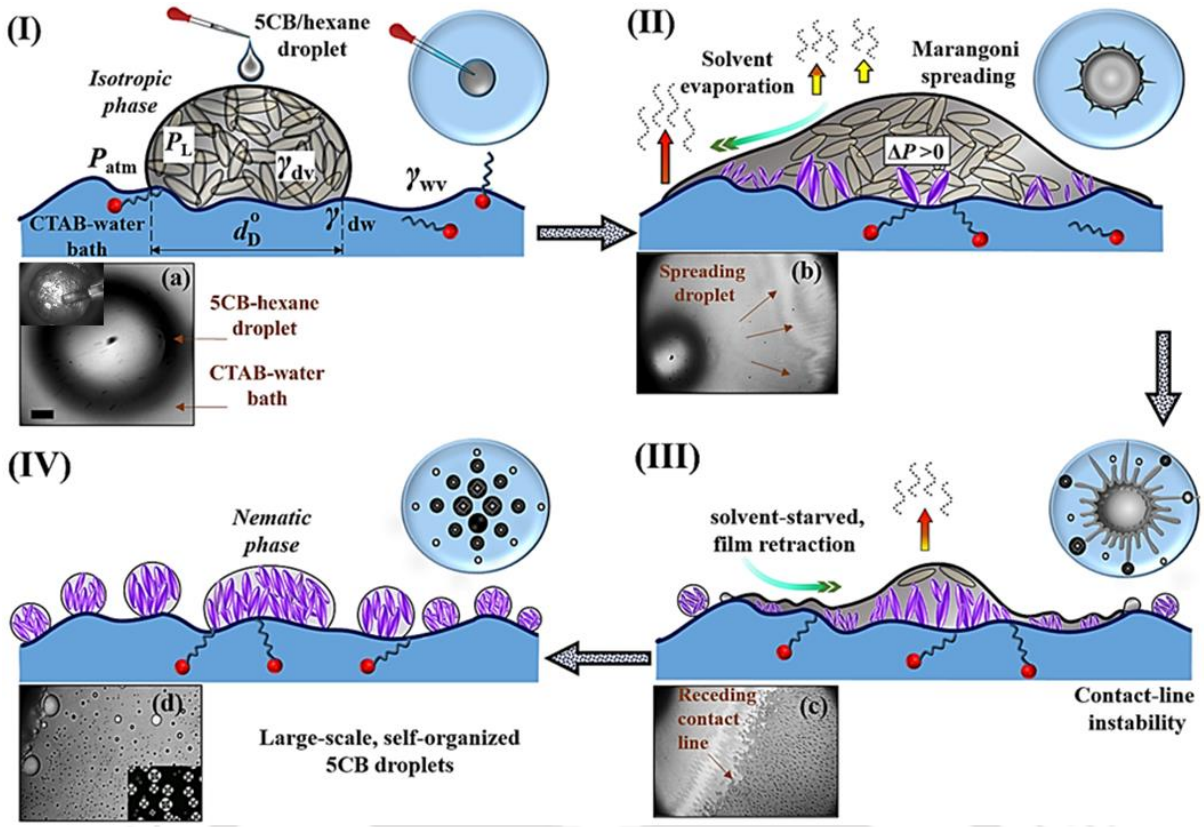

Figure 4.1 Schematics (I) – (IV) showing the side and top views of the stages of spreading and dewetting of 5CB-hexane droplet on a CTAB-water interface wherein the insets (a) – (d) show the optical and polarized optical micrographs – POMs. (I) The pressure in the solvent rich isotropic droplet (initial diameter, d_D^0) is P_L while the same outside is P_{atm}. The top view through POM in the inset (a) indicate the absence of director orientation. (II) Spreading of the droplet and a rapid expulsion of the hexane vapors. Image (b) shows the droplet spreading on the surfactant bath. (III) Retraction of the contact-line due to solvent evaporation and the onset of the fingering instability followed by the droplet formation, as shown by POMs in the inset (c). (IV) Ensemble of 5CB droplets on the water bath wherein the POM inset (d) indicates the restoration of the nematic order in the droplets. The experimental insets (a) – (d) at different time intervals represent a 5CB mixture in hexane (5 mM) dispensed on a 0.01 mM CTAB-water bath. Scale bar for above images is of length 50 µm.

4.2.2.2 Soft-Photolithography

For the SPL experiments, initially a Si wafer was cut into small substrates of dimensions 1 cm x 1 cm and cleaned according to a standard protocol that has been mentioned in the **Appendix**. The fluidic photo-mask composed of multitude of LC droplets was prepared by coating a cover glass with 200 µL of 10 mM CTAB/water solution and then dispensing 2 µL of 50 mM 5CB/hexane solution on it. The fluidic mask was carefully placed on the PR coated substrate ensuring a soft-contact between the two surfaces. At the beginning, Si substrates were spin-coated with HMDS solution (primer) at 4000 rpm for 60 s. The coated substrates were then

heated at 170 °C for 20 min to remove the excess solution. After allowing it to cool down to room temperature, the substrates were then coated with respective PPR and NPR tones for obtaining the desired patterns. For PPR coating, S1813 solution was spin-coated at 3500 rpm for 60 s that resulted in a film thickness of 1-2 μm. This was followed by direct exposure to UV-illumination for 40 s under the LC droplet mask. Thereafter, the substrates were submerged in the developer solution for 1 min and rinsed thoroughly with water. The developed substrates were dried with N_2 gas and heated at 80 °C for 10 min (post-baking) to harden the developed features. For NPR coating, SU-8 2002 solution was spin-coated at 500 rpm for 30 s, followed by 3500 rpm for 90 s resulting in a film thickness of 40-45 μm. The coated substrates were then pre-baked at 80°C for 3 min, followed by at 110 °C for 6 min. Subsequently, they were exposed to UV-illumination for 40 s under the LC droplet mask and then those substrates were heated at 80 °C for 1 min, followed by 110 °C for 5 min. Afterwards, the substrates were submerged in the developer solution for 6 min and then in IPA for 20 s. The developed substrates were cleaned using N_2 gas and heated at 170 °C for 10 min to harden the patterned features.

4.3 Results and Discussion

4.3.1 Single-Step 5CB-Droplet Generation

Initially, a single step methodology has been formulated to generate a multitude of 5CB droplets. For this purpose, a petri dish (area ~16 cm^2), filled with 5 mL of aqueous CTAB solution, is used as the bath on which a 2 μL droplet of 5CB-hexane solution is dispensed. The droplet rapidly spread on the aqueous surfactant bath because, when the hexane-LC droplet is dispensed on the water-surfactant bath, the combination of materials results in a positive spreading coefficient (S). The spreading coefficient of the droplet on the water bath has been defined as, $S = \gamma_{wv} - \gamma_{dv} - \gamma_{dw}$ wherein the interfacial tensions at the hexane-air, water-air, and hexane-water interfaces are represented by γ_{dv}, γ_{wv}, and γ_{dw}. The different stages of 5CB droplet spreading have been depicted in **Figure 4.1**. **Figure 4.1 (I)** schematically shows the formation of a lens of the 5CB-laden hexane droplet on the water-surfactant bath at the time of dispensation. At this stage, the initial diameter of the droplet-lens is denoted as, d_D^0, while the Laplace pressure in the droplet is represented as P_L and the pressure outside is the atmospheric pressure, P_{atm}. The optical micrograph in the inset (a) shows the top view of the 5CB droplet lens at the time of dispensation.

Following this, within a few ms, the droplet spreads rapidly on the water surface owing to the S ~ 6 mN/m.[47] Subsequently, a rapid expansion of the TPCL of the 5CB-hexane droplet on the

water bath is observed until an equilibrium contact angle is achieved, as schematically represented in the **Figure 4.1 (II)**. The image (b) depicts a snapshot of the spreading droplet from the top using the optical microscope when the 5CB loading is 5 mM in hexane and CTAB concentration in water is 0.01 mM. The spreading of the droplet leads to a large increase in the area of the hexane-air interface as well as hexane-water-air TPCL which in turn facilitates a faster rate of evaporation of the hexane from the droplet matrix with a relatively high vapor pressure of 20 kPa.

Subsequently, the loss of solvent from the 5CB-hexane droplet results in a number of interesting phenomena, (i) transformation of hexane rich droplet into a 5CB rich one with progressive restoration of the orientational ordering of the 5CB molecules; (ii) transformation of the droplet into a nonuniform 5CB rich film, as schematically shown by **Figures 4.1 (II)** and **4.1 (III)**; (iii) the dewetting of the film with the formation of holes followed by their expansion and coalescence before forming ribbons and droplets, as schematically shown by **Figures 4.1 (III)** and **4.1 (IV)**; (iv) the retracting TPCL of the 5CB rich hexane droplet show a the formation of periodic fingers along the contact line, which rapidly ejects an array of uniformly sized droplets during the retraction, as shown by the image (c). A rapid and non-uniform evaporation of the hexane is expected to generate a gradient of surface tension near the TPCL which in turn generate the required solutal Marangoni stress for the 'finger' at the receding edge of the contact line.[48] Subsequently, as a result of the CI instability, an array of trails of 5CB droplets are generated from the leading edge of the fingers; (v) finally, the mechanisms discussed in the points (iii) and (iv) lead to the formation of a collection of 5CB droplets on the water-CTAB bath as shown in the image (d) and **Figure 4.1 (IV)**; (vi) during the dewetting and subsequent 5CB drop formation we also observe the presence of periodic "humps" on the contact line near the dewetting front which is a typical characteristic of the slip-induced dewetting on a soft and slippery surface.[49,50]

Importantly, the size of the LC droplets formed is found to progressively increase as one moves from the TPCL to the center of the main droplet. Again, the size and polydispersity of the 5CB droplets could be tuned by changing the 5CB loading in hexane and CTAB in water. It may be noted that, since 5CB is initially dissolved in hexane, it is completely in the isotropic state when the droplet is dispensed. Post-dispensation, a rapid loss of solvent engenders a progressive phase transition from isotropic to the nematic state. Importantly, after the phase transition the nematogens anchored in a very different manner at the bulk and TPCL of the 5CB droplets formed, which has been discussed in detail with the application later. Interestingly, the droplets are found to be stable for long periods of time (~ 3 h) because the coalescence is restricted by

the elastic energy barrier of the miniaturized 5CB droplets.[51] Further, a quasi-monodispersity in the size of the droplets also slowed down the rate of coalescence providing a kinetic stability to the miniaturized droplets. Interestingly, when the collection of miniaturized droplets shown in the image (d) has been exposed to a solvent vapor to cause a nematic to isotropic transition they gradually coalesced. The control experiment corroborated towards the correctness of the aforesaid hypothesis of the stability of the 5CB droplets in their nematic state.

4.3.2 Effects of solvent and surfactant

The solvent employed to dissolve and spread the 5CB droplet plays a vital role in determining the overall droplet distribution after fragmentation. In this study, we show the results for three such spreading solvents (SS) for the creation of miniaturized 5CB droplets on the water bath. The solvents hexane, heptanol, and toluene differ in polarity, volatility, viscosity, density, miscibility with water, and surface tension, as shown in the **Table 4.1**.

Table 4.1 Physical properties of three different solvents employed to dissolve 5CB

Solvent	Solubility in water (g/100 mL)	Volatility (kPa)	Surface tension (mN/m)	Interfacial tension (mN/m)	Viscosity (mPa.s)	Density (kg/m^3)	References
Heptanol	0.1	0.135	26	7 -7.5	3.95	819	52
Toluene	0.05	3	28.5	37.5-38	0.56	857	53
Hexane	0.0009	20	18	50-51.5	0.3	655	47,54

Since heptanol and toluene are relatively more miscible and have a lower surface tension their spreading has been far more rapid. However, in case of the non-volatile heptanol, once the TPCL attain an equilibrium configuration upon spreading, it is able to retain the same for a longer time (>150 s) as compared to more volatile toluene (~ 100 s), before it eventually retracts. This is in stark contrast to the case with the most volatile hexane wherein the spreading as well as retraction have been fast and completed within ~ 30 s, before the miniaturized 5CB droplets are formed. As mentioned earlier, rate of solvent evaporation from the droplet interface plays a decisive role in controlling the droplet size distribution. Lower volatility and higher viscosity of heptanol and toluene in comparison to hexane, cause the droplets to be ejected at a lower rate from the TPCL having a larger size. Further, the size distribution of droplets is observed to be maximum for heptanol followed by toluene and is minimum for hexane.

Table 4.2 Surface tension values of the SDS and CTAB solutions.

Nature of surfactant	Conc. (mM)	Avg. surface tension (mN/m)
SDS (Anionic)	1	42.8
	10	37
	100	33
CTAB (Cationic)	0.01	56.4
	0.1	48.7
	1	37
	10	35.3
	100	34.2

In addition to the solvent type, the type of surfactant mixed to the water bath also play a pivotal role on the size and distribution of the droplets. Thus, apart from cationic CTAB, the anionic SDS has also been employed for the experiments, as shown in the **Table 4.2**. In this regard, surfactant concentrations near and well beyond the CMC limit have been utilized to test their effects on the size of the miniaturized droplets and their distribution. For example, a 2 µL droplet of 5CB/SS (0.1% v/v) has been dispensed on a 5 mL SDS-water bath and the subsequent daughter droplet dimensions has been analyzed, as presented in the **Figure 4.2 (I)**. Further, when the surfactant loading is less (10 mg/mL), larger 5CB droplets are formed when heptanol (105±15 µm) is used whereas smaller droplets are observed for hexane (50±20 µm). On the other hand, high surfactant concentrations produce larger droplets in toluene (60±40 µm) and smaller in hexane (30±10 µm). Further, since heptanol has the highest polarity among the solvents reported, its interaction with the surfactant bath underneath also established a stability towards the 5CB-heptanol film.

In addition to this, as concentrations beyond CMC, the presence of the micelles at the water-air interface produced a gradient of interfacial tension, which influence the movement of the TPCL and subsequent ejection of the drops from the 'fingers'. However, this influence is found to be less for hexane. The aforesaid control experiments have helped us in deciding the solvent to be hexane for further experiments where for which we observe less size-variation in the miniaturized 5CB droplets, high density of droplets, and a smaller time scale of dewetting. Remarkably, when the surfactant loading has been well below the CMC in the water bath, the dewetting of the film follow a spinodal pathway.[55,56] In contrast, when the surfactant loading has been near CMC or well beyond the same, the defect induced heterogeneous nucleation has been observed.[57] In a way, when the water surface is sparsely populated with surfactant

molecules, the spinodal pathway is preferred.[56,58] However, the presence of the micelles at the water air interfaces acts as the nucleation sites of hole formation for the solvent-5CB film, which eventually promotes the defect guided dewetting.

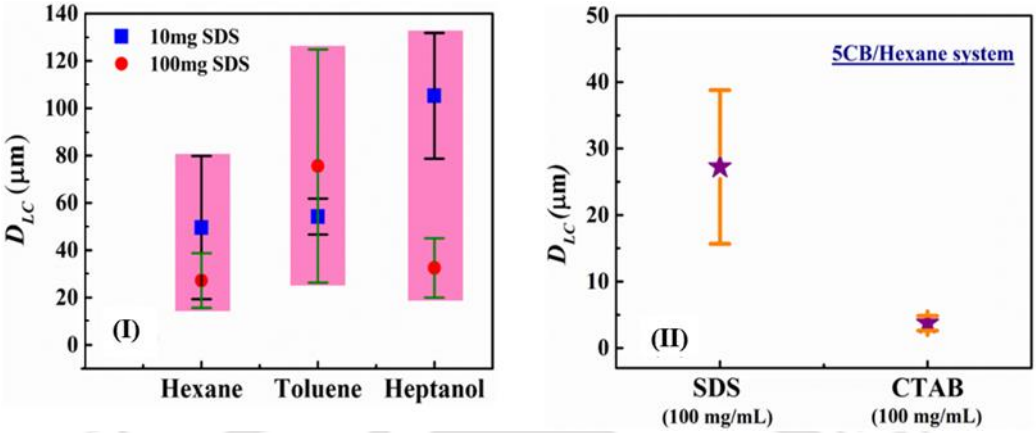

Figure 4.2 Effect of variation of different parameters on the LC droplet diameter. (I) spreading solvent, (b) nature of surfactant – anionic and cationic. For the case (b), hexane was chosen as the spreading solvent for dissolving 5CB molecules. The 5CB concentration in all the cases were maintained 0.1% (v/v).

In addition, among the anionic SDS and cationic CTAB, the latter produce much smaller 5CB droplets with a more uniform size distribution, as shown in the **Figure 4.2 (II)**. Further, we perform a few experiments wherein a 2 µL 5CB-hexane droplet is dispensed on a water-surfactant bath (5 mL) containing equal amount of SDS and CTAB (100 mg/mL). It is well known that the limiting surface area and MW of SDS (288.37 g/mol) is lower as compared to CTAB (364.65 g/mol). Further, the conditions ensure that the surfactant loading has been well beyond CMC for both SDS (~ 8 mM) and CTAB (~ 1 mM).[59] In such a scenario, presence of a large number of micellar structures is found to contribute towards an uneven droplet distribution. It is also known that the length of aliphatic chains of surfactant molecules can significantly influence the molecular orientation in an LC droplet.[59,60,61] Since SDS contains $(SO_4)^-Na^+$ as the head group and CTAB contains $(CH_3)_3N^+Br^-$, a 5CB molecule with biphenyl structures along with a CN group at one end, may have a tendency towards attracting positively charged species. Thus, the electrostatic interactions of the 5CB nematogen with the CTAB may have entailed higher surface coverage area and aided in generation of smaller and uniform droplets. Therefore, CTAB has been selected as the surfactant for further experiments.

Figure 4.3 (I) presents the plot wherein the 5CB concentration (C_{LC}) is varied in a 2 µL of 5CB-hexane drop across two orders of magnitude for three different values, 5 mM, 50 mM and 500 mM while CTAB concentration (C_{CTAB}) is varied from 0.01 mM to 100 mM. The plot

suggests that, at low 5CB concentrations, droplet sizes (d_D^0) vary from 95±10 µm (C_{CTAB} = 0.01 mM) to 0.8±0.3 µm (C_{CTAB} = 10 mM). Importantly, for C_{CTAB} = 100 mM the droplets are not visible under an optical microscope, which indicate the possibility of the formation of nanodroplets under such circumstances.

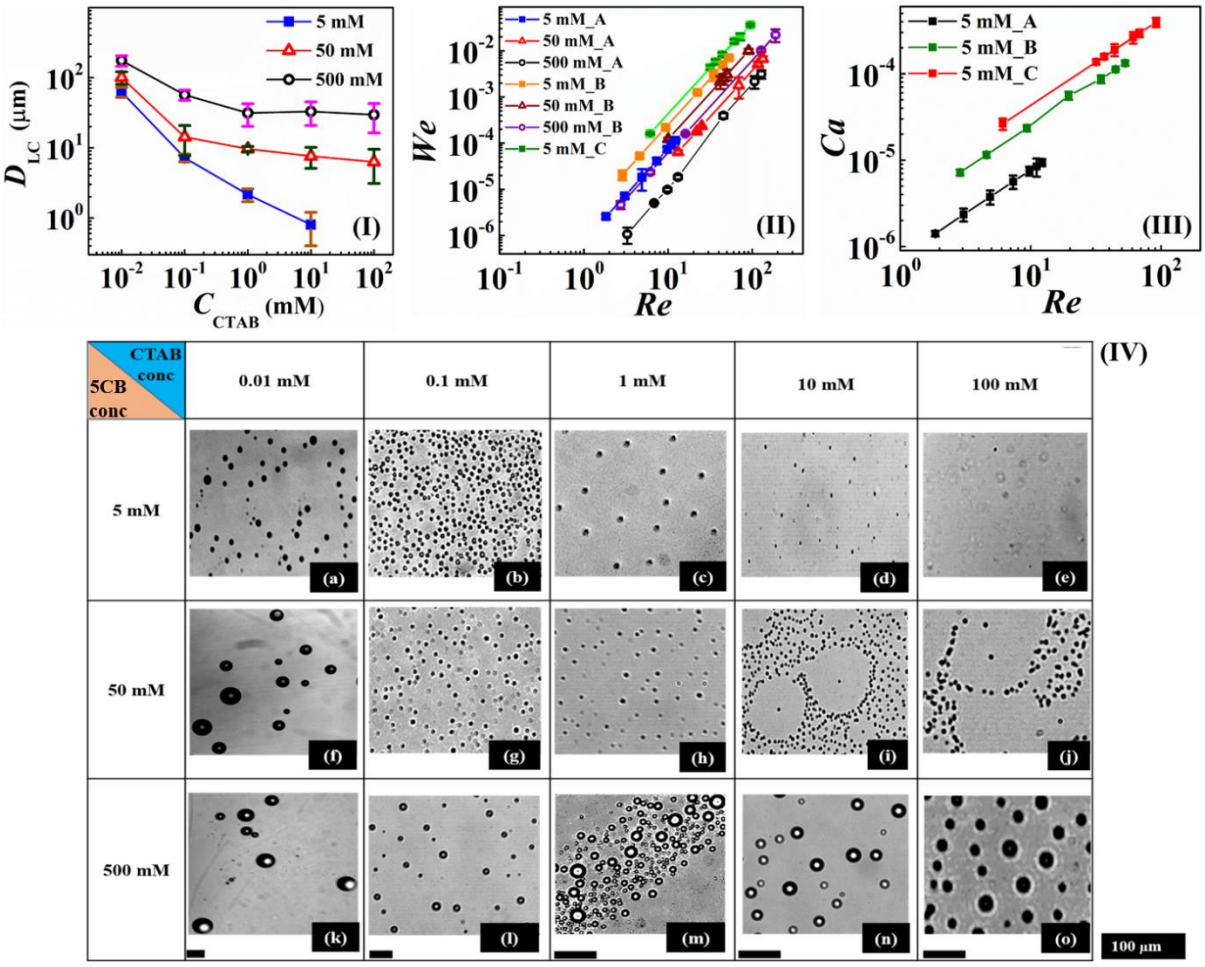

Figure 4.3 (I) Effects of LC loading (C_{LC}) and CTAB concentration (C_{CTAB}) on the average droplet diameter (d_D^0). (II) Plot shows the variation in Weber number ($We = \rho_D v_D^2 d_D^0/\gamma_m$) with Reynolds number ($Re = \rho_D v_D d_D^0/\mu_D$) at different C_{LC} (5 mM, 50 mM and 500 mM in hexane) and C_{CTAB} in water bath ("A" refers to 0.01 mM, "B" refers to 0.1 mM and "C" refers to 1 mM CTAB concentration). (III) Plot shows the variation in Capillary number ($Ca = \mu_D v_D/\gamma_m$) with *Re* for different C_{CTAB} but at the same C_{LC} of 5 mM. (IV) Optical micrographs of 5CB droplets (a-o) obtained by varying C_{LC} and C_{CTAB}. Images for 5 mM and 50 mM were taken at 10x, while for 500 mM, they were taken at 2.5x. Scale bar is of length 100 µm.

Increasing C_{CTAB} from 0.01 mM to 10 mM results in reduction in surface tension of the water bath from 49 mN/m to 35 mN/m, as shown in **Table 4.2**. Thus, the size of the 5CB droplets significantly reduce to the nanoscale especially when the 5CB loading in hexane is small (filled square, blue symbols). However, increasing C_{LC} further and C_{CTAB} well beyond CMC (~ 1

mM) does not help for size reduction (circular and triangular symbols). Overall, the plot indicates a reduction in LC loading in the solvent and use of optimal surfactant concentration in the water bath near CMC may lead to the formation of nanostructures with a higher density and reduced polydispersity. The optical micrographs (a) – (d) in the **Figure 4.3 (II)** shows progressive reduction of micro to nanostructures at 5 mM initial 5CB loading in hexane and with the variation in C_{CTAB} at the water bath. The images (a) – (d), (e) – (h), and (i) – (l) together suggest that the 5CB droplets are, (i) of bigger size at lower C_{CTAB} and higher C_{LC}, (ii) monodispersed and miniaturized in size near or little beyond CMC, (iii) larger in size at lower C_{CTAB} and higher C_{LC}, (iv) monodispersed and of microscale at higher C_{CTAB} and C_{LC}; (v) nanoscale at higher C_{CTAB} and lower C_{LC}. It may be noted here that the optical micrographs reported are taken from regions where droplets are present on the water surface.

The dynamics of the dewetting phenomenon has also been analyzed using the following parameters, which influence most, such as initial 5CB drop diameter (d_D^0), instantaneous velocity of retracting film (v_D), density of the solvent (ρ_D), viscosity of the solvent (μ_D) and interfacial tension of the hexane-water interface (γ_{dw}). A dimensional analysis using these parameters have led to the formation of following dimensionless numbers, such as, Reynolds ($Re = \rho_D v_D d_D^0/\mu_D$), Weber ($We = \rho_D v_D^2 d_D^0/\gamma_m$) and capillary ($Ca = \mu_D v_D/\gamma_m$) numbers, which help in understanding the science behind the phenomena. **Figure 4.3 (III)** shows the variation in *Re* with *We* when C_{LC} and C_{CTAB} are varied. For an increased C_{LC} at a fixed C_{CTAB}, it is observed that the inertial forces dominate the initial droplet spreading dynamics, as indicated by the higher values of *Re* number. This eventually results in the formation of larger 5CB droplets at the end. Increasing C_{CTAB} for a fixed C_{LC}, reduce the surface tension, which increase the *We*. This initiates a faster retraction of the TPCL and generate smaller droplets. The systems leading to the parameters $Re > 2 \times 10^2$ and $We > 10^{-2}$, could not be captured under microscope due to enhanced perturbations. **Figure 4.3 (IV)** suggests that increasing C_{CTAB} for a fixed C_{LC} lead to an increase in increased *Ca*, indicating the reduction in the capillary forces near the interface. This leads to a rapid spreading and subsequent retraction regime suitable for the generation of sub-micron 5CB droplets with a higher density and monodispersity.

4.3.3 Triplet of Modes

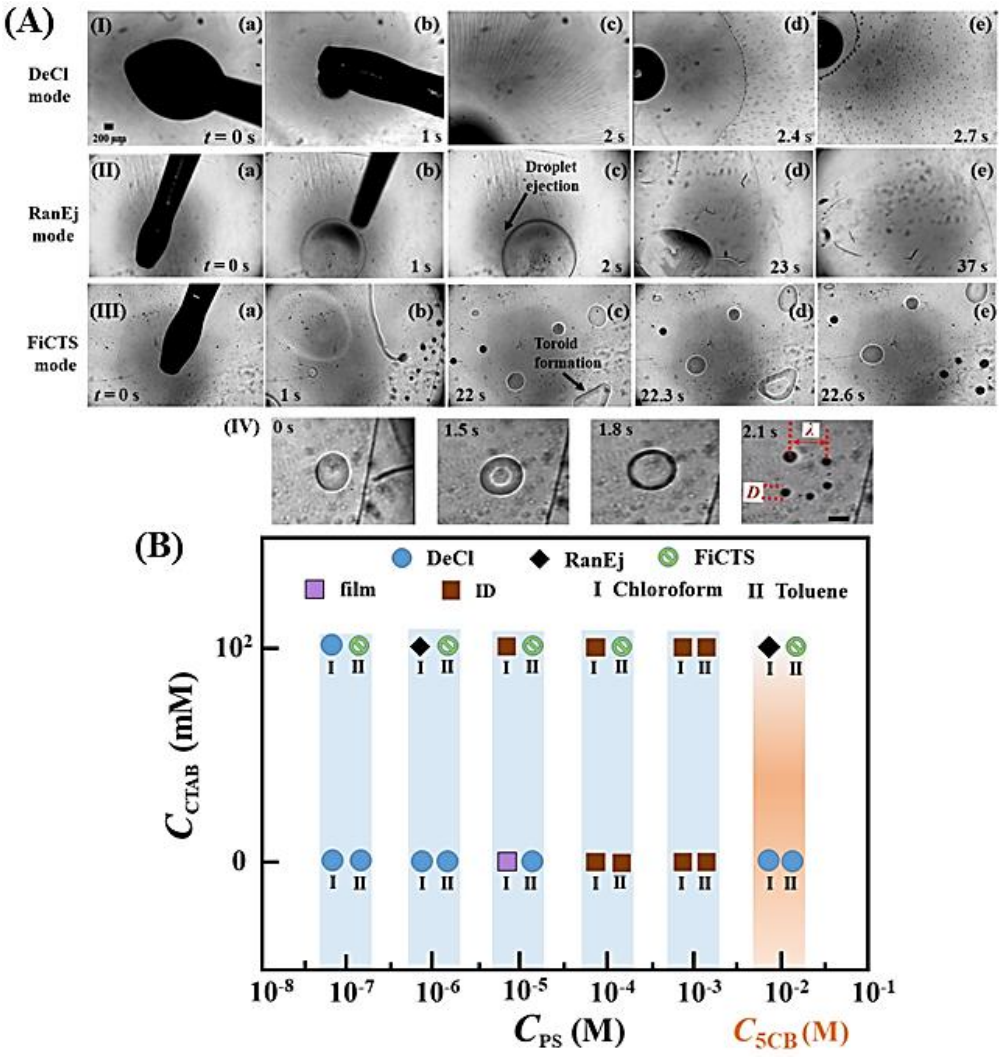

Figure 4.4 Different modes of droplet formation on a CTAB-water bath when the solvent used are hexane, chloroform, and toluene. The images I(a) – (e) showing the DeCI mode, II(a) – (e) showing the RanEj mode, and III (a) – (e) showing the FiCTS mode. (IV) Optical micrographs representing the different phases of toroid formation with the resultant droplet diameters highlighted as D_{LC} and the spacing between them as λ_{LC}. (B) Composite plot highlighting the different dewetting mechanisms presented by dewetting of a LC/SS droplet on a surfactant/no surfactant bath. Interestingly, similar dewetting mechanisms were also displayed by polystyrene/SS droplets, albeit at different concentrations. SS utilized were chloroform and toluene. Scale bar in the image is of 50 μm length.

If a summary is made from all the experiments performed with the different solvents and surfactants, we identify the presence of three distinct modes of droplet generation: (i) images (a) – (e) in the **Figure 4.4 (A) (I)** showing the one discussed in the previous section is termed as dewetting and contact line instability (DeCI) mode when the solvent is hexane; (ii) images (a) – (e) in the **Figure 4.4 (A) (II)** showing the random ejection (RanEj) mode when the solvent

is chloroform;[36] and (iii) images (a) – (e) in the **Figure 4.4 (A) (III)** showing the 'fire cracker' toroid splitting (FiCTS) mode when the solvent is toluene. The images clearly suggest that for the DeCI mode the droplet spread rapidly to form a film before the solvent evaporated and the TPCL retracted to stimulate the contact line instability. Subsequently, the film dewets while retracting contact line ejects an array of 5CB droplets.

In comparison, the RanEj mode (**Figure 4.4 (A) (II)**) shows that the 5CB-chloroform droplet does not spread and forms a lens because the droplet dimension has been more than its capillary length of ~ 4 μm. In such a scenario, the droplet is found to be under continuous self-propelling motion on the water-surfactant bath while ejecting an array of 5CB droplets through the TPCL.[62] In fact, the recoiling motion due to the asymmetry in the droplet ejection from the non-circular TPCL decides the direction of the movement of the primary droplet lens. The propulsion is found to be as high as 10 body-lengths per second while the droplet size is progressively reduced with the continuous ejection of the secondary droplets. The primary lens diminishes in size over a period of time with the random ejection of the secondary droplets. Notably, the bigger secondary droplets with adequate solvent further eject third and fourth generation of droplets. Thus, in under 40 s, one can observe droplets miniaturized by 6 orders of magnitude in volume, from 10^{-12} m^3 for 100 μm droplets to 10^{-18} m^3 for 1 μm droplets. Importantly, the frequency of random ejection of the droplets has been found to be very high ~200-300 Hz in the beginning while the same reduce to ~20-30 Hz near the end when the primary droplet size reduce. Finally, as chloroform evaporate, a collection of 5CB droplets are obtained on the water bath.

However, the most interesting and attractive one is the FiCTS mode (**Figure 4.4 (A) (III)** wherein the 5CB-toluene drop initially spreads rapidly to form a film with the simultaneous evaporation of the toluene from the matrix on a water bath with 100 mM CTAB. The 5CB-toluene droplet (10 mM) spread on the CTAB-water surface because S ~ 40 mN/m.[63] For droplets with diameter more than ~10 μm, capillary forces dominated the inertial forces, which results in the breakup of the stretched film into multiple droplets. In a way, the film dewets in parallel to contact line instability at the TPCL to form droplets, as observed in the case of DeCI mode. Since the vapor pressure of toluene is relatively lower (~1/7th of hexane) the dewetting happens for a longer duration. The daughter droplets also display a lateral and longitudinal motion on the soft and slippery water surface as the motion was assisted by the low interfacial tension of the bath. Interestingly, at the intermediate stage, the solvent rich droplets start forming metastable fluidic structures resembling 'donut' or 'toroidal' shapes as the solvent is progressively evaporated from the droplet matrix.[64] The spatiotemporal 'fission' of the

metastable donut and toroidal liquid structures also resemble the 'flower pot' shaped explosions of 'fire crackers' leading to the generation of an array of miniaturized droplets. Such breakup of toroidal structures on a slippery liquid surface can also be interpreted as a special case of Plateau-Rayleigh instability.[23] Interestingly, such explosions happen at all length scales – for the droplets with bigger to smaller sizes where there is adequate solvent present. For example, after ~ 4 s all droplets with dimensions below 400 μm display the FiCTS mode of droplet disintegration.

Figure 4.4 (A) (IV) shows the steps of hole and toroid formation and then the breakup into the droplets in the FiCTS mode. The figure suggests that, initially, the 5CB-droplet lens undergoes a faster evaporation of the solvent through the center of the droplet rather than the 'hidden' TPCL under the droplet lens, which facilitates the formation of the primary hole at the center. During this stage, the droplet expands to maximum normalized diameter, D_{max}/D_d ~ 1.8-1.9, before the hole appears. Here, D_{max} refers to the maximum droplet diameter before disintegrating and D_d refers to initial diameter of the particular droplet that is about to undergo dewetting. Subsequently, the metastable toroidal structure is created on the water bath, which has a pair of TPCL at the inner and outer rings.[65,64,66] The hole formed at the center of the droplet expand because the TPCL of the newly created inner ring tries to achieve equilibrium contact angle. Subsequently, the toroidal structure expands before undergoing a Plateau-Rayleigh instability to form droplets. The cascading effects of the FiTCS mode is evidenced through the self-organized breakup of first generation of the droplets to second generation one then into the third-generation ones and so on. Such droplet breakup leads to the reduction in the droplet diameter form ~100 μm to ~ 10 μm in ~ 2 s.

Importantly, the modes discussed in this section is not material-specific. **Figure 4.4 (B)** highlights the different kinds of interaction observed for the polystyrene-solvent (PS-SS) droplets interacting with CTAB-water bath. For PS, chloroform and toluene are selected as the Hansen solubility parameters for both solute and solvent is not too different.[67] The figure also maps the results of the 5CB-SS system to have a better clarity on the happenings. The plots suggest that at higher PS concentrations (C_{PS} ~ 10^{-3} M) an incomplete DeCI mode is observed for both the solvents on the 0 mM and 100 mM CTAB-water bath. However, at lower PS concentrations, RanEj mode is observed in chloroform when C_{PS} ~ 10^{-6} M and FiCTS mode is observed in toluene when C_{PS} ~ 10^{-7} to 10^{-4} M. Importantly, for the 5CB systems same happens at slightly higher LC loading (C_{LC} ~ 10^{-3} M). The plots (A) – (D) in the **Figure 4.5** show the typical reduction in the droplet diameter with time in the different solvents for both PS and 5CB. The plot (A) suggests that the 5CB droplets could reduce from ~ 200 μm until < 1 μm in

only 25 s. The sizes of the 5CB drops can further be reduced just by reducing the 5CB loading in the droplets.

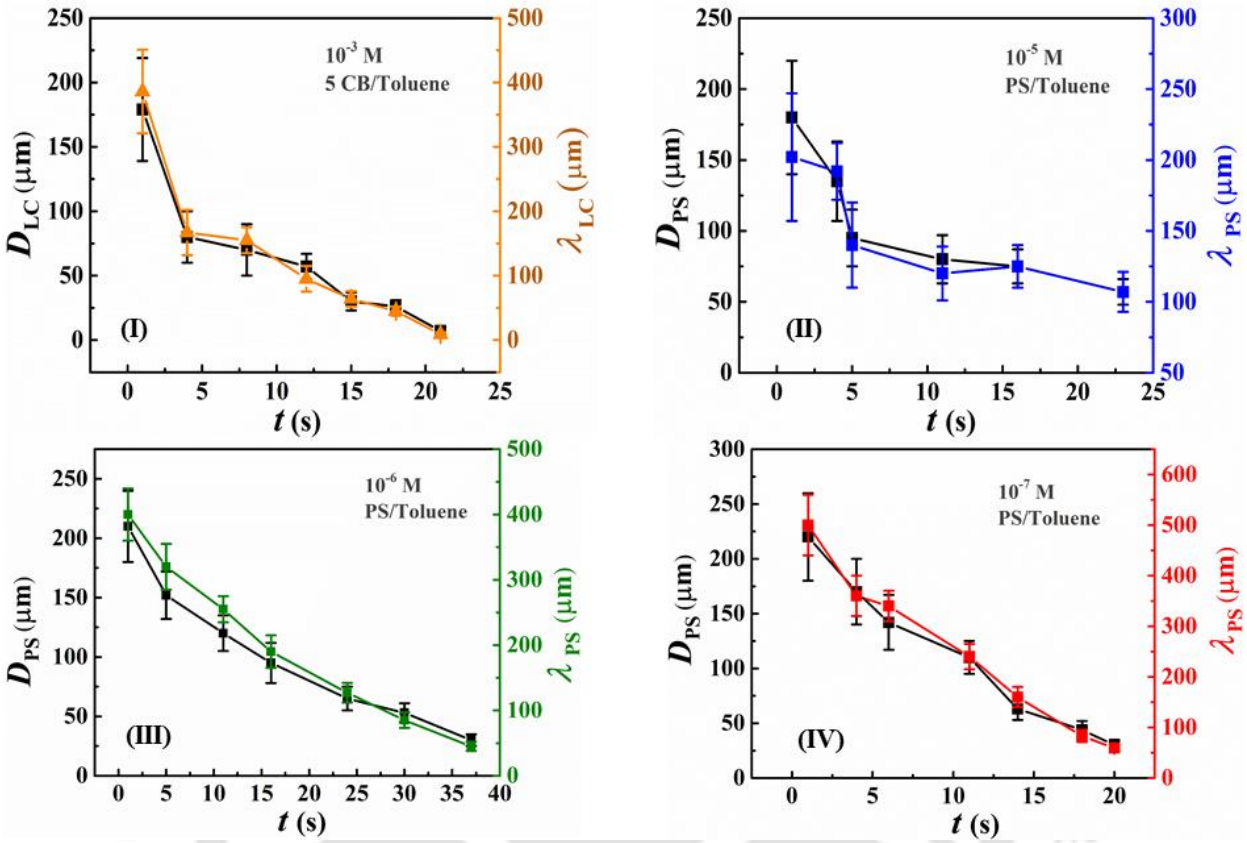

Figure 4.5. Plots (I) to (IV) shows the daughter droplet diameter and spacing for LC (D_{LC},λ_{LC}) and for PS (D_{PS}, λ_{PS}) profile representing the FiCTS dewetting mode. A 5CB mother droplet (10^{-3} M 5CB/hexane) and PS mother droplet (10^{-5} M to 10^{-7} M PS/toluene) was deposited on a 100 mM CTAB bath. Scale bar in the image is of 50 μm length.

For the PS/toluene system, a range of PS concentrations from 10^{-7} M to 10^{-5} M were observed in plots II, III and IV. The closest resemblance to the 5CB/hexane configuration in terms of D_{PS} and λ_{PS} was observed at a PS concentration of 10^{-6} M. It may be noted that from the experiments conducted, decreasing the PS concentrations led to a reduction in the D_{PS} value while it increased the λ_{PS} value. Diluting the solutions led to the reduction in the overall droplet viscosity which afforded more elasticity to the corresponding droplets on low IFT bath. This in turn facilitated higher spreading. Thinner films resulted in creation of smaller droplets with higher droplet spacing. Smallest droplets observed were ~ 5-10 μm in diameter. Overall, the modes reported in this section highlights the potential of the proposed methodology in the disintegration of the LC loaded solvent droplets into their miniaturized forms from nearly milliscale to the submicron scales within a minute. The study also shows that by maintaining

the surfactant loading on the water bath one can impose quasi-monodispersity to the size of the droplets, which can suitable for the SPL applications as disclosed below.

4.3.4 Application

4.3.4.1 Soft Photolithography

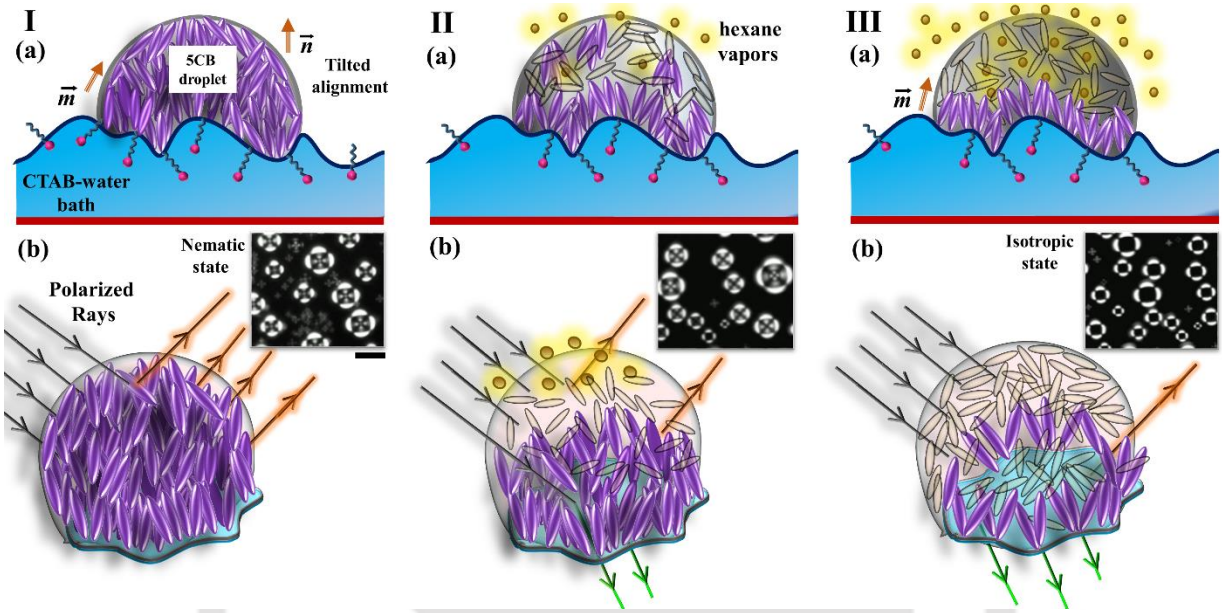

Figure 4.6 Solvent-vapor annealing of the 5CB droplets on the CTAB-water bath. Scheme I(a) shows a tilted alignment of nematogens in the bulk of the LC droplet while I(b) shows the isometric view of the same wherein the incoming polarized rays are reflected, as shown in by the POM inset. Scheme II(a) shows a partial phase-transition in the bulk of the droplet ensued upon solvent exposure while the same is unable to destroy the orientational order near the TPCL, as shown by the scheme II(b) and the respective POM inset. Scheme III(a) showing the complete destruction of the nematic order in the bulk through solvent vapor exposure while the retention of the same at TPCL, as shown by the scheme III(b) and the respective POM inset. In this case, the incoming rays passed through the bulk while reflected back from the TPCL as shown in the POM inset. For a 2 µl droplet on a 1 cm × 1 cm water bath, it takes ~ 15 s for the 5CB droplets to undergo a transition to an isotropic phase in the presence of the hexane solvent. Scale bar is of length 20 µm.

Employing the aforesaid methodologies, once the nematic 5CB droplets are decorated on the CTAB-water bath, they may possess different types of director orientation at the different parts of the droplet. For example, the 5CB molecules are expected to have a tilted or angular director orientation both at the free 5CB-air and confined 5CB-water soft interfaces.[68] Further, the polar- and weakly polar interaction between the surfactant and 5CB molecules at the 5CB-water interface is also expected influence such director orientations.[25,59] For example, at a higher surfactant concentrations, e.g., especially beyond CMC, a different type of tilted

orientation of the nematogens is expected near the interfacial region.[25,69] This may allow a more effective intermolecular interaction between the surfactant molecules and 5CB to lower the overall free energy at the interface.[69] In fact, prior-art suggest that the order parameter, $s = \frac{3}{2}cos^2\theta - \frac{1}{2}$, to be finite in such locations where θ is the angle between the long axis of the nematogen and director.[69] Importantly, the TPCL of the 5CB droplet may also have a different type of tilted director orientation with larger stability towards its orientation due to the preferential anchoring of the 5CB molecules at the contact line.[70]

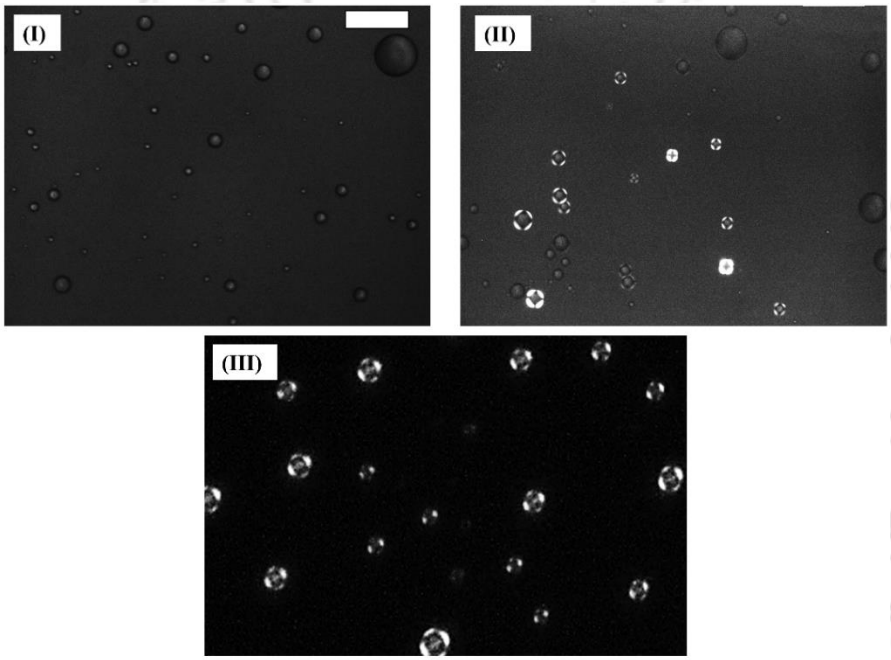

Figure 4.7 Effect of variation in CTAB concentration on the oil droplet texture. (I) At low CTAB concentration of 0.1 mM, no feature around the oil droplet boundary was visible at 10x magnification. (II) Under the same magnification, at higher CTAB concentration of ~ 0.7-1 mM, birefringence pattern around the oil droplet could be observed. (III) For 5CB (50 mM conc.) nematic droplets, however a different was obtained at the same CTAB concentration of ~ 0.7-1 mM. Scale bar is of length 50 µm.

Figure 4.6 shows the evidence of such hypotheses when such a 5CB laden water bath is exposed to the hexane vapor. In this figure, while the top row schematically shows the director orientation at the initial, intermediate and longtime vapor exposure, the bottom row shows the fate of a light exposure to the system. The insets show the respective POMs of the 5CB droplets floating on the water bath. The figures in the column (I) suggests that before the exposure the polarized lights are reflected by the 5CB droplets. The figures in the column (II) suggest that,

upon introduction of hexane vapor, a solvent vapor induced phase transition is initiated at room temperature.[71] At the intermediate stages, the droplet matrices allow a partial transfer of the light process in the 5CB droplets present on the CTAB-water layer was initiated. However, near the TPCL the 5CB molecules remain anchored even after a long-time exposure, as depicted by the images in the column (III). In such a scenario, the polarized lights could pass through the droplet matrix but reflected back from the TPCL. This results in the formation of transparent 5CB droplets with a reflective TPCL.

Control experiments are also performed using a sunflower oil droplet to check whether the "highly reflective" TPCL for isotropic materials. **Figure 4.7** shows the absence of such patterns for the isotropic materials confirming the property to be specific towards the LCs at low surfactant concentrations.[72] Experiments were performed to verify the origin of different optical textures within and around the 5CB droplet. Initially, for observing the effect of surfactant towards generating the various optical textures, 10 μL of sunflower oil droplets was dispensed on a 0.1 mM CTAB solution. No particular feature around the oil droplets could be observed under polarized optical microscope as shown in **Figure 4.7 (I)**. However, upon increasing the CTAB concentration to ~ 0.8 mM, the surfactant packing around the oil droplets displayed the characteristic birefringence pattern of that of 4-arc shaped structures in most of the oil droplet as shown in **Figure 4.7 (II)**. It must be noted that, under the same CTAB conc. of ~ 0.8 mM, 5CB droplets displayed a different droplet texture when compared to the oil droplets, as shown in **Figure 4.7 (III)**. The different molecular arrangement displayed by the nematogens in the bulk and around the 5CB droplet was a result of the interactions with the surfactant and water molecules. In the bulk, a radial alignment of the director existed whereas at the periphery a tilted alignment was present. LC packing of surfactants could also have contributed towards the reflective droplet boundary albeit at higher surfactant concentrations. In a way, the 5CB molecules anchored strongly at TPCL to retain the LC properties under the exposure of the hexane vapor while the same is lost in the droplet matrix, which eventually allowed the light to pass through the droplet matrix and reflect from the TPCL.

Subsequently, we employ such optically responsive droplets to be used as photomasks for creating 2-D and 3-D patterned features on the photoresist surfaces. Towards this end, experiments are performed utilizing a simple setup, which consists of a light source, a polarizer lens, a thin layer of CTAB solution dispensed on a cover slip, and the PR substrate. **Figure 4.8 (A)** presents the schematic diagram of the prepared unconventional PL setup. The light source (360 nm) is kept at a fixed distance of 15 cm from the photomask. The photomask unit consists of a cover glass (thickness ~ 110 μm) on which 200 μL of 1 mM CTAB/water solution is

dispensed. About 2 µL of 50 mM 5CB/hexane solution is then drop-casted on it, which results in the generation of a large array of 5CB droplets covering the entire substrate. The cover glass is softly placed on top of the PR coated Si wafer ensuring a proximity contact between them. Details regarding the PR spin coating process has been provided in the materials and methods section. The diffused light exposure intensity is fixed at 20 mW/cm^2 and a constant exposure duration of 50 s has been applied for both PR tones – +ve (S1813) and –ve (SU8 – 2002). The setup is kept on top of a platform with the surroundings constantly monitored to prevent any disturbance to the soft photomask layer.

Figure 4.8 (B) presents the optical pathway followed by the incoming radiations on their way from the LC droplet to the PR layer. The 5CB droplets has an effective refractive index (*n*) of ~ 1.6 [73,74] and thus could focus the incoming rays from the ambient surroundings, *n* ~ 1. The surrounding surfactant-water medium broaden the pathway of the incoming rays and direct them away from normal, due to the presence of a lower *n* ~ 1.33. The rays undergo a contraction towards the normal axis near the water-glass interface with *n* ~ 1.5. Focused rays eventually reach the PR layer and depending upon the nature of the PR layer generate the patterns on it accordingly. **Figure 4.8 (C)** shows the AFM profiles of the PPR layer in presence and absence of the fluidic photomasks. Image (I) *inset* presents the AFM profile of a developed substrate, which is exposed to UV-light in absence of any photomask placed on top. The details of the developing process of the PR substrate have been outlined in the materials and methods section. Since there is no photomask, the entire substrate is uniformly exposed, resulting in no particular feature formation. Image (I) highlights the profile of the etched PPR layer obtained in the presence of a photomask. Island-like structures (aspect ratio 1:13) on a large-scale are obtained that are spatially distributed throughout the substrate. Height distribution of the patterns are not exactly uniform and may have been caused due to uneven distribution of refracted light on the PR layer. The diverse size distribution of the droplets may have contributed towards non-uniform light exposure on substrate. The patterns generated are due to nature of the PPR layer itself. It may be noted that, the 5CB droplets remain in nematic phase at the air-water interface offering a radial configuration and are generally translucent in nature. They would have reflected most of the light falling on the droplets itself, while allowing the light to transmit through the remaining regions. This would have caused reduced light-induced exposure in droplet-covered areas, enhanced exposure in other regions, resulting in island-like structures.

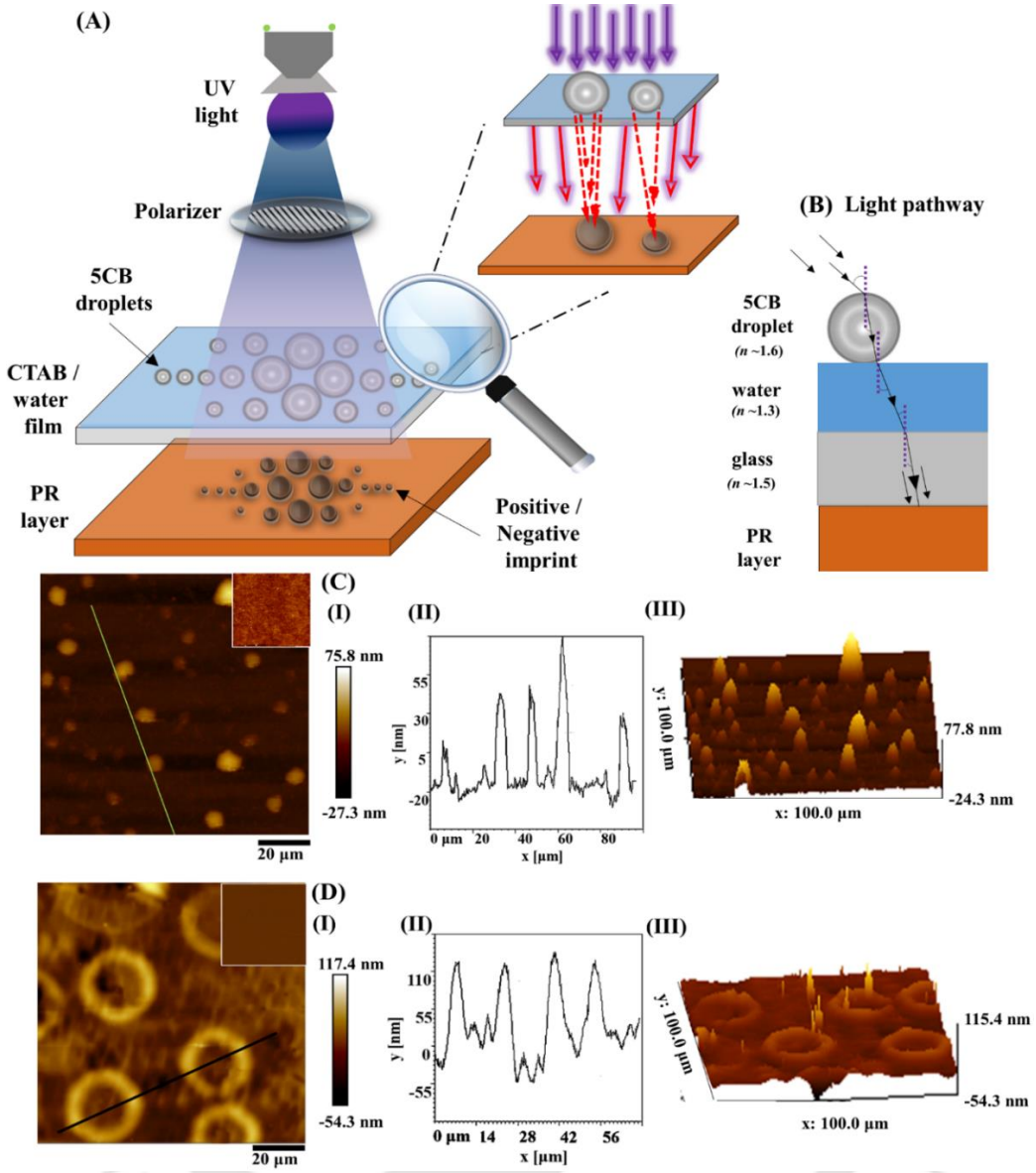

Figure 4.8 (A) Schematic diagram representing the fluidic lenses-enabled SPL process. (B) Optical pathway followed by the UV-light radiations from the LC droplet to the PR layer. Image (C) (I) depicts the topography of the modified PR surface in the presence of 5CB fluidic lenses. On +ve toned PR (S1813) substrates, pillar like features with an aspect ratio of 1:13 were generated. (*inset*) shows the topography of a blank PPR substrate that has been etched in absence of any fluidic lens. Image (II) shows A line profile (green-colored line on the image (I)) of the patterned substrate obtained during an AFM scan. Image (III) presents the 3D morphology of the respective image I. Image (D) (I) presents the topography of the modified NPR (SU8-2002) in presence of fluidic lenses. High-aspect ratio donut-like features were generated owing to the 5CB droplet sensitivity towards modulating the incoming radiations. (*inset*) presents the blank substrate etched in the absence of any 5CB lens. Image (II) shows A line plot (black line). Image (III) presents a 3D surface morphology of the respective image I. Light exposure intensity (20 mJ/cm^2) and exposure time (45s) was kept constant while the substrates were exposed to a UV light (360 nm) source from a distance of 11 cm.

The cross-sectional profile corresponding to the selected green line in **Figure 4.8 (C) (I)** has been provided in **Figure 4.8 (C) (II)**, which indicates an avg. height of 65 nm with a base of 2-4 µm over a 100 µm × 100 µm area. Moreover, **Figure 4.9** presents a Raman plot of the patterned substrate. Higher Raman intensity has been observed on the island structures as compared to the surrounding region, indicating a higher amount of material present.[75] Nematic 5CB droplet photomasks would have restricted the transmission of light through them, resulting in relatively higher exposure of the neighboring regions in the below PR surface with their eventual removal through developing process. This may have led to generation of island-like structures on the PR surface 3D profile of the obtained structures has been provided in **Figure 4.8 (C) (III)**. Multiple structures in a definite region correspond to the high-density of droplet-based masks.

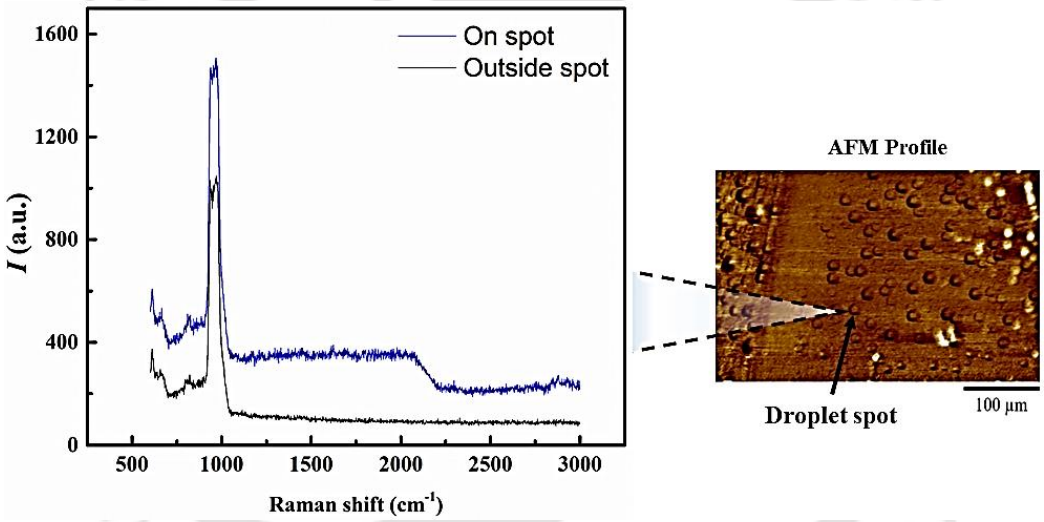

Figure 4.9 (*left)* Raman spectra of a +ve photoresist (S1813) surface highlighting the presence of etched patterns. Flattened-droplet structures produced a higher intensity as compared to the nearby etched surface. (*right*) AFM profile of the developed +ve PR surface, when it was etched in the presence of 5CB fluidic lens. Scale bar is of length 20 µm.

Figure 4.8 (D) highlights the profiles developed on the NPR substrate in the presence and absence of the droplet photomask. Image (I) *inset* presents the profile of the substrate developed in absence of droplet masks on top of it. **Figure 4.8 (D) (I)** presents the patterns obtained on the PR layer when LC droplets are utilized, which eventually lead to donut-like features with thick rims surrounding a receded central portion. Since the bulk of the nematic 5CB droplets allow the passage of light while the TPCL reflect back, a higher etch-out is observed near the zones where the light is pasting through the bulk while the formation of rim-like structures happen in the zones where the light reflects back from the TPCL.[23] **Figure 4.8 (D) (II)** shows

the plot having the line-profile of the patterned substrate across the selected black line, which also provides an aspect ratio of ~ 1:12 for the structures obtained. The 3D surface profile in **Figure 4.8 (D) (III)** offers a better visualization of the patterns obtained.

Experimental investigations have also been carried out to utilize the solvent vapor-induced phase-transition property of 5CB droplets for employing them as tunable photomasks. **Figure 4.10 (I)** depicts the schematic of the overall setup. A glass petridish is utilized to hold the LC droplets as photomasks and NPR film as well as containers of the solvent vapors are kept within the chamber as shown.

Following this, hexane vapor is introduced into the chamber to induce a phase transition in the 5CB droplets.[71] Although the change in 5CB phase occurs in few seconds, to prevent the disturbance in the liquid photomask layer due to Marangoni-driven motion, 3 min of exposure time has been provided. Subsequently, the polarized light rays are transmitted through the transparent enclosure and focused on the underlying layers. **Figure 4.10 (II) (A)** depicts the POM image of the nematic 5CB droplets, in absence of any solvent vapors within the chamber. **Figure 4.10 (II) (B)** presents the optical micrograph of multitude of island like features obtained on the NPR substrate. The patterns are obtained on a large-scale corresponding to the high density of the droplet photomasks. **Figures 4.10 (II) (C)** and **II (D)** present the 2-D and 3-D AFM profiles of the features present on the NPR substrate. Excessive light transmitted through the bulk of the nematic droplets results miniaturized island-like structures while the retention of the LC properties at the TPCL again restricts the light transmissions leading to the formation of 'castle moats' surrounding each island. After phase transition, similar experimental conditions were maintained to obtain features on the NPR. **Figure 4.10 (III) (A) s**hows the POM image of the isotropic 5CB droplet configuration. **Figure 4.10 (III) (B)** shows the optical micrograph of multitude of island like features obtained on the NPR substrate. **Figures 4.10 (III) (C)** and **III(D)** present the 2-D and 3-D profiles of the features obtained on the NPR substrate.

In another proof-of-concept experiment, large-area pattern surfaces are generated by varying the phase of 5CB droplet photomasks and directing the transmitted light onto the NPR surface via TEM grid. **Figures 4.10 (IV)** depicts the schematic of the experimental setup and the results obtained employing the modified setup. Utilization of a pre-patterned template such as TEM grid allowed for the creation of specific patterns on definite regions. **Figure 4.10 (V)** shows the schematic of the entire process.

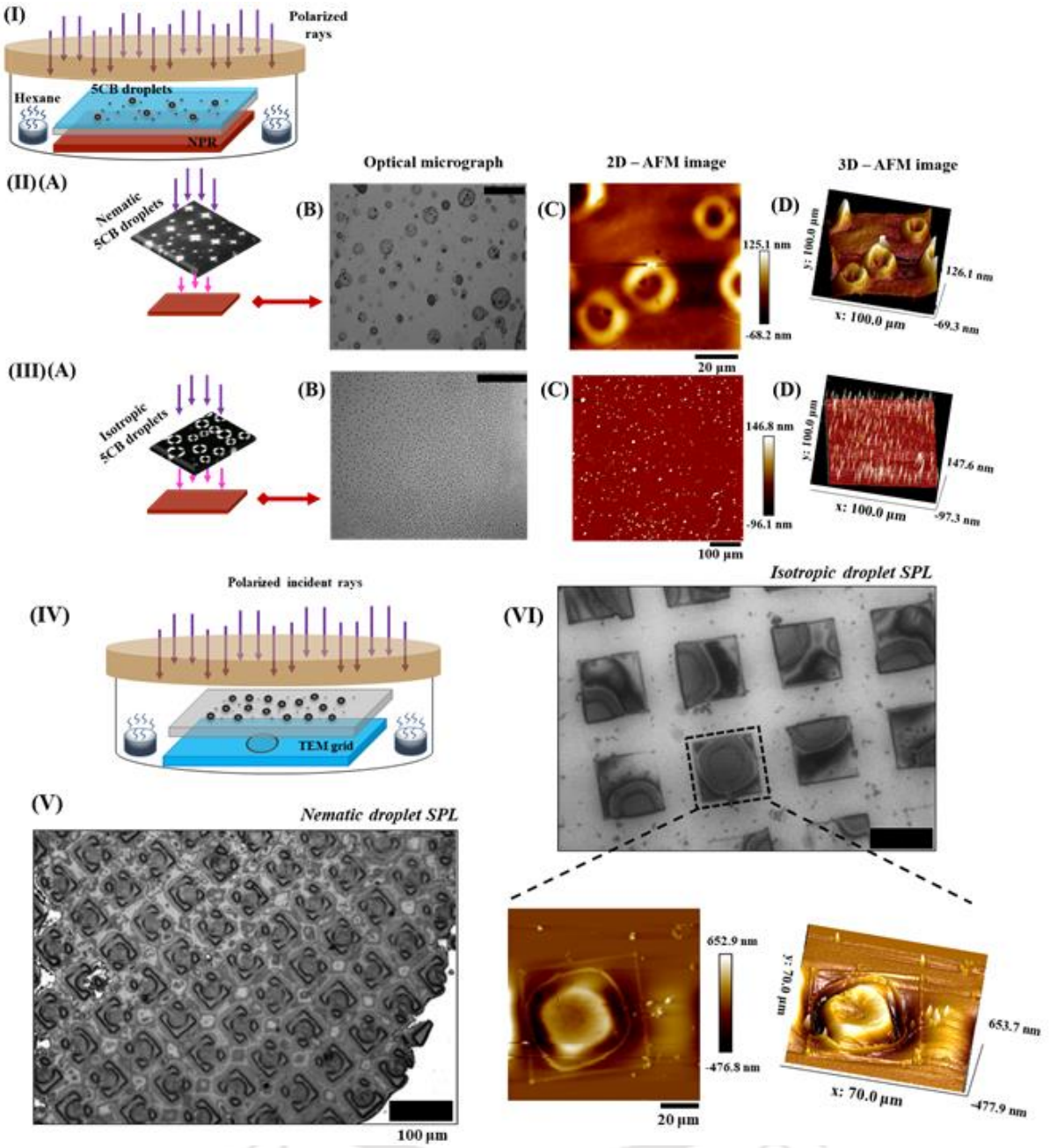

Figure 4.10 Effect of solvent-vapor annealing on the obtained patterns. (I) Schematic of the setup to perform SPL experiment on a NPR substrate. (II) Initially, the patterns are obtained in absence of any solvent vapor. (A) POM image of 5CB droplets possessing a radial configuration. (B) Optical micrograph of the pattern on the NPR substrate. (C) and (D) represent corresponding 2-D and 3-D AFM images. (III) In presence of hexane solvent, the 5CB droplets undergo a phase transition. (A) POM image of 5CB droplets in an isotropic state. (B) Optical micrograph of the patterns obtained with the photomasks in an isotropic phase. (C) and (D) represent the corresponding 2-D and 3-D AFM profiles of the patterns. Scale bar in images II (A) and III (A) correspond to 50 µm and 100 µm respectively. Effect of using TEM grids as pseudo-masks during solvent vapor annelaed SPL. (IV) Schematic of the overall setup wherein the incident polarized light passed through 5CB droplets and reached the NPR substrate as directed by the TEM grids. (V) Optical micrographs of the patterns obtained when the 5CB droplets were in the nematic phase. (VI) Optical micrographs of the patterns obtained

when the 5CB droplets were in the isotropic phase. (*bottom*) Corresponding 2D and 3D AFM profiles of patterned obtained in image (III). Scale bar for images (II) and (III) is 100 µm and 50 µm, respectively.

TEM grid was softly placed on the NPR surface, which was exposed to polarized rays from the above. **Figure 4.10 (VI)** shows the optical micrograph of patterns obtained on the TEM-grid masked region of the NPR substrate. Each square region of the grid was about 58 µm x 58 µm. The 5CB droplet photomask was generated by drop-casting a 2 µL droplet of 500 mM 5CB solution on a 10 mM CTAB-water bath. This resulted in generation of droplets of 45-60 µm diameter. Almost matching imprints of the droplets could be obtained within the square regions on the NPR substrate. **Figure 4.10 (VII)** (*top*) shows the optical micrograph of the patterns obtained in presence of solvent vapor annealing. Nematic to isotropic configuration resulted in altering the internal molecular order of the 5CB droplets, which allowed light to travel in a different orientation onto the NPR substrate. 2-D and 3-D AFM profiles for a particular grid has been shown in **Figure 4.10 (VII)** (*bottom*), where the altered topography attained in presence of the isotropic 5CB photomasks can be clearly observed. The central portion of the 5CB droplet allowed light to pass through which resulted in that particular area on the NPR substrate to be cross-linked, while at the edges the planar configuration along with the surfactant LC configuration, reflected incoming light which led to the grooves obtained upon developing.

4.3.4.2 Measurement of Order Parameter of LC

Amount of transmitted light is a function of the molecular order existing within the optically active 5CB droplets. While the nematic phase results in limited transmission of incident light owing to its translucent nature, isotropic state allows higher amount of transmitted light owing to its transparent nature. Experiments were performed to understand and analyze the differences in the obtained patterns on the account of different transmitted light intensity and orientation. **Figure 4.11 I (a)** and **(b)** presents the 2-D and 3-D AFM profiles of features obtained on a PPR substrate, in absence of any hexane vapor. Since limited light was transmitted across the nematic droplet photomasks, it resulted in over-exposure of outside droplet regions and under-exposure of regions beneath the droplets, lying on the PPR substrate. This led to generation of island like structures after developing. **Figure 4.11 (II)** presents the schematic of the overall process employed to quantify the variation in transmitted light intensity as a function of the hexane vapor annealing. Light dependent resistor (LDR) was utilized to capture the transmitted light and produce corresponding change in resistance.

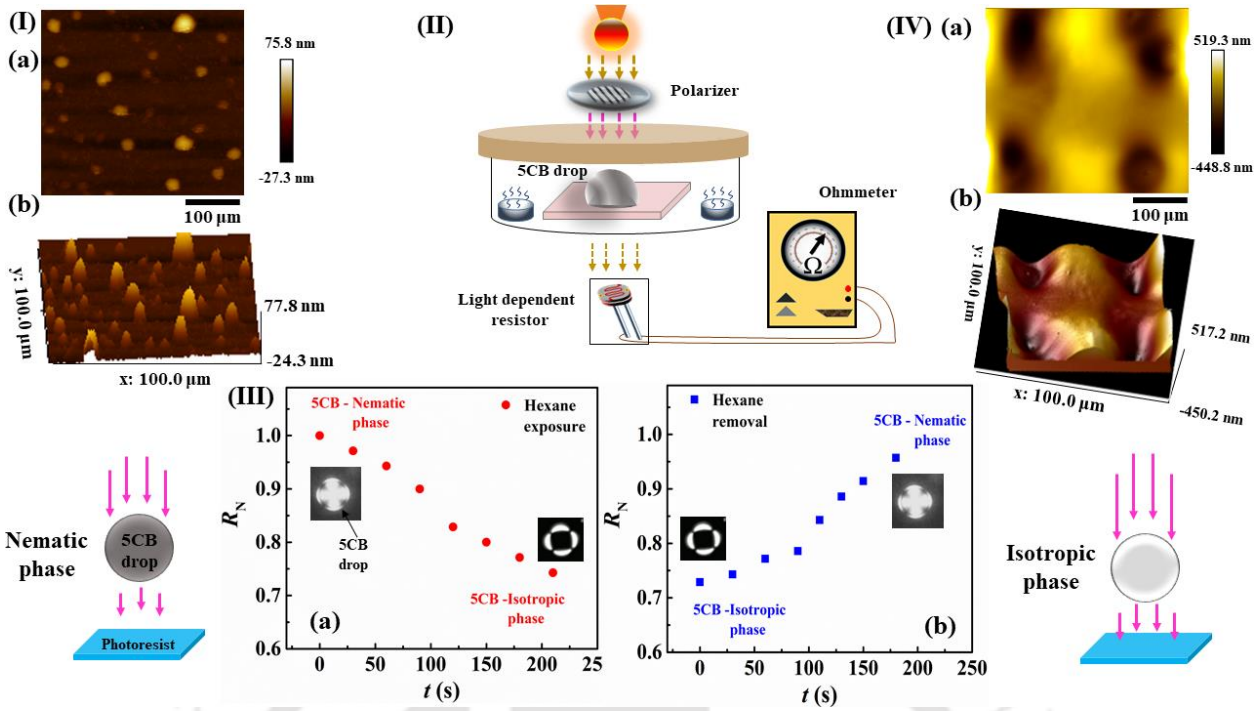

Figure 4.11 Variation in transmitted light intensity as a function of hexane vapor annealing of 5CB droplets. (I) (a) and (b) 2-D and 3-D AFM profiles of the patterns on the PPR substrate obtained during the nematic state of the 5CB droplet photomask. Patterns were obtained in absence of any solvent vapor annealing, and on the account of the limited light passing through the translucent, nematic 5CB drop. (II) Schematic of the setup utilized to assess the effect of solvent vapor annealing on the transmitted light intensity. The light passing through the 5CB drop interacted with the light dependent resistor (LDR), which resulted in generation of electrical current in the circuit. (III) (a) and (b) Plots showing the variation in normalized electrical resistance (R_N) in the circuit as a function of the solvent vapor annealing process. (IV) 2-D and 3-D AFM profiles of the patterns on the PPR substrate obtained during the isotropic state of the 5CB droplet photomask.

In order to analyze the output light intensity, two plots depicting the changes in electrical resistance across the LDR as a function of solvent annealing time were developed, as shown in **Figure 4.11 (III)**. Plot (a) presents the changes occurred when the 5CB droplet was converted from the nematic configuration to the isotropic configuration. The amount of transmitted light intensity increased with solvent exposure time, as it led to destruction of order within the 5CB droplet making it more transparent. This led to a gradual reduction in resistance across the LDR and hence, decreased the R_N value. Upon solvent removal, as the hexane vapors exited the isotropic droplet due to vapor pressure difference, molecular order gradually started to develop within the 5CB droplet and as a result the droplet's intensity reduced, as shown in the Plot (b). Changes in the light intensity as a function of the vapor annealing process resulted in drastically different patterns as depicted in **Figure 4.11 (IV)**. **Figure 4.11 IV (a)** and **(b)** presents the 2-D and 3-D AFM profiles of the features obtained on the PPR substrate, due to the isotropic configuration in the 5CB droplet photomask. Crater-like structures were obtained on the PPR

surface because of maximum light transmittance through the isotropic 5CB droplets and lensing effect of the 5CB droplets. Areas surrounding the crater-like structures on the PPR substrate were at a higher elevation (relatively less etched), probably owing to the reduced light transmittance from the reflective droplet boundaries. Furthermore, the better transmitted light intensity in the isotropic phase as compared to the nematic phase resulted in higher interaction with the underlying PR surface and consequently, led to higher aspect-ratio structures. The plot resembles the variation in the order parameters of a LC with temperature or solvent exposure.[76] The simple setup shown here highlight a method to experimentally measure the order parameter of an array of microdroplets of LC.

4.4 Conclusions

In summary, a liquid-on-liquid dewetting technique involving a 5CB-hexane droplet on a CTAB/water bath was employed for generation of an array of nematic 5CB droplets. The 5CB droplets were kinetically stabilized by internal LC ordering as well as external surfactant coverage. Two distinct ordering of the LC nematogens was observed within the 5CB droplets, in the bulk and at the periphery, owing to the presence of polar interactions with the surfactant medium. The 5CB-hexane droplet dewetting dynamics on the surfactant bath, involved inertia-dominated, rapid spreading of the TPCL on a low IFT surface until it reached equilibrium. Thereafter, solvent evaporation induced the change in S which led to the retraction of the TPCL. This facilitated large-scale droplet generation from the receding droplet periphery due to the CI instability over a soft, slippery interface. Additionally, it was observed that the sudden expansion of the 5CB-hexane droplet over the surfactant bath gave way to spinodal dewetting along with CI instability at low surfactant concentrations, and nucleation dewetting at high surfactant concentrations. Laminar retraction of the 5CB droplet leading edge over the surfactant bath was observed from $10^0<Re<10^2$, $10^{-6}<We<10^2$. Beyond this regime, turbulent conditions prevented analysis of the retracting edge. Control studies were also performed over the selection of SS and nature of surfactant. Finally, the potential of this system towards employing large-scale, tunable, optically active droplets as soft photomasks in PL setup was realized. Two kinds of PR substrates were selected, which after etching revealed different kinds of micron-scale features. Furthermore, solvent vapor annealing of the 5CB droplets modulated the internal structure of the droplets and controlled the amount of light transmitted through them. This provided another handle over development of unique 3-D patterns on the PR substrates. Interestingly, the 5CB droplet over the CTAB-water bath displayed various dewetting modes when other SS such as toluene and chloroform were employed. Moreover,

the dewetting mechanisms were not material-specific and were also observed in PS/SS mixtures over the CTAB-water bath. During the dewetting analysis, 5CB and PS toroids were also observed in presence of toluene as the SS.

References

(1) Martínez-Cuenca, R.; Saavedra, G.; Martínez-Corral, M.; Javidi, B. Extended Depth-of-Field 3-D Display and Visualization by Combination of Amplitude-Modulated Microlenses and Deconvolution Tools. *IEEE/OSA J. Disp. Technol.* **2005**, *1*, 321–326.

(2) Meng, X.; Lu, Y.; Yang, B.; Yi, G.; Jia, J. Fabrication and Photoelectrochemical Characteristics of the Patterned CdS Microarrays on Indium Tin Oxide Substrates. *ACS Appl. Mater. Interfaces* **2010**, *2*, 3467–3472.

(3) Peri-Naor, R.; Pode, Z.; Lahav-Mankovski, N.; Rabinkov, A.; Motiei, L.; Margulies, D. Glycoform Differentiation by a Targeted, Self-Assembled, Pattern-Generating Protein Surface Sensor. *J. Am. Chem. Soc.* **2020**, *142*, 15790–15798.

(4) Fan, X.; White, I. M. Optofluidic Microsystems for Chemical and Biological Analysis. *Nat. Photonics*. **2011**, *5*, 591–597.

(5) Giordano, M. C.; Sacco, F. Di; Barelli, M.; Portale, G.; Buatier De Mongeot, F. Self-Organized Tailoring of Faceted Glass Nanowrinkles for Organic Nanoelectronics. *ACS Appl. Nano Mater.* **2021**, *4*, 1940–1950.

(6) Thakur, S.; Rarotra, S.; Bhattacharjee, M.; Mitra, S.; Natu, G.; Mandal, T. K.; Dasmahapatra, A. K.; Bandyopadhyay, D. Self-Organized Large-Scale Integration of Mesoscale-Ordered Heterojunctions for Process-Intensified Photovoltaics. *Phys. Rev. Appl.* **2018**, *10*, 064012-064026.

(7) Xia, Y.; Whitesides, G. M. Soft Lithography. *Annu. Rev. Mater. Sci.* **1998**, *28*, 153–184.

(8) Ng, R.; Levoy, M.; Br, M.; Duval, G.; Horowitz, M.; Hanrahan, P.; Design, D. Light Field Photography with a Hand-Held Plenoptic Camera. *Stanford Tech Rep. CTSR* **2005**, *02*.

(9) Helmbrecht, M. A.; Srinivasan, U.; Rembe, C.; Howe, R. T.; Muller, R. S. Micromirrors for Adaptive-Optics Arrays. In *Transducers '01 Eurosensors XV*; Springer Berlin Heidelberg, **2001**.

(10) Yeow, T. W.; Eddie, K. L.; Goldenberg, A. MEMS Optical Switches. *IEEE Commun. Mag.* **2001**, *39*, 158–163.

(11) Symes, R.; Sayer, R. M.; Reid, J. P. Cavity Enhanced Droplet Spectroscopy: Principles, Perspectives and Prospects. *Phys. Chem. Chem. Phys.* **2004**, *6*, 474–487.

(12) Nagelberg, S.; Zarzar, L. D.; Nicolas, N.; Subramanian, K.; Kalow, J. A.; Sresht, V.; Blankschtein, D.; Barbastathis, G.; Kreysing, M.; Swager, T. M.; Kolle, M. Reconfigurable and Responsive Droplet-Based Compound Micro-Lenses. *Nat. Commun.* **2017**, *8*, 1–9.

(13) Zarzar, L. D.; Kalow, J. A.; He, X.; Walish, J. J.; Swager, T. M. Optical Visualization and Quantification of Enzyme Activity Using Dynamic Droplet Lenses. *Proc. Natl. Acad. Sci. U. S. A.* **2017**, *114*, 3821–3825.

(14) Serra, F.; Gharbi, M. A.; Luo, Y.; Liu, I. B.; Bade, N. D.; Kamien, R. D.; Yang, S.; Stebe, K. J. Curvature-Driven, One-Step Assembly of Reconfigurable Smectic Liquid Crystal "Compound Eye" Lenses. *Adv. Opt. Mater.* **2015**, *3*, 1287–1292.

(15) Hahm, S. G.; Ko, Y. G.; Rho, Y.; Ahn, B.; Ree, M. Liquid Crystal Alignment in Advanced Flat-Panel Liquid Crystal Displays. *Curr. Opin. Chem. Eng.* **2013**, *2*, 71–78.

(16) Meng, C.; Chen, E.; Wang, L.; Tang, S.; Tseng, M.; Guo, J.; Ye, Y.; Yan, Q. F.; Kwok, H. Color-Switchable Liquid Crystal Smart Window with Multi-Layered Light Guiding Structures. *Opt. Express* **2019**, *27*, 13098-14007.

(17) Kumar, M.; Kumar, S. Liquid Crystals in Photovoltaics: A New Generation of Organic Photovoltaics. *Polymer Journal.* **2017**, *49*, 85–111.

(18) Zhang, Y.; Weng, X.; Liu, P.; Wu, C.; Sun, L.; Yan, Q.; Zhou, X.; Guo, T. Electrically High-Resistance Liquid Crystal Micro-Lens Arrays with High Performances for Integral Imaging 3D Display. *Opt. Commun.* **2020**, *462*, 125299-125308.

(19) Kim, Y. H.; Yoon, D. K.; Jeong, H. S.; Lavrentovich, O. D.; Jung, H.-T. Smectic Liquid Crystal Defects for Self-Assembling of Building Blocks and Their Lithographic Applications. *Adv. Funct. Mater.* **2011**, *21*, 610–627.

(20) Zola, R. S.; Bisoyi, H. K.; Wang, H.; Urbas, A. M.; Bunning, T. J.; Li, Q. Dynamic Control of Light Direction Enabled by Stimuli-Responsive Liquid Crystal Gratings. *Adv. Mater.* **2019**, *31*, 1806172-1806180.

(21) Fang, M.; Lin, H.; Cheung, H. Y.; Xiu, F.; Shen, L.; Yip, S.; Pun, E. Y. B.; Wong, C. Y.; Ho, J. C. Polymer-Confined Colloidal Monolayer: A Reusable Soft Photomask for Rapid Wafer-Scale Nanopatterning. *ACS Appl. Mater. Interfaces* **2014**, *6*, 20837–2084.

(22) Lin, Y. H.; Wang, Y. J.; Reshetnyak, V. Liquid Crystal Lenses with Tunable Focal Length. *Liq. Cryst. Rev.* **2017**, *5*, 111–143.

(23) Kim, Y. H.; Lee, J.-O.; Jeong, H. S.; Kim, J. H.; Yoon, E. K.; Yoon, D. K.; Yoon, J.-B.; Jung, H.-T. Optically Selective Microlens Photomasks Using Self-Assembled Smectic Liquid Crystal Defect Arrays. *Adv. Mater.* **2010**, *22*, 2416–2420.

(24) Urbanski, M.; Reyes, C. G.; Noh, J.; Sharma, A.; Geng, Y.; Subba Rao Jampani, V.; Lagerwall, J. P. F. Liquid Crystals in Micron-Scale Droplets, Shells and Fibers. *J. Phys. Conden. Matter*. **2017**, *29*, 133003-133057.

(25) Dubtsov, A. V.; Pasechnik, S. V.; Shmeliova, D. V.; Saidgaziev, A. S.; Gongadze, E.; Iglič, A.; Kralj, S. Liquid Crystalline Droplets in Aqueous Environments: Electrostatic Effects. *Soft Matter* **2018**, *14*, 9619–9630.

(26) Popov, P.; Mann, E. K.; Jákli, A. Thermotropic Liquid Crystal Films for Biosensors and Beyond. *J. Mater. Chem. B*. **2017**, *5*, 5061–5078.

(27) Bolleddu, R.; Chakraborty, S.; Bhattacharjee, M.; Bhandaru, N.; Thakur, S.; Gooh-Pattader, P. S.; Mukherjee, R.; Bandyopadhyay, D. Pattern-Directed Phase Transitions and VOC Sensing of Liquid Crystal Films. *Ind. Eng. Chem. Res.* **2020**, *59*, 1902–1913.

(28) Ravi, B.; Bhattacharjee, M.; Ghosh, A.; Bandyopadhyay, D. Fabrication of Pixelated Liquid Crystal Nanostructures Employing the Contact Line Instabilities of Droplets. *Nanoscale* **2019**, *11*, 1680–1691.

(29) Ravi, B.; Chakraborty, S.; Bhattacharjee, M.; Mitra, S.; Ghosh, A.; Gooh Pattader, P. S.; Bandyopadhyay, D. Pattern-Directed Ordering of Spin-Dewetted Liquid Crystal Micro- or Nanodroplets as Pixelated Light Reflectors and Locomotives. *ACS Appl. Mater. Interfaces* **2017**, *9*, 1066–1076.

(30) Yin, Y.; Lu, Y.; Gates, B.; Xia, Y. Template-Assisted Self-Assembly: A Practical Route to Complex Aggregates of Monodispersed Colloids with Well-Defined Sizes, Shapes, and Structures. *J. Am. Chem. Soc.* **2001**, *123*, 8718–8729.

(31) Xu, T.; Xu, L. P.; Zhang, X.; Wang, S. Bioinspired Superwettable Micropatterns for Biosensing. *Chem. Soc. Rev*. **2019**, *48*, 3153–3165.

(32) Xia, Y.; Yin, Y.; Lu, Y.; McLellan, J. Template-Assisted Self-Assembly of Spherical Colloids into Complex and Controllable Structures. *Adv.Func. Mat.* **2003**, *13*, 907–918.

(33) Truzzolillo, D.; Cipelletti, L. Off-Equilibrium Surface Tension in Miscible Fluids. *Soft Matter*. **2017**, *1*, 13–21.

(34) Bates, C. M.; Stevens, F.; Langford, S. C.; Dickinson, J. T. Motion and Dissolution of Drops of Sparingly Soluble Alcohols on Water. *Langmuir* **2008**, *24*, 7193–719.

(35) Wyart, F. B.; Martin, P.; Redon, C. Liquid/Liquid Dewetting. *Langmuir* **1993**, *9*, 3682–3690.

(36) Pimienta, V.; Brost, M.; Kovalchuk, N.; Bresch, S.; Steinbock, O. Complex Shapes and Dynamics of Dissolving Drops of Dichloromethane. *Angew. Chemie Int. Ed.* **2011**, *50*, 10728–10731.

(37) Sharma, R.; Kalita, R.; Swanson, E. R.; Corcoran, T. E.; Garoff, S.; Przybycien, T. M.; Tilton, R. D. Autophobing on Liquid Subphases Driven by the Interfacial Transport of Amphiphilic Molecules. *Langmuir* **2012**, *28*, 15212–15221.

(38) Keiser, L.; Bense, H.; Colinet, P.; Bico, J.; Reyssat, E. Marangoni Bursting: Evaporation-Induced Emulsification of Binary Mixtures on a Liquid Layer. *Phys. Rev. Lett.* **2017**, *118*, 074504-074509.

(39) Yamamoto, D.; Nakajima, C.; Shioi, A.; Krafft, M. P.; Yoshikawa, K. The Evolution of Spatial Ordering of Oil Drops Fast Spreading on a Water Surface. *Nat. Commun.* **2015**, *6*, 1–6.

(40) Pahlavan, A. A.; Cueto-Felgueroso, L.; Hosoi, A. E.; McKinley, G. H.; Juanes, R. Thin Films in Partial Wetting: Stability, Dewetting and Coarsening. *J. Fluid Mech.* **2018**, *845*, 642–681.

(41) Scriven, L. E.; Sternling, C. V. The Marangoni Effects. *Nature* **1960**, *187*, 186–188.

(42) Berg, S. Marangoni-Driven Spreading along Liquid-Liquid Interfaces. *Phys. Fluids* **2009**, *21*, 032105-032111.

(43) Nagai, K.; Sumino, Y.; Kitahata, H.; Yoshikawa, K. Mode Selection in the Spontaneous Motion of an Alcohol Droplet. *Phys. Rev. E - Stat. Nonlinear, Soft Matter Phys.* **2005**, *71*, 065301-065310.

(44) Tran, K. T. M.; Nguyen, T. D. Lithography-Based Methods to Manufacture Biomaterials at Small Scales. *J. Sci-Adv Mater. Dev.* **2017**, *2*, 1–14.

(45) French, R. H.; Tran, H. V. Immersion Lithography: Photomask and Wafer-Level Materials. *Annu. Rev. Mater. Res.* **2009**, *39*, 93–126.

(46) Chowdhury, F. A.; Chau, K. J. Variable Focus Microscopy Using a Suspended Water Droplet. *J. Opt.* **2012**, *14*, 055501-055509.

(47) Saien, J.; Gorji, A. M. Simultaneous Adsorption of CTAB Surfactant and Magnetite Nanoparticles on the Interfacial Tension of N-Hexane–Water. *J. Mol. Liq.* **2017**, *242*, 1027–1034.

(48) Wodlei, F.; Sebilleau, J.; Magnaudet, J.; Pimienta, V. Marangoni-Driven Flower-like Patterning of an Evaporating Drop Spreading on a Liquid Substrate. *Nat. Commun.* **2018**, *9* , 820-830.

(49) Sharma, A. Auto-Optimization of Dewetting Rates by Rim Instabilities in Slipping Polymer Films. *Phys. Rev. Lett.* **2001**, *87*, 166103-166110.

(50) Bäumchen, O.; Marquant, L.; Blossey, R.; Münch, A.; Wagner, B.; Jacobs, K. Influence of Slip on the Rayleigh-Plateau Rim Instability in Dewetting Viscous Films. *Phys. Rev.*

Lett. **2014**, *113*, 014501-014510.

(51) Tixier, T.; Heppenstall-Butler, M.; Terentjev, E. M. Spontaneous Size Selection in Cholesteric and Nematic Emulsions. *Langmuir* **2006**, *22*, 2365–2370.

(52) Chavepeyer, G.; Salajan, M.; Platten, J. K.; Smet, P. Interfacial Tension and Surface Adsorption in I-Heptanol/Water Systems. *J. Colloid Interface Sci.* **1995**, *174*, 112–116.

(53) Bąk, A.; Podgórska, W. Interfacial and Surface Tensions of Toluene/Water and Air/Water Systems with Nonionic Surfactants Tween 20 and Tween 80. *Colloids Surfaces A Physicochem. Eng. Asp.* **2016**, *504*, 414–425.

(54) Saien, J.; Rezvani Pour, A.; Asadabadi, S. Interfacial Tension of the N-Hexane-Water System under the Influence of Magnetite Nanoparticles and Sodium Dodecyl Sulfate Assembly at Different Temperatures. *J. Chem. Eng. Data* **2014**, *59*, 1835–1842.

(55) Kargupta, K.; Sharma, A. Creation of Ordered Patterns by Dewetting of Thin Films on Homogeneous and Heterogeneous Substrates. *J. Colloid Interface Sci.* **2002**, *245*, 99–115.

(56) Yilixiati, S.; Wojcik, E.; Zhang, Y.; Sharma, V. Spinodal Stratification in Ultrathin Micellar Foam Films. *Mol. Syst. Des. Eng.* **2019**, *4*, 626–638.

(57) Kargupta, K.; Konnur, R.; Sharma, A. Instability and Pattern Formation in Thin Liquid Films on Chemically Heterogeneous Substrates. *Langmuir* **2000**, *16*, 10243–10253.

(58) Woodward, J. T.; Schwartz, D. K. Dewetting Modes of Surfactant Solution as a Function of the Spreading Coefficient. *Langmuir* **1997**, *13*, 6873–6876.

(59) Kulkarni, S.; Thareja, P. Experimental Study of Surfactant Driven Nematic Liquid Crystal (NLC) Anchoring Transitions at Solid Surfaces: Role of Solid Surface Energy and Anisotropic NLC - Solid Interfacial Energy. *J. Adhes. Sci. Technol.* **2016**, *30*, 1371–1390.

(60) Niu, X.; Luo, D.; Chen, R.; Wang, F.; Sun, X.; Dai, H. Optical Biosensor Based on Liquid Crystal Droplets for Detection of Cholic Acid. *Opt. Commun.* **2016**, *381*, 286–291.

(61) Brake, J. M.; Mezera, A. D.; Abbott, N. L. Effect of Surfactant Structure on the Orientation of Liquid Crystals at Aqueous-Liquid Crystal Interfaces. *Langmuir* **2003**, *19*, 6436–6442.

(62) Tadmouri, R.; Micheau, J. C.; Pimienta, V. Autocatalysis in Liquid/Liquid Surfactant Transfer. *Soft Matter* **2011**, *7*, 8741–8744.

(63) Saien, J.; Asadabadi, S. Synergistic Adsorption of Triton X-100 and CTAB Surfactants at the Toluene+water Interface. *Fluid Phase Equilib.* **2011**, *307*, 16–23.

(64) Pairam, E.; Vallamkondu, J.; Koning, V.; Van Zuiden, B. C.; Ellis, P. W.; Bates, M. A.; Vitelli, V.; Fernandez-Nieves, A. Stable Nematic Droplets with Handles. *Proc. Natl. Acad. Sci. U. S. A.* **2013**, *110*, 9295–9300.

(65) Kumar, S.; Ghosh, A.; Chaudhuri, J.; Timung, S.; Dasmahapatra, A. K.; Bandyopadhyay, D. Self-Organized Spreading of Droplets to Fluid Toroids. *J. Colloid Interface Sci.* **2020**, *578*, 738–748.

(66) Brown, R. A.; Scriven, L. E. The Shape and Stability of Rotating Liquid Drops. *Proc. R. Soc. London. A. Math. Phys. Sci.* **1980**, *371*, 331–357.

(67) García, M. T.; Gracia, I.; Duque, G.; Lucas, A. de; Rodríguez, J. F. Study of the Solubility and Stability of Polystyrene Wastes in a Dissolution Recycling Process. *Waste Manag.* **2009**, *29*, 1814–1818.

(68) Kim, J.; Khan, M.; Park, S. Y. Glucose Sensor Using Liquid-Crystal Droplets Made by Microfluidics. *ACS Appl. Mater. Interfaces* **2013**, *5* (24), 13135–13139.

(69) Uline, M. J.; Meng, S.; Szleifer, I. Surfactant Driven Surface Anchoring Transitions in Liquid Crystal Thin Films. *Soft Matter* **2010**, *6*, 5482–5490.

(70) Kulkarni, S.; Thareja, P. Surfactant Induced Interfacial Anchoring Transitions In Nematic Liquid Crystal Droplets On Glass Surfaces. *Surf. Rev. Lett.* **2017**, *24*, 1750044-1750060.

(71) Ravi, B.; Mukherjee, R.; Bandyopadhyay, D. Solvent Vapour Mediated Spontaneous Healing of Self-Organized Defects of Liquid Crystal Films. *Soft Matter* **2015**, *11*, 139–146.

(72) Engels, T.; Von Rybinski, W. Liquid Crystalline Surfactant Phases in Chemical Applications. *J. Mater. Chem.* **1998**, *8* (6), 1313–1320.

(73) Pan, R. P.; Hsieh, C. F.; Pan, C. L.; Chen, C. Y. Temperature-Dependent Optical Constants and Birefringence of Nematic Liquid Crystal 5CB in the Terahertz Frequency Range. *J. Appl. Phys.* **2008**, *103*, 093523-093531.

(74) Tkachenko, V.; Marino, A.; Abbate, G. Study of Nematic Liquid Crystals by Spectroscopic Ellipsometry. *Mol. Cryst. Liq. Cryst.* **2010**, *527*, 80/[236]-91/[247].

(75) Hsia, B.; Kim, M. S.; Vincent, M.; Carraro, C.; Maboudian, R. Photoresist-Derived Porous Carbon for on-Chip Micro-Supercapacitors. *Carbon N. Y.* **2013**, *57*, 395–400.

(76) Ranjkesh, A.; Choi, J. C.; Park, J. S.; Park, M. K.; Kiani, S.; Zakerhamidi, M. S.; Kim, H. R. Order Parameter and Crossover Temperature from Temperature-Dependent Refractive Indices for Low Birefringence Liquid Crystals. *J. Mol. Liq.* **2017**, *230*, 280–289.

Chapter 05

Chemotactic Dewetting of a Nematic Droplet on a Water Bath

This manuscript is under preparation and is titled as “Thakur, S.; Vanarse, V; Dasmahapatra, A. K.; Bandyopadhyay D. Chemotactic Dewetting of a Nematic Droplet on a Water Bath.”

Abstract

Dewetting of anisotropic liquids such as liquid crystal (LC) presents a facile and rapid pathway for realizing large-scale, self-organized optically active droplets. This study uncovers the striking fluid dynamics associated with a 5CB droplet in presence of a hexane droplet on a water bath. Hexane interaction with the 5CB droplet leads to genesis of a number of instabilities. Solutal Marangoni driven recirculation in the droplet bulk is observed. A pair of vortices form primarily and grow with time, on one half of 5CB droplet as it experiences an asymmetrical exposure to hexane source. The recirculation rate grows with time due to increasing surface tension gradient between bulk and surface. Beyond a critical rate, the centripetal forces generated as a result momentarily dominate the surface tension forces and lead to droplet distortion. This leads to a cessation of the vortices and restoration of the circular droplet periphery, leading to initiation of another such cycle. Another effect of hexane interaction concerned the 5CB droplet motility on the water bath. Beyond a critical water volume in the bath, the gradient in the spreading coefficient across the 5CB droplet three-phase contact line initiates 5CB droplet movement in direction of high surface tension. The convective flow in the underlying water bath as a result of recirculation in the 5CB droplet assists the droplet motility towards hexane source. Consequently, hexane droplet was observed to move away from the 5CB droplet. An additional instability manifestation was also observed near the leading edge of the 5CB droplet. As the 5CB droplet spreading occurs, hexane evaporation rate increases and it results in localized change in interfacial tension value. 5CB droplet retraction over the water bath is induced. This enforces the setting up of capillary instability at the leading edge which results in generation of numerous miniaturized 5CB droplets. The influence of Marangoni stresses as additional destabilizing forces is reflected in finger spacing (λ) to droplet diameter (R_{5CB}) ratio analysis. Influence of temperature variation in water bath on the recirculation rate is also analyzed. Existence of thermal Marangoni stresses encourages higher recirculation rate while reducing the recirculation time period. Furthermore, increasing the polarity of the underlying also increases the recirculation rate as enhanced electrostatic interactions stabilizes droplet periphery.

5.1 Introduction

Liquid droplets at the air-water interface display a variety of striking behaviour due to asymmetrical variation in the interfacial properties as a result of change in the external field. Notable examples include attractive capillary interaction between neighbouring droplets due to "Cheerios effect",[1] chemical gradient driven surfactant-stabilized systems [2,3] and evaporation-induced thermocapillary driven autonomous systems.[4] Not surprisingly, the distinct motion displayed by droplets on the surface have been considered towards a variety of applications such as cargo carriers,[5] self-sustained cleaners,[6] microfluidic mixers,[7] self-aligning liquid-lens,[8] and triboelectric energy generators.[9,10] Furthermore, these fluidic elements have also prompted extensive research towards obtaining a fundamental understanding of, (a) the self-propelled active objects with their dynamical, collective behaviour,[11,12] and (b) methods designed towards self-organization at the meso-scale.[13,14]

The interface between two immiscible fluid phases is never at rest. Any change in the surface curvature is accommodated by a proportional change in the interfacial tension. Of late, increasing number of works have focused on uncovering the mechanisms associated with the genesis of interfacial gradient due to: thermal[15,16], surface-active agent[17] and solutal effects[7,18]. It may be noted that any change in the surface tension results in development of shear stress that is enforced on the bulk fluid, leading to its flow. This movement of layers due to the change in chemical potential of the system is commonly referred to as Marangoni-driven flow.[12,19] Solutal driven Marangoni (SM) flows have found utility in different applications of late such as volatile organic contaminants detection[20], energy harvesting[21], and droplet sorting[8]. This method of engendering convective flows within the droplets does not require much additional conditions such as thermal gradients or surfactants, and also does not lead to droplet contamination.[22] In this regard, droplets of isotropic materials such as water have been extensively studied.[2,3,11] Distinct recirculation dynamics initiated by the SM effect have been observed in pure water droplet based-systems as well as surfactant-laden droplets.[2] In order to visualize and quantify the recirculation in the liquid bulk due to SM driven effects, studies concerning utilization of liquid crystal (LC) droplets have been reported.[23]

Active emulsions employing LC droplets are primary candidates for studies that focus on uncovering fundamental mechanisms of self-propelled droplets undergoing symmetry breaking. In a related study, surfactant moieties were introduced to LC droplets in a microchannel and the ensuing dynamics associated with collective motion of the LC droplets was analysed[23]. Individual LC droplets dissolved near the three-phase contact line following a

micellar pathway that engendered an interfacial tension gradient leading to droplet motility. Furthermore, due to the birefringence nature of 5CB droplets the dynamic interactions with the surfactant moieties were observed due to variation of director field within droplets.[24] These systems highlight the importance of anisotropic emulsions that aid in visualization of flow fields developed in presence of an external field gradient.

Identification of diverse drop fragmentation pathways is critical for the design of systems incorporating pristine or complex droplets. These droplets are routinely utilized in applications such as pharmaceuticals[25], food and beverage industries[26] as well as in fundamental analysis for mimicking biological and artificial systems such as synthetic cells[27], membraneless organelles[28] and microbots[29]. Current approaches towards droplets generation includes high energy intensive methods such as mechanical homogenization[30], and low-energy emulsification processes including droplet-based microfluidics[31], bubble bursting[32] and phase inversion[33]. Latter set of techniques are particularly useful towards large-scale droplet generation as they allow large-scale droplet generation via minimal consumption in terms of interfacial shearing of confined liquids[34] and usage of nanoparticles-stabilized emulsions[33].

Of late, unconventional approaches such as wetting transition induced self-emulsification of multi-phase bilayer system[35], condensation of water vapor onto subcooled oil/surfactant solutions[36], thermally stimulated breakup of liquid droplets into smaller dimensions[37], and evaporation induced Marangoni flows in compound droplets can lead to formation of 2D assemblies of microdroplets[38]. These techniques possess the potential for translation to bigger platforms as they provide a facile and rapid approach towards large-scale production of miniaturized droplets. Certain limitations of these methodologies such as utilization of complex, multi-component phase-separating mechanisms and inclusion of secondary volatile component does necessitate the need for further research. However these works inspires development of novel techniques that employ a quick, controlled disintegration of pristine droplets without any contamination[39,40].

As mentioned earlier, utilization of techniques that employ dewetting of a liquid layer on another wetting/partially wetting soft, deformable substrates offer certain advantages in comparison to utilization of solid substrates[41,42]. Reduced resistance to inertial-dominated flow of top layer (subphase) and absence of contact line pinning allows rapid spreading of subphase such that minor disturbances in the three-phase contact line, such as gradient in interfacial tension, can lead to onset of instabilities[43]. Furthermore, presence of a net variation in the spreading co-efficient across the droplet periphery may lead to an autonomous motion of droplet driven by gradient in chemical potential. Hence, this pathway can be utilized to

supplement complex, expensive techniques employed to generate miniaturized compound reactors[44] or anisotropic lenses[45], thereby providing a facile and scalable route.

In the present work, we explore the dynamics associated with the chemotacticity-driven dewetting of a 5CB droplet in presence of a hexane droplet, on a water bath. In the vicinity of the volatile solvent drop, solutal-Marangoni driven recirculation are engendered in the bulk of the 5CB droplet whilst at its TPCL, an oscillatory contact line instability (CLI) is established. The latter phenomenon succeeds the 5CB droplet spreading on the water bath. The leading edge of the 5CB droplet undergoes CLI and eventually breaks up into numerous miniaturized LC droplets. Extensive experimental investigations have been carried out in order to uncover the recirculation dynamics in bulk and CLI, which occur at the leading edge. These phenomena result from the interplay of solutal-Marangoni effects and wetting transition at the TPCL, both of which are induced by rapid evaporation of hexane. Experimental investigations involving effects of 5CB droplet volume, hexane droplet volume, height, polarity and temperature of underlying water bath, on the rate of recirculation and corresponding droplet motility over water bath have been performed.

5.2 Materials and Methods

5.2.1 Materials

4-Cyano-4'-pentylbiphenyl (5CB) was purchased from Sigma Aldrich, India. Ammonia, hydrogen peroxide (30% v/v), hexane, ethanol and acetone were purchased from Merck, India. The AR grade chemicals were directly used for experiments without any further purification. Glass petridish (45 mm diameter) was supplied from Borosil. Milli-Q grade water was employed to prepare the bath and for cleaning the glassware.

5.2.1.1 Characterization

Surface morphologies were characterized by an optical microscope (Leica, DM 2500 upright microscope, with polarized optical microscopy (POM) mode). Thermal imaging of the droplet systems was performed using infrared (IR) camera.

5.2.2 Methods

5.2.2.1 Spreading of 5CB droplet on a water bath in presence of hexane

Initially a glass petridish was filled with 2 mL DI water. A 2 μL drop of 5CB was dispensed on the water bath. The drop spread to a limited amount owing to the presence of a positive spreading coefficient (*S*, 14 mN/m). Thereafter, a 10 μL hexane droplet was deposited in the vicinity of 5CB droplet at an edge-to-edge distance of ~ 1.5 mm. Due to favorable *S* value for

hexane (2 mN/m), it wetted the water surface and reduced the distance between the leading edge of two droplets. Furthermore, due to a relatively high volatility rate of hexane, its vapors were adsorbed relatively faster on the front-facing 5CB droplet region. As a result of the change in 5CB droplet surroundings, different types of instabilities set in the 5CB droplet. Within a period of 2-3 s, a pair of recirculation sets in the 5CB droplet on the account of solutal Marangoni effect. Thereafter, due to increasing rate of recirculation and occurrence of a net *S* value across the droplet periphery, beyond a certain water level in the bath, droplet motility over the liquid substrate was observed. Furthermore, at the 5CB droplet region nearest to the hexane source, the three-phase contact line expanded and contracted in a non-monotonous manner. The spreading of the 5CB droplet interface gave way led to thinning of the LC film which underwent capillary instability. Subsequently, threads of LC columns destabilized and underwent dewetting to give way to generation of numerous daughter droplets. Thus, a facile method for generation of large-area, miniaturized optically active droplets was achieved. The various stages of the 5CB dewetting process were recorded under a POM microscope (Leica DM 2500) attached with a high-speed resolution digital camera (Fastcam Mini UX100, Photron Ltd.)

5.3 Results and Discussion

5.3.1 The Phenomenon

Figure 1 presents the overall schematic of the phenomenon. Initially, experiments were carried out in order to explore the dynamic interactions between a LC droplet and solvent droplet on a soft, slippery interface. A 2 µL 5CB droplet dispensed on a DI water bath, underwent spreading owing to Laplace pressure gradient as well as a favorable spreading co-efficient (*S*, ~ 11 mN/m) as shown in **Figure 5.1 (I) (A) - (C)**. Thereafter, a 10 µL hexane droplet was dispersed such that droplet-to-droplet distance was < 2 mm. Ambient conditions such as relative humidity of ~80% and temperature 21°C were maintained throughout the analysis.

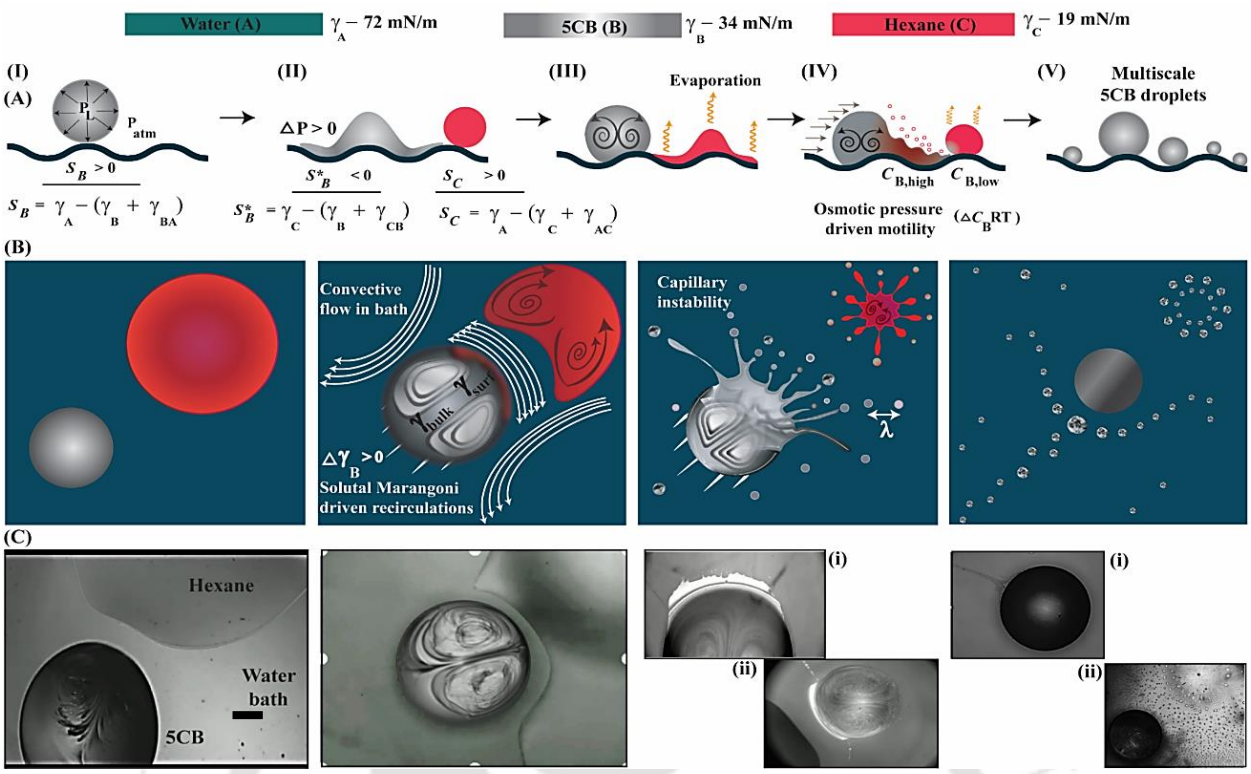

Figure 5.1 Schematic diagram depicting the entire phenomenon. (I) (A) A 5CB droplet on a water bath undergoes spreading due to Laplace pressure difference and favourable *S*. (II) (A) Hexane droplet undergoes spreading due to similar reasons. However, the 5CB droplet undergoes change in *S* due to interaction with hexane and retracts. (III) (A) As hexane evaporates, its vapor gets adsorbed on 5CB surface and solutal Marangoni driven recirculation is set in. (IV) (A) After interaction with the hexane droplet, the 5CB droplet also undergoes a convective motion on water bath due to osmotic pressure gradient. (V) (A) Enhanced spreading of 5CB droplet on water bath, due to reduction in interfacial tension results in generation of miniaturized droplets from the contact line. (I) – (V) (B) represents the different stages of the dewetting phenomenon schematically from a top view. (I) – (V) (C) POM imaging of different stages of 5CB droplet (2 µL) with hexane droplet (10 µL) on a water bath (5 mL). Scale bar in the image is 500 µm.

Hexane spreading on water surface disrupted the 5CB contact line equilibrium such that a retraction in its periphery was observed, due to change in the *S* (4 mN/m) as shown in **Figure 5.1 (II) (A)**. Additionally, due to its high vapor pressure, hexane droplet started evaporating almost immediately. The time scale for sensing of the hexane vapors by 5CB droplet (t_{sense}) was ~ 1-2 s for a 2 µL 5CB droplet on a 2 mL water bath, as $t_{sense} = \frac{d^2_{BTW}}{D_{hexane\text{-}air}}$. Here, d_{BTW} is the distance between the 5CB droplet and hexane droplet and $D_{hexane\text{-}air}$ is the diffusivity of hexane in air. Thus, within 1-2 s, recirculation sets in the 5CB droplet due to the solutal-Marangoni effect as hexane vapors were adsorbed on the 5CB droplet. An asymmetrical hexane exposure led to preferential adsorption of vapors on one-half of the 5CB droplet that was facing the

hexane droplet. This resulted in formation of two vortices within the bulk, which facilitated the movement of 5CB moieties from a region of low-surface tension near the periphery to a region of high surface-tension in the bulk, as depicted in **Figure 5.1 (III) (A)**. The reduction in surface tension was further caused by interaction of the 5CB droplet contact line with the hexane layer on water bath, which led to the formation of an osmotic pressure gradient.

The recirculation rate beyond a certain value, along with the presence of an osmotic pressure gradient, initiated droplet motility on the water bath as presented in **Figure 5.1 (IV) (A)**. Recirculation in the 5CB droplet, led to the viscous dissipation in the water bath which facilitated the 5CB droplet motion, as shown in **Figures 5.1 (II) (B) - (C)**. The 5CB droplet movement was in the direction of the hexane droplet, which in turn, was seeming to move away from the 5CB droplet. The movement of the water layers in the opposite direction (to the direction of recirculation in 5CB droplet) engendered a movement of the water bath such that the hexane droplet was pushed away. As the 5CB droplet was approaching the hexane droplet (due to osmotic pressure gradient), the underlying water bath caused the hexane droplet to move in an opposite direction. Interestingly, the reduction in interfacial tension near the three-phase contact line (TPCL) of the 5CB droplet facing hexane, facilitated its spreading on the water bath. This resulted in the distortion of the droplet geometry in that region as droplet curvature prevented resisted deformation of the TPCL. Increase in the surface area of the 5CB film facilitated faster evaporation of hexane. This led to the change in the *S* near the TPCL such that a droplet retraction phase was observed. The receding TPCL underwent capillary instability that led to the generation of daughter 5CB droplets, as observed in **Figures 5.1 (III) (B) and 5.1 (III) (C) – (i)**, **(ii)**.

Miniaturized 5CB droplets could also be generated from the initial 5CB droplet resulting in a final volume reduction of ~ 10^{-12} m^3. Hence, this technique presented a controlled pathway for the generation of a large number of miniaturized nematic 5CB droplets as depicted in **Figures 5.1 (IV) (B) – (C) and 5.1 (V) (A)**. It may also be noted that, since hexane had initially spread on the water bath, its contact with 5CB droplets also allowed to enrich itself with LC moieties. It is well known that 5CB is highly miscible in hexane.[20] Thus, when the hexane droplet evaporated on the water bath, it left behind multitude of 5CB droplets which were also generated from the TPCL due to capillary instability. POM images of the different stages of the process have been shown in **Figures 1 (I)** – **(IV) (C)**. for the system consisting of a 2 μL 5CB droplet and a 10 μL hexane droplet on the water bath. The distance between the 5CB and hexane droplets played a vital role in sustaining the phenomenon. If the distance between the two droplets was more than ~ 5 mm, no recirculation was observed to set-in with no apparent

5CB droplet motility. However, if the droplets were dispensed such that both contacted, coalescence of both drops occurred due to high degree of solubility of 5CB in hexane.

5.3.2 Effect of Varying Bath Volume on Recirculation Rate

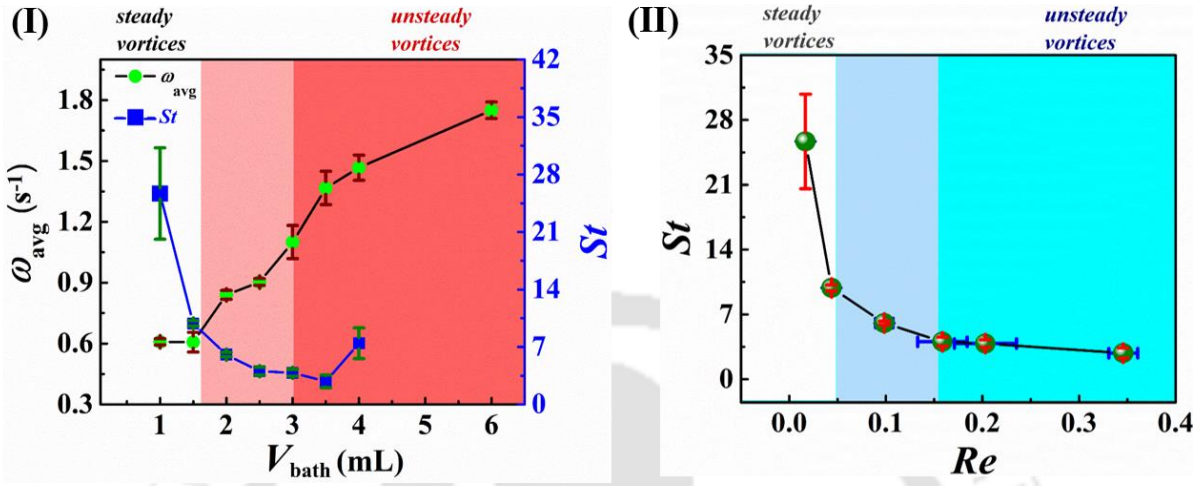

Figure 5.2 Average recirculation velocity (ω_{avg}) within the 5CB droplet varies with volume of water in underlying bath. (I) Change in the nature of recirculation from steady to unsteady occurs. The modified Strouhal number (*St*, $St = \omega_{avg} D_{5CB,M} / V_{avg}$) also increases as ω_{avg} increases with increase in V_{bath} for a fixed 5CB droplet diameter. (II) Plot depicting the variation in *St* as a function of Reynolds number (*Re*, $Re = \rho_{5CB} V_{avg} D_{5CB,M} / \mu_{5CB}$). Unsteady vortices are characterized by larger ω_{avg} values. Beyond *Re* 0.15, unsteady vortices are generated.

The water level in the bath had an influence on the 5CB droplet motility. Changing the volume of water in the container (corresponding water level height, *H*) led to varying rates of droplet motility, as shown in **Figure 5.2 (I)**. At smaller V_{bath} values, droplet ω_{avg} was limited as well as the average droplet velocity V_{avg} on the water bath was also low. With rise in the V_{bath} value from 1 to 6 mL, ω_{avg} value increased from 0.6 s^{-1} to 1.8 s^{-1}. Also, V_{avg} value increased from 0.07 mm/s to 1.54 mm/s for corresponding rise in water amount from 1 to 4 mL. Beyond 4 mL, V_{avg} calculation was challenging as the droplet displayed erratic motion. Enhancement in the droplet recirculation velocity due to solutal Marangoni effect was captured by the reduction in the advection time-scale ($t_{advection} = \frac{R_{5CB,M}}{V_{avg}}$). Here, $R_{5CB,M}$ refers to the radius of mother 5CB droplet. Reduction in $t_{advection}$ was observed from ~21 s to ~ 1 s, as V_{bath} increased from 1 mL to 4 mL.

It may be noted that the change in *H* affected the viscous dissipation in the underlying water bath due to the recirculation in the 5CB droplet. For a 2 µL 5CB droplet in presence of a 2 µL hexane droplet on a 2 mL water bath, the sustained movement of the 5CB droplet was observed

between 33-38 s. Flow in the water bath develops close to the lower surface of the 5CB droplet, from a boundary layer thickness of $\delta(t) \sim \sqrt{(vt)}$, where v is the kinematic viscosity of water. For H ~ 5 mm (V_{bath} ~ 2 mL), δ reaches H within a time period of ~ 35 s. This period reduced gradually to ~ 5 s, as H increased to 12 mm (V_{bath} ~ 6 mL). At low water levels in the container, movement of water just beneath the rotating 5CB droplet was impeded due to influence of boundary layer near the glass substrate. Since the motion was restricted, flow capable of initiating 5CB droplet movement on the water layer could not be established. However, with rising water levels, the recirculation within the 5CB droplet induced faster movement of water layers such that a flow could be developed in the water bath. As the recirculation within the 5CB droplet stopped, the 5CB droplet motility also ceased.

Furthermore, variation in the S between the two halves of 5CB droplet (droplet facing side and droplet back side) led to the disturbance of equilibrium near the TPCL. A net positive value of S such that $\int_0^{2\pi} S\, d\theta \gg 0$ (θ being the central angle), caused the movement of the 5CB droplet in the direction of low surface tension towards the hexane droplet.[7] The convective flow within the water bath assisted the 5CB droplet motion such that with increasing volume of water, higher values of V_{avg} were observed. Interestingly, the increase in recirculation rate beyond a critical value led to the disruption in the droplet geometry as the centripetal forces overcame the surface tension forces. The sudden expansion of the droplet was followed by an instantaneous restoration of droplet shape as the recirculation ceased and surface tension forces prevailed. This transition from steady to unsteady vortices was observed beyond 1.5 mL water in the bath (~ 4 mm water column). This transition in the nature of recirculation was also characterized with the aid of dimensional analysis.

Parameters such as mother 5CB droplet diameter ($D_{5CB,M}$), average recirculation rate (ω_{avg}), recirculation velocity (V_{5CB}), 5CB density (ρ_{5CB}) and 5CB viscosity (μ_{5CB}) [46] were employed to obtain dimensionless numbers such as modified Strouhal number ($St, St = \frac{\omega_{avg} D_{5CB,M}}{V_{avg}}$) and Reynolds number ($Re, Re = \frac{\rho_{5CB} V_{avg} D_{5CB,M}}{\mu_{5CB}}$). In the beginning, the St decreased with increase V_{bath} as the average flow velocity of 5CB droplet, V_{avg}, increased. However, beyond the $\omega_{avg,critical}$ an increment in the St was observed owing to the enhanced V_{avg} values. V_{bath} (> 4 mL) facilitated rapid recirculation as well as droplet motility in seemingly random manner, such that it was challenging to calculate St value. **Figure 5.2 (II)** highlights the transition from steady to unsteady vortices, as the Re increased with increasing V_{bath}. Higher ω_{avg} within the

5CB droplet induced the droplet motility over the water bath. This further aided in increasing the inertial forces of the 5CB droplet such that it could overcome the drag. Moreover, beyond $\omega_{avg,critical}$, since the droplet was unable to withstand the centripetal forces generated by the recirculation, it led to disruption of the droplet geometry as was observed at higher *Re* numbers. As mentioned earlier, with increase in V_{bath} the ω_{avg} increased until it reached a critical point. Beyond this point, as the 5CB droplet was unable to maintain its shape, it distorted at the droplet end nearest to the hexane droplet. The recirculation within the 5CB droplet gradually increased owing to the dynamic change in the surface tension gradient between the 5CB droplet surface and the bulk, as depicted in the plot of **Figure 5.3**. The number of recirculation (N_R) increased with time and reached a maximum at the $\omega_{avg,\,critical}$. As a limited region of the droplet expanded due to imbalance in surface tension and centripetal forces, it instantaneously went back to its original shape. The droplet curvature and *S* prevented in the distortion of the 5CB droplet geometry on the "other half", such that a limited portion of the 5CB droplet was destabilized. As the droplet expanded and contracted, the N_R value within the recirculation ceased to exist. The peak of chemical to mechanical energy manifestation was attained as the 5CB droplet expanded due to increase in the inertial forces. As soon as the droplet expanded, there was an imbalance of recirculation within the droplet and net magnitude of centripetal forces decreased. This was immediately followed by the contraction stage as the surface tension forces overcame leading to cessation of the recirculation and restoration of the circular geometry of the 5CB droplet. Gradually the cycle repeated as the surface tension gradient was again established because of the recirculation. With time, the N_R value decreased as the 5CB droplet started to saturate with hexane. This not only reduced the surface tension gradient across the 5CB droplet but also led to the transition from nematic to isotropic phase.

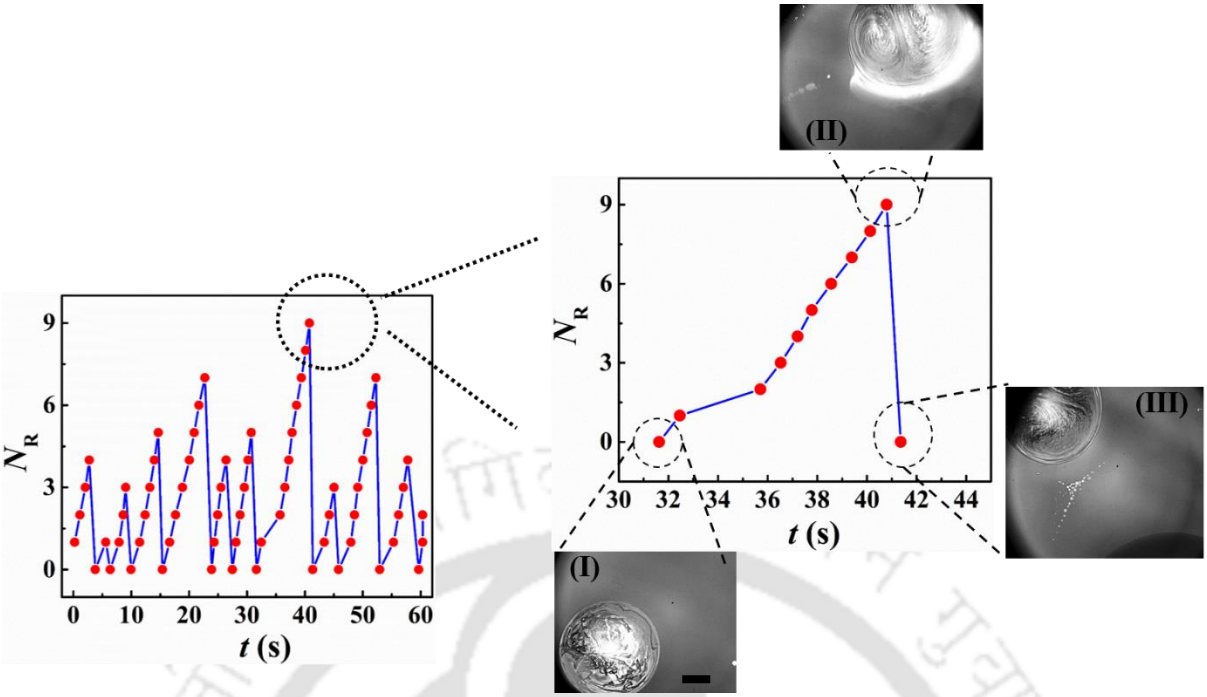

Figure 5.3 Nature of recirculation within 5CB droplet. N_R within a definite period increases with time as more vapor gets adsorbed on the surface. Image (I) presents the POM image of a 5CB droplet (2 µL) in absence of hexane droplet (10 µL). Once hexane droplet is deposited in its vicinity, ω_{avg} increases as does N_R. Beyond a $\omega_{avg,critical}$ value, at max. N_R, sudden distortion in droplet geometry occurs as shown in image (II). Image (III) presents the 5CB droplet state at the beginning of another cycle. Scale bar is of length 500 µm.

5.3.3 Effect of Varying 5CB and Hexane Volume on Recirculation Rate

Experiments were also carried out to understand the effect of fixed vapor amount on the recirculation rates when the volume of 5CB droplets were increasing. **Figure 5.4 (I)** presents the plot depicting the variation in the ω_{avg} with V_{5CB}. It was observed that for a fixed hexane droplet volume (2 µL), increasing the 5CB droplet volume led to a gradual reduction in the ω_{avg}. For smaller 5CB droplet (1-2 µL) the hexane vapor concentration in its vicinity was sufficient to generate high recirculation rates. As the V_{5CB} increased, and since the amount of hexane was definite, higher resistance in the form of diffusion and viscous forces in the bulk of the 5CB droplet, prevented the establishment of high recirculation rates. This was also evident as the time of recirculation also reduced with increasing V_{5CB}. It was also observed that there was a steady rise in the *St* with increasing V_{5CB}. This would have occurred due to increase in the droplet dimensions as well as reduction in the V_{avg}. The bulk droplet velocity reduced with increasing V_{5CB} as lesser magnitude of surface tension gradient was attained within the droplets due to limited amount of hexane vapor. The hexane vapor penetration in to the bigger droplets would have reduced due to diffusion-based mass transfer resistance.

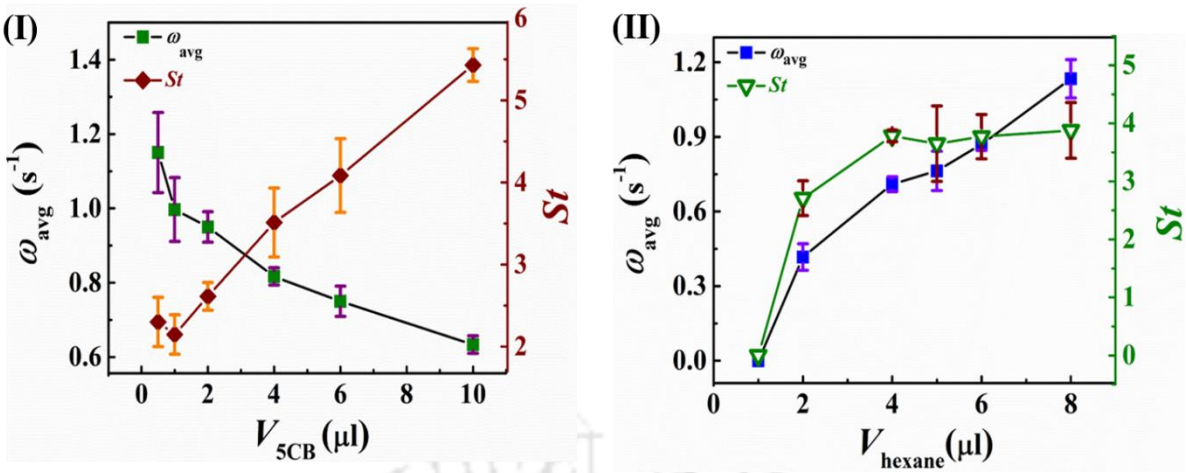

Figure 5.4 Effect of varying 5CB droplet volume on rate of recirculation for a fixed hexane droplet volume. (I) Plot shows the variation in ω_{avg} with initial 5CB volume. Increasing the droplet volume, increases the resistance to recirculation in the form of inertial forces. A limited increase in *St* is observed owing to the increment in droplet diameter and reduction in bulk droplet velocity (II) Increasing the hexane droplet volume assists in the recirculation as the change in surface tension gradient is enhanced due to higher availability of hexane. Simultaneous increment in *St* takes place for a fixed 5CB droplet volume as ω_{avg} increases.

In order to elaborate the effect of increasing 5CB droplet radius on the solutal-Marangoni driven recirculation a simple mathematical model was utilized.[7,47] Initially, hexane vapor concentration in air (C_{hex}) was determined using a steady-state Poisson diffusion equation. Few assumptions were made while solving: hexane vapor propagated along the radial direction along the water bath due to its relatively large molecular weight; region for diffusion was half as the droplet was asymmetrically exposed to hexane vapor, this subsequently led to doubling of vapor concentration near 5CB droplet facing side; and, point source of hexane vapor led to representation of the equation in spherical co-ordinates. Schematic diagram of the setup is presented in **Figure 5.5**. Thus, the concentration profile obtained at z=0 is,

$C_{hex}(x,y) = \frac{1}{2}\frac{C^0_{hex} \times 2R_{hex}}{\sqrt{(d+R_{5CB}-x)^2+(y)^2}}$, where C^0_{hex} is initial hexane concentration near hexane droplet, R_{hex} is radius of hexane droplet and L is the distance between 5CB droplet and hexane droplet (assumed to be a constant value of ~ 2 mm). For purpose of simplification, G (= $\sqrt{(d+R_{5CB}-x)^2+(y)^2}$), is used to represent the gap between the point source and 5CB droplet. The concentration equation satisfies conditions $C_{hex} = 0$ as $G \rightarrow \infty$ and $C_{hex} = C^0_{hex}$ as $G \rightarrow R_{hex}$. From the experiments it was observed that the recirculation in the 5CB droplet were observed mostly in regions marginally larger than one-half of the droplet, facing the point source. Thus,

the modified concentration equation is $C^* = C^0_{hex} \times R_{hex}\left(\frac{1}{L} - \frac{1}{\sqrt{(L+R_{5CB})^2+(R_{5CB})^2}}\right)$, where C^* is the concentration gradient between 5CB droplet periphery and centre. Estimation of the C^0_{hex} was obtained using Dalton's law and the value was ~ 0.61 kg/m^3 at NTP.

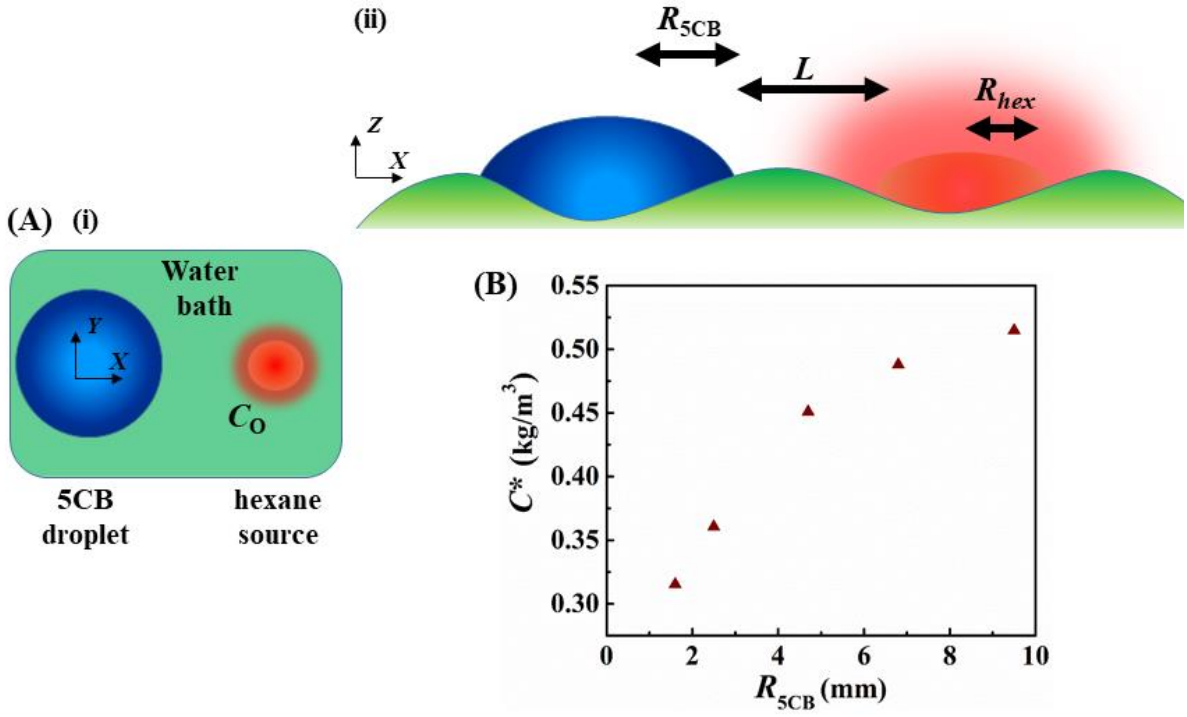

Figure 5.5 (A) (i) Schematic diagram of experimental setup. Hexane source kept close to 5CB droplet has an initial concentration of C_o (~ 0.65 kg/m^3) in air. (ii) The hexane source (having a radius R_{hex}) is dispensed at a distance L from the 5CB droplet (having a radius R_{5CB}). (B) Plot of concentration gradient of hexane at 5CB surface (C^*) as a function of 5CB droplet radius.

It may be noted that in this study the value of *Re* within the 5CB droplet is usually < 1. Hence, the forces generated due to solutal-Marangoni effect ($\frac{\Delta\gamma}{R^2_{5CB}}$) were balanced by the viscous forces within the 5CB droplet ($\frac{\mu V_{5CB}}{hR_{5CB}}$), where $\Delta\gamma$ is the change in surface tension at 5CB surface and $\boldsymbol{h_{5CB}}$ is the droplet height.[47] Plot of $V_{5CB,\ calc}$ with $\Delta\gamma$ variation could not be constructed as parameters linked to it such as diffusion co-efficient of hexane in 5CB, constants defining hexane conc. gradient-surface tension relationship of 5CB, are unavailable in literature. However, variation in C^* with R_{5CB}, provides a demonstrative idea of the phenomenon.

Figure 5.5 (A) depicts the droplets arrangement on the water bath. C_o represents the hexane concentration in air close to source. The different parameters such as C_o, L, R_{5CB} and R_{hex} have

been represented in **Figures 5.5 (A) (i) and (ii)**. As the hexane evaporated into the air, its concentration close to the source droplet was highest. With gradually increasing distance its concentration varied due to diffusion in air. As a result, increasing the radius of the 5CB droplet, increased the gap between the 5CB droplet centre and 5CB droplet surface, where hexane concentration was highest. The variation in the hexane concentration gradient existing at the 5CB droplet surface has been shown in **Figure 5.5 (B)**. Hence, with increasing R_{5CB}, the surface tension gradient required to generate recirculation increased. However, a reduced ω_{avg} was observed with V_{5CB}, since the hexane vapor had to diffuse through a larger distance in order to initiate the movement of layers, which also faced resistance due to viscous forces.

Another set of experiments were carried out to determine the effect of increasing solvent vapor amount on the ω_{avg} when the 5CB droplet volume was fixed at 2 μL. To begin with, no recirculation was observed in the 5CB droplet in the absence of any hexane source. As the V_{hexane} increased, the ω_{avg} also started to rise and displayed a direct relationship with the volume of hexane droplet. From experimental findings it was revealed that presence of a minimum V_{hex} of 2 μL was required for ~ 3-4 s at L of 2 mm, to initiate the recirculation in a 2 μL 5CB droplet on a 2 mL water bath. As the vapor concentration in the droplet ambience increased, the magnitude of surface tension gradient set-in increased. This led to establishment of higher ω_{avg} for the 5CB droplet of fixed volume. Presence of hexane vapor for longer time-period not only induced faster recirculation but the time period for recirculation also increased. It was also observed that there was a gradual rise in the St with the rise in V_{hexane}, as shown in **Figure 5.4 (II)**. This was attributed to the enhanced recirculation rates for a fixed 5CB droplet diameter. Although, there was a simultaneous increment in the V_{avg}, the rise in the recirculation rates was more. Volume of water in the bath was fixed at 5 mL for the experiments conducted. Hence the amount of time required to initiate flow in the underlying water bath was much longer than that required for initiating recirculation. The development of flow in the underlying water bath was important as it was required to sustain the bulk 5CB droplet motility on the water bath.

5.3.4 Effect of Varying Salt Concentration on Recirculation Rate

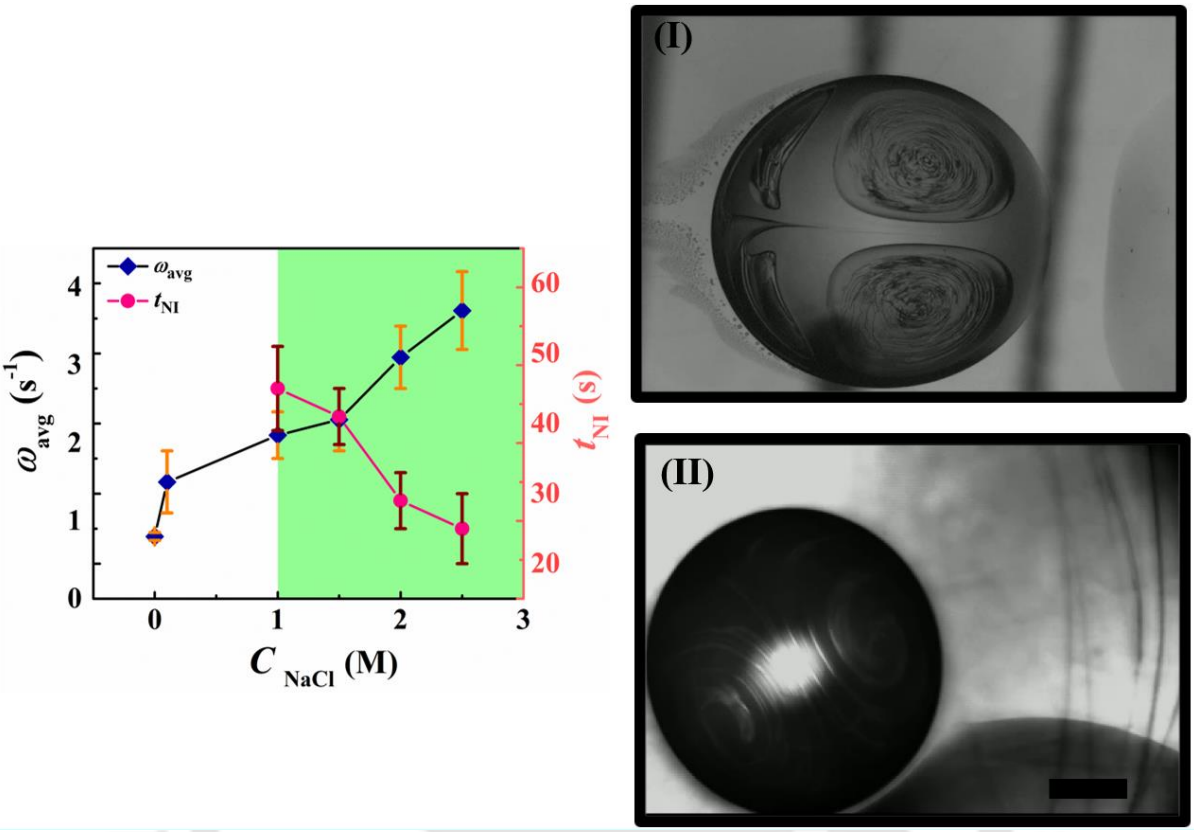

Figure 5.6 Salt concentration in the underlying bath influences the rate of recirculation as well as phase transition time within the 5CB droplet. Plot presents the effect of changing NaCl concentration in water on ω_{avg} and time for nematic-to-isotropic transition (t_{NI}). Optical micrographs (I) and (II) highlight the 5CB droplet on water bath in absence and presence of 1 M NaCl, respectively. Scale bar is of length 500 µm. Grey region in the POM image of 5CB droplets highlight the nematic phase, while the black regions highlight the isotropic phase.

Further experiments were carried out to understand the role played by the physico-chemical characteristics of the water bath on the nature of 5CB recirculation. 5CB has been known to have favourable interactions with air-water interface towards formation of stable films. [48,49] The polar mesogens of 5CB (dipole moment ~ 5D [50]) interact with the highly polar water molecules via electrostatic interactions. As a result, strong anchoring is imposed on the LC surface as witnessed in the LC droplets [50], fibres [51] or films [52] in aqueous environment. In the present study, effect of anionic salt addition in the water bath (NaCl) on the rate of recirculation was investigated. In the absence of electrolyte, ω_{avg} for a 2 µL 5CB droplet in the presence of 5 µL hexane droplet was around 1 s^{-1} for a bath containing 5 mL water. However, under similar experimental conditions much faster rate of recirculation was observed in presence of varying concentrations of NaCl (C_{NaCl}), as can be seen in **Figure 5.6**. With gradual increase in the C_{NaCl}

from 0 to 2.5 M (near solubility limit at room temp.[53], there was a noticeable enhancement in the ω_{avg} from 1 s^{-1} to 3.5 s^{-1}.

Moreover, the high rate of recirculation also did not disturb the droplet geometry, which was in stark contrast to 5CB droplet dynamics witnessed in earlier experiments. Since the 5CB droplet displayed rapid, steady twin-vortices, no transition to unsteady vortices was observed in the presence of electrolyte solution. The addition of NaCl to the water bath increased the polarity of the medium. This improved the dipole-induced dipole interactions between the polar nitrile-head (-C≡N) of 5CB mesogens and the underlying ionic solution. It is hypothesized that along with the surface tension forces, this interaction between the 5CB and salt solution imparted stability to the TPCL of the 5CB droplet such that a stable interface existed between the droplet and water bath, which prevented the distortion of droplet geometry at high ω_{avg}.

It may also be noted that in the presence of salt solution and under 10X magnification, it was observed that the 5CB droplet end close to the hexane droplet did not distort and engender generation of many daughter 5CB droplets. Furthermore, due to the high recirculation rates existing within the nematic 5CB droplet, hexane diffusion was enhanced which led to faster phase transition. **Figure 5.6 (I)** and **(II)** reflect the state of the 5CB droplets which were exposed to hexane for similar period on a water bath containing no NaCl, and 1 M NaCl, respectively. Transition from nematic phase (grey region) to isotropic phase (black region) took less time (t_{NI}) as the salt concentration in the underlying bath increased. It was observed that while t_{NI} was ~ 45 s in a 5CB droplet on 1 M NaCl bath, it was reduced to ~ 25 s for a 5CB droplet on a 2.5 M NaCl bath. Thus, naturally the period of recirculation within the 5CB droplet also decreased with increasing C_{NaCl} in the water bath, as the 5CB droplet became saturated with hexane at a faster rate.

5.3.5 Effect of Varying Bath Temperature on Recirculation Rate

The recirculation within the 5CB bulk may have occurred either as a result of density driven flows (Rayleigh-Bénard (RB) instability) or surface tension difference, as depicted in **Figure 5.7 (I)**. Considering the droplet diameter was near its capillary length, gravity may have necessitated flow within the droplet due to evaporation induced temperature changes. In order to verify this hypothesis, an IR camera was employed to detect the temperature changes during the entire analysis. For a 2 µL 5CB droplet, temperature at its surface was monitored in the presence of a 2 µL hexane droplet on the water bath.

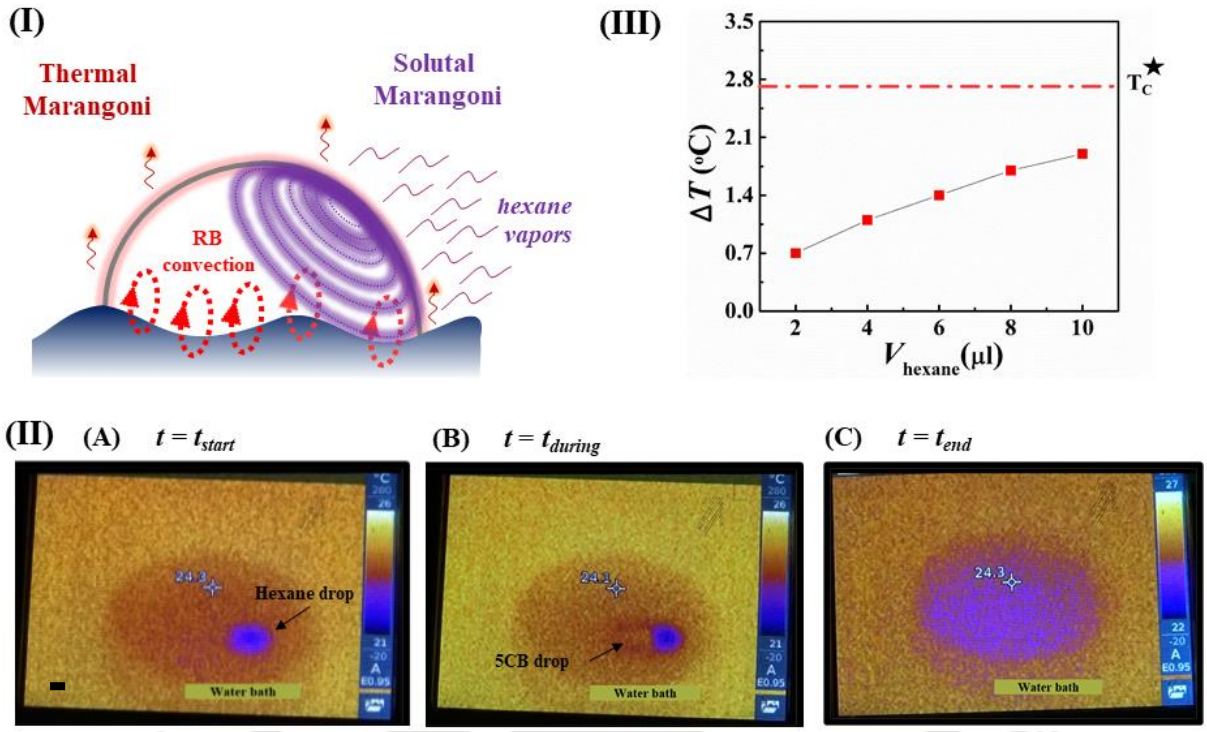

Figure 5.7 (I) Generation of recirculation within the 5CB droplet affected by solutal Marangoni effect and thermal Marangoni effect. Influence of RB instability on the recirculation rate was not significant. (II) IR profiles of 5CB-hexane droplets on the water bath. (A) Image represents the temperature profile of 5CB drop and hexane drop, at the time of deposition of hexane on water bath. 5CB drop (not visible) is present on the water bath having a temperature ~ 24.3 °C. (B) After a period of ~ 5s, the 5CB drop starts moving towards hexane drop, however the 5CB temperature has still not significantly changed (~ 24 °C). (C) After the entire hexane evaporates, the change in 5CB temperature is minimal (~ 23 °C). (III) Plot depicting the variation in 5CB droplet temperature (ΔT) as a function of hexane volume (V_{hexane}). Here T_c^* represents the minimum critical temperature required to initiate Rayleigh-Bernard recirculation within the 5CB droplet. Scale bar in the image is of length 2 mm.

The temperature of the entire setup at different time intervals has been presented in **Figure 5.7 (II)**. IR profile of 5CB-loaded water has been depicted in **Figure 5.7 (II) (A)** wherein hexane droplet was just dispensed. Average temperature of water bath and 5CB was around 24.3 °C whereas hexane droplet was ~ 23 °C. Thereafter, on the account of variation in *S*, droplet motility of 5CB towards hexane was observed after a period of ~5s, as shown in **Figure 5.7 (II) (B)**. As the hexane droplet evaporated its temperature reduced further.

Moreover, it was observed that the interaction of the hexane vapor with the 5CB droplet did not result in significant change in 5CB temperature (ΔT). The temperature change at the end of the process when hexane evaporated led to a decrease in 5CB droplet temperature to a minimum of ~ 23 °C, as shown in **Figure 5.7 (II) (C)**. Increasing the hexane droplet volume increased the temperature gradient at the 5CB surface as more hexane adsorption and desorption occurred. However, the temperature change required to initiate flow within 5CB

droplet due to RB instability did not reach the critical value (T_c^*) within the present set of experimental conditions, as depicted in **Figure 5.7 (III)**. Hence, the recirculation was primarily due to surface tension gradient generated at the 5CB droplet periphery.

In order to understand the origin of recirculation within the 5CB droplet, whether it was Thermal or solutal Marangoni driven, a simple analysis was performed. It may be noted that at room temperature under similar experimental conditions as mentioned in above experiments (V_{5CB} – 2 µL, V_{hexane} – 10 µL, V_{bath} – 2 mL), the thermal-driven Marangoni effect either due to ambient conditions or due to evaporation, was not significant. Thermal Marangoni number (Ma_T, $Ma_T = \frac{\dot{\sigma}\Delta T_{max} R_{5CB}}{\mu_{5CB}\alpha_{5CB}}$) < 1, where $\dot{\sigma}$ is the rate of change of surface tension in 5CB as a function of temperature [54], ΔT_{max} is the maximum temperature change observed within the 5CB droplet during analysis and $\boldsymbol{\alpha_{5CB}}$ is the thermal diffusivity of 5CB.[55] The rate of change of fluid movement within the droplet due to thermal diffusion was similar to that generated due to thermally-varying surface tension gradient. Moreover, the limited contribution of thermal effects at room temperature towards inducing recirculation was also highlighted by the marginal value of thermally-driven Marangoni convection velocity ($V_{thermal}$, $V_{thermal} = \frac{\dot{\sigma}\Delta T_{max}}{\mu_{5CB}}$) of value ~ 0.4 mm/s. Furthermore, for 5CB mother droplets having V_{5CB} smaller than 4 µL , the Bond number (Bo, $Bo = \frac{\rho_{5CB} g h_{5CB}^2}{\gamma_{5CB}}$) was < 1, where ρ_{5CB} is the density of 5CB, h_{5CB} is the 5CB droplet height and $\boldsymbol{\gamma_{5CB}}$ is the interfacial tension at 5CB-water interface. As a result, the interfacial driven forces governed the droplet dynamics compared to the gravitational forces.

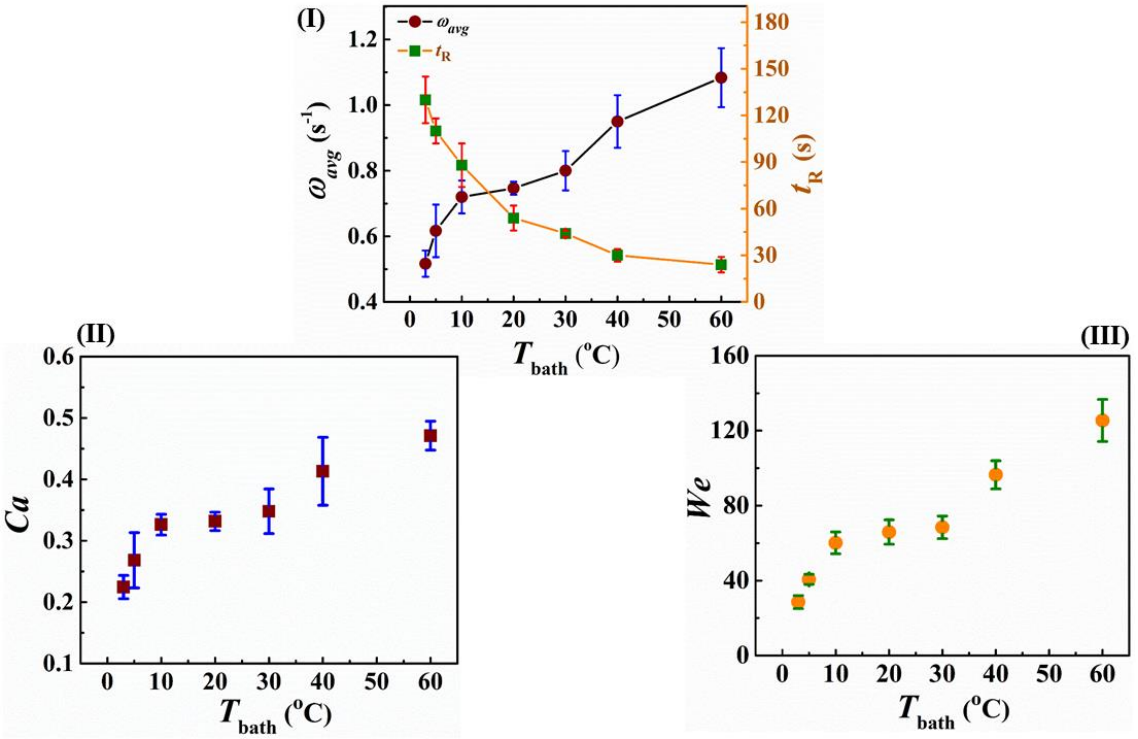

Figure 5.8 Effect of variation in the bath temperature (T_{bath}) on the 5CB droplet recirculation. Plot (I) presents the change in ω_{avg} as a function of T_{bath}. With increasing temperature of underlying bath, ω_{avg} values increased. Plot (II) presents the variation in Capillary number (*Ca*, $Ca = \mu_D V_{avg} / \gamma_m$) with bath temperature. Higher surface tension gradient generated due to larger hexane availability near 5CB surface, led to rise in *Ca* with increment in T_{bath}. Moreover, at higher T_{bath} conditions, the enhanced recirculation also increased the Weber number (*We*, $We = \rho_D V_{avg} d_D^0 / \gamma_m$) since the availability of hexane in addition to the thermal Marangoni stresses improved the convective flow within the droplet.

The consequence of this was that the recirculation generated due to buoyancy driven forces was also weak, the magnitude of which was represented by the $V_{buoyant}$ (~ $V_{buoyant} = \frac{g\beta\Delta T_{max}}{\nu_{5CB}}$).

Here, g is the gravitational constant, β is the expansion co-efficient for nematic liquid crystal [56] and ν_{5CB} is kinematic viscosity of 5CB. For V_{5CB} < 4 μL, $V_{buoyant}$ was around 0.04 mm/s. Hence, the recirculation due to density-driven was not significant for smaller 5CB droplets. However, changing ambient parameters and employing larger 5CB droplets led to conditions which involved interplay of gravitational and thermocapillary effects.

Changing the underlying bath temperature (T_{bath}) influenced the recirculation rate within the 5CB droplets considerably. Since the dimension of the 5CB droplet having V_{5CB} ~ 2 uL was near its capillary length (L_c, $L_c = \sqrt{\frac{\sigma_{5CB}}{\Delta\delta g}}$) of value ~ 2.3 mm, gravitational effects would have also determined the movement of fluid within the 5CB droplet. Density-variations as a result

of thermal gradients around the droplet periphery had to be considered. **Figure 5.8 (I)** presents the effect of T_{bath} on the rate and the period of recirculation (t_R). It was observed from the experiments that at lower bath temperatures (0-10 °C), ω_{avg} had a lower value compared to what it was at room temperature. Since the recirculation in the 5CB droplet was solutal-Marangoni driven; at lower T_{bath}, low volatility of hexane solvent contributed towards presence of reduced surface tension gradient at the 5CB surface. Additionally, the density variation due to difference in temperatures between 5CB-air interface and 5CB-water interface, would have facilitated movement of 5CB fluid in a direction that opposed the surface-tension driven flow. With increasing T_{bath}, ω_{avg} improved considerably. Rise in recirculation within the 5CB droplet would have been primarily due to a faster hexane evaporation rate, and thermocapillary effects. Higher hexane evaporation would have led to generation of high vapor pressure near droplet periphery and consequently, higher absorption within the 5CB droplet. Furthermore, a heated water bath would have allowed stronger convection currents to develop in the 5CB droplet such that the movement of fluid from the 5CB-air interface towards 5CB-water interface would have assisted the solutal-Marangoni driven flow. With increasing T_{bath}, t_R reduced gradually. As the volatile solvent droplet evaporated faster with rising T_{bath}, the driving force required to sustain the recirculation within the droplet waned. Also, as more hexane diffused within 5CB droplet, the net hexane concentration gradient in the droplet diminished leading to establishment of a low surface tension gradient.

Convective flow magnitude within the 5CB droplet was also studied employing parameters such as initial 5CB drop diameter (d_D^0), average recirculation rate (ω_{avg}), average recirculation velocity (V_{avg}), drop density (ρ_D), drop viscosity (μ_D) and IFT between the 5CB-hexane drop and surfactant-water bath (γ_{5CB}). This analysis led to formation of dimensionless numbers such as Capillary number (Ca, $Ca = \mu_D V_{avg} / \gamma_m$) and Weber number (We, $We = \rho_D V_{avg} d_D^0 / \gamma_m$) which helped in understanding the interplay of viscous, inertial, capillary and centripetal forces. **Figure 5.8 (II)** depicts typical variation in the droplet Ca number when T_{bath} was changed. At lower bath temperatures as the recirculation velocity was low, the surface tension forces dominated the flow profile resulting in the existence of a low Ca number. However, with increasing water temperature, the rate of recirculation within the 5CB droplet enhanced such that the V_{avg} improved, leading to an overall increase in the Ca number from 0.25 at 3 °C to ~ 0.5 at 60 °C. As the inertial forces dominated, simultaneous improvement in the We number also took place from 30 at 3 °C to ~ 130 at 60 °C, as depicted in **Figure 5.8 (III)**. The rise in

We was relatively higher to *Ca* number under the same temperature range, suggesting enhanced influence of inertial forces w.r.t capillary forces in determining the recirculation dynamics. Additionally, with increase in the centripetal forces as a result of enhanced recirculation, the droplet stability was affected and occurrence of unsteady vortices was observed at temperatures beyond 40 °C. It must be noted that there was a marked change in the respective slopes of Ca number and We number profiles as T_{bath} was increased. The change occurred in the region of 5CB phase transition, between 35-40 °C.[57] As the droplet transitioned from a nematic to an isotropic state, an enhancement in the rate of recirculation was observed owing to the reduction in the 5CB droplet viscosity at higher temperatures. Moreover, an increase in the surface tension gradient at higher T_{bath} did occur due to higher hexane evaporation and thermocapillary effects. However, the change in the V_{avg} was considerable due to viscous dissipation in the underlying bath such that a net increment in the *Ca* and *We* numbers was still observed.

Besides solutal-Marangoni driven recirculation and oscillatory contact line instability, another phenomenon was observed at the TPCL of the 5CB droplet in presence of hexane on the water bath. The 5CB droplet half facing hexane droplet displayed spreading dynamics on the water bath. Since there was a net difference in the *S* around the 5CB droplet, due to favourable conditions, a limited region of the 5CB droplet extended over the bath to form a "film". As the droplet spread, surface area of the formed 5CB film increased which led to higher evaporation rate of hexane. This induced a change in the sign of *S* such that a retraction of the leading edge was observed. This resulted in the characteristic contact line instability phenomenon. Near the leading edge, the curvature forces overcame the surface tension forces to initiate the disintegration of the film into miniaturized 5CB droplets in the range 6-22 μm as depicted in the **Figure 5.9 (I)**.

Thus, this chemotacticity driven 5CB droplet dewetting phenomenon enables production of 5CB droplets whose volume spans about 4 orders of magnitude. Moreover, the liquid threads developed at the leading edge demonstrated a definite wavelength, λ as shown in **Figure 5.9 (II)**. Interestingly, the oscillatory contact line motion influenced the spreading dynamics of the 5CB film on the water bath, such that dewetting of the film was more visible as the droplet proceeded in direction of hexane droplet than when the droplet was receding. This occurred due to change in the *S* value as the droplet neared the hexane droplet resulting in higher surface tension gradient. **Figure 5.9 (III)** shows the leading edge of the 5CB droplet disintegrating to generate daughter droplets.

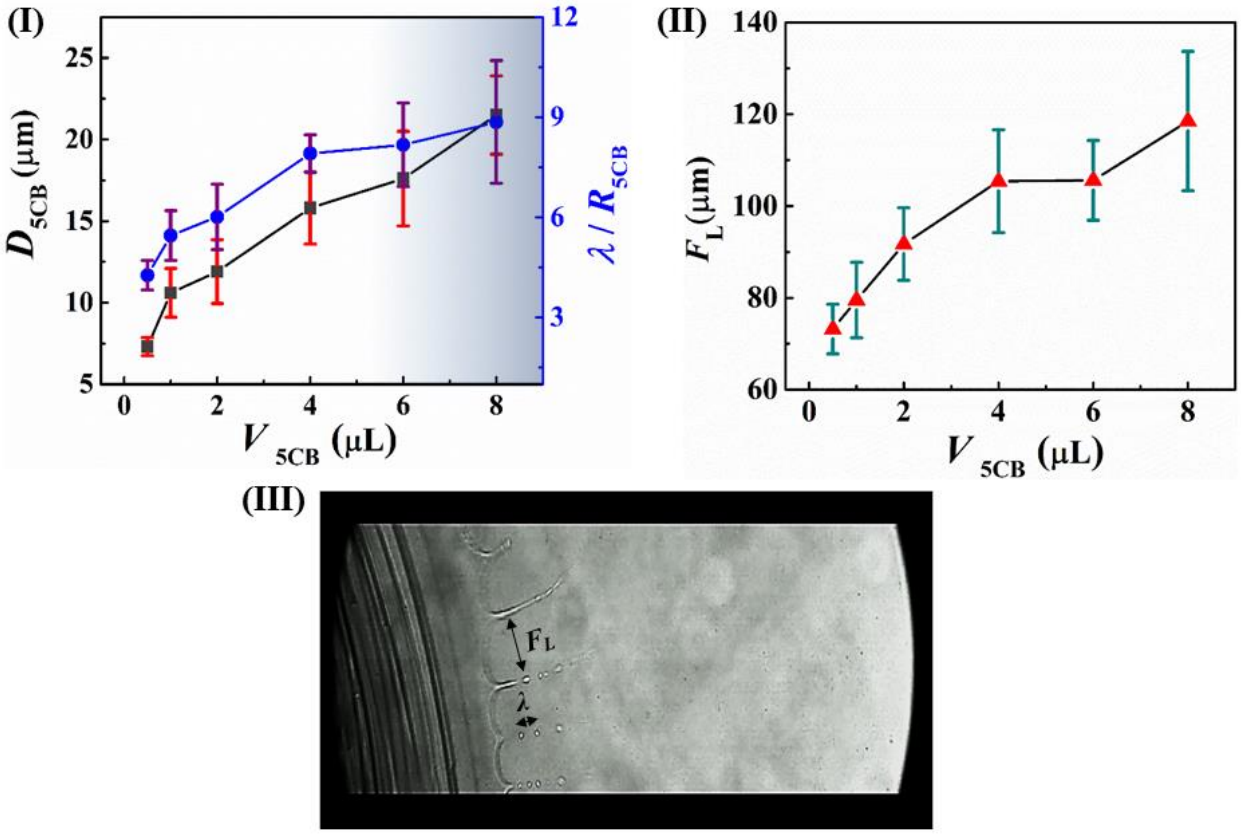

Figure 5.9 Contact line instability induced dewetting. Plot (I) presents the effect of variation in 5CB droplet volume on the generated daughter droplets and droplet spacing (λ). Higher 5CB droplets leads generation of larger daughter droplets. Plot (II) presents the variation in the finger spacing (F_L) on the account of changing the V_{5CB} value. Higher F_L values are observed for bigger 5CB droplets. Image (III) shows an optical micrograph of the leading edge of 5CB droplet (2 μL) undergoing dewetting while displaying fingers with a spacing λ.

Varying the 5CB droplet size resulted in generation of different droplet dimensions as well as λ/R_{5CB} ratio. Larger 5CB droplets (> 6μL) resulted in the generation of daughter droplets having 15-20 μm diameter. As the recirculation set-in the 5CB droplet, due to larger inertial forces dominating the flow characteristics, the region of the droplet undergoing spreading over the water bath would have had higher thickness than the film formed due to spreading in the 5CB droplet of lower volume (0-2 μL). Stabilizing forces such as Nematic elasticity and intermolecular forces would have delayed the onset of dewetting in these films such that it would have resulted in more spacing between fingers and resultant daughter droplets with larger dimensions.

On the other hand, in case of spreading in 5CB droplets of lower volume (0-2 μL), the film formed on the water bath would have been relatively thinner. This would have allowed destabilizing forces such as Marangoni stress and surface tension to dominate the dewetting dynamics and result in generation of narrower finger spacing with smaller daughter droplets.

This was observed in the plot also as λ/R_{5CB} ratio decreased from the standard value of ~ 8.85-9 observed in curvature-driven dewetting in case of Rayleigh-Plateau (RP) instability to < 4, observed under conditions wherein additional destabilizing forces such as surface tension dominates.

5.4 Conclusions

This study investigates the striking contact line dynamics displayed by the pristine 5CB droplet in presence of a hexane droplet on a water bath. This mechanism of liquid-on-liquid dewetting also presents a facile route for obtaining multitude of miniaturized 5CB droplets. The phenomenon initiates via interaction of the 5CB droplet with the hexane source that leads to a change in the 5CB droplet composition. Surface tension gradient leads to generation of the solutal Marangoni stresses in the 5CB droplet which leads to the generation of bulk recirculation. The recirculation grows gradually with time leading to a critical value. Spontaneous deformation of the circular periphery as a result of dominance of centripetal forces is observed. This results in stopping of the recirculation and an instantaneous restoration of the droplet geometry. This cycle was observed to repeat in time. Variation in the 5CB droplet for a fixed hexane amount, resulted in reduction of the recirculation rates due to dominance of viscous forces over inertial forces. Changing the hexane droplet volume enhanced the recirculation rate within the 5CB droplet as a result of prolonged surface tension gradient presence near the 5CB droplet. Increasing the bath temperature led to faster recirculation on the account of thermal Marangoni effects, however it reduced the recirculation time period as 5CB phase transition occurred early. Polarity of the water bath also had an effect on rate of recirculation as increasing the salt content facilitated higher recirculation rates. Higher polar interactions with the 5CB droplet allowed for balancing of the centripetal forces such that unsteady recirculation was prevented. Another interaction near the droplet three-phase contact line occurred due to an osmotic pressure gradient that caused 5CB droplet motility over the water bath. Experiments uncovered that variation in the water bath level changes the rate of droplet locomotion. Presence of the hexane source also facilitated droplet spreading on the water bath. This led to localized hexane evaporation resulting in variation of interfacial tension gradient. Capillary instability in the retracting 5CB droplet was observed before spontaneous disintegration of the film into miniaturized 5CB droplets. Influence of destabilizing surface tension forces could be identified as reducing the 5CB loading resulted in reduction of droplet spacing and droplet diameter, with their ratio being less than that observed during RP instability.

References

(1) Vella, D.; Mahadevan, L. The "Cheerios Effect." *Am. J. Phys.* **2004**, *73*, 817–825.

(2) Maass, C. C.; Krüger, C.; Herminghaus, S.; Bahr, C. Swimming Droplets. *Annu. Rev. Condens. Matter Phys.* **2016**, *7*, 171–193.

(3) Izri, Z.; Van Der Linden, M. N.; Michelin, S.; Dauchot, O. Self-Propulsion of Pure Water Droplets by Spontaneous Marangoni-Stress-Driven Motion. *Phys. Rev. Lett.* **2014**, *113*, 248302-248307.

(4) Liu, D.; Tran, T. Vapor-Induced Attraction of Floating Droplets. *J. Phys. Chem. Lett.* **2018**, *9*, 4771–4775.

(5) Kagan, D.; Campuzano, S.; Balasubramanian, S.; Kuralay, F.; Flechsig, G. U.; Wang, J. Functionalized Micromachines for Selective and Rapid Isolation of Nucleic Acid Targets from Complex Samples. *Nano Lett.* **2011**, *11*, 2083–2087.

(6) Guix, M.; Orozco, J.; Garcia, M.; Gao, W.; Sattayasamitsathit, S.; Merkoči, A.; Escarpa, A.; Wang, J. Superhydrophobic Alkanethiol-Coated Microsubmarines for Effective Removal of Oil. *ACS Nano* **2012**, *6*, 4445–4451.

(7) Park, J.; Ryu, J.; Sung, H. J.; Kim, H. Control of Solutal Marangoni-Driven Vortical Flows and Enhancement of Mixing Efficiency. *J. Colloid Interface Sci.* **2020**, *561*, 408–415.

(8) Cira, N. J.; Benusiglio, A.; Prakash, M. Vapour-Mediated Sensing and Motility in Two-Component Droplets. *Nature* **2015**, *519*, 446–450.

(9) Liu, C.; Sun, J.; Zhuang, Y.; Wei, J.; Li, J.; Dong, L.; Yan, D.; Hu, A.; Zhou, X.; Wang, Z. Self-Propelled Droplet-Based Electricity Generation. *Nanoscale* **2018**, *10*, 23164–23169

(10) Thakur, S.; Dasmahapatra, A. K.; Bandyopadhyay, D. Functional Liquid Droplets for Analyte Sensing and Energy Harvesting. *Adv. Colloid Interface Sci.* **2021**, 102453-102483.

(11) Suematsu, N. J.; Nakata, S. Evolution of Self-Propelled Objects: From the Viewpoint of Nonlinear Science. *Chem. - A Eur. J.* **2018**, *24*, 6308–6324.

(12) Velarde, M. G. Drops, Liquid Layers and the Marangoni Effect. *Philos. Trans. R. Soc. A Math. Phys. Eng. Sci.* **1998**, *35*, 829–844

(13) Whitesides, G. M.; Grzybowski, B. Self-Assembly at All Scales. *Science*. **2002**, *295*, 2418–2421.

(14) Golubina, E. N.; Kizim, N. F. Interfacial Synthesis: Morphology, Structure, and

Properties of Interfacial Formations in Liquid–Liquid Systems. *Russ. J. Phys. Chem. A* **2021**, *95*, 659–676.

(15) Baroud, C. N.; Delville, J. P.; Gallaire, F.; Wunenburger, R. Thermocapillary Valve for Droplet Production and Sorting. *Phys. Rev. E - Stat. Nonlinear, Soft Matter Phys.* **2007**, *75*, 046302-046307.

(16) Reichert, B.; Cam, J.-B. Le; Saint-Jalmes, A.; Pucci, G. Active Volatile Drops on Liquid Baths. *APS Division of Fluid Dynamics Meeting Abstracts*. **2020**, 1-8.

(17) van Gaalen, R. T.; Diddens, C.; Wijshoff, H. M. A.; Kuerten, J. G. M. Marangoni Circulation in Evaporating Droplets in the Presence of Soluble Surfactants. *J. Colloid Interface Sci.* **2021**, *584*, 622-633.

(18) Ryu, J.; Kim, J.; Park, J.; Kim, H. Analysis of Vapor-Driven Solutal Marangoni Flows inside a Sessile Droplet. *Int. J. Heat Mass Transf.* **2021**, *164*, 120499-120505.

(19) SCRIVEN, L. E.; STERNLING, C. V. The Marangoni Effects. *Nature* **1960**, *18*, 186–188.

(20) Bolleddu, R.; Chakraborty, S.; Bhattacharjee, M.; Bhandaru, N.; Thakur, S.; Gooh-Pattader, P. S.; Mukherjee, R.; Bandyopadhyay, D. Pattern-Directed Phase Transitions and VOC Sensing of Liquid Crystal Films. *Ind. Eng. Chem. Res.* **2020**, *59*, 1902–1913.

(21) Bhattacharjee, M.; Pasumarthi, V.; Chaudhuri, J.; Singh, A. K.; Nemade, H.; Bandyopadhyay, D. Self-Spinning Nanoparticle Laden Microdroplets for Sensing and Energy Harvesting. *Nanoscale* **2016**, *8*, 6118–6128.

(22) Hegde, O.; Chakraborty, S.; Kabi, P.; Basu, S. Vapor Mediated Control of Microscale Flow in Sessile Droplets. *Phys. Fluids* **2018**, *30*, 122103-122110.

(23) Herminghaus, S.; Maass, C. C.; Krüger, C.; Thutupalli, S.; Goehring, L.; Bahr, C. Interfacial Mechanisms in Active Emulsions. *Soft Matter* **2014**, *10*, 7008–7022.

(24) Carlton, R. J.; Zayas-Gonzalez, Y. M.; Manna, U.; Lynn, D. M.; Abbott, N. L. Surfactant-Induced Ordering and Wetting Transitions of Droplets of Thermotropic Liquid Crystals “Caged” inside Partially Filled Polymeric Capsules. *Langmuir* **2014**, *30*, 14944–14953.

(25) Tadros, T. F. Emulsion Formation, Stability, and Rheology. In *Emulsion Formation and Stability*; Wiley-VCH Verlag GmbH & Co. KGaA: Weinheim, Germany, **2013**; 1–75.

(26) Sjobolm, J. *Emulsions and Emulsion Stability*, 2nd ed.; CRC Press: Boca Raton, **2005**.

(27) Strulson, C. A.; Molden, R. C.; Keating, C. D.; Bevilacqua, P. C. RNA Catalysis through Compartmentalization. *Nat. Chem.* **2012**, *4*, 941–946.

(28) Linsenmeier, M.; Kopp, M. R. G.; Grigolato, F.; Emmanoulidis, L.; Liu, D.; Zürcher, D.; Hondele, M.; Weis, K.; Capasso Palmiero, U.; Arosio, P. Dynamics of Synthetic Membraneless Organelles in Microfluidic Droplets. *Angew. Chemie - Int. Ed.* **2019**, *58*, 14489–14494.

(29) Čejková, J.; Banno, T.; Hanczyc, M. M.; Štěpánek, F. Droplets As Liquid Robots. *Artificial Life*, **2017**, *23*, 528–549.

(30) Wang, T.; Si, Y.; Li, N.; Dong, Z.; Jiang, L. Bioinspired Tip-Guidance Liquid Jetting and Droplet Emission at a Rotary Disk via a Surface Energy Gradient. *ACS Nano* **2019**, *13*, 13100–13108.

(31) Theberge, A. B.; Courtois, F.; Schaerli, Y.; Fischlechner, M.; Abell, C.; Hollfelder, F.; Huck, W. T. S. Microdroplets in Microfluidics: An Evolving Platform for Discoveries in Chemistry and Biology. *Angewandte Chemie - International Edition*. **2010**, *49*, 5846–5868.

(32) Feng, J.; Roché, M.; Vigolo, D.; Arnaudov, L. N.; Stoyanov, S. D.; Gurkov, T. D.; Tsutsumanova, G. G.; Stone, H. A. Nanoemulsions Obtained via Bubble-Bursting at a Compound Interface. *Nat. Phys.* **2014**, *10*, 606–612.

(33) Binks, B. P.; Lumsdon, S. O. Catastrophic Phase Inversion of Water-in-Oil Emulsions Stabilized by Hydrophobie Silica. *Langmuir* **2000**, *16*, 2539–2547.

(34) Ding, Y.; Howes, P. D.; Demello, A. J. Recent Advances in Droplet Microfluidics. *Analytical Chemistry*. **2019**, *92*, 132–149.

(35) Chao, Y.; Hung, L. T.; Feng, J.; Yuan, H.; Pan, Y.; Guo, W.; Zhang, Y.; Shum, H. C. Flower-like Droplets Obtained by Self-Emulsification of a Phase-Separating (SEPS) Aqueous Film. *Soft Matter* **2020**, *16*, 6050–6055.

(36) Guha, I. F.; Anand, S.; Varanasi, K. K. Creating Nanoscale Emulsions Using Condensation. *Nat. Commun.* **2017**, *8*, 1–7.

(37) Tcholakova, S.; Valkova, Z.; Cholakova, D.; Vinarov, Z.; Lesov, I.; Denkov, N.; Smoukov, S. K. Efficient Self-Emulsification via Cooling-Heating Cycles. *Nat. Commun.* **2017**, *8*, 1–11.

(38) Wodlei, F.; Sebilleau, J.; Magnaudet, J.; Pimienta, V. Marangoni-Driven Flower-like Patterning of an Evaporating Drop Spreading on a Liquid Substrate. *Nat. Commun.* **2018**, *9*, 820.

(39) Yamamoto, D.; Nakajima, C.; Shioi, A.; Krafft, M. P.; Yoshikawa, K. The Evolution of Spatial Ordering of Oil Drops Fast Spreading on a Water Surface. *Nat. Commun.* **2015**, *6*, 1–6.

(40) Bates, C. M.; Stevens, F.; Langford, S. C.; Dickinson, J. T. Motion and Dissolution of Drops of Sparingly Soluble Alcohols on Water. *Langmuir* **2008**, *24*, 7193–7199.

(41) Wyart, F. B.; Martin, P.; Redon, C. Liquid/Liquid Dewetting. *Langmuir* **1993**, *9*, 3682–3690.

(42) Ravi, B.; Bhattacharjee, M.; Ghosh, A.; Bandyopadhyay, D. Fabrication of Pixelated Liquid Crystal Nanostructures Employing the Contact Line Instabilities of Droplets. *Nanoscale* **2019**, *11*, 1680–1691.

(43) Pimienta, V.; Brost, M.; Kovalchuk, N.; Bresch, S.; Steinbock, O. Complex Shapes and Dynamics of Dissolving Drops of Dichloromethane. *Angew. Chemie Int. Ed.* **2011**, *50*, 10728–10731.

(44) Pan, L. J.; Tu, J. W.; Ma, H. T.; Yang, Y. J.; Tian, Z. Q.; Pang, D. W.; Zhang, Z. L. Controllable Synthesis of Nanocrystals in Droplet Reactors. *Lab on a Chip*. **2018**, *1*, 41–56.

(45) Kim, Y. H.; Lee, J.-O.; Jeong, H. S.; Kim, J. H.; Yoon, E. K.; Yoon, D. K.; Yoon, J.-B.; Jung, H.-T. Optically Selective Microlens Photomasks Using Self-Assembled Smectic Liquid Crystal Defect Arrays. *Adv. Mater.* **2010**, *22*, 2416–2420.

(46) Martinoty, P.; Kiry, F.; Nagai, S.; Candau, S.; Debeauvais, F. Viscosity Coefficients in the Isotropic Phase of a Nematic Liquid Crystal. *J. Phys.* **1977**, *38*, 159–162.

(47) Malinowski, R.; Volpe, G.; Parkin, I. P.; Volpe, G. Dynamic Control of Particle Deposition in Evaporating Droplets by an External Point Source of Vapor. *J. Phys. Chem. Lett.* **2018**, *9*, 659–664.

(48) Xue, J.; Jung, C. S.; Kim, M. W. Phase Transitions of Liquid-Crystal Films on an Air-Water Interface. *Phys. Rev. Lett.* **1992**, *69*, 474–477.

(49) de Mul, M. N. G.; Mann, J. A. Multilayer Formation in Thin Films of Thermotropic Liquid Crystals at the Air–Water Interface. *Langmuir* **1994**, *10*, 2311–2316.

(50) Dubtsov, A. V.; Pasechnik, S. V.; Shmeliova, D. V.; Saidgaziev, A. S.; Gongadze, E.; Iglič, A.; Kralj, S. Liquid Crystalline Droplets in Aqueous Environments: Electrostatic Effects. *Soft Matter* **2018**, *14*, 9619–9630.

(51) Urbanski, M.; Reyes, C. G.; Noh, J.; Sharma, A.; Geng, Y.; Subba Rao Jampani, V.; Lagerwall, J. P. F. Liquid Crystals in Micron-Scale Droplets, Shells and Fibers. *Journal of Physics Condensed Matter*. **2017**, *29*, 133003-133057.

(52) Brake, J. M.; Mezera, A. D.; Abbott, N. L. Effect of Surfactant Structure on the Orientation of Liquid Crystals at Aqueous-Liquid Crystal Interfaces. *Langmuir* **2003**, *19*, 6436–6442.

(53) Carlton, R. J.; Ma, C. D.; Gupta, J. K.; Abbott, N. L. Influence of Specific Anions on the Orientational Ordering of Thermotropic Liquid Crystals at Aqueous Interfaces. *Langmuir* **2012**, *28*, 12796–12805.

(54) Tintaru, M.; Moldovan, R.; Beica, T.; Frunza, S. Surface Tension of Some Liquid Crystals in the Cyanobiphenyl Series. *Liq. Cryst.* **2001**, *28*, 793–797.

(55) Yilmaz, S.; Yildirim, A. Numerical Determination of Thermal-Diffusivity Coefficients of Some Nematic Liquid Crystals in Situ. *Int. J. Thermophys.* **2009**, *30*, 2015–2020.

(56) Kim, Y. K.; Senyuk, B.; Lavrentovich, O. D. Molecular Reorientation of a Nematic Liquid Crystal by Thermal Expansion. *Nat. Commun.* **2012**, *3*, 1–7.

(57) Ravi, B.; Mukherjee, R.; Bandyopadhyay, D. Solvent Vapour Mediated Spontaneous Healing of Self-Organized Defects of Liquid Crystal Films. *Soft Matter* **2015**, *11*, 139–146.

Chapter 06

Conclusions and Future Scope

6.1 Conclusions

This thesis presents proof-of-concept setups that have employed simple droplet configuration upon solid and liquid substrates for catering to biosensing, energy harvesting and patterning applications. Functional nature of liquid droplets has been exploited by incorporation of suitable materials for obtaining tailored responses. The following sections provide a brief overview of the key results from the different chapters and also highlight the avenues for future research in these areas.

6.1.1 Acoustic Wave Catalyzed Urea Detection Utilizing a Pulsatile Microdroplet Sensor

In this chapter we employ an external sound-stimulated conducting water microdroplet for the purpose of functioning as a biosensing setup as well as a sound detector. Variations in the electrical resistance of the oscillating droplet can be mapped with the analyte concentration (biosensor) as well as with the characteristics (pitch, tempo) of the external sound (sound detector). The main conclusions of this study are:

- Stimulating the droplet with acoustic waves results in generation of recirculation within the droplet. The sound pressure waves isotropically impact the three-phase contact line of the incompressible fluid, resulting in generation of a symmetrical fluid displacement. The convective flow within the conducting water droplet results in displacement of ions. At the resonant frequency of the setup, maximum displacement of ions results in the maximum decrease in electrical resistance across the droplet as measured with the help of two Cu wires and a multimeter. Furthermore, the oscillations also distort the droplet geometry which further contributes towards the change in ionic distribution within the droplet.
- Employing a free droplet configuration wherein one of the surfaces was exposed to surroundings while the other was resting on substrate, a sound sensor was developed. The microdroplet was acoustically stimulated with sounds from different instruments such as harmonium, flute and tabla. Depending upon the characteristic of the external sound, the change in electrical resistance was observed. The droplet was successfully able to distinguish between the different octaves and *bol* depending upon their pitch and tempo.
- Employing a sandwich configuration wherein the droplet was attached to the glass substrate on either end, a biosensing application was performed. Incorporating Au/CdS attached urease nanocomposite to the acoustically stimulated droplet facilitated the construction of a urea biosensor. The Au/CdS nanocomposite was added to improve the interfacial area of enzymatic reaction and also improve the conductivity of the system. *In*

situ droplet experiments performed by utilizing a particular enzyme concentration for a range of urea concentrations led to the development of a calibration chart. Depending upon the amount of urea present in the droplet, its decomposition in the presence of urease resulted in generation of ions which contributed to the decrease in the electrical resistance across the droplet. Thus, for different values of urea concentration, different electrical resistance values of the droplet were obtained. Interestingly, it was observed that the enzymatic reaction rate was enhanced in the presence of nanocomposite and external acoustic waves. The standard Michaelis-Menten kinetics was replaced by a faster, first order rate kinetics for a longer time period. From a device point of view, this aided to reduce the sensing time of the setup.

- The calibration chart was used to detect urea concentration in unknown serum samples. The results obtained from the microdroplet sensor were compared with a standard laboratory technique. The difference between the results was less than 15% on average.

To conclude, this study presents a facile way of developing a droplet-based sound sensor. Moreover, the same microdroplet in a different configuration was also used to develop a urea biosensor. Externally stimulating the droplet with acoustic signals led to a faster enzymatic rate kinetics, which reduced the response time. Thus, this technique provides a simple and robust way of developing point-of-care biosensor.

6.1.2 Microdroplet photofuel cells to harvest high-density energy and dye degradation

In this chapter we investigate the utility of a hybrid microdroplet photofuel cell that is capable of simultaneously harvesting electrochemical energy while being engaged in dye degradation. Incorporation of photonic NPs assists in enhancing the overall power and current density value of the cell. A VLSI configuration of cells results in generation of 7 mW/cm^2, which is significant considering the volume of fuel used is ~1 mL. Incorporation of a pollutant in the droplet setup, results in its degradation while energy is continuously harvested from the setup at 0.6 mW/cm^2 for 0.05 mL of fuel consumed. Overall, the major findings of the study are:

- A membraneless microdroplet photofuell cell has been constructed with H_2O_2 as the fuel and oxidant, a photosensitive semiconductor, ZnPC, along with a metal support, Cu, as the cathode and Al as the anode. Addition of HCl is performed to stabilize the peroxide decomposition and allow the cell to operate for a longer time. NaCl is added to improve the ionic conductivity. As the cell components are connected, Fermi energy equilibration across the different materials occur. In the presence of external illumination and external

bias, change in the Fermi energy levels gives way to transfer of charges from one electrode to another.

- Addition of Au NPs to the microdroplet setup in presence of external illumination enhances the output parameters significantly. LSPR effect of these photonic NPs stimulates the charge transfer characteristics as it not only encourages exciton formation in the ZnPC electrode but also provides a route for charge extraction, thereby improving the overall potential difference. Au NPs also play the role of redox carriers and aid in charge transfer between the electrodes. These NPs also improve the ionic mobility of the solution.
- Au/CdS NPs are added to assist in the dye degradation process. Although they tend to reduce the overall power density as they act as redox centre for peroxide decomposition and prevent the fuel from being degraded at the electrode. Increasing the amount of Au/CdS NPs present in the solution increases power density value linearly until a particular value. Thereafter, further addition of NPs does not lead to a proportional increase in the output, as mass transfer limitations near the electrodes limit the interactions. With regards to the dye degradation application, in presence of Rhodamine 6G dye, Au/CdS NPs promotes the formation of ROS which breakdown the recalcitrant molecule. Spectral overlap between Au and CdS bands assist in the charge transfer characteristics which degrade the dye molecule. For a single photofuell cell consisting of Au/CdS NPs, dye degradation of ~ 85 % is accomplished within 1 hr while simultaneously generating ~ 0.6 mW/cm^2.
- To enhance the overall performance of the photofuel cell, multiple cells (10) in parallel are connected in a VLSI configuration. For Au NPs laden cells, this improves the power density value from ~ 0.8 mW/cm^2 per cell to 7 mW/cm^2 per cell, at an overall efficiency of 3.5 %. Furthermore, the current density also increases from 1.5 mA/cm^2 per cell to ~ 9 mA/cm^2 per cell. For the Au NPs laden microdroplet photofuel cells in a network configuration, the thermodynamic, photovoltaic and electrochemical efficiencies are 0.63 %, 0.1 % and 0.53 %, respectively.

In summary, a facile method for harvesting electrochemical energy from a photofuell cell setup has been presented. Utilization of photonic NPs has been shown to improve the output parameter of the system. An *in situ* dye degradation process is also carried out while also harvesting energy from the constituents. This technique presents a combined approach towards developing multi-functional systems that are capable of being deployed in remote locations.

6.1.3 Self-Organized Liquid Crystal Droplets as Tunable Soft-Photomasks

In this chapter we explore the pathway to obtain large-scale, self-organized, optically active 5CB droplets for usage as soft photomasks towards photolithography application. A liquid-on-liquid dewetting process has been tuned accordingly for the generation of 5CB droplets of controlled sizes. Experiments have been performed by varying the surfactant concentration and solvent type for realizing smallest droplet structures. The droplet structures obtained have been employed for tuning the incoming radiations so that diverse patterns on the PR surfaces can be developed. The key results from the study are:

- 5CB/hexane droplet deposition on a CTAB bath results in striking spreading dynamics that precedes spontaneous dewetting. The spreading of the 5CB droplet on the CTAB bath is inertia dominated and facilitated by a change in the *S* value of the droplet. After achieving maximum spreading, the equilibrium configuration of the three phase contact line experiences retraction owing to the change in the interfacial tension value. As hexane evaporates, it changes the local surface tension gradient and facilitates dewetting of the 5CB droplet. Capillary instability near the contact line results in spontaneous ejection of daughter droplets.
- Varying the solvent, 5CB loading and underlying CTAB concentration leads to an optimized droplet generation process. In comparison to heptane and toluene, using hexane as solvent not only leads to faster dewetting dynamics but also minimizes droplet dimensions. With regards to 5CB loading, increasing the 5CB content in the droplet leads to bigger dimension of daughter droplets. For a fixed 5CB loading, increasing the CTAB concentration leads to two different dewetting mechanisms: at low concentrations, spinodal dewetting is observed while at higher concentration, random dewetting is observed due to presence of micelles. Beyond a critical surfactant concentration, analysis of the retraction process of leading edge in terms of *Re*, *Ca* and *We* was not possible as the dynamics become erratic.
- Dewetting experiments of the 5CB droplet (10^{-2} M) over the CTAB bath was also performed employing toluene and chloroform as solvents. Different dewetting mechanisms were observed. Metastable structures such as 5CB toroids could also be obtained. Interestingly, this mechanism was not 5CB specific. Dewetting experiments with PS as solute (10^{-7} - 10^{-4} M), also led to similar fluid dynamics, albeit at much lower

concentrations than 5CB. The difference primarily would have been due to higher viscosity of PS solutions.

- The self-organized droplet structures were employed as soft photomasks in an unconventional photolithography setup. Two types of PR substrates were used – positive tone (S1813) and negative tone (SU8). Diverse patterns such as donuts, pillars, craters and islands were generated. In order to obtain large-area patterns, a TEM grid was also utilized which further focused the incoming radiations that fell on the PR surface. An additional handle over light modulation was achieved by using solvent vapor technique to induce phase changes within the 5CB droplet. It was observed that the nematic state of the 5CB droplet (translucent) transmitted less light as compared to the isotropic phase (transparent). This feature of 5CB was used to generate different patterns by simply varying the hexane exposure time over the droplet structures.

Thus, this chapter presents a one-step methodology for obtaining large area droplets whose size and molecular orientation can be controlled via simple experimental handles. In comparison to the conventional techniques of lithography, soft lithography techniques such as this can be optimized accordingly for obtaining unique 3D patterns. Furthermore, using solvent vapor annealing, LC droplets can be accordingly tuned for generating desired patterns.

6.1.4 Chemotactic liquid/liquid dewetting of a nematic droplet

In this chapter, we investigate the dewetting of a nematic LC droplet over a water bath and in presence of a solvent droplet, enroute to generation of multiple, miniaturized LC droplets. Extensive experimental investigations have been performed to analyze the salient features of the chemotactic driven dewetting of the nematic LC droplet. The major observations of the study are:

- A 5CB droplet on a water bath in the vicinity of a hexane droplet displays numerous instabilities. As the hexane drop evaporates (high volatility) it adsorbs asymmetrically on the 5CB droplet surface. This engenders a gradient in surface tension between the bulk and droplet surface that is nearest to the hexane droplet. As a result of this surface tension gradient, a number of instabilities originate in the 5CB bulk as well as on the surface.
- Solutal Marangoni driven recirculation originate in the bulk of the 5CB droplet. A pair of vortices, in their early stages, form mostly in one-half of the 5CB droplet that is close to hexane. Strength of the recirculation gradually grows with time as more hexane gets adsorbed. Beyond a critical recirculation rate, it is observed that the recirculation

engenders a spontaneous deformation of the 5CB droplet surface. Centripetal forces generated as result of convective flow, overpowers the surface tension forces. However, as the droplet periphery deforms it immediately leads to cessation of the recirculation and surface tension forces immediately restore the circular periphery.

- Beyond a critical bath level, 5CB droplet motility over the water bath was observed. As the volume of water in the bath increases, the boundary level effect due to underlying glass substrate reduces, hence the recirculation within the water bath increases. This flow aids in the movement of the 5CB droplet. Furthermore, due to interaction of hexane with the 5CB contact line, an osmotic pressure gradient is created. This directs the movement of the 5CB droplet towards the hexane droplet. However, due to convective flow in the water bath, the hexane droplet does not remain stationary and it moves away from the 5CB droplet as a result.
- Hexane adsorption also causes net change in the *S* value along the droplet three phase contact line. Combined with the recirculation flow within the 5CB bulk, an oscillatory contact line instability is witnessed on a macroscale. On the microscale, due to localized spreading of the 5CB droplet, hexane evaporates faster in the region and it results in increasing the interfacial tension value. This is followed by the dewetting stage wherein the receding edge of the 5CB droplet breaks down into liquid threads as the surface tension destabilizes the droplet periphery. Thereafter, these liquid threads disintegrate into miniaturized 5CB droplets via Rayleigh Plateau instability.
- The influence of temperature variation of the water bath on the recirculation rate was also analyzed. With increase in bath temperature although the recirculation rate increased due to thermal Marangoni effect, the recirculation time decreased. As hexane amount in the 5CB droplet increased, the surface tension gradient decreased. This reduced the driving force required to sustain convective flow in the bulk.

To conclude, an experimental analysis of the various instability modes depicted by the 5CB droplet on the water bath is discussed. The study performed throws light on a facile methodology developed to create miniaturized, optically active nematic droplets. An alternative method for stimulating mixing within anisotropic materials such as LC droplets has been shown.

6.2 Future Scope of Research

The different fluid dynamic phenomena associated with droplets in presence of acoustic, light and chemical potential gradient has been presented here. These systems provide various avenues of fundamental research for improving the efficacy of techniques presented as well as for modifying the application according to the objectives. The following paragraphs highlights few prospective areas of research from the chapters presented.

- Acoustically stimulated microdroplets for sensing purpose can be utilized for development of multi-analyte sensing. Utilization of multiple droplets in an array which can be simultaneously stimulated may lead to development of a multiplex detection setup. Responses can be made more precise and accurate by understanding the influence of substrate-droplet interactions during oscillation. 3D numerical simulations of the sensing mechanism may shed more light with regards to contact angle variation during oscillation, influence of pressure wave distribution over mixing of constituents and charge transfer characteristics near electrodes. Theoretical investigation of the effect of acoustic energy on reaction kinetics can be an interesting area of research that can aid in development of robust sensors.
- Scaling up of membraneless photofuel cell setups employing a microdroplet configuration can be a lucrative area of research with real world implications. Modifications within the setup concerning low-onset potential cathodes, high density fuel, inert electrodes and addition of NPs for enhancing performance, may lead to designing of problems which improve overall attributes of the device. Employing hybrid functionalities to the droplet photofuel cell such as sensing capabilities may lead to generation of systems that can be deployed in remote locations. Moreover, better dye degradation capabilities can be imparted by addition of photocatalysts with appropriate Fermi energy level.
- Liquid-on-liquid dewetting systems can be harnessed for a number of applications such as developing drug carriers, microbots for surface algae removal, energy harvesting and *in situ* reactors. Developing techniques for incorporating doped LC-composite materials towards generating large-area, functional droplets that can be employed in sensing applications can be an interesting research domain. From a fundamental viewpoint, non-linear stability analysis of the dewetting dynamics can further explore the phenomenon for eventually obtaining monodispersed droplets. Utilization of LC droplets besides nematic, such as smectic and cholesteric, can be employed to develop tunable photomasks.

Developing methodologies for incorporating such optically active photomasks in a soft photolithography application can be a potent area of research.

- Dewetting of a nematic LC droplet on a water bath can lead to a number of exciting research problems. Understanding oscillatory contact line instability for anisotropic systems on a soft, deformable interface can lead to better control over obtained miniaturized droplets. Further, droplet motility over the liquid substrate can be tuned in accordance with external gradient for application in energy harvesting, targeted drug delivery and sensing. 3D numerical simulations representing the experimental setup employed can be instrumental in developing models for validating the experimental observations. A non-linear stability analysis concerning the capillary instability induced LC droplet generation over a liquid substrate can be a stimulating area of research.

Appendix

Cleaning procedure for Glass substrates

Glass substrates of dimension 2.5 cm × 2.5 cm were employed in the experiments. The substrates were initially cut and placed in a detergent solution (SDS/water). They were rinsed with DI water and brushed. Then they were placed in a beaker containing SDS solution and sonicated for 30 min. Thereafter, the substrates were washed with DI water and submerged in boiling acetone and ethanol solutions for 10 min, respectively. The substrates were then removed were then removed and placed in a boiling solution of ammonia, hydrogen peroxide and water in 1:1:5 ratio. After maintaining the temperature for 30 min, the beaker was cooled to room temperature gradually. The substrates were then rinse with DI water and dried with N_2 gas.

Cleaning procedure for Si substrates

Si substrates with dimension 1 cm × 1 cm were employed in the experiments. The substrates were initially placed in a detergent solution (SDS/water) and a beaker containing the same was sonicated for 30 min. Thereafter, the substrates were washed with DI water and submerged in boiling acetone and ethanol solutions for 10 min, respectively. They were then removed and placed in a solution containing ammonia, hydrogen peroxide and water in 1:1:5 ratios. The solution was heated to its boiling point, and the same temperature was maintained for 30 min. After the substrates cooled down, they were thoroughly rinsed with water and dried with N_2 gas. Before using them for experiments, they were UV/Ozone treated for 15 min.

Research Output

Publications

From Thesis:

- Thakur, S., Dasmahapatra, A. K. and Bandyopadhyay D. Self-Organized Liquid Crystal Droplets as Phototunable Softmasks. *ACS Appl. Mater. Interfaces* **2021** (Accepted).
- Thakur, S.; Dasmahapatra, A. K.; Bandyopadhyay, D. Functional Liquid Droplets for Analyte Sensing and Energy Harvesting. *Adv. Colloid Interface Sci* **2021**, *294*, 102453-102483.
- Thakur, S., Bhattacharjee, M., Dasmahapatra, A. K. and Bandyopadhyay D. Acoustic Wave Catalyzed Urea Detection Utilizing a Pulsatile Microdroplet Sensor, *ACS Sustainable Chem. Eng.* **2019**, *7*, 12069-12082.
- Thakur, S., Das, N. M., Kumar, S., Dasmahapatra, A. K. and Bandyopadhyay D. Microdroplet photofuel cells to harvest high-density energy and dye degradation, *Nanoscale Adv.* **2020**, *2*, 1613-1620.
- Thakur, S., Vinod, V., Dasmahapatra, A. K. and Bandyopadhyay D. Chemotactic liquid/liquid dewetting of a nematic droplet. (*Manuscript under preparation*)

Outside Thesis:

- **Thakur, S.**, Rarotra, S., Bhattacharjee, M., Mitra, S., Natu, G., Mandal, T. K., Dasmahapatra, A. K. and Bandyopadhyay D. Self-Organized Large-Scale Integration of Mesoscale-Ordered Heterojunctions for Process-Intensified Photovoltaics, *Phys. Rev. Applied* **2018**, *10*, 064012-26.
- Ravi, B., Chakraborty, S., Bhattacharjee, M., Bhandaru, N., **Thakur, S**., Pattader, P.S.G., Mukherjee, R., Bandyopadhyay, D. Pattern Directed Phase Transitions and VOC Sensing of Liquid Crystal Films. *Ind. Eng. Chem. Res.* **2020**, *59*, 1902-1913.

Patent

Bhattacharjee, M., **Thakur, S.**, Bandyopadhyay, D. and Indian Institute of Technology Guwahati. Acoustic diagnostic point-of-care testing device for blood urea detection, Indian patent, 201731037223, 2017.

Book Chapter

Thakur, S., Dasmahapatra, A. K. and Bandyopadhyay D. "Emergence of Multi-faceted Nano/Micro Scale Technologies for Sustainable Energy Harvesting", Sustainable Fuel Technologies Handbook, Elsevier, 2020.

Conferences

"Oscillatory Microdroplet Constituted Urea Biosensor Stimulated by Acoustic Waves", Gordon Research Conference on Colloidal, Macromolecular and Polyelectrolyte Solutions, Ventura, CA, USA. February 2–7, 2020. (***SERB, Govt. Of India ITS***)

"Acoustic Wave Stimulated Microdroplet Based Urea Biosensor", COMPFLU, 13th International Conference on Complex Fluids and Soft Matter, IISER Bhopal, December 5-7, 2019.

"Acoustic Wave Stimulated Microdroplet: A Sound Sensor and Urea Biosensor", Research Conclave, IIT Guwahati, 14-17 March, 2019. (***Best Poster Award***)

"Large Scale Self-Organized Conducting Polymer Heterostructures for Photovoltaic Applications". Oral presentation at COMPFLU, 12th International Conference on Complex Fluids and Soft Matter, IIT Roorkee, December 6-9, 2018.